DEVELOPING A SYNTHETIC TOOLKIT FOR MULTI-COMPONENT METAL–ORGANIC FRAMEWORKS

A Dissertation

by

SHUAI YUAN

Submitted to the Office of Graduate and Professional Studies of
Texas A&M University
in partial fulfillment of the requirements for the degree of

DOCTOR OF PHILOSOPHY

Chair of Committee,	Hong-Cai Zhou
Committee Members,	Marcetta Y. Darensbourg
	François P. Gabbaï
	Xiaofeng Qian
Head of Department,	Simon W. North

August 2018

Major Subject: Chemistry

ABSTRACT

Metal–organic frameworks (MOFs) are an emerging class of porous materials constructed from metal-containing nodes and organic linkers. Due to their structural and functional tunability as well as their ever-expanding application scope, MOFs have become one of the most fascinating class of materials for both scientists and engineers. MOFs provide ideal platforms to arrange various functional groups at atomic precision within the periodic lattice, leading to emergent synergistic effects in catalysis and gas adsorption. This requires the construction of MOFs from multiple metal nodes and/or organic linkers. However, the structural and compositional compilation of multi-component MOFs have posed a challenge for their synthesis. The complexity of MOFs is ultimately limited by the conventional "one-pot" synthetic method, which lacks control over the assembly of each framework component. By judicious kinetic control, we have developed stepwise synthetic strategies to build multi-component MOFs by "layer-on" molecular elaborations to preformed frameworks. A series of synthetic strategies have been developed which together form a synthetic toolkit through which a target multi-component MOF can be retro-synthetically designed and synthesized.

The first section briefly summarized the development of MOFs to provide an overview on their structural design, synthesis and potential applications.

In the second section, we focused on the synthesis of heterometallic MOFs using preformed heterometallic clusters to avoid undesired by products formed by other metal clusters.

In the third section, the mixed-linker MOFs with crystallographically ordered structures were constructed using sequential linker installation.

In the fourth section, we enriched the MOF synthetic toolkit by introducing linker labilization, in which selective linkers were exchanged, cleaved, and removed to create controlled defects in MOFs. The defective MOFs act as versatile platforms to create hierarchical structures and incorporate other coordinative assemblies.

In the fifth section, we realized the "retrosynthesis" multi-component MOFs by sequentially applying the above mentioned synthetic methods under kinetic considerations.

In summary, a series of synthetic methods were developed to construct multi-component MOFs with unprecedented complexity. These methods allow the rational design and synthesis of MOFs for specific applications including gas storage and separation, chemical sensing, energy harvesting and storage, catalysis, and biomedicine.

DEDICATION

This work is dedicated to my beloved family and friends for their constant support.

ACKNOWLEDGEMENTS

I would like to thank my committee chair, Dr. Hong-Cai Joe Zhou, and my committee members, Dr. François Gabbaï, Dr. Marcetta Darensbourg, and Dr. Xiaofeng Qian, for their guidance and support throughout the course of this research.

I am thankful to all the group members especially Dr. Jun-Sheng Qin and Dr. Ying-Pin Chen for their help during my graduate studies.

Thanks also go to the collaborators especially Dr. Jinglin Zuo and Mr. Jian Su from Nanjing University, Dr. Xiaodong Zou and Dr. Zhihao Huang from Stockholm University, Dr. Hailong Jiang and Ms. Haiqun Xu from University of Science and Technology of China, Dr. Zhiyuan Gu and Ms. Ming Xu from Nanjing Normal University. Their great work strongly supported our research.

Thanks also go to my friends and colleagues and the department faculty and staff for making my time at Texas A&M University a great experience.

Finally, thanks to friends, families for their encouragement. I would especially like to thank my fiancée her patience and love.

CONTRIBUTORS AND FUNDING SOURCES

Contributors

This work was supervised by a dissertation committee consisting of Professor Hong-Cai Zhou [advisor], Professor François Gabbaï, Professor Marcetta Darensbourg of the Department of Chemistry [Home Department], and Professor Xiaofeng Qian of the Department of Materials Science and Engineering [Outside Department]. The advisor and committee members provided insightful suggestions on the dissertation.

All work for the dissertation was completed by the student, in collaboration with Jun-Sheng Qin, Ying-Pin Chen, Lanfang Zou, Tian-Fu Liu of the Department of Chemistry, Texas A&M University. Thanks also go to the collaborators outside the university including Dr. Jinglin Zuo and Mr. Jian Su from Nanjing University, Dr. Xiaodong Zou and Dr. Zhihao Huang from Stockholm University, Dr. Hailong Jiang and Ms. Haiqun Xu from University of Science and Technology of China, Dr. Zhiyuan Gu and Ms. Ming Xu from Nanjing Normal University.

Funding Sources

This work was supported by: 1) Center for Gas Separations Relevant to Clean Energy Technologies, an Energy Frontier Research Center funded by the U.S. Department of Energy, Office of Science, Office of Basic Energy Sciences under Award Number DE-SC0001015; 2) the Hydrogen and Fuel Cell Program under Award Number DE-FC36-07G017033; 3) U.S. Department of Energy, Office of Fossil Energy, National Energy Technology Laboratory (DE-FE0026472); 4) Robert A. Welch Foundation (A-0030); 5) National Science Foundation Small Business Innovation Research (NSF-SBIR) under Grant No. 1632486.

NOMENCLATURE

ABTS	2,2'-Azino-Bis(3-Ethylbenzothiazoline-6-Sulphonic acid)
AcOH	Acetic Acid
BDC	Terephthalate
BET	Brunauer-Emmett-Teller
CB	Conduction Band
CBM	Conduction Band Minimum
cRED	Continuous Rotation Electron Diffraction
CYCU	Chung Yuan Christian University
Cyt c	Cytochrome Complex
DCDPS	4,4'-Dicarboxydiphenylsulfone
DFT	Density Functional Theory
DME	Ethylene Glycol Dimethyl Ether
DMF	N,N-Dimethylformamide
DMSO	Dimethyl sulfoxide
DOS	Density of State
EPR	Electron Paramagnetic Resonance
FT-IR	Fourier transform infrared
GC	Gas Chromatograph
H_2AZDC	Azobenzene-4,4'-Dicarboxylic Acid
H_2BDC	Terephthalic Acid
H_2BDDC	4,4'-(1,3-Butadiyne-1,4-Diyl)Bis(3-Methylbenzoic Acid)

H_2BPDC	4,4'-Biphenyldicarboxylate
H_2BPYDC	2,2'-Bipyridne-5,5'-Dicarboxylic Acid
H_2CBAB	4-Carboxybenzylidene-4-Aminobenzoic Acid
H_2FA	Fumaric Acid
H_2NDC	2,6-Naphthalene-Dicarboxylic Acid
H_2TPDC	2',5'-Dimethylterphenyl-4,4"-Dicarboxylic Acid
HKUST	Hong Kong University of Science and Technology
HOMO	Highest Occupied Molecular Orbital
INA	Isonicotinate
LMCT	Ligand to Metal Charge Transfer
LUMO	Lowest Unoccupied Molecular Orbitals
MOF	Metal-Organic Framework
MTV-MOFs	Multivariable MOFs
NDC	2,6-Naphthalenedicarboxylate
NMR	Nuclear Magnetic Resonance
o-PDA	o-Phenylenediamine
PCN	Porous Coordination Network
PCP	Porous Coordination Polymer
PSM	Post-Synthetic Modification
PTBB	para-tert-Butylbenzoate
PXRD	Powder X-Ray Diffraction
SBU	Secondary Building Unit
SC-XRD	Single Crystal X-Ray Diffraction

SEM	Scanning Electron Microscopic
TAS	Transient Absorption Spectroscopy
TCPP	Tetrakis(4-Carboxyphenyl)Porphyrin
TEM	Transmission Electron Microscopy
TEOA	Triethanolamine
TGA	Thermal Gravimetric Analysis
TPA	4,4',4''-Tricarboxytriphenylamine
UiO	Universitetet i Oslo
VB	Valence Band
VBM	Valence Band Maximum

TABLE OF CONTENTS

Page

LIST OF FIGURES

Page

LIST OF TABLES

Page

1. INTRODUCTION*

According to IUPAC, metal–organic frameworks, or MOFs, are defined as coordination networks with organic ligands containing potential voids.[1] As shown in Figure 1a, MOFs are usually constructed from inorganic nodes and organic linkers which are connected into framework structures through coordination bonds. The void created between periodically arranged framework fragments are ideal for the adsorption and, in some cases, conversion of guest molecules. MOFs are among one of the most porous materials, with the record high Brunauer–Emmett–Teller (BET) surface area of 7,140 $m^2 \cdot g^{-1}$.[2] More importantly, the structure and pore environment of MOFs can be tailored with exquisite precision by the design of metal nodes and organic linkers. The inorganic nodes are usually single metal cations or metal clusters,[3-4] while the organic linkers of MOFs can be carboxylates, heterocyclic compounds, etc.[5] Almost all the metals elements in the periodic table can be used to construct inorganic nodes of MOFs. (Figure 1b).

Compared with inorganic porous materials such as zeolites and mesoporous metal oxides, the structures and functions of MOFs can be readily tuned by organic linkers.[6] Linkers with desired coordination moieties, functional groups, lengths, and geometries can be rationally designed to build MOFs (Figure 1c). The ability to vary both the metal and organic ligands within the framework has led to the discovery of more than 70,000 MOFs over the past two decades.[7] Potential applications of MOFs range from H_2 storage, CH_4 storage, CO_2 capture, separations,

*Reproduced in part with permission from: Yuan, S.; Qin, J.-S.; Lollar, C. T.; Zhou, H.-C., Stable Metal–Organic Frameworks with Group 4 Metals: Current Status and Trends. *ACS Cent. Sci.*, **2018**, *4*, 440-450. Copyright 2018 American Chemical Society. Yuan, S.; Qin, J.-S.; Li, J.; Huang, L.; Feng, L.; Fang, Y.; Lollar, C.; Pang, J; Zhang, L.; Sun, D.; Alsalme, A.; Cagin, T.; Zhou, H.-C. Retrosynthesis of multi-component metal−organic frameworks, *Nat. Commun.* **2018**, *9*, 808. Copyright 2018 Nature Publishing Group.

catalysis, sensing, and biomedicine, with many more areas waiting to be explored.[8-10] There is no doubt that MOFs are among one of the fastest growing class of materials.

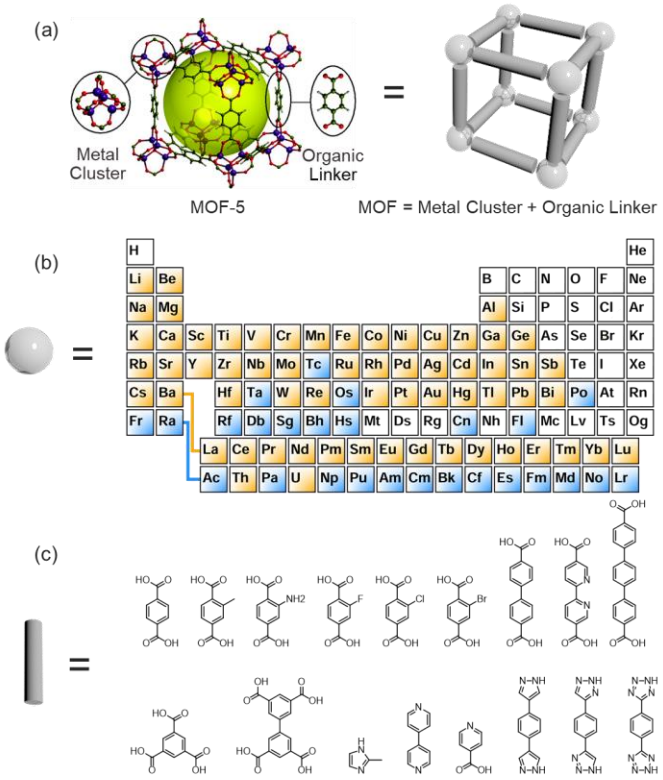

Figure 1. (a) A representative MOF structure composed of metal nodes and organic linkers. (b) Metal elements that have been reported as nodes of MOFs (colored by orange) highlighted in a Periodic Table. (c) Examples of organic linkers featuring different functional groups, lengths, connection numbers, and coordination groups.

1.1 A Brief History

To understand the current status and trends of MOF field, it is necessary to briefly introduce its history (Figure 2). MOFs are essentially a subclass of coordination polymers with intrinsic porosity. Coordination polymers with framework structures similar to that of MOFs have been existing for a long time. Prussian blue, $Fe_4[Fe(CN)_6]_3$, was synthesized as early as 1700s, in which six-coordinated Fe^{2+} and Fe^{3+} were bridged by CN^- to form a 3D framework with cubic network

topology. Although the cavity of this material is too small for any substrate, it inspires researchers to construct porous frameworks with similar structures.

With the development of supramolecular chemistry, coordination polymers bearing large cavities were assembled in 1990s.[11] For example, the combination of Cu^{+} with tetracyano ligands gave rise to a network with diamond structures. The open cavity within the structure allows the incorporation of guest molecules. However, this type of coordination polymers does not possess permanent porosity because their structures tend to collapse after the removal of solvents or guest molecules. Coordination polymers were long believed to be too frail to maintain permanent porosity without guest molecules.

The report of MOF-5 in 1999 represents a breakthrough in the field.[12] MOF-5 is composed of Zn_4O node connected by 1,4 benzenedicarboxylate (BDC) ligand into a cubic network. The rigid framework maintained its porous structure after the exchange and removal of solvents. The periodically arranged micropores and highly exposed inner surface make MOF-5 the most porous material at that time. The field of MOFs has been flourishing ever since. Researchers are trying to extend the pore size, enhance the stability and discover new properties of MOFs.

Although efforts were made to make rigid MOFs with permanent porosity, it is not surprising to find that some MOFs can be flexible. In fact, the framework collapse of many early MOFs upon guest uptake/removal can be regarded as a flexible behavior. Therefore, it is difficult to find the first flexible MOF. A prominent example of framework flexibility is the “breathing behavior” firstly observed in MIL-53 series in 2002, in which the framework experiences a reversible structural change as a result of gas adsorption/desorption.[13] Later on, flexible MOFs that undergoes phase transformation upon stimuli such as guest molecules, temperature, or pressure

were synthesized, which promotes the development of smart absorbents with higher storage capacities and efficient gas release.[14]

In the early stages of MOF research, most of MOFs are microporous with pore size smaller than 2nm. The microporous MOFs are suitable for gas adsorption. However, the limited pore size excludes larger guests and thus hinders their applications in catalysis. The report of ultra-porous MIL-101 in 2006 has broken through the limitation.[15] MIL-101 features two mesopores with diameters of 2.9 and 3.4 nm. Although MIL-101 is not the first mesoporous MOF, the good chemical stability and facile synthesis of this material has significantly expanded the applications of MOFs in catalysis and biomedicine.

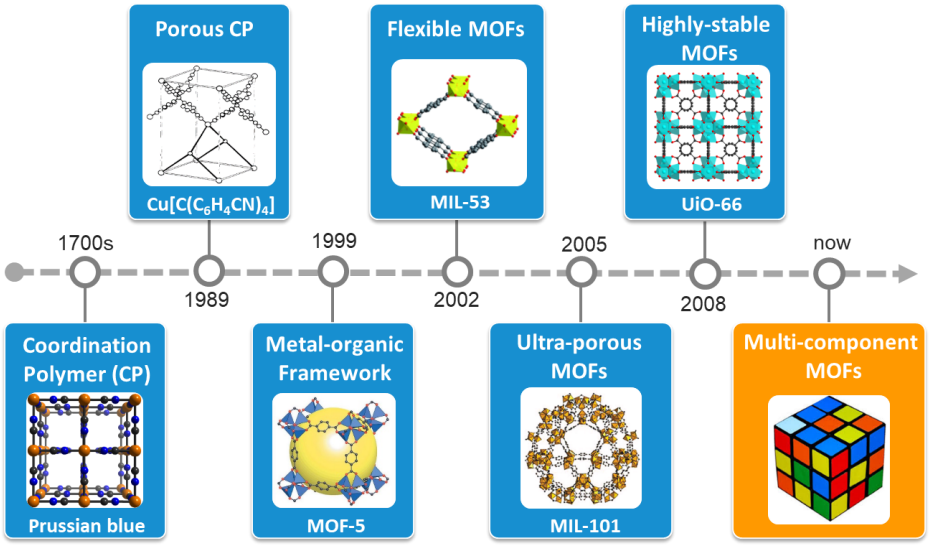

Figure 2. A history timeline of MOFs.

With the continuously expanded application fields of MOFs, their stability has become a major limitation. Therefore, researchers have been focusing on the development of high-valent metal-based MOFs with enhanced chemical stability due to the strong metal–ligand bonds. In 2008, the first Zr-MOF, UiO-66, was reported. Since then, Zr-MOFs have drawn increasing attention because of their high stability which promises wide range of applications.[16] Within ten

years, UiO-66, a representative example of Zr-MOFs, has almost dethroned MOF-5 as a one of the benchmark MOFs.

What is the future of MOFs? The current status and trends of MOF research indicate that the next generation of MOFs should be multi-component MOFs combining synergistic functional groups with controlled sequences in an ordered framework structure.[17-37] The ability to arrange multiple metals and organic functional groups in desired proximity at atomic precision within a periodic lattice is expected to promote fascinating developments in basic sciences and applications. For example, the combination of diverse metal clusters in heterometallic MOFs can lead to emergent synergistic effects in catalysis and gas adsorption.[38-41] Therefore, this thesis focus on the investigation of multicomponent MOFs in expecting to expand the complexity and diversity of known porous materials.[42-43]

1.2 Multi-component MOFs

Yaghi and coworkers proposed that the materials beyond should have multiple building units arranged in specific sequences within a MOF crystal.[44] Kitagawa also predicted that the future porous materials should possess features include hierarchy, hybrid, anisotropy, asymmetry, disorder and defect. Constructing MOFs from multiple components is a way to achieve complex structures and sophisticated applications.

Multiple components can be incorporated into MOFs in different ways (Figure 3). Various functional groups can be anchored onto different linkers to form mixed-linker MOFs. Multiple metals can be introduced into two or more inorganic nodes to form heterometallic MOFs. Defective MOFs represent another class of multi-components MOFs in which defects offers additional opportunities to tailor their functions. Herein, different types of multi-component MOFs will be outlined.

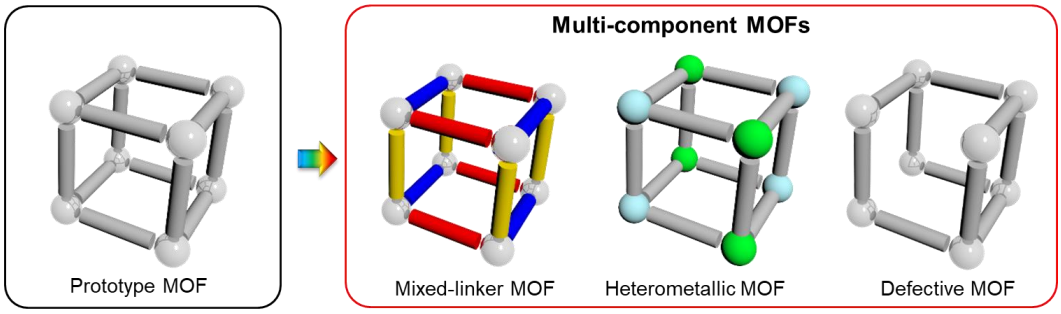

Figure 3. Strategies to construct multi-component MOFs using mixed-linkers, mixed metals or creating defects.

1.2.1 Mixed-Linker MOFs

A simple approach towards multi-component MOFs is to adopt a series of organic linkers that have the same length, geometry and connectivity but different substitutes. Yaghi and coworkers have incorporated up to eight different functionalities in to a MOF-5 backbone which produces MTV-MOFs (multivariable MOFs) with emergent properties that are different from any of the single linker based MOFs.(Figure 4a)[42] However, the position of these functional groups are difficult to control because of the disorder distribution of linkers.[45] This problem can be solved by using linkers with different symmetry and/or connectivity. Organic linkers with different connection numbers, symmetries and/or lengths can be differentiated from one another in the crystal lattice. This strategy has been well demonstrated by Telfer and coworkers who reported the synthesis of a family of isoreticular MOFs with three topologically distinct carboxylate linkers and Zn_4O inorganic nodes (Figure 4b).[46] Considering the complexity of the quaternary system, one challenge of this method is the design of structure and formulation of compatible linkers. Another challenge is to control the purity of the product as multiple phases can be formed from the multi-component system.[47] To address those problems, linker installation method was developed to construct quaternary MOFs that contains up to three linkers with different lengths (Figure 4c). This

strategy utilizes a stable MOF with inherent coordination-unsaturated-sites as matrix and post synthetically installs linkers with different functionality and length through kinetic control.[29] Complex yet controllable pore environments can therefore be formed, leading to emerging properties in gas adsorption and catalysis.

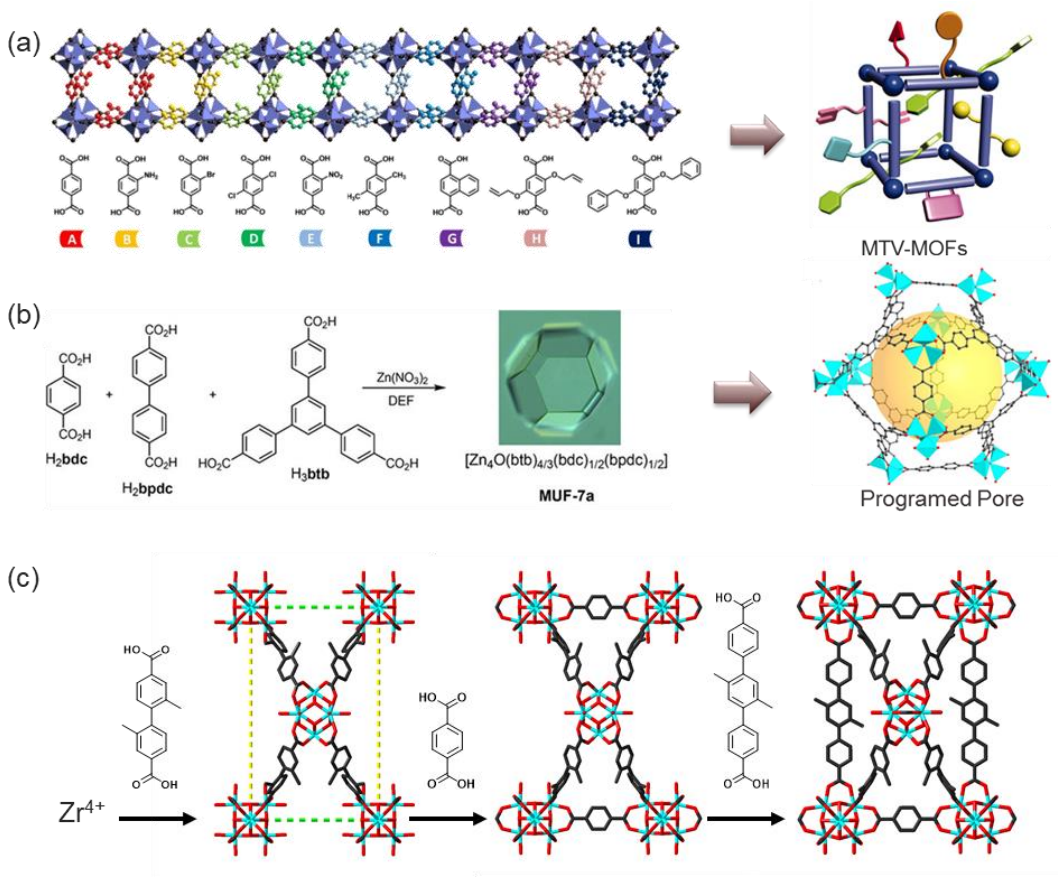

Figure 4. Three methods to synthesize mixed-linker MOFs. (a) MTV-MOF synthesized by copolymerization of linkers with the same length, geometry and connectivity but different substitutes.(b) Programed pore architecture synthesized by multiple linkers with different symmetry and/or connectivity. (c) Sequential linker installation.

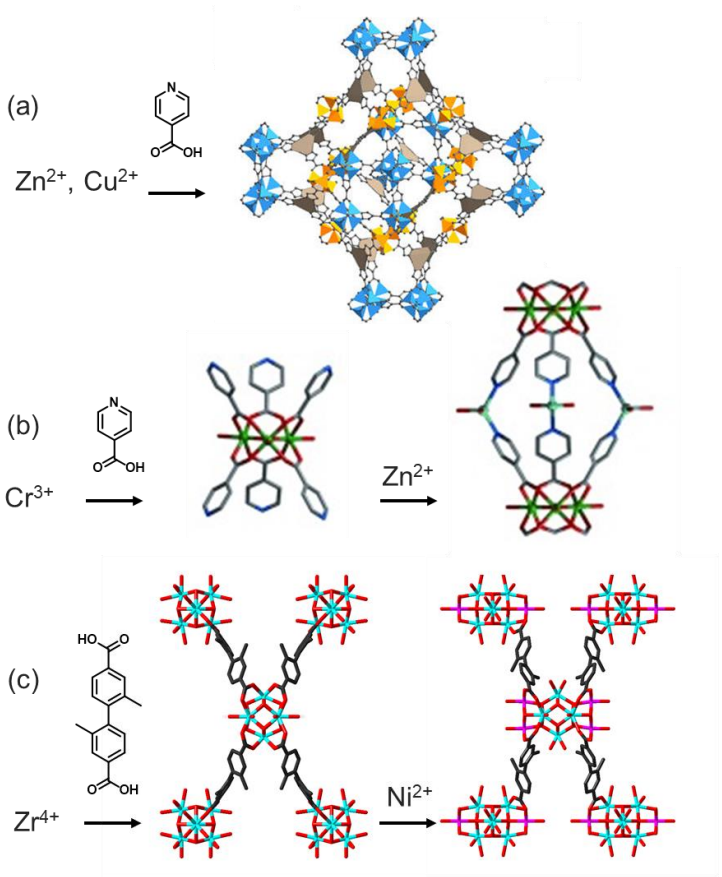

Figure 5. Three methods to synthesize heterometallic MOFs including (a) one pot reaction, (b) stepwise assembly, and (c) cluster metalation.

1.2.2 Heterometallic MOFs

In addition to mixing linker strategy, the complexity of MOFs can also be increased by employing multiple metals or inorganic secondary building units (SBUs). Among the limited number of heterometallic MOFs with different metal SBUs, most of the structures are synthesized in "one-pot" reactions using bifunctional linkers that bind to two different metal clusters. A handful of porous heterometallic frameworks were reported using bifunctional linkers such as pyrazolecarboxylate, isonicotinate and their derivatives.[48-51] For example, Qiaowei Li and coworkers reported the one-pot synthesis of a heterometallic MOF combining Zn-based octahedral SBUs, Zn-based square pyramidal SBUs, and Cu-based triangular SBUs (Figure 5a).[43] Very

recently, this "one-pot" strategy was further developed by Rosi group in a comprehensive work.[52] They used bifunctional INA linker to connect hard-acid metal cations (Zr^{4+}, Hf^{4+}, and Dy^{3+}) and soft metal cations (Co^{2+}, Ni^{2+}, Cu^{+}, Cu^{2+}, and Cd^{2+}) into a series of bimetallic MOFs with controlled topologies.

Compared with mixed-linker MOFs, it is more challenging to synthesize multi-component MOFs with different inorganic SBUs. The synthetic difficulty of heterometallic MOFs is attributed to the sensitivity of cluster formation to reaction conditions and, in many cases, the incompatibility of the formation conditions of different clusters. This limitation has prevented the integration of different inorganic SBUs into MOFs in "one-pot" reactions. Stepwise synthetic methods were explored to take control over the formation of different metal clusters independently within a heterometallic MOF. For example, the preformed clusters terminated by pyridyl groups were used as starting material to generate heterometallic MOFs by combining with various soft metal cations (Figure 5b).[53-54] Postsynthetic modification (PSM) brings new opportunity to generate heterometallic MOFs from monometallic MOFs as templates. Heterometals can be anchored onto the chelating sites of organic ligands or incorporated into the inorganic SBUs by metathesis.[55-56] Furthermore, recent development of Zr-MOFs enables the application of a wider range of PSM reactions due to their high stability and strong tolerance towards defects.[31] Metal cations and metal-organic complexes can be attached to the coordinatively unsaturated Zr_6 clusters without losing the structural integrity.[29, 57-58] For example, Hupp et al reported a series of mixed metal MOFs with different catalytic properties by depositing metal ions on Zr_6 clusters.[59] We provided clear single crystal crystallographic evidence for the formation process of a Zr_6Ni_4 cluster based MOF by the metalation of a Zr-MOF (Figure 5c).[60] However, most of the modification processes rely on the metalation of ligand or the replacement of metal cations of inorganic SBUs, which do not alter the

topology of the frameworks. Therefore, the structural diversity of heterometallic MOFs cannot be fully explored by the traditional PSM method. Recently, we developed a series of methods to sequentially install metal clusters and organic linkers into a preformed Zr-MOF, which leads to the discovery of various multi-component coordination assemblies.[24, 28] Along this line, a variety of heterometallic MOFs with desired structures and functions were designed by incorporating heterometals into existing MOFs.

1.2.3 Defective MOFs

Although often being overlooked, defective MOFs represent a unique type of multi-components MOFs. Technically, defect sites can be regarded as a component with different properties than that of original metals or ligands in MOFs. Theoretically, any MOF should contain certain amounts of defects.[61-65] A representative example is the Zr-MOF which can tolerant a high concentration of defects while maintain the crystallinity and chemical stability.[66-67] The defects strongly affects many properties of MOFs including the pore size, surface area, and catalytic activity. For example, the defects created by partially removal of linkers will expose coordinatively unsaturated metal sites for various catalytic reactions, such as ring-opening of epoxides,[68] cross-aldol condensation reactions,[69] isomerization of α-pinene oxide,[70] and Meerwein–Ponndorf–Verley reactions.[71] Furthermore, the coordination vacancy on the defect sites provides a chemical handle to modify MOFs with organic moieties and metal species.[33, 72]

1.3 Aims of the Project

Despite numerous of advantages, the structural and compositional compilation of multi-component MOFs has posed a challenge for their synthesis. The traditional one-pot synthesis of MOFs lacks control over framework assembly, therefore limited complexity of multi-component MOFs. This dissertation aims to develop stepwise synthetic methods to build multi-component

MOFs in a controlled manner. By judicious kinetic control, we have developed a series of stepwise synthetic strategies to build multi-component MOFs by "layer-on" molecular elaborations to preformed frameworks. Together, these strategies form a synthetic toolkit through which a target MOF can be retrosynthetically designed and synthesized (Figure 6). In this dissertation, we will introduce the synthetic toolkit and their applications in the construction of complex MOFs that would otherwise be difficult or unforeseeable to prepare.

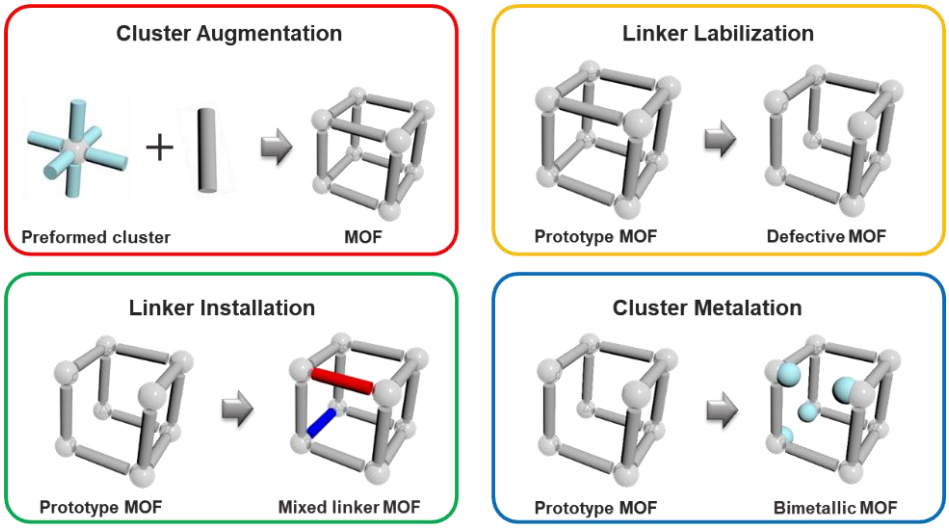

Figure 6. Synthetic methods for multi-component MOFs in this project.

Firstly, the method of cluster augmentation was explored to construct bimetallic MOFs from preformed bimetallic clusters as starting materials to control the framework structures and avoid by-products formed from other clusters.[35] Secondly, linker labilization method was invented, in which selective linkers were exchanged, cleaved, and removed to create defective MOFs controllably.[17] The defects not only expanded the pore sizes, but also act as chemical handles to further anchor linkers and metals into MOFs.[31, 34] Taking advantage of defects, linker installation and cluster metalation methods were developed to precisely place functionalized organic linkers or redox active transition metals in a defective MOF matrix.[19, 24, 29] Together, the synthetic toolkit

enables the preparation of a target MOF retrosynthetically, just like that of a natural product.[28] These MOFs are critical for a variety of applications including gas storage, separation, energy harvesting, and catalysis.

2. STEPWISE SYNTHESIS OF BIMETALLIC MOFS*

2.1 Introduction

Because of their intrinsically porous structures and unlimited tunability, MOFs have attracted considerable research interest in the past decades.[52, 73-78] Among the numerous MOFs, heterometallic MOFs represent a unique class of MOFs that compose of heterometallic clusters or different inorganic secondary building units (SBUs).[79-80] The combination of multiple metals has contributed to the structural diversity and functional complexity of MOF materials. Furthermore, the ability to arrange different metals at atomic precision within a porous framework has promoted fascinating developments in basic sciences and applications. For example, the combination of diverse metal clusters in heterometallic MOFs can lead to emergent synergistic effects in catalysis and gas adsorption.[38-41] However, the structural and compositional compilation of heterometallic MOFs posed a challenge for the synthesis.

Among the limited number of heterometallic MOFs, most of the structures are synthesized in "one-pot" reactions using a mixture of metal salts as starting materials. For example, Rosi group recently reported a series of bimetallic MOFs with controlled topologies by connecting hard-acid metal cations (Zr^{4+}, Hf^{4+}, and Dy^{3+}) and soft metal cations (Co^{2+}, Ni^{2+}, Cu^{+}, Cu^{2+}, and Cd^{2+}) with a bifunctional isonicotinate (INA) linker. The synthetic difficulty of heterometallic MOFs is attributed to the sensitivity of cluster formation to reaction conditions and, in many cases, the incompatibility of the formation conditions of different clusters. This limitation has prevented the

*Reproduced in part with permission from: Yuan, S.; Qin, J.-S.; Xu, H.-Q.; Su, J.; Rossi, D.; Chen, Y.; Zhang, L.; Lollar, C.; Wang, Q.; Jiang, H.-L.; Son, D. H.; Xu, H.; Huang, Z.; Zou, X.; Zhou, H.-C., "$[Ti_8Zr_2O_{12}(COO)_{16}]$ Cluster: An ideal inorganic building unit for photoactive metal–organic frameworks." *ACS Cent. Sci.*, **2018**, *4*, 105-111. Copyright 2018 American Chemical Society.

integration of different metals into MOFs in "one-pot" reactions. To take control over the formation of heterometallic MOFs, we propose to use preformed heterometallic metal clusters as starting materials. The preassembled heterometallic metal clusters will maintain their structures throughout the reaction, avoiding the formation of by product caused by other metal clusters. A bimetallic cluster, $[Ti_8Zr_2O_{12}(COO)_{16}]$, was discovered as a nearly ideal building unit for MOFs. The Ti-Zr bimetallic cluster act as a $Ti_x/Zr_{(1-x)}O_2$ nanoparticles which endows photocatalytic activity to the framework. A family of isoreticular photoactive MOFs were assembled and their orbital alignments were fine-tuned by rational functionalization of organic linkers under computational guidance. These MOFs demonstrate high porosity, excellent chemical stability, tunable photo-response, and good activity towards photocatalytic hydrogen evolution reactions.[35]

2.2 Experimental Section

2.2.1 Materials and Instrumentation.

All reagents and solvents were commercially available and used as received. Powder X-ray diffraction (PXRD) was carried out with a Bruker D8-Focus Bragg-Brentano X-ray Powder Diffractometer equipped with a Cu sealed tube (λ = 1.54178 Å) at 40 kV and 40 mA. The UV-Vis absorption spectra were recorded on a Shimadzu UV-2450 spectrophotometer.

2.2.2 MOF Syntheses

Synthesis of $[Ti_8Zr_2O_{12}(MeCOO)_{16}]$. $ZrCl_4$ (50 mg), $Ti(O^iPr)_4$ (0.1 mL), acetic acid (0.5 mL), and acetonitrile (3 mL) were charged in a Pyrex vial. The mixture was heated in a 100 ºC oven for 24 h. After cooling down to room temperature, colorless crystals were harvested.

Synthesis of $[Ti_8Zr_2O_{12}(EtCOO)_{16}]$. $ZrCl_4$ (50 mg), $Ti(O^iPr)_4$ (0.1 mL), propionic acid (0.5 mL), and acetonitrile (3 mL) were charged in a Pyrex vial. The mixture was heated in a 100 ºC oven for 24 h. After cooling down to room temperature, colorless crystals were harvested.

Synthesis of [$Ti_8Zr_2O_{12}(PhCOO)_{16}$]. $ZrCl_4$ (50 mg), $Ti(O^iPr)_4$ (0.1 mL), benzoic acid (500 mg), and DMF (1 mL) were charged in a Pyrex vial. The mixture was heated in a 140 ºC oven for 24 h. After cooling down to room temperature, colorless crystals were harvested.

Synthesis of [$Ti_8Zr_2O_{12}$(p-TolCOO)$_{16}$]. $ZrCl_4$ (50 mg), $Ti(O^iPr)_4$ (0.1 mL), p-toluic acid (500 mg), and DMF (1 mL) were charged in a Pyrex vial. The mixture was heated in a 140 ºC oven for 24 h. After cooling down to room temperature, colorless crystals were harvested.

Synthesis of [$Ti_8Zr_2O_{12}(PTBB)_{16}$]. $ZrCl_4$ (50 mg), $Ti(O^iPr)_4$ (0.1 mL), p-*t*-butyl benzoic acid (500 mg), and acetonitrile (3 mL) were charged in a Pyrex vial. The mixture was heated in a 100 ºC oven for 24 h. Colorless crystals were directly collected from hot acetonitrile.

Synthesis of PCN-415. [$Ti_8Zr_2O_{12}(MeCOO)_{16}$] cluster (100 mg), terephthalic acid (800 mg), trifluoroacetic acid (1 mL), and DMF (15 mL) were charged in a Pyrex vial. The mixture was heated in a 140 ºC oven for 24 h. Alternatively, [$Ti_8Zr_2O_{12}(MeCOO)_{16}$] cluster can be formed *in situ* without separation in the following manner: $ZrCl_4$ (50 mg), $Ti(O^iPr)_4$ (0.1 mL), acetic acid (0.5 mL), and DMF (5 mL) were charged in a Pyrex vial and heated in a 100 ºC oven for 24 h. Terephthalic acid (800 mg), trifluoroacetic acid (1 mL), and DMF (10 mL) were subsequently added to the mixture. The resulting mixture was heated in a 140 ºC oven for another 24 h. After cooling down to room temperature, a white crystalline powder was harvested.

Synthesis of PCN-416. $ZrCl_4$ (50 mg), $Ti(O^iPr)_4$ (0.1 mL), acetic acid (0.5 mL), and DMF (5 mL) were charged in a Pyrex vial and heated in a 100 ºC oven for 24 h. To the mixture was added 2,6-naphthalenedicarboxylic acid (1000 mg), trifluoroacetic acid (1 mL), and DMF (25 mL). The mixture was heated in a 140 ºC oven for another 24 h. After cooling down to room temperature, a pale yellow crystalline powder was harvested.

Synthesis of PCN-415-$(NH_2)_{0.3}$. $ZrCl_4$ (50 mg), $Ti(O^iPr)_4$ (0.1 mL), acetic acid (0.5 mL), and DMF (5 mL) were charged in a Pyrex vial and heated in a 100 ºC oven for 24 h. Terephthalic acid (560 mg), 2-aminoterephthalic acid (262 mg), trifluoroacetic acid (1 mL), and DMF (10 mL) were subsequently added to the mixture. The resulting mixture was heated in a 140 ºC oven for another 24 h. After cooling down to room temperature, a yellow crystalline powder was harvested. The mole ratio of amino-functionalized linker was determined to be 16% by ^{1}H-NMR.

Synthesis of PCN-415-$(NH_2)_{0.5}$. $ZrCl_4$ (50 mg), $Ti(O^iPr)_4$ (0.1 mL), acetic acid (0.5 mL), and DMF (5 mL) were charged in a Pyrex vial and heated in a 100 ºC oven for 24 h. Terephthalic acid (400 mg), 2-aminoterephthalic acid (436 mg), trifluoroacetic acid (1 mL), and DMF (10 mL) were subsequently added to the mixture. The resulting mixture was heated in a 140 ºC oven for another 24 h. After cooling down to room temperature, a yellow crystalline powder was harvested. The mole ratio of amino-functionalized linker was determined to be 35% by ^{1}H-NMR result.

Synthesis of PCN-415-$(NH_2)_{0.7}$. $ZrCl_4$ (50 mg), $Ti(O^iPr)_4$ (0.1 mL), acetic acid (0.5 mL), and DMF (5 mL) were charged in a Pyrex vial and heated in a 100 ºC oven for 24 h. Terephthalic acid (240 mg), 2-aminoterephthalic acid (610 mg), trifluoroacetic acid (1 mL), and DMF (10 mL) were subsequently added to the mixture. The resulting mixture was heated in a 140 ºC oven for another 24 h. After cooling down to room temperature, a yellow crystalline powder was harvested. The mole ratio of amino-functionalized linker was determined to be 59% by ^{1}H-NMR result.

Synthesis of PCN-415-NH_2. $ZrCl_4$ (50 mg), $Ti(O^iPr)_4$ (0.1 mL), acetic acid (0.5 mL), and DMF (5 mL) were charged in a Pyrex vial and heated in a 100 ºC oven for 24 h. 2-Aminoterephthalic acid (872 mg), trifluoroacetic acid (1 mL), and DMF (10 mL) were subsequently added to the mixture. The resulting mixture was heated in a 140 ºC oven for another 24 h. After cooling down to room temperature, a yellow crystalline powder was harvested.

Synthesis of PCN-415-($2NH_2$)$_{0.5}$. $ZrCl_4$ (50 mg), Ti(O^iPr)$_4$ (0.1 mL), acetic acid (0.5 mL), and DMF (5 mL) were charged in a Pyrex vial and heated in a 100 ºC oven for 24 h. Terephthalic acid (400 mg), 2,5-diaminoterephthalic acid (472 mg), trifluoroacetic acid (1 mL), and DMF (10 mL) were subsequently added to the mixture. The resulting mixture was heated in a 140 ºC oven for another 24 h. After cooling down to room temperature, a brown crystalline powder was harvested. The mole ratio of diamino-functionalized linker was determined to be 28% by ^{1}H-NMR result.

Synthesis of PCN-416-($2NH_2$)$_{0.5}$. $ZrCl_4$ (50 mg), Ti(O^iPr)$_4$ (0.1 mL), acetic acid (0.5 mL), and DMF (5 mL) were charged in a Pyrex vial and heated in a 100 ºC oven for 24 h. To the mixture was added 2,6-naphthalenedicarboxylic acid (500 mg), 4,8-diaminonaphthalene-2,6-dicarboxylic acid (570 mg), trifluoroacetic acid (1 mL), and DMF (25 mL). The mixture was heated in a 140 ºC oven for another 24 h. After cooling down to room temperature, a pale yellow crystalline powder was harvested. The mole ratio of diamino-functionalized linker was determined to be 32% by ^{1}H-NMR result.

N_2 Sorption Isotherm. Before gas sorption experiments, as-synthesized samples were washed with DMF and immersed in acetone for 3 days, during which the solvent was decanted and freshly replenished three times. The solvent was removed under vacuum at 100 ºC, yielding porous material. Gas sorption measurements were then conducted using a Micrometritics ASAP 2020 system.

2.2.3 Materials Characterization

^{1}H NMR Spectroscopy. For ^{1}H NMR spectroscopy, the activated samples (around 5 mg) were dissolved by saturated Na_2CO_3 aqueous solution (1 mL), neutralized by 10 M HCl aqueous

solution, and dried in a 100 ^{o}C oven. The solid was dissolved in ~0.5 mL DMSO-d_6 for ^{1}H NMR analysis. ^{1}H NMR data were collected on a Mercury 300 spectrometer.

Scanning Electron Microscopic (SEM) And Transmission Electron Microscopic (TEM) Analysis. Images and analyses of SEM/EDX were taken by FEI Quanta 600 FE-SEM. The Quanta 600 FEG is a field emission scanning electron microscope capable of generating and collecting high-resolution and low-vacuum images. It is equipped with a motorized x-y-z-tilt-rotate stage, providing the following movements: x = y = 150 mm (motorized); z = 65 mm (motorized); Tilt +70 degrees to –5 degrees (motorized); Source: Field emission gun assembly with Schottky emitter source. Voltage: 200 V to 30 kV. Beam Current: >100 nA. Transmission electron microscopy (TEM) experiments were conducted on a FEI Tecnai G2 F20 ST microscope (America) operated at 200 kV (Figure 7-10).

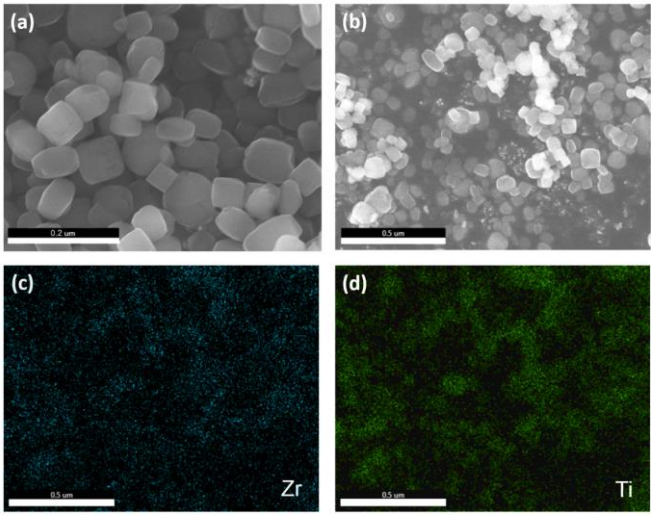

Figure 7. The SEM images (a and b) and corresponding elemental mapping (c and d) of PCN-415.

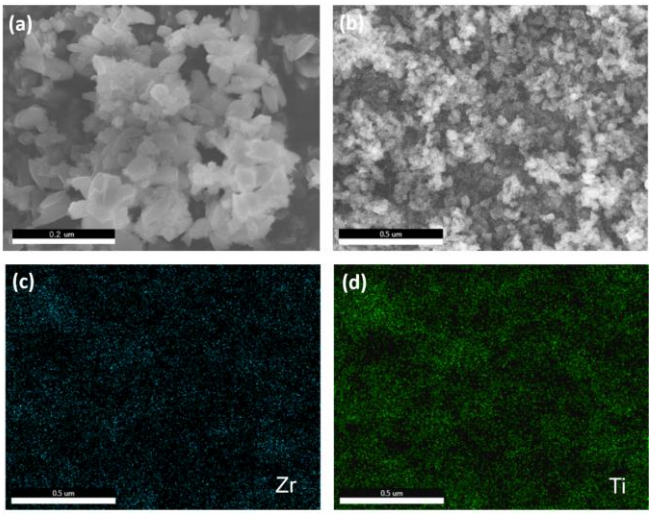

Figure 8. The SEM images (a and b) and corresponding elemental mapping (c and d) of PCN-416.

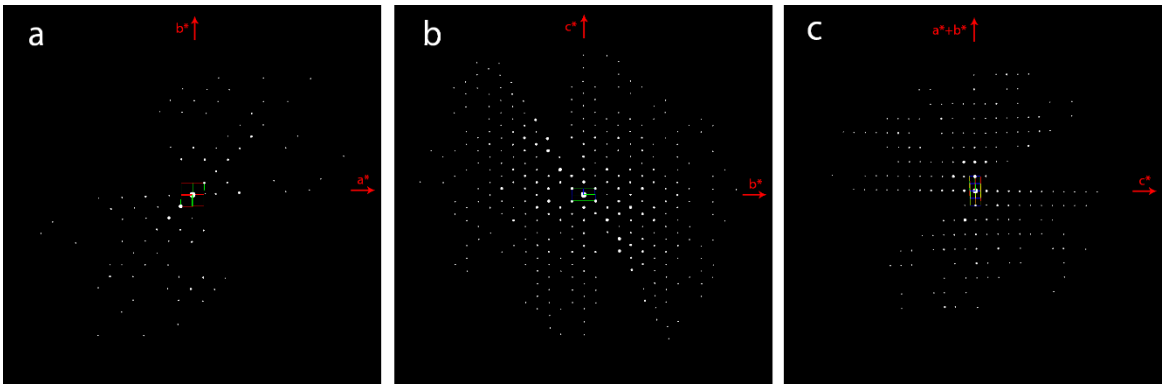

Figure 9. 2D slices cut from the reconstructed 3D reciprocal lattice of PCN-415 showing the (a) *hk*0, (b) 0*kl*, and (c) *hhl* plane.

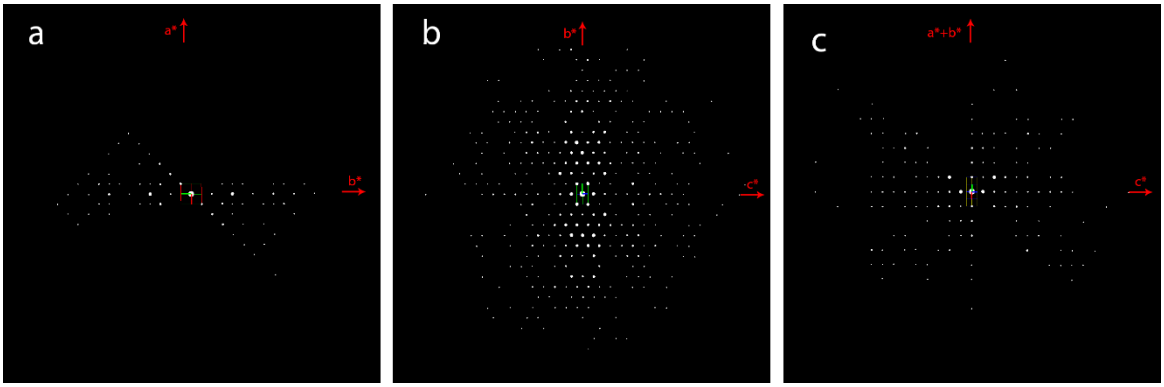

Figure 10. 2D slices cut from the reconstructed 3D reciprocal lattice of PCN-416 showing the (a) *hk*0, (b) 0*kl*, and (c) *hhl* plane.

ICP-MS Analysis. Samples were prepared in triplicate with weights of around 3 mg. Each sample was dissolved in J.T. Baker Ultrex® II Ultrapure 70% nitric acid at 70 °C for 12 hours. Samples were then diluted to 150x in 1% nitric acid and 18.2 MΩ water from a Millipore Milli-Q® water purification system. Calibration standards were prepared from certified reference standards from RICCA Chemical Company. Samples were further analyzed with a Perkin Elmer NexION® 300D ICP-MS. Resulting calibration curves have minimum $R^2 = 0.9999$. Additionally, in order to maintain accuracy, quality control samples from certified reference standards and internal standards were utilized. The individual results of the triplicate samples were averaged to determine the metal ratios (Table 1).

Table 1. SEM-EDX and ICP data for PCN-415 and PCN-416

MOF	**PCN-415**	**PCN-416**
Theoretical Ti/Zr ratio	4	4
Ti/Zr ratio based on EDX	4.3	3.3
Ti/Zr ratio based on ICP	3.8	3.6

Single Crystal X-ray Crystallography. All crystals were taken from the mother liquid without further treatment, transferred to oil and mounted into a loop for single crystal X-ray data collection. Diffraction was measured on a Bruker D8 Venture or D8 Quest diffractometer equipped with a Mo-Kα sealed-tube X-ray source (λ = 0.71073 Å, graphite monochromated) at low temperature device (100 K). The data frames were recorded using the program *APEX2* and processed using the program *SAINT* routine within *APEX2*.[1] The data were corrected for absorption and beam corrections based on the multi-scan technique as implemented in *SADABS*.[2]

The structures were solved by direct methods using *OLEX2* software packages, and refined by full-matrix least-squares on F^2 using *SHELXL* software.[3]

For the refinements, all non-hydrogen atoms were refined with anisotropic displacement parameters. Those with enormous thermal ellipsoids were refined with the help of *EADP* restrains on each ligand to clear the warnings about non-positive definite matrices. For $[Ti_8Zr_2O_{12}(RCOO)_{16}]$ (R = Me, p-Tol and PTBB), the solvent mask procedure in *OLEX2* was employed,[4] because the solvent molecule can be neither identified nor modeled. For $[Ti_8Zr_2O_{12}(RCOO)_{16}]$ (R = PTBB), the FragmentDB constrains in *OLEX2* was adopted for the refinement of *tert*-Butyl-C fragment.[5]

It should be noted that the crystal quality of $[Ti_8Zr_2O_{12}(RCOO)_{16}]$ (R = PTBB) is not good because it is directly taken from hot acetonitrile. On the one hand, the acetonitrile molecules on the surface of crystals would be rapidly evaporated, leading to the formation of crack in the crystal. On the other hand, the excessive *p*-*t*-butylbenzoic acid in the hot acetonitrile would be remained on the surface of crystals with the leaving of acetonitrile. In addition, the Mo-Kα sealed-tube as X-ray source for the single crystal diffraction makes a relatively weaker diffraction data. However, the significant Fourier peaks were clear to construct the *p*-*t*-butylbenzoic acid ligands coordinated on the Ti_8Zr_2 clusters. Also the Ti_8Zr_2 clusters are isostructural to coordinate with different terminal carboxylic acids. We believe this proposed structure is well-determined for this compound (Table 2).

Table 2. Crystal data and structure refinements for $[Ti_8Zr_2O_{12}(RCOO)_{16}]$ clusters

	R = Me	**R = Et**	**R = Ph**
CCDC	1568410	1568409	1568406
Empirical formula	$C_{288}H_{432}N_{48}O_{264}Ti_{48}Zr_{12}$	$C_{48}H_{80}O_{44}Ti_8Zr_2$	$C_{224}H_{160}O_{88}Ti_{16}Zr_4$
M_w	12184.63	1926.76	5390.79
Color/Shape	Colorless block	Colorless block	Colorless block
Crystal system	Cubic	Triclinic	Monoclinic
Space group	*Im*-3*m*	*P*-1	$P2_1/n$
a (Å)	24.260(4)	12.064(3)	14.896(4)
b (Å)	24.260(4)	13.543(3)	24.070(6)
c (Å)	24.260(4)	13.806(3)	15.304(4)
α (deg)	90	104.331(3)	90
β (deg)	90	109.519(3)	91.287(4)
γ (deg)	90	110.620(3)	90
V (Å^3)	14279(7)	1811.3(8)	5486(2)
Z	1	1	1
T (K)	296(2)	293(2)	296(2)
Wavelength (Å)	0.71073 (MoK$_\alpha$)	0.71073 (MoK$_\alpha$)	0.71073 (MoK$_\alpha$)
D_c (Mg·m^{-3})	1.417	1.766	1.632
Abs. coeff. (mm^{-1})	0.925	1.206	0.824
R_{int}	0.0440	0.0488	0.0793
F(000)	6144	976	2720
reflns collected	92448	23285	48548
Independent reflns	1969	9407	12788
GOF on F^2	1.137	1.031	1.026
R_1 [$I > 2\sigma(I)$][a]	0.0137	0.0425	0.0474
wR_2 [$I > 2\sigma(I)$][a]	0.0514	0.0887	0.0987
R_1 (all data)[b]	0.0219	0.0667	0.0773
wR_2 (all data)[b]	0.0530	0.0998	0.1108

Table 2. Continued.

	R = p-Tol	R = PTBB
CCDC	1568407	1568408
Empirical formula	$C_{134}H_{126}N_2O_{46}Ti_8Zr_2$	$C_{176}H_{209}O_{44}Ti_8Zr_2$
M_w	3066.00	3594.06
Color/Shape	Colorless block	Colorless block
Crystal system	Trigonal	Monoclinic
Space group	*R*-3*c*	$P2_1$
a (Å)	32.890(7)	15.818(12)
b (Å)	32.890(7)	35.48(3)
c (Å)	73.485(15)	18.356(14)
α (deg)	90	90
β (deg)	90	108.901(12)
γ (deg)	120	90
V (Å^3)	68844(31)	9745(13)
Z	18	2
T (K)	296(2)	296(2)
Wavelength (Å)	0.71073 (MoK_α)	0.71073 (MoK_α)
D_c (Mg·m^{-3})	1.331	1.225
Abs. coeff. (mm^{-1})	0.601	0.480
R_{int}	0.1043	0.3746
F(000)	28224	3746
reflns collected	118987	82153
Independent reflns	17545	28257
GOF on F^2	1.006	0.967
R_1 [$I > 2\sigma(I)$][a]	0.0586	0.1497
wR_2 [$I > 2\sigma(I)$][a]	0.1409	0.3343
R_1 (all data)[b]	0.1289	0.3537
wR_2 (all data)[b]	0.1828	0.4518

[a] $R_1 = \Sigma||F_o| - |F_c||/\Sigma|F_o|$.
[b] $wR_2 = |\Sigma w(|F_o|^2 - |F_c|^2)|/\Sigma|w(F_o^2)^2|^{1/2}$.

Continuous Rotation Electron Diffraction (*c*RED) Collection. The crystal sizes of PCN-415 and -416 are less than 1 μm, which is too small to be solved by single crystal X-ray diffraction. Therefore continuous rotation electron diffraction (*c*RED) was applied for solving and refining their structures. Samples of as-made PCN-415 and -416 for TEM investigations were dispersed in acetone. A droplet of the suspension was transferred onto a carbon-coated copper grid. *c*RED data collection was performed on a JEOL JEM2100 microscope and operated at 200 kV (Cs 1.0 mm, point resolution 0.23 nm). Images and electron diffraction patterns were recorded with a Timepix pixel detector QTPX-262k (512 x 512 pixels, pixel size 55 μm, Amsterdam Sci. Ins.) under low-dose conditions. The data were collected using the software *cREDCollection*.[6] A single-tilt tomography sample holder was used for the data collection, which could tilt from -70° to +70° in the TEM. The area for *c*RED data collection was selected using the selected area aperture with about 1.0 μm in diameter. The speed of goniometer tilt was 0.10° - 0.45° s^{-1}, and the exposure time was 0.1 - 0.5 s per frame. Ultrafast 3D *c*RED data collection was carried out in 17 s – 3 min to minimize the beam damage and to maximize the data quality. The data was processed by using XDS package,[7] and two data sets were merged for PCN-416. The *c*RED data resolution reached 0.75 Å for PCN-415 and 1.05 Å for PCN-416. The data completeness is 99.0 % for PCN-415 and 100.0% for PCN-416.

The unit cell and possible space groups were easily determined from the 3D reciprocal lattice of PCN-415 and -416 reconstructed using the *RED processing software*.[6] They crystallize in *I*-centered tetragonal unit cells with cell parameters of a = 14.38 Å and c = 26.98 Å for PCN-415, and a = 16.50 Å and c = 29.95 Å for PCN-416. The reflection conditions of PCN-415 and -416 were clearly deduced from the 2D slices cut from the reconstructed 3D reciprocal lattice.

Considering the reflection conditions and the symmetry of the linkers, *I*4/*mmm* and *I*-42*m* space groups were chosen for PCN-415 and -416, respectively.

The framework structures were determined by direct methods using the program Shelx-2014.[8] For PCN-415, all the atoms were directly found. For PCN-416, all the Zr, Ti, O atoms, and 16 C atoms were directly found, and the remaining two C atoms were located from difference Fourier maps. The final refinement was done by using Shelxl-2014 with only soft restrains on the ligand molecules and based on the kinematic intensities. The data converged to R1 = 0.233 for PCN-415 and 0.258 for PCN-416. The high R1 value is mainly caused by the dynamical effects that make the *c*RED intensities deviating from the kinematic intensities. The details of data collection and refinement are summarized in Tables 3.

Table 3. Crystallographic details for the refinement of PCN-415 and -416 against the *c*RED data.*

Name	PCN-415	PCN-416
Wavelength (Å)	0.0251	0.0251
Program	Shelxl-2014	Shelxl-2014
Tilt range	-31.9°-43.0°	-60.4 °-40.7°
Total number of frames	340	458
Space group	*I*4/*mmm*	*I*-42*m*
Unit cell parameter	*a*=14.4Å, *c*=26.4 Å	*a*=16.7Å, *c*=30.1 Å
Resolution (Å)	0.75	1.05
Completeness	99.0	100.0
No. unique reflections	1970	1918
No. observed reflections ($I > 2$ sigma(I))	1384	912
R1 ($I > 2$ sigma(I))	0.233	0.258
R1 (all reflections)	0.248	0.317
Goof	2.01	1.50

* Hydrogen atoms were not included in the refinement.

Rietveld Refinement. The structures of PCN-415 and -416 obtained from *c*RED data were further refined against synchrotron powder X-ray diffraction (PXRD) data (λ = 0.72768 Å). Synchrotron powder X-ray diffraction (PXRD) was collected on the beamline 17-BM at the Advanced Photon Source, Argonne National Laboratory. Rietveld refinement[9] was performed using TOPAS Academic V4.1.

For PCN-415, the background was fitted with an 11th order Chebychev polynomial. The refinement was conducted using a Pearson VII type peak profile function, followed by refinement of the unit cell and zero-shift. Soft-restrains were applied to the Ti-O and Zr-O distances by 2.00 Å and 2.20 Å, respectively. Rigid bodies were applied on the ligands. The guest species in the cages could not be located due to their partial occupancies and low symmetry. Instead, five oxygen atoms were added at random positions inside the cages to compensate for the contributions of the guest species, and refined subsequently. Finally, R-value was converged to R_p= 0.03243, R_{wp}= 0.04954, R_{exp}= 0.03572, and GOF= 1.387.

For PCN-416, the background was fitted with a 14th order Chebychev polynomial. The refinement was conducted using a Pearson VII type peak profile function, followed by refinement of the unit cell and zero-shift. Soft-restrains were applied to the Ti-O and Zr-O distances by 2.00 Å and 2.20 Å, respectively. Rigid bodies were applied on the ligands. The guest species in the cages could not be located owing to their partial occupancies and low symmetry. Instead, six oxygen atoms were added at random positions inside the cages to compensate for the contributions of the guest species, and refined subsequently. Finally, R-value was converged to R_p= 0.03840, R_{wp}= 0.05313, R_{exp}= 0.04694, and GOF= 1.132. The details of PXRD data collection and refinement are summarized in Tables 4 and 5.

Table 4. Crystallographic data, powder X-ray collection conditions, and Rietveld refinement results of PCN-415 and -416.

Name	**PCN-415**	**PCN-416**
Chemical formula	$C_{32}H_{16}O_{37.08}Ti_4Zr$	$C_{48}H_{24}O_{39.68}Ti_4Zr$
Formula weight	1276.43	1518.25
Crystal system	Tetragonal	Tetragonal
Space group	*I*4/*mmm*	*I*-42*m*
a/Å	14.3801(11)	16.496(3)
c/Å	26.976(2)	29.947(5)
Z	4	4
Temperature/K	298(2)	298(2)
Wavelength/Å	0.72768	0.72768
2θ range/°	1.00 - 21.99	1.00 - 21.99
Number of reflections	160	225
Number of structural variables	58	66
R_p	0.03243	0.03840
R_{wp}	0.04954	0.05313
R_{exp}	0.03572	0.04694
GOF	1.387	1.132

Table 5. Atomic position difference of PCN-415 from refinement against ED and PXRD.

Atom	Difference (Å)
Zr1	0.049
Ti1	0.014
Average Zr, Ti	0.032
O1	0.063
O2	0.035
O3	0.060
O4	0.146
O5	0.075
C1	0.136
C2	0.088
C3	0.064
C4	0.036
C5	0.023
C6	0.073
C7	0.058
Average O, C	0.071

EPR Analysis. Electron Paramagnetic Resonance (EPR) measurement was conducted on a Bruker Elexsys II E500 EPR spectrometer equipped with a Bruker ER4131VT variable-temperature unit. About 10 mg of PCN-415-NH_2 sample and 1 mL methanol were sealed in a 1.5 mm quartz tube. The tube was kept sealed throughout the measurement. The spectra of samples before and after light irradiation were measured. The spectra were recorded at 75 K with 0.6325 mW microwave power and a modulation amplitude of 5.0 G. The microwave frequency was set at 9.374 GHz. The field was centered at 3500G with a sweep width of 2000G. Each spectrum was integrated from 60 scans.

Transient Absorption Measurement. Transient absorption was measured in the pump−probe setup monitoring the change of absorption peak at 580 nm after band gap excitation. The 400 nm pump was generated from 100 fs, 800 nm wavelength, Ti-sapphire laser operating at 82 MHz by second harmonic generation. Several μJ of a 800 nm beam were focused onto the translating CaF_2 window to generate a stable supercontinuum, which was used as the probe beam. The probe beam centered at 580 nm was selected with the bandwidth (fwhm) of ∼10 nm before the sample using a chirp compensating prism pair and a spatial filter. The instrument-limited response time was ∼80 fs. In a typical experiment 20 mg MOF was dispersed in acetonitrile (20 mL) and sonicated for 30 min. In order to separate large particles, the suspension was then centrifuged for 20 min at 6000 rpm. The supernatant was placed in a 2 mm stirred quartz cuvette for the measurements. Multiexponential fitting to this asymptotic recovery gives rise to two characteristic time constants, τ_1 = 1 ps and τ_2 = 80 ps. Notably, the nearly perfect parallelism between the asymptote and the $\Delta OD = 0$ line suggests that the eventual recovery to $\Delta OD = 0$ features an extremely long lifetime (τ_3), probably a few nanoseconds or longer.

Photocatalytic Hydrogen Production. The photocatalytic hydrogen production experiments were carried out in a 160 mL optical reaction vessel with stirring at ambient temperature using a 300 W Xe lamp equipped with a UV cut-off filter (λ > 380 nm). In the reaction vessel, 5 mg of the MOF catalyst was dispersed in 28 mL acetonitrile with 0.2 mL deionized water, 2 mL triethanolamine (TEOA) as a sacrificial reagent, and ~50 μg of Pt nanoparticles as co-catalyst. The suspension was stirred and purged with nitrogen for ~60 min to remove air. Hydrogen gas was measured by gas chromatography (Shimadzu GC-2014, argon as a carrier gas) using a thermal conductivity detector (TCD).

DFT Calculations. First-principles calculations were based on the density functional theory (DFT) as implemented in the Vienna Ab-initio Simulation Package[10]. The core-valence interactions were described by projector augmented-wave (PAW) potentials within the Perdew-Burke-Ernzerhof (PBE) approximation for the exchange-correlation energy[11]. Plane waves with a kinetic energy cutoff of 500 eV were used as the basis set. We used the conjugate gradient method to optimize the atomic positions, and the energy convergence criterion between two consecutive steps was 10^{-5} eV. The maximum allowed force on the atoms is 10^{-3} eV/Å. Note that the DFT predictions are useful for a quantitative comparison between themselves. The absolute band gap energy, however, is underestimated when compared to the experimentally measured optical band gaps. This discrepancy in the band gap is a classic occurrence in DFT ground state predictions which arises from the approximations in the exchange-correlation. In addition, defects in MOFs may change the band gap, but the effect of which is difficult to estimate in DFT calculations.

2.3 Results and Discussion

2.3.1 $[Ti_8Zr_2O_{12}(RCOO)_{16}]$ Clusters

As reflected by the large number of Ti-oxo-clusters in the literature, the cluster chemistry of Ti^{4+} is rich and versatile.[81] Indeed, carboxylate-based Ti-oxo-clusters show a large panel of nuclearities and geometries, depending on the synthetic conditions such as metal/ligand ratio, solvent, reaction time, temperature, and pressure. Although numerous molecular Ti-clusters have been documented, it has been difficult to directly utilize them as starting building blocks for MOF synthesis.[82] The main reason is the sensitivity of cluster formation to reaction conditions and, in many cases, the incompatibility of such conditions with those required for MOF synthesis and crystallization.[83] For example, many Ti-oxo-clusters crystallize in acetonitrile or methanol whereas *N*,*N*-dimethylformamide (DMF) is usually required as solvent for the synthesis of MOFs. In addition, some Ti-oxo-clusters terminated by alkoxides are water-sensitive which are prone to undergo fast and spontaneous hydrolysis during MOF synthesis. These limitations have largely prevented the incorporation of vast, diverse Ti-oxo-clusters into MOF structures.

In contrast, the $[Zr_6O_4(OH)_4(COO)_{12}]$ cluster (Figure 11a) has been shown to be a nearly ideal inorganic building unit for the construction of MOFs.[84] Various MOFs based on the $[Zr_6O_4(OH)_4(COO)_{12}]$ cluster have been synthesized under similar synthetic conditions.[24, 85-88] This encourages us to find a Ti-containing cluster with behavior similar to $[Zr_6O_4(OH)_4(COO)_{12}]$ for MOF synthesis.[89] Efforts were made in our group to build Ti-MOFs using existing Ti-oxo clusters in the literature but to no avail. These clusters tend to dissociate or transform during the MOF synthesis.[90] While existing monometallic clusters do not meet the requirement for MOF synthesis, bimetallic clusters have brought new opportunities. During our continued interest in

cluster chemistry, a $[Ti_8Zr_2O_{12}(COO)_{16}]$ cluster (Figure 11c) was discovered as a promising inorganic building unit for MOF synthesis.

The $[Ti_8Zr_2O_{12}(RCOO)_{16}]$ (R = Me, Et, Ph, p-Tol and PTBB) clusters (Figure 11d-h) were synthesized by the solvothermal reactions of Zr^{4+}, Ti^{4+}, and an excess amount of carboxylic acids, similar to the synthetic conditions for $[Zr_6O_4(OH)_4(RCOO)_{12}]$ clusters and most Zr-MOFs. Single crystals were successfully isolated for all the $[Ti_8Zr_2O_{12}(RCOO)_{16}]$ (R = Me, Et, Ph, p-Tol, and PTBB) clusters. Structure analysis reveals that the bimetallic decanuclear cluster is composed of a Ti_8-cube capped by two Zr^{4+} centers on the top and bottom. Four μ_2-O rest on the equatorial plane, each bridging a pair of Ti^{4+} to form a $[Ti_8O_4]^{24+}$ center. Two Zr^{4+} on the top and bottom were further connected to the $[Ti_8O_4]^{24+}$ center by eight μ_3-O, generating the $[Ti_8Zr_2O_{12}]^{16+}$ core. The $[Ti_8Zr_2O_{12}]^{16+}$ core was terminated by 16 carboxylates fulfilling a neutral $[Ti_8Zr_2O_{12}(COO)_{16}]$ cluster (Figure 11c). In fact, the $[Ti_8Zr_2O_{12}(COO)_{16}]$ cluster is structurally related to the $[Zr_6O_4(OH)_4(COO)_{12}]$ cluster (Figure 11b). It can be derived from the $[Zr_6O_4(OH)_4(COO)_{12}]$ cluster by replacing four equatorial Zr^{4+} by a Ti_8-cube. As a result, four carboxylate ligands within the equatorial plane that bridges the Zr_4-square are replaced by eight carboxylate ligands perpendicular to the equatorial plane, which bridges the Ti_8-cube.

Interestingly, the $[Ti_8Zr_2O_{12}(RCOO)_{16}]$ (R = Me, Et, Ph, p-Tol, and PTBB) clusters are dominating products under a variety of conditions. They tolerate the modification of substituents with different sizes on the carboxylate linker and the variation of synthetic conditions without altering the $[Ti_8Zr_2O_{12}]^{16+}$ core structure. For example, the $[Ti_8Zr_2O_{12}(PhCOO)_{16}]$ cluster can be obtained regardless of the solvents (DMF, methanol, and acetonitrile), temperatures (from 80 to 150 °C), and Ti/Zr ratios (from 1 to 10), as long as the carboxylic acid is in excess. Therefore, the

robust $[Ti_8Zr_2O_{12}(COO)_{16}]$ cluster represents a nearly ideal Ti-containing substitute of the $[Zr_6O_4(OH)_4(COO)_{12}]$ cluster for the construction of photoactive MOFs.

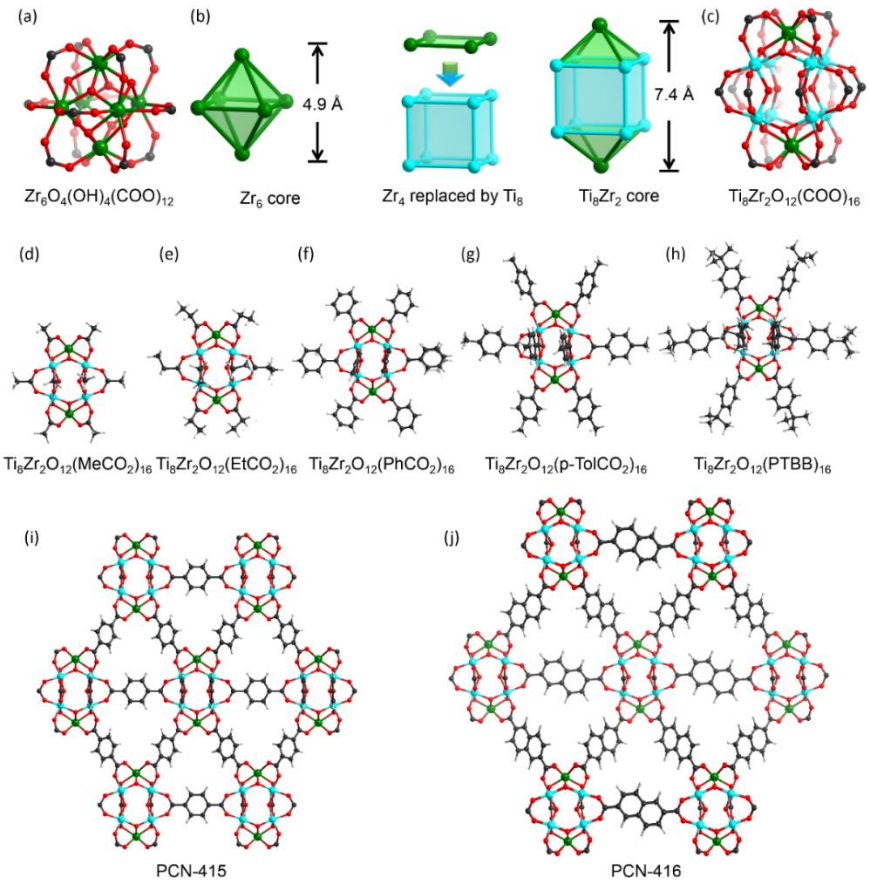

Figure 11. Coordination compounds based on $[Ti_8Zr_2O_{12}(RCOO)_{16}]$ cluster. (a) $[Zr_6O_4(OH)_4(COO)_{12}]$ cluster; (b) the relationship between $[Zr_6O_4(OH)_4(COO)_{12}]$ and $[Ti_8Zr_2O_{12}(COO)_{16}]$ clusters; (c) $[Ti_8Zr_2O_{12}(COO)_{16}]$ cluster; (d)-(h) discrete $[Ti_8Zr_2O_{12}(RCOO)_{16}]$ clusters formed with different carboxylate ligands; (i) and (j) MOFs based on $[Ti_8Zr_2O_{12}(RCOO)_{16}]$ clusters and different carboxylate linkers.

2.3.2 $[Ti_8Zr_2O_{12}(COO)_{16}]$ Cluster-based MOFs

The solvothermal reaction between the $[Ti_8Zr_2O_{12}(MeCOO)_{16}]$ cluster and H_2BDC (terephthalic acid) gives rise to the desired MOF, PCN-415 (Figure 11i), under similar synthetic conditions used for the syntheses of Zr-MOFs. The acetate terminated $[Ti_8Zr_2O_{12}(MeCOO)_{16}]$ cluster was adopted as the starting material because of its good solubility in DMF. The preformed

cluster as starting material is the key for the formation of pure PCN-415 because it eliminates numerous competing side reactions. For comparison, the synthesis of PCN-415 was attempted using a mixture of stoichiometric Zr^{4+} and Ti^{4+} metal salts which leads to low crystallinity PCN-415 with UiO-66 impurity (UiO stands for Universitetet i Oslo). In addition, an excess amount of carboxylic acid as modulating reagent is also necessary for the formation of highly crystalline product. The carboxylic acid acts as a modulator that competitively coordinates with the metals and slows down crystal growth to help producing highly crystalline products. Furthermore, isoreticular expansion of PCN-415 can be realized by elongation of BDC into NDC (2,6-naphthalenedicarboxylate), which gives rise to an isoreticular MOF, PCN-416 (Figure 11j).

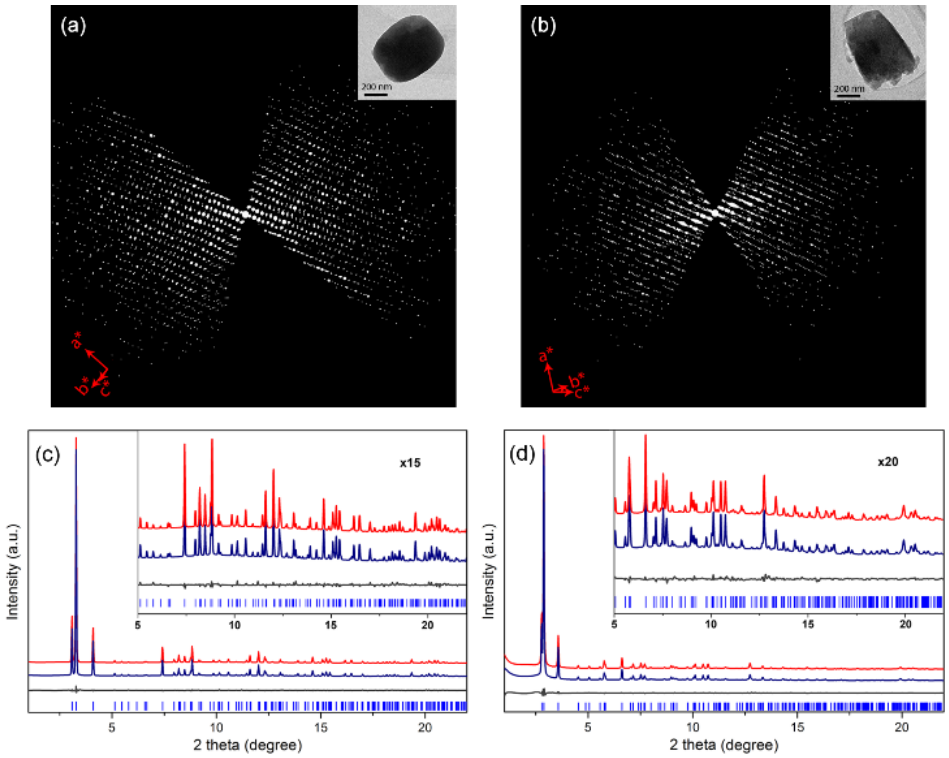

Figure 12. Reconstructed 3D reciprocal lattice and Rietveld refinement. Reconstructed 3D reciprocal lattice of (a) PCN-415 and (b) PCN-416 from *c*RED data. Inset is the crystal from which the RED data was collected. PXRD Rietveld refinement of (c) PCN-415 and (d) PCN-416 displaying the observed pattern (navy), calculated pattern (red), difference plot (grey), and Bragg positions (blue bars) (λ = 0.72768 Å).

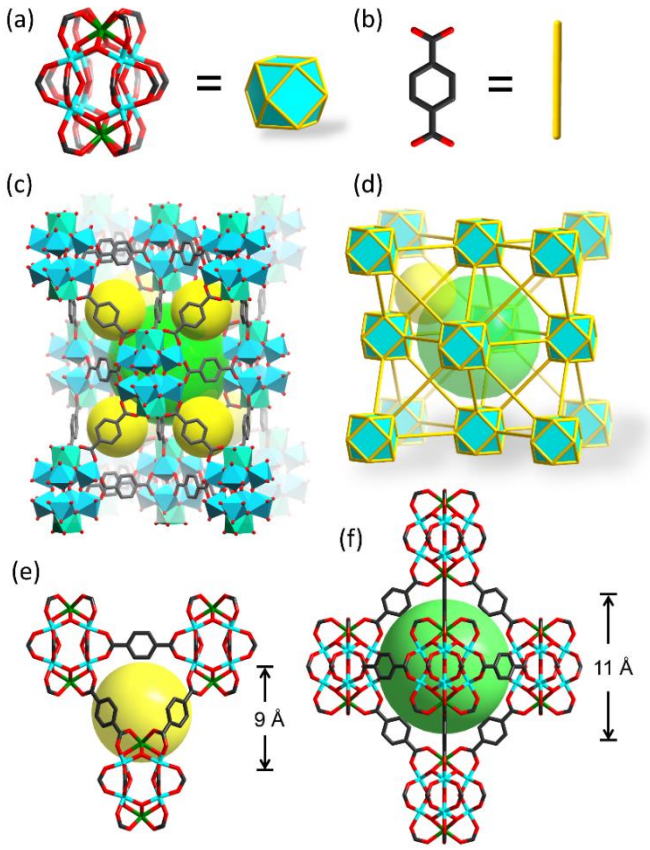

Figure 13. Structural analysis. Topological simplification of (a) the $[Ti_8Zr_2O_{12}(COO)_{16}]$ cluster and (b) the BDC linker; (c) crystal structure and (d) topological presentation of PCN-415 as an **fcu** net; (e) small tetrahedral cage and (f) large octahedral cage in PCN-415.

Since the crystal sizes of PCN-415 and -416 are too small for single crystal X-ray diffraction, their structures are directly solved from continuous rotation electron diffraction (*c*RED) and confirmed by Rietveld refinement against synchrotron PXRD data (Figure 12). The structure models refined against *c*RED and PXRD show excellent agreement with each other, and the atomic positions differ on average only by 0.032 Å for Zr/Ti and by 0.071 Å for O/C. In the crystal structure of PCN-415, each $[Ti_8Zr_2O_{12}(COO)_{16}]$ cluster (Figure 13a) is connected to 16 linear BDC linkers (Figure 13b) to form a 3D framework (Figure 13c). There is a tetragonal cage with a diameter of 9 Å and an octahedral cage with a diameter of 11 Å (Figure 13e and f). Two

types of symmetrically independent BDC linkers are observed. Topologically, a pair of parallel BDC linkers within the equatorial plane is regarded as one edge. Therefore, eight equatorial BDC linkers are simplified into four edges. On the other hand, eight BDC linkers above and below the equatorial plane are simplified into eight edges. As a result, the $[Ti_8Zr_2O_{12}(COO)_{16}]$ cluster acts as a 12-connected node, affording a network with **fcu** topology (Figure 13d).[91-94] PCN-416 is isoreticular to PCN-415 with the same $[Ti_8Zr_2O_{12}(COO)_{16}]$ cluster and elongated linkers. The distance between each pair of parallel NDC linkers is 3.5 Å, indicating a π–π interaction between naphthalene moieties. A small tetragonal cage and large octahedral cage were observed in PCN-416 with diameters of 11 and 13 Å, respectively. Since PCN-416 is an isoreticular expansion of PCN-415, they share the same **fcu** topology.

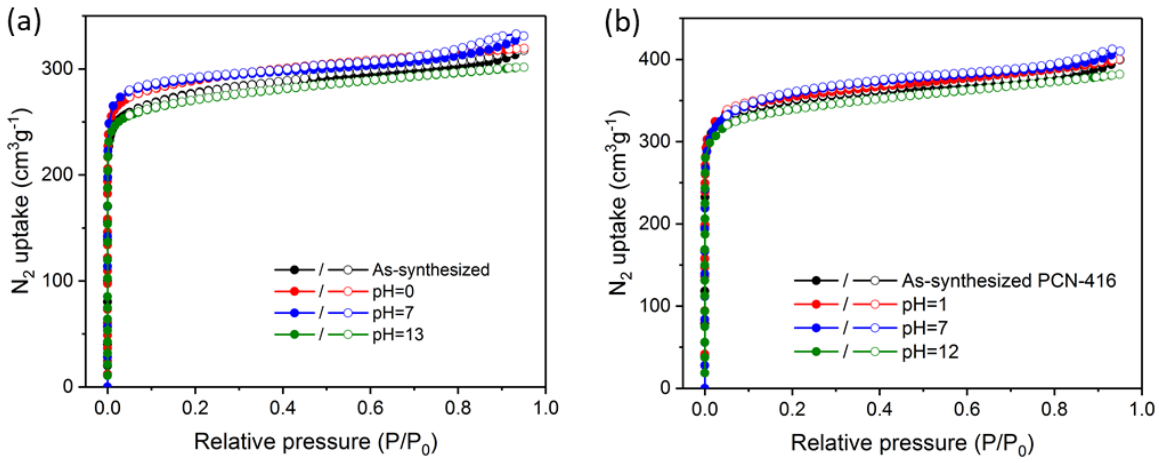

Figure 14. N_2 adsorption-desorption isotherms of (a) PCN-415 and (b) PCN-416 after immersion in aqueous solutions with different pH values at room temperature for 24 h.

2.3.3 Porosity and Stability

The porosity of PCN-415 and PCN-416 is estimated by N_2 sorption measurements at 77 K. Both PCN-415 and PCN-416 are highly porous with BET surface areas of 1050 and 1337 $m^2 \cdot g^{-1}$, respectively. More importantly, PCN-415 and PCN-416 exhibit excellent chemical stabilities in

aqueous solutions with a wide pH range for at least 24 h. The N_2 adsorption isotherms (Figure 14) and PXRD patterns (Figure 15) of MOF samples are not altered after stability tests, indicating maintained crystallinity and intact porosity. The remarkable chemical stability of PCN-415 and PCN-416 can be attributed to the strong M^{4+}–O (M = Ti or Zr) bond and the highly connected cluster, which resist the attack of water and other guest species.

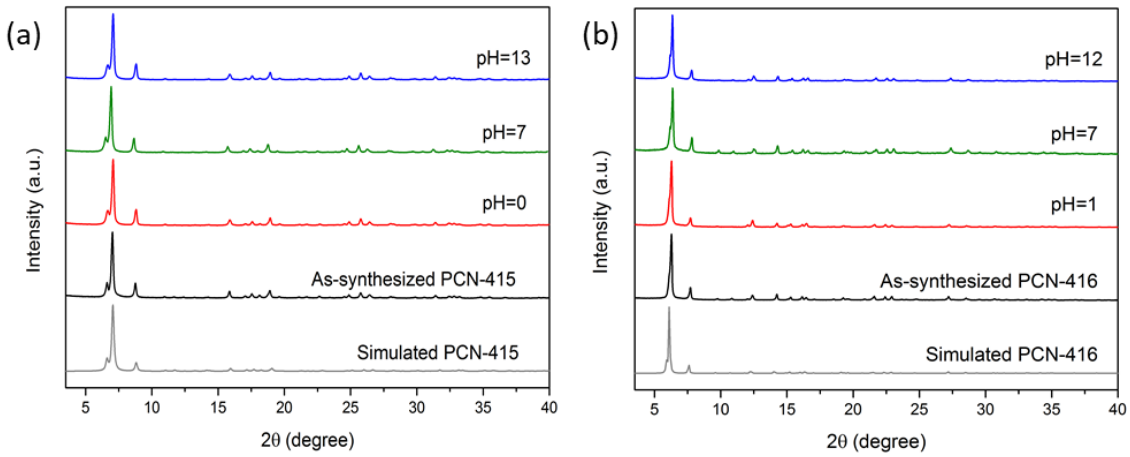

Figure 15. PXRD patterns of (a) PCN-415 and before and after immersion in aqueous solutions with different pH values at room temperature for 72 h. (b) PXRD patterns of PCN-416 before and after immersion in aqueous solutions with different pH values at room temperature for 24 h.

2.3.4 Engineering of Optical Response

The optical band gap of PCN-415 was calculated to be 3.3 eV based on the UV-Vis spectrum (Figure 16a), indicating no adsorption in the visible light range. This has limited the application of PCN-415 in visible-light-induced catalysis. The amine-functionalized BDC linkers were reported to provide an extra absorption band in the visible region, which has been encountered in UiO-66[95-96] and MIL-125.[97-98] Therefore, the optical response of PCN-415 were tuned by introducing amino groups on BDC linker.

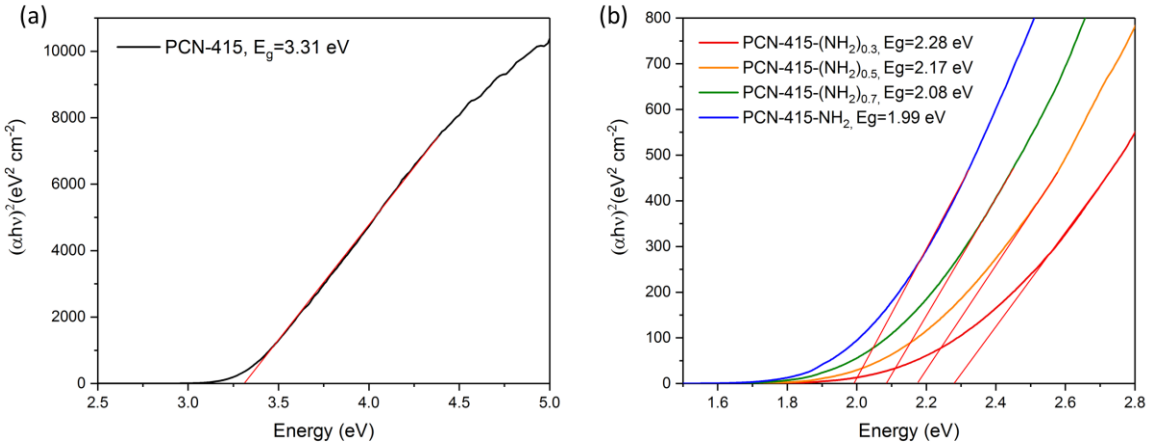

Figure 16. Calculations of band-gaps for PCN-415 and its amine functionalized derivatives using Tauc plots.

PCN-415 with different concentrations of monoaminated BDC-NH_2 (2-aminoterephthalate) were synthesized by varying the ratios of BDC-NH_2 in the starting material (i.e., 30%, 50%, 70%, and 100%). The resulting MOFs were named as PCN-415-$(NH_2)_{0.3}$, PCN-415-$(NH_2)_{0.5}$, PCN-415-$(NH_2)_{0.7}$, and PCN-415-NH_2, respectively. In addition, the diamine functionalized PCN-415-$(2NH_2)_{0.5}$ was also synthesized by introducing 50% of diaminated BDC-$2NH_2$ (2,5-diaminoterephthalate). The amine functionalized derivatives possess the same structure as PCN-415 as suggested by PXRD patterns and N_2 adsorption isotherms. UV-Vis spectra indicate an obvious red shift of absorption peaks and a reduction of band gap upon the introduction of amino groups (Figure 17b). The absorption onsets (from 544 to 623 nm) and band gaps (from 2.28 to 1.99 eV) do not largely vary for all of the monoaminated samples, but the molar extinction coefficient notably increased with increasing BDC-NH_2 contents. This feature was reflected in the physical appearance which shows increased yellow color intensity with increasing amount of BDC-NH_2. The diamine functionalized sample, PCN-415-$(2NH_2)_{0.5}$, shows a further band gap decrease with an optical band gap of 1.2 eV, shifting the absorption onset to the red/IR region.

To understand the origin of band-gap reduction by amino functionalization, electronic structure calculations were performed for PCN-415 and its derivatives using density functional theory (DFT). The calculated band gap of PCN-415 is larger than that of PCN-415-NH_2 indicating that the introduction of -NH_2 decreases the band gap. By shifting the Fermi level to align the conduction band minimums (CBMs) of the two structures, one can find that the band gap decrease is attributed to the midgap flat bands generated in PCN-415-NH_2 (Figure 17c). The comparison of density of states (DOSs) for PCN-415 and PCN-415-NH_2 further illustrates this point (Figure 17d). The upper valence bands (VBs) are composed of BDC aromatic 2p orbitals while bottom conduction bands (CBs) are dominated by the Ti 3d orbitals. Therefore, the excitation of PCN-415 by UV light transfers the electron from VBs at BDC to CBs at Ti, corresponding to the ligand to metal charge transfer (LMCT). Introducing amino groups on the BDC linker pushes the VB into a high energy occupied state. Midgap states were introduced into the band gap that corresponded to the N and C 2p orbitals from BDC-NH_2. On the other hand, the CBs are minimally affected by the amino groups on the linkers, which matched well with the Mott-Schottky plots. This phenomenon is a close remittance of the N doped TiO_2 in which the N 2p orbital created midgap band to narrow the overall band gap. The diamine functionalized sample shows further reduced bandgap because of the strong electron donating characteristics of aromatic diamines. The contributions of ligand orbitals to the CBs are also increased in the diamine functionalized sample, suggesting an increased proportion of ligand based excitation as compared to LMCT. The calculated band-gap of PCN-416 is inherently smaller than that of PCN-415, which was further reduced by amino functionalization. Overall, the localized electronic modification results in flat bands in k-space, indicating the absence of long-range interactions. The CBM and valence band maximum (VBM) in MOFs can be regarded as the lowest unoccupied and highest occupied molecular orbitals

(LUMO and HOMO), respectively. Although the terms for semiconductors (VB, CB, and band gap) have been commonly used to describe MOFs, theoretical studies indicated the insulating nature of PCN-415, as suggested by the localized electronic states.

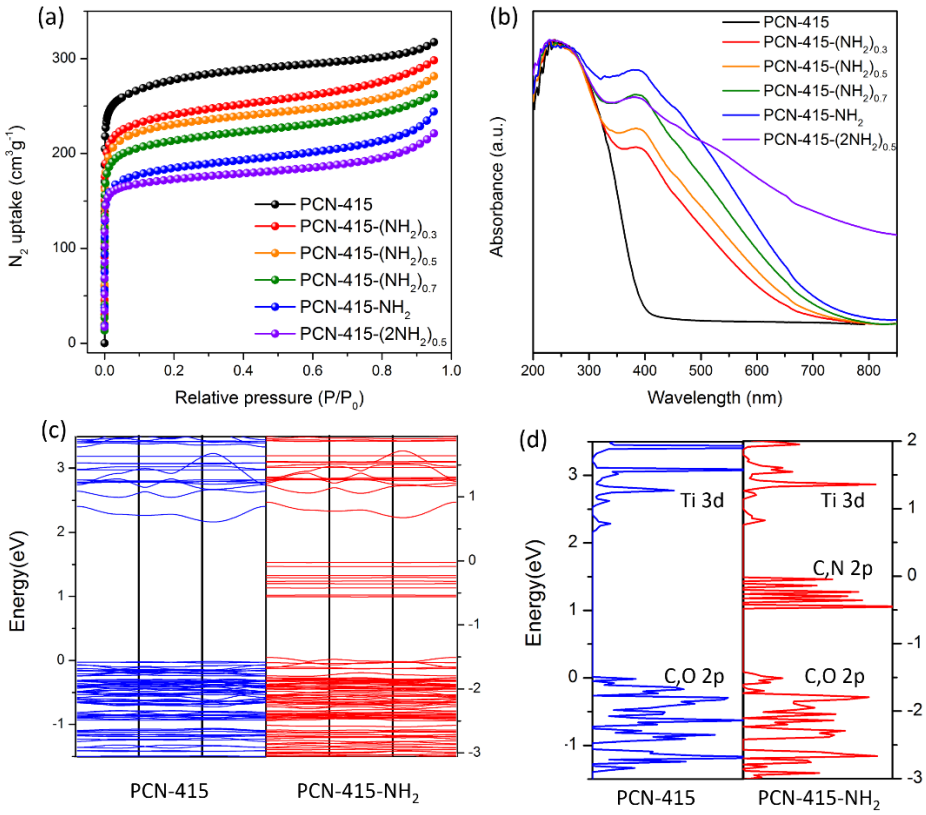

Figure 17. Engineering the optical response of PCN-415. (a) N_2 adsorption isotherms, (b) UV-Vis spectra, (c) DFT calculated band structures, and (d) DOSs for PCN-415 and PCN-415-NH_2.

2.3.5 Photochemical Hydrogen Production

With the high porosity, excellent chemical stability, tunable optical response, and photoactive clusters, PCN-415 and PCN-416 provide ideal platforms for the design of MOF photocatalysts. As a proof of concept, the photochemical hydrogen production catalyzed by PCN-415 and its derivatives were tested. The photocatalytic hydrogen generation was performed in acetonitrile and H_2O with triethanolamine (TEOA) as a sacrificial agent and Pt nanoparticles as

co-catalysts under 300 W Xe lamp equipped with a UV cut-off filter (λ > 380 nm). The formation of H_2 was detected by gas chromatograph (GC). No H_2 was detected in the dark showing the photocatalytic nature of the reaction. The inactivity of the parent PCN-415 under the same conditions confirms that the photocatalytic activity is attributed to the amino functionality. The H_2 generation efficiency notably increased with the BDC-NH_2 content and then leveled off. Among all the tested materials, PCN-415-NH_2 shows the highest activity with an H_2 evolution rate of 594 μmol g^{-1} h^{-1} (Table 6).

Table 6. Catalytic Performance of MOFs in the Photocatalytic Hydrogen Generation

Entry	Photocatalysis	H_2 (μmol·g^{-1}·h^{-1})[a]
1	PCN-415	44
2	PCN-415-$(NH_2)_{0.3}$	469
3	PCN-415-$(NH_2)_{0.5}$	503
4	PCN-415-$(NH_2)_{0.7}$	514
5	PCN-415-NH_2	594
6	PCN-415-$(2NH_2)_{0.5}$	130
7	PCN-416	484
8	PCN-416-$(2NH_2)_{0.5}$	51
9	UiO-66-NH_2	94
10	PCN-415-NH_2, cycle 1	495
11	PCN-415-NH_2, cycle 2	465
12	PCN-415-NH_2, cycle 3	513

[a]Reaction conditions: 5 mg catalyst, 28 mL CH_3CN, 2 mL TEOA, 200 μL H_2O, 50 μg Pt, 300 W Xe lamp with a UV cut-off filter (λ > 380 nm), 4 h. Cycling experiments were conducted by adding 2 mL TEOA as sacrificial reagent at the end of each reaction. The reaction mixture was purged with nitrogen for 60 min before the next reaction cycle.

To test the photocatalytic stability of PCN-415-NH_2, cycling experiments were conducted. The catalytic activity was well-maintained after three cycles. The PXRD patterns after the photocatalytic reaction reveal the stability of PCN-415 during the reaction (Figure 18). Although the diamine functionalized sample have small band gaps and strong visible light absorption, they show relatively low activity. In fact, the excitations of PCN-415-$(2NH_2)_{0.5}$ and PCN-416-$(2NH_2)_{0.5}$ are more ligand-based instead of LMCT, which have a short lifetime accounting for the low catalytic performance. This is in line with the computational results, which suggested a significant contributions of ligand orbitals to both VBs and CBs. Therefore, the photocatalytic activity of MOFs cannot be directly correlated with band gaps. For comparison, the performance of UiO-66-NH_2 was also tested as a Zr-only analogue of PCN-415-NH_2 which showed much lower activity. This result highlights the effect of Ti^{4+} in PCN-415 as a photoactive species for photochemical hydrogen production.

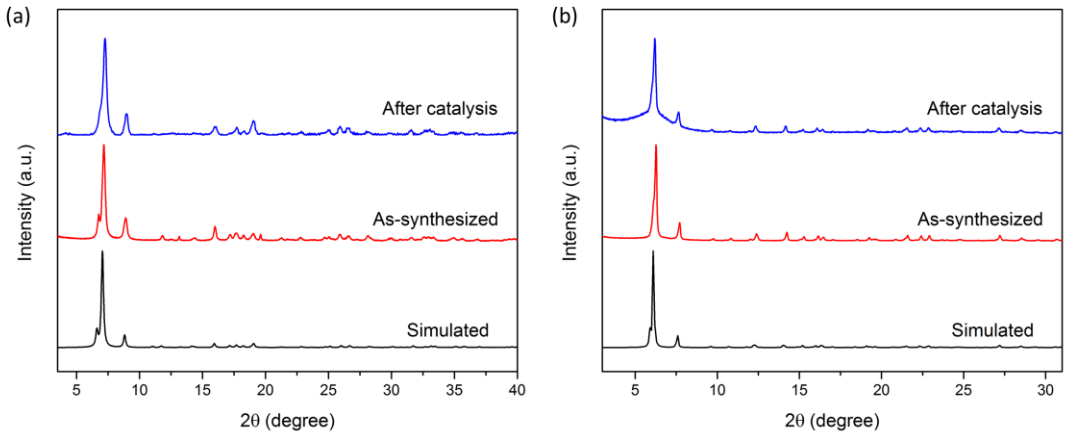

Figure 18. The PXRD patterns of (a) PCN-415-NH_2 and (b) PCN-416 before and after photocatalytic hydrogen generation.

In order to investigate the nature of excited states in the PCN-415-NH_2, we carried out electron transient absorption spectroscopy (TAS) and paramagnetic resonance spectroscopy (EPR)

measurements. For EPR studies, PCN-415-NH_2 was subjected to conditions similar to those during photocatalytic reaction but without Pt co-catalysts. Illuminating PCN-415-NH_2 leads to the appearance of an intense paramagnetic signal ascribed to Ti^{3+} (Figure 19). This is in line with the observation that the color of the reaction suspension changes from the original yellow to green upon light irradiation, and quickly changed back upon exposure to O_2. UiO-66-NH_2 exposed to the same conditions did not develop any additional paramagnetic features upon illumination. The EPR results suggest that light irradiation promotes transfer of photogenerated electrons from the excited BDC-NH_2 to the $[Ti_8Zr_2O_{12}(COO)_{16}]$ cluster, resulting in the formation of Ti^{3+} species. Transient absorption spectroscopy (TAS) was further applied to study the lifetime of the excited states. Excitation of PCN-415-NH_2 at 400 nm results in an intense transient signal with a maximum at 580 nm with a moderately long lifetime of up to 9 ns (Figure 20). For comparison, the UiO-66-NH_2 shows a broad transient signal at 750 nm which decays rapidly within 10 ps. The main difference between the PCN-415-NH_2 and UiO-66-NH_2 is the occurrence of absorption bands at much lower wavelengths, which is tentatively assigned to the stabilized holes on the linker and the formation of Ti^{3+} species.

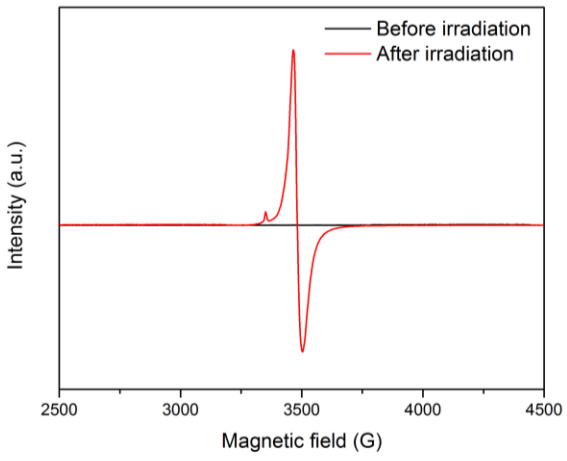

Figure 19. The EPR spectra of PCN-415-NH_2 before and after light irradiation.

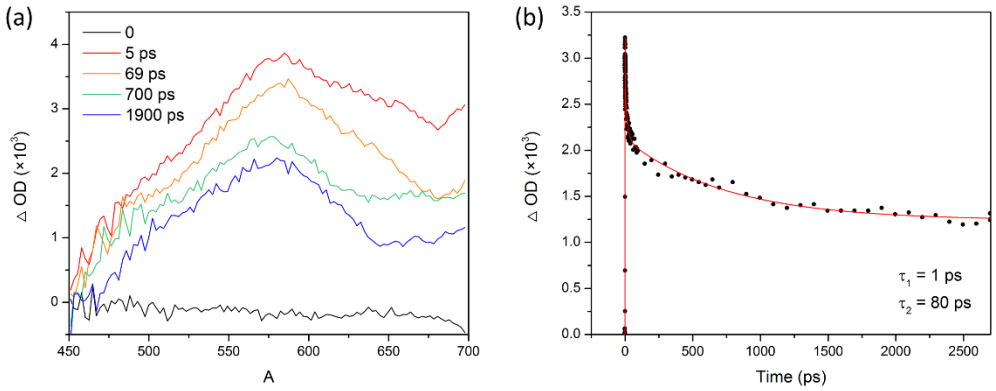

Figure 20. Transient absorption spectroscopy. (a) Differential transient absorption spectra for PCN-415-NH_2 upon excitation at 400 nm; (b) TA kinetics of PCN-415-NH_2 taken at the probing wavelength of 580 nm.

Based on these results and literature, a LMCT mechanism was proposed for the hydrogen generation reaction (Figure 21). The BDC-NH_2 linkers serve as antennas to absorb light and transfer the photoexcited electrons to the $[Ti_8Zr_2O_{12}(COO)_{16}]$ cluster forming Ti^{3+} species. The photogenerated electrons on the Ti^{3+} were then transferred to the Pt surface where the proton reduction takes place. Meanwhile, the photogenerated holes on the BDC-NH_2 linkers were reduced by TEOA as electron donors, fulfilling the catalytic cycle. The remarkable difference between PCN-415-NH_2 and UiO-66-NH_2 in photocatalytic activity is therefore explained by the stabilized excited state of PCN-415-NH_2 by the formation of Ti^{3+}, whereas the UiO-66-NH_2 does not promote the formation of corresponding intermediates. Previously reported computational results also indicate that the HOMO-LUMO transitions of UiO-66-NH_2 are purely ligand-based as the d-orbitals of Zr do not overlap with the π^* orbital of the ligand. In contrast, LMCT can be achieved in PCN-415-NH_2 to allow long-lived charge separation and efficient utilization of the photogenerated electrons. These results signify the importance of Ti^{4+} on the excitation lifetime and photocatalytic performance in hydrogen production reactions.

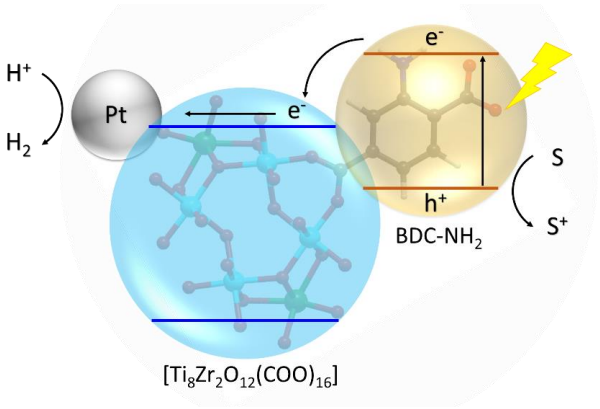

Figure 21. Proposed mechanism of the hydrogen generation reaction catalyzed by Pt@PCN-415-NH_2.

2.4 Conclusions

In conclusion, we have discovered a $[Ti_8Zr_2O_{12}(COO)_{16}]$ cluster as an inorganic building unit for the synthesis of heterometallic MOFs. The preformed cluster as starting material is the key for the MOF synthesis because it eliminates numerous competing side reactions. The resulting MOFs, namely the PCN-415 and PCN-416 series, demonstrate high porosity, excellent chemical stability, tunable photo-responsivity, and good catalytic activity towards water reduction. We expect that the $[Ti_8Zr_2O_{12}(COO)_{16}]$ cluster will act as a Ti-containing replacement of the $[Zr_6O_4(OH)_4(COO)_{12}]$ cluster, which promises the construction of various robust and photoactive MOFs. In addition, the facile synthesis of versatile Ti-containing MOFs shall accelerate the development of MOF-based photocatalysts.

3. DEFECTIVE MOFS CREATED BY LINKER LABILIZATION*

3.1 Introduction

In addition to the heterometal and mixed-linker based MOFs, defective MOFs represents another type of complex MOFs. For example, heterogeneously arranged mesopores can be introduced into microporous MOF crystals by defects engineering, resulting in hierarchically porous structures. The coordination vacancy on the defective sites further provides a chemical handle to further incorporate complex coordinative assemblies through postsynthetic modifications. It has been proven that defects exist in almost any MOFs, such as MOF-5 and HKUST-1.[61-65] However, Zr-MOFs have attracted particular attention because of their remarkable tolerance towards a high concentration of defects without suffering from severe loss of crystallinity or stability.[66-67] This is related to the high connectivity of Zr_6 clusters and their capability to reduce their connection number. Take the Zr-MOF, UiO-66 as an example, two types of defects were observed: missing-linkers and missing-clusters.[99] The missing linker defect is generated by the removal of an organic linker from a pair of adjacent Zr-clusters, leaving coordination vacancies.[67] The coordination vacancy on the Zr-cluster is believed to be terminated by a monocarboxylate or a pair of $–OH^-/H_2O$ to balance the charge.[100] The missing cluster defect is resulted from the removal of a Zr_6 cluster, along with the 12 surrounding linkers.

The concentration of defects can be affected by synthetic conditions including the metal to ligand ratio, type of modulators, modulator concentration, reaction temperature, and so on.[100-102]

*Reproduced in part with permission from: Yuan, S.; Zou, L.; Qin, J.-S.; Li, J.; Huang, L.; Feng, L.; Wang, X.; Bosch, M.; Alsalme, A.; Cagin, T.; Zhou, H.-C. "Construction of hierarchically porous metal−organic frameworks through linker labilization", *Nat. Commun.* **2017**, *8*, 15356. Copyright 2017 Nature Publishing Group.

Generally, a less defective MOF can be generated with low metal to ligand ratios at high temperature.[101] However, defects that can be created in a one-pot reactions are still limited, because highly defective structures with relatively low stability cannot survive harsh solvothermal synthetic conditions.

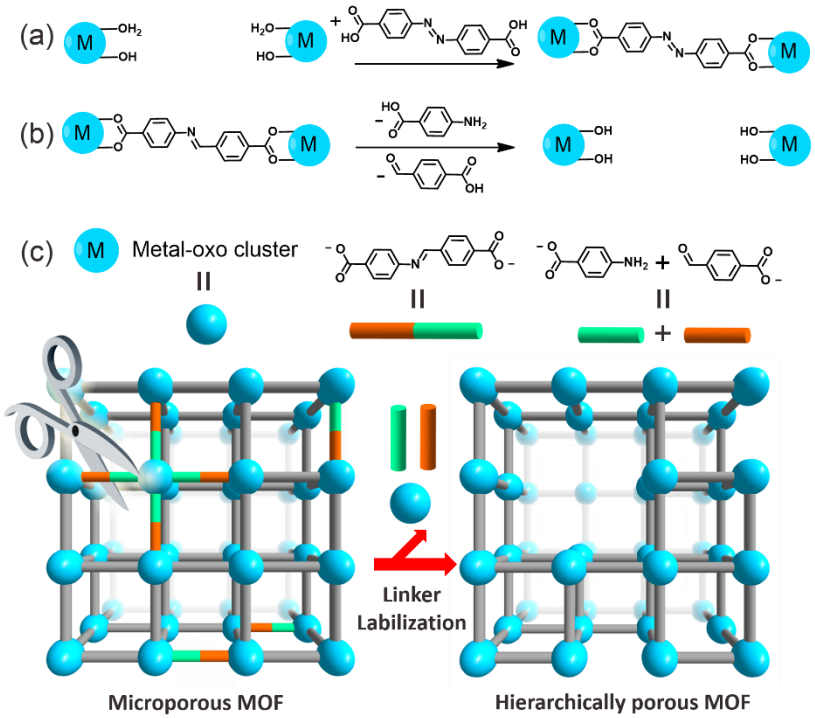

Figure 22. Schematic representation of linker installation (a), linker labilization (b), and hierarchically porous MOF developed by linker labilization (c).

We developed a method, namely linker labilization, to controllably introduce defects into MOFs.[17] This strategy was inspired by the linker installation introduced in the previous section.[24, 29] The linker installation method utilize MOFs with coordinatively-unsaturated $Zr_6O_4(OH)_8(H_2O)_4$ clusters and postsynthetically incorporate linear linkers or terminal ligands on the Zr_6 clusters by replacing the terminal –OH/H_2O with carboxylates (Figure 22a). Linker labilization is a reverse process to linker installation: a MOF is initially constructed with coordinatively-saturated clusters and a "pro-labile" linker; the pro-labile organic linkers are subsequently "labilized" by splitting

into two removable monocarboxylates under acidic conditions to introduce defects (Figure 22b, c). Taking advantage of the acid stability of high valence metal based MOFs and their strong tolerance towards defects,[16, 100-101, 103] the crystallinity and porosity of hierarchical-pore MOFs are well maintained after acid treatment, water treatment, and solvent removal. As many properties are strongly affected by defects, it is possible to tailor the performance of MOFs by defect engineering.[65-66] We demonstrate that linker labilization can create hierarchically porous structures with different levels of porosity, which allows for efficient diffusion of guests throughout the framework, making them promising materials for a wide range of applications including adsorption and catalysis.

3.2 Experimental Section

3.2.1 Materials and Instrumentation

All the reagents and solvents were commercially available and used as received except for 4-carboxybenzylidene-4-aminobenzoic acid (H_2CBAB), and azobenzene-4,4'-dicarboxylic acid (H_2AZDC). Powder X-ray diffraction (PXRD) was carried out with a Bruker D8-Focus Bragg-Brentano X-ray Powder Diffractometer equipped with a Cu sealed tube (λ = 1.54178 Å) at 40 kV and 40 mA. Nuclear magnetic resonance (NMR) data were collected on a Mercury 300 spectrometer. The UV-vis absorption spectra were recorded on a Shimadzu UV-2450 spectrophotometer. ICP-MS data were collected with a Perkin Elmer NexION® 300D ICP-MS. Thermogravimetry analysis (TGA) was conducted on a TGA-50 (SHIMADZU) thermogravimetric analyzer. Fourier transform infrared (IR) measurements were performed on a SHIMADZU IR Affinity-1 spectrometer.

3.2.2 Ligand Syntheses

Synthesis of H_2CBAB. In separate beakers, 4-amino benzoic acid (1.4 g, 10 mmol) and 4-formylbenzoic acid (1.5 g, 10 mmol) were dissolved respectively in 50 mL methanol. The solutions were mixed in a 500 mL flask and refluxed for 3 h under continuous stir. After cooling to room temperature, the precipitates were collected by filtration and washed with methanol (2.5 g, yield: 92%). ^{1}H-NMR (300 MHz, DMSO-d_6) δ 8.74 (s, 1H), 8.08 (d, 4H), 8.00 (m, 2H), 7.36 (m, 2H).

Synthesis of H_2AZDC. The H_2AZDC was synthesized according to the literature with slight modification.[1] In a 500 mL flask, p-nitrobenzoic acid (11 g, 66 mmol) and sodium hydroxide (40 g, 100 mmol) were dissolved in 150 ml of water. The temperature of the mixture was controlled at 50 °C in a water bath. A solution of glucose (90 g in 100 ml of water) was added dropwise over 60 min. The mixture was air bubbled under continuous stir overnight and 50 mL methanol was added. The precipitates were collected by filtration, washed with methanol and dissolved in hot water. The solution was acidified with 10% HCl aqueous solution and the product was collected by filtration (6.1 g, yield: 68%). ^{1}H-NMR (300 MHz, DMSO-d_6) δ 8.17 (m, 4H), 8.02 (m, 4H).

3.2.3 MOF Syntheses

Synthesis of PCN-160. $ZrCl_4$ (200 mg), H_2AZDC (100 mg), trifluoroacetic acid (1.0 mL) and DMF (20 mL) were charged in a Pyrex vial. The mixture was heated in 120 ºC oven for 72 h. After cooling down to room temperature, the red crystals were harvested (95 mg, yield: 67%).

Synthesis of PCN-160-R%. PCN-160-R% (R=6, 9, 17, 31, 43, and 65) were synthesized by the linker exchange of PCN-160 with CBAB solution of different concentration (2.5, 5, 10, 20, 40, and 80 mM, respectively). Generally, crystals of PCN-160 (100 mg) were incubated with the solution of H_2CBAB in DMF (20 mL) at 75 ºC for 10 h. PCN-160-100% were synthesized by repeatedly exchange the supernatant with fresh CBAB stock solution (80 mM) every 5 h for 4

times. The crystals of PCN-160-R% were collected by filtration and washed with fresh DMF 3 times.

Synthesis of PCN-160-R%-*C*. PCN-160-R%-*C* (*C* = 0.5, 1, and 2) was synthesized by treating the crystals of PCN-160-R% with different concentration of acetic acid (AcOH) in DMF solution (0.5, 1, and 2 M, respectively). Generally, crystals of PCN-160-R% (100 mg) were incubated with the solution of AcOH in DMF (20 mL) at 40 ºC for 24 h. The crystals were collected by filtration and washed with fresh DMF and water to remove any remaining acetic acid.

Synthesis of CYCU-3. $AlCl_3$ (75 mg), H_2AZDC (150 mg), acetic acid (0.15 mL) and DMF (15 mL) were charged in a Pyrex vial. The mixture was heated in 120 ºC oven for 24 h. After cooling down to room temperature, the yellow crystalline powders were harvested (65 mg, yield: 37%).

Synthesis of CYCU-3-22%. $AlCl_3$ (75 mg), H_2AZDC (100 mg), H_2CBAB (50 mg), acetic acid (0.15 mL) and DMF (15 mL) were charged in a Pyrex vial. The mixture was heated in 120 ºC oven for 24 h. After cooling down to room temperature, the yellow crystalline powders were harvested (55 mg, yield: 32%). The CBAB in the product is 22% determined by UV-vis spectroscopy.

Synthesis of CYCU-3-22%-0.1. CYCU-3-22% (100 mg) were incubated with the solution of HCl in DMF (0.1 mM, 20 mL) at 40 ºC for 24 h. The products were collected by filtration and washed with fresh DMF and water to remove any remaining acid.

Synthesis of CYCU-3-22%-0.2. CYCU-3-22% (100 mg) were incubated with the solution of HCl in DMF (0.2 mM, 20 mL) at 40 ºC for 24 h. The products were collected by filtration and washed with fresh DMF and water to remove any remaining acid.

3.2.4 Single Crystal X-Ray Crystallography

All crystals were taken from the mother liquid without further treatment, transferred to oil and mounted into a loop for single crystal X-ray data collection. Diffraction was measured on a Bruker Venture CMOS diffractometer equipped with a Cu-K_α sealed-tube X-ray source (λ = 1.5406 Å) at room temperature. The data frames were recorded using the program APEX2 and processed using the Apex3 suite of programs.[2] The data were corrected for absorption and beam corrections based on the multi-scan technique as implemented in SADABS. The structures were solved by direct method using SHELXS and refined by full-matrix least-squares on F^2 using SHELXL software.[3]

Refinement Details of PCN-160. Diffraction frames were integrated in Cubic F by APEX2 and determined with the R(sym) of 0.051 by *XPREP*. *XPREP* suggested that $Fm\bar{3}m$ be the best centrosymmetric space group (COM=4.81). The AZDC ligand is two-fold disordered in the structure. By careful restraints of the ligand geometry and the atomic displacement parameters, *R*1 value is 0.1069 before *SQUEEZE* treatment and 0.0663 after *SQUEEZE* treatment. The squeezed void volume was 18776 Å^3, equivalent to 73.4% of the unit cell.

Refinement Details of PCN-160-100%. Diffraction frames were integrated in Cubic F by APEX2. Based on our previous experience on the isostructural PCN-160, $Fm\bar{3}m$ was selected to describe the structure. The CBAB ligand is two-fold disordered in the structure. By careful restraints of the ligand geometry and the atomic displacement parameters, *R*1 value is 0.1347 before *SQUEEZE* treatment and 0.1308 after *SQUEEZE* treatment. The squeezed void volume was 18430 Å^3, equivalent to 72.6% of the unit cell.

Refinement Details of PCN-160-31%. Diffraction frames were integrated in Cubic F by APEX2. Based on our previous experience on the isostructural PCN-160, $Fm\bar{3}m$ was selected to

describe the structure. According to the UV-vis results, this structure contains both AZDC (~66.67%) and CBAB ligand (~33.33%). The each ligand is two-fold disordered in the structure. By careful restraints of the ligand geometry and the atomic displacement parameters, *R*1 value is 0.1085 before *SQUEEZE* treatment and 0.0731 after *SQUEEZE* treatment. The squeezed void volume was 18912 $Å^3$, equivalent to 73.2% of the unit cell.

Refinement Details of PCN-160-31%-2. Diffraction frames were integrated in Cubic F by APEX2. Based on our previous experience on the isostructural PCN-160, $Fm\bar{3}m$ was selected to describe the structure. According to the UV-vis results, this structure contains both AZDC (77.78%) and CBAB ligand (22.22%). The each ligand is two-fold disordered in the structure. The occupancy of the ligand is refined as 75% and the occupancy of terminal -OH/H_2O is refined as 25%, corresponding to the experimental result that about 25% of the ligand is replaced by terminal -OH/H_2O as crystal defects. By careful restraints of the ligand geometry and the atomic displacement parameters, *R*1 value is 0.1097 before *SQUEEZE* treatment (Figure 23, Table 7).

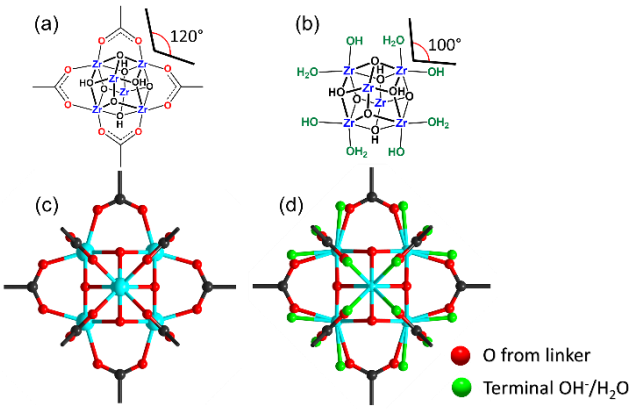

Figure 23. Scheme representation of Zr_6 clusters terminated by carboxylates (a) and –OH/H_2O (b) highlighting different O−Zr−O bond angles; single-crystal structure of PCN-160-31% (left) and PCN-160-31%-2 (right), showing the emergence of terminal –OH/H_2O as an indication of defects.

Table 7. Crystal data and structure refinements.

Name	PCN-160	PCN-160-100%	PCN-160-31%	PCN-160-31%-2
Empirical formula	$C_{336}H_{192}N_{48}O_{128}Zr_{24}$	$C_{360}H_{216}N_{24}O_{128}Zr_{24}$	$C_{344}H_{200}N_{40}O_{128}Zr_{24}$	$C_{256}H_{148}N_{32}O_{128}Zr_{24}$
	$[Zr_6O_8]_4$ $[(C_{14}H_8O_4N_2)_{24}]$	$[Zr_6O_8]_4$ $[(C_{15}H_9O_4N)_{24}]$	$[Zr_6O_8]_4$ $[(C_{14}H_8O_4N_2)_{16}]$ $[(C_{15}H_9O_4N)_8]$	$[Zr_6O_8]_4$ $[(C_{14}H_8O_4N_2)_{14}]$ $[(C_{15}H_9O_4N)_4][O_{24}]$
Formula weight	9138.66	9114.85	9130.72	7909.34
Color/Shape	Orange octahedron	Yellow octahedron	Orange octahedron	Orange octahedron
Temperature/K	110(2)	100(2)	110(2)	103(2)
Crystal system	Cubic	Cubic	Cubic	Cubic
Space group	Fm-3m	Fm-3m	Fm-3m	Fm-3m
a/Å	29.4701(10)	29.3907(11)	29.5566(9)	29.590(10)
b/Å	29.470	29.391	29.557	29.590
c/Å	29.470	29.391	29.557	29.590
α/°	90.00	90.00	90.00	90.00
β/°	90.00	90.00	90.00	90.00
γ/°	90.00	90.00	90.00	90.00
Volume/Å^3	25594.4(9)	25388.1(10)	25820.4(8)	25907(9)
Z	1	1	1	1
ρ_{calc} g/cm^3	0.593	0.596	0.587	0.507
μ/mm^{-1}	0.267	0.269	0.265	0.259
F(000)	4528.0	4528.0	4528.0	3892.0
Wavelength (Å)	0.71073 (MoKα)	0.71073 (MoKα)	0.71073 (MoKα)	0.71073 (MoKα)
2Θ range for data collection/°	4.58 to 54.96	4.6 to 54.96	4.58 to 54.84	4.56 to 54.78
Completeness	100%	100%	100%	100%
Reflections collected	34837	102552	63472	62181
Independent reflections	1513	1499	1518	1518
R_{int}	0.0454	0.0905	0.0571	0.0663
Data	1513	1499	1518	1518
Restraints	8	8	8	8
Parameters	27	30	30	33
GOF on F^2	1.074	1.740	1.061	1.110
R_1 [I > 2σ(I)][a]	0.0663	0.1308	0.0731	0.1097
wR_2 [I > 2σ(I)][b]	0.1794	0.2904	0.2017	0.3090
R_1 (all data)[a]	0.0722	0.1390	0.0777	0.1166
wR_2 (all data)[b]	0.1842	0.2942	0.2071	0.3156
Residue peak / hole (eÅ^{-3})	1.51/-1.01	1.17/-0.68	1.25/-0.96	2.04/-1.33

[a] $R_1 = \Sigma||F_o| - |F_c||/\Sigma|F_o|$.

[b] $wR_2 = |\Sigma w(|F_o|^2 - |F_c|^2)|/\Sigma|w(F_o^2)^2|^{1/2}$.

3.2.5 Linker Exchange

No weight loss was observed for MOF samples during linker exchange process suggesting that linker exchange happen without dissolving or destruction of framework. Therefore, the moles of AZDC in the solution equals to the moles of CBAB being exchanged into the framework. The exchange ratio in MOFs (R%), defined as moles of CBAB divided by the moles of organic linkers (i.e. CBAB+AZDC), was calculated from AZDC concentration in solution determined by UV-vis spectra.

$$R\% = \frac{\mathrm{MW_{AZDC}} \cdot \mathrm{C_{AZDC}} \cdot \mathrm{V_{solution}}}{\mathrm{m_{MOF}} \cdot 69\%}$$

The exchange ratio in MOFs were further confirmed by the ^{1}H-NMR results of digested samples. For ^{1}H NMR spectroscopy, the dry samples (around 5 mg) were dissolved in about 1 mL 5% D_2SO_4/DMSO-d_6. The CBAB was decomposed into 4-amino benzoic acid and 4-formylbenzoic acid under acetic condition. Therefore, the exchange ratios were calculated by the integration of H from AZDC and 4-formylbenzoic acid (Table 8).

Table 8. The exchange ratio in MOFs calculated by UV-vis and ^{1}H-NMR spectra, respectively.

CBAB concentration(mM)	**0**	**5**	**10**	**20**	**30**	**40**	**80×5**
Exchange ratio by UV	0	9%	17%	31%	43%	65%	100%
Exchange ratio by ^{1}H-NMR	0	8%	16%	27%	39%	59%	100%

The maintenance of crystallinity and porosity of PCN-160-R% were proved by PXRD patterns and N_2 sorption isotherms. Before gas sorption experiment, MOF samples was washed with DMF and water, and exchanged by acetone for 3 days, during which the solvent was decanted and freshly replenished three times. The solvent was removed under vacuum at 100 ^{o}C for 10 h,

yielding porous material. Gas sorption measurements were then conducted using a Micrometritics ASAP 2020 system (Figure 24).

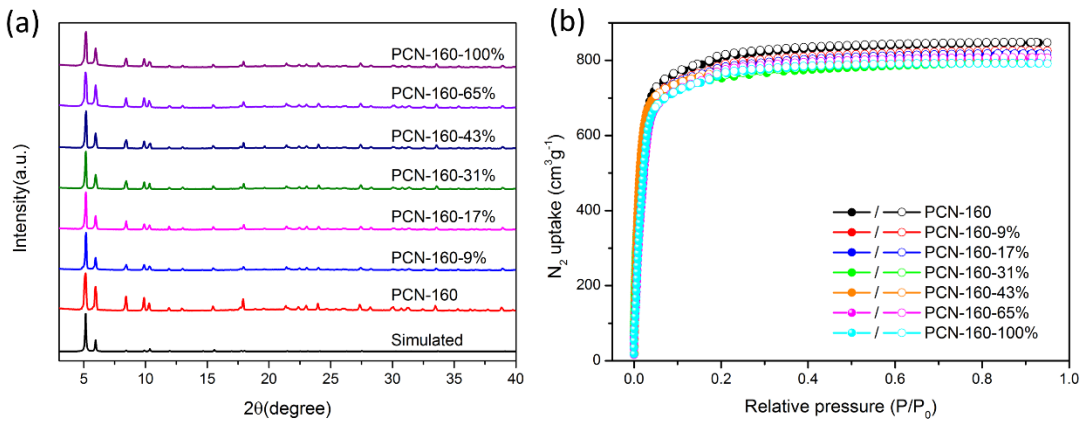

Figure 24. (a) PXRD patterns and (b) N_2 sorption isotherms of PCN-160-R%.

3.2.6 Linker Labilization

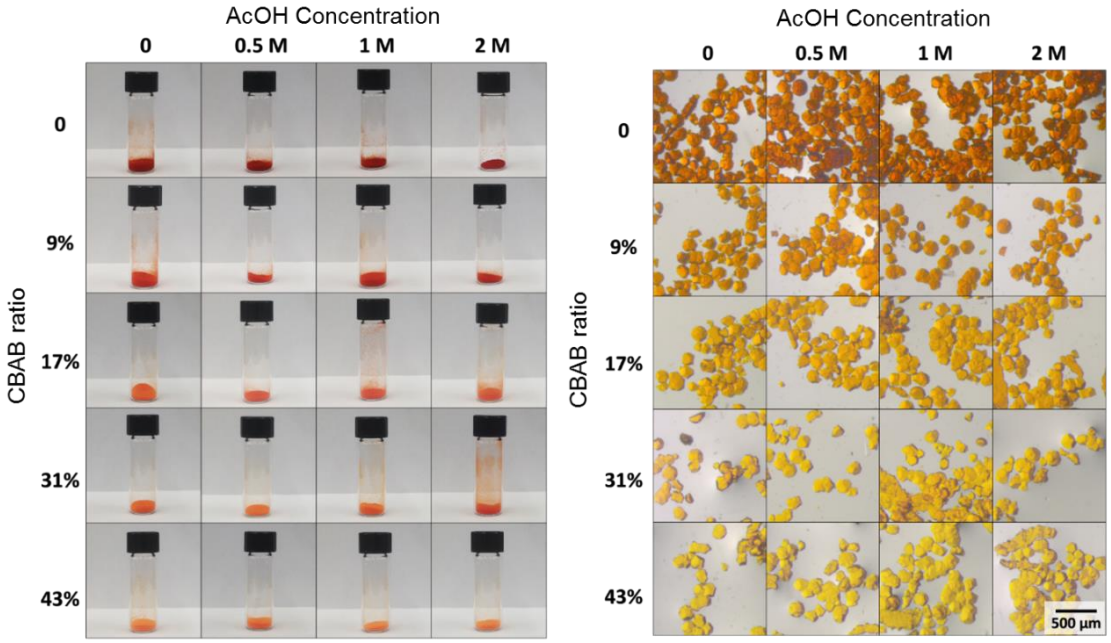

Figure 25. Photographs and microscopic images of PCN-160-R%-*C* samples.

The AZDC with azobenzene moiety has distinguishable red color whereas the color of CBAB is pale yellow. Therefore, the MOF samples with different exchange ratio have different

colors. As shown in Figure 25, the morphology of PCN-160-R%-*C* crystals are not affected by the acid treatment.

The maintenance of crystallinity and porosity of PCN-160-R%-*C* after acid treatment were proved by PXRD patterns and N_2 sorption isotherms. Before gas sorption experiment, MOF samples was washed with DMF and water, and exchanged by acetone for 3 days, during which the solvent was decanted and freshly replenished three times. The solvent was removed under vacuum at 100 ^{o}C for 10 h, yielding porous material (Figure 26, Table 9).

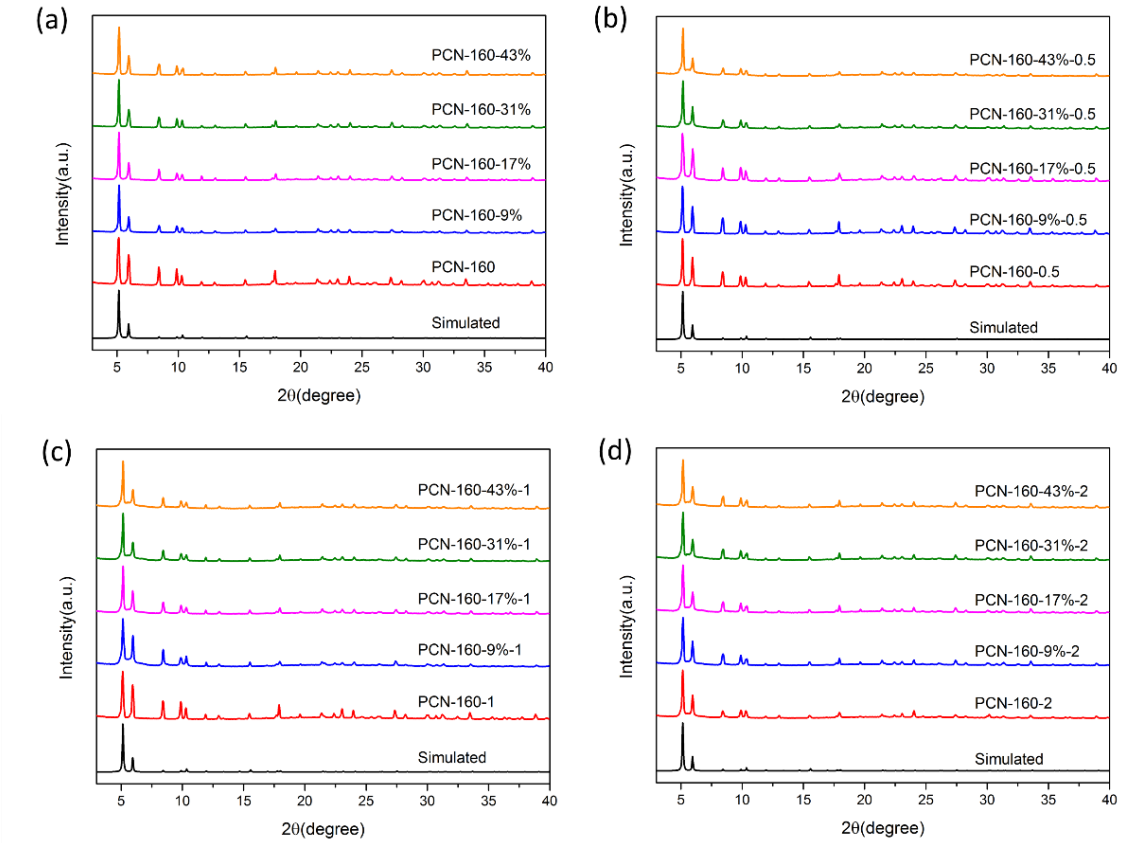

Figure 26. PXRD patterns of PCN-160-R%-*C* treated with (a) 0, (b) 0.5 M, (c) 1 M, (d) 2 M AcOH/DMF solutions.

Table 9. Maximum pore size (Å) of PCN-160-R%-*C* calculated by DFT method.

Exchange ratio (%)	0	9%	17%	31%	43%
0 AcOH	13.6	13.6	14.8	14.8	14.8
0.5 M AcOH	14.8	25.1	25.1	25.1	54.3
1 M AcOH	14.8	25.1	58.7	93.1	137
2 M AcOH	14.8	68.0	108	137	186

3.2.7 Defect Analysis

Scheme 1. Proposed mechanism of linker labilization.

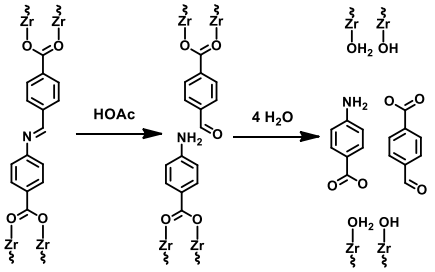

We proposed that labile CBAB linker is partially dissociated and removed during acid treatment to create missing-linker defects (Scheme 1). Although the exact identity of defect sites is unknown, most likely, missing linkers would be replaced with $–OH_2$ and –OH groups in such a way as to compensate for the charge loss from the linkers. The weight percent of CBAB and AZDC in PCN-160-31%-*C* treated by different concentration of AcOH were analyzed by UV-vis spectra. About 50 mg PCN-160-31%-*C* samples were precisely weighted and dissolved in 50 mL K_2CO_3 aqueous solution (5%) to get a clear solution. The concentration of AZDC and CBAB were analyzed by the comparison of the UV-vis absorbance (at λ = 432 and 266 nm, respectively). Note that the CBAB was decomposed into 4-amino benzoate and 4-formylbenzoate in K_2CO_3 aqueous

solution. The concentration of CBAB was analyzed by measuring the UV-vis absorbance of 4-amino benzoate. The composition and connection number (CN) of Zr_6 cluster of each sample are calculated according to the weight percent of CBAB and AZDC (Table 27, Table 10).

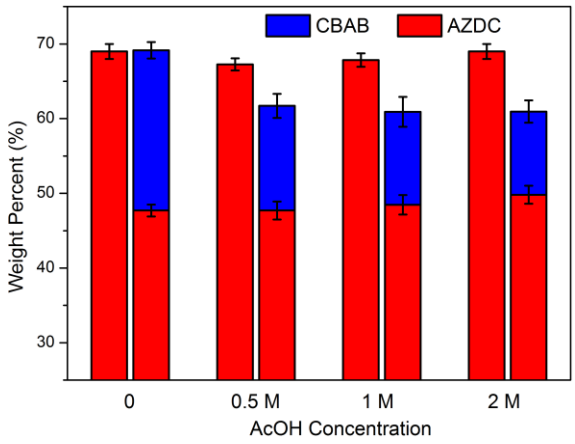

Figure 27. Weight percent of CBAB and AZDC in PCN-160 and PCN-160-31% treated by different concentrations of AcOH.

Table 10. Composition and CN of cluster of PCN-160-R%-*C*.

Exchange ratio	C_{AcOH}	Composition	CN of Cluster
0	**0**	$Zr_{12}O_8(OH)_8$ $AZDC_{11.5}\cdot(H_2O)(OH)$	11.5
0	**0.5 M**	$Zr_{12}O_8(OH)_8$ $AZDC_{11.0}\cdot(H_2O)_2(OH)_2$	11.0
0	**1 M**	$Zr_{12}O_8(OH)_8$ $AZDC_{11.2}\cdot(H_2O)_{1.6}(OH)_{1.6}$	11.2
0	**2 M**	$Zr_{12}O_8(OH)_8$ $AZDC_{11.5}\cdot(H_2O)(OH)$	11.5
31%	**0**	$Zr_{12}O_8(OH)_8$ $AZDC_{8.0}$ $CBAB_{3.6}\cdot(H_2O)_{0.8}(OH)_{0.8}$	11.6
31%	**0.5 M**	$Zr_{12}O_8(OH)_8$ $AZDC_{7.1}$ $CBAB_{2.1}\cdot(H_2O)_{5.6}(OH)_{5.6}$	9.2
31%	**1 M**	$Zr_{12}O_8(OH)_8$ $AZDC_{7.1}$ $CBAB_{1.8}\cdot(H_2O)_{6.2}(OH)_{6.2}$	8.9
31%	**2 M**	$Zr_{12}O_8(OH)_8$ $AZDC_{7.3}CBAB_{1.6}\cdot(H_2O)_{6.2}(OH)_{6.2}$	8.9

The concentration of CBAB and AZDC in the solution after linker labilization process were also analyzed by UV-vis spectra. Crystals of PCN-160-R% (~100 mg) were incubated with

the solution of AcOH in DMF (20 mL) at 40 ºC for 24 h. 0.1 mL of solution was sampled and added with 1.9 mL K_2CO_3 aqueous solution for UV-vis absorbance measurements. The concentration of CBAB is much higher than that of AZDC, indicating the exclusive removal of labile CBAB linker instead of AZDC linker. Meantime, the appearance of Zr^{4+} in the solution suggests the missing-cluster defects (Figure 28).

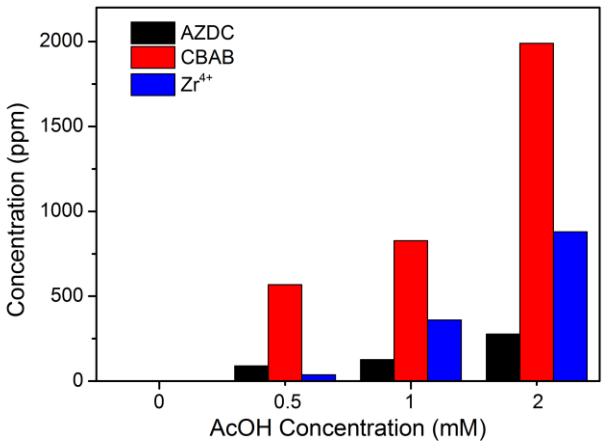

Figure 28. Concentration of AZDC, CBAB and Zr^{4+} in the solution when PCN-160-31%-*C* was treated with different concentration of AcOH.

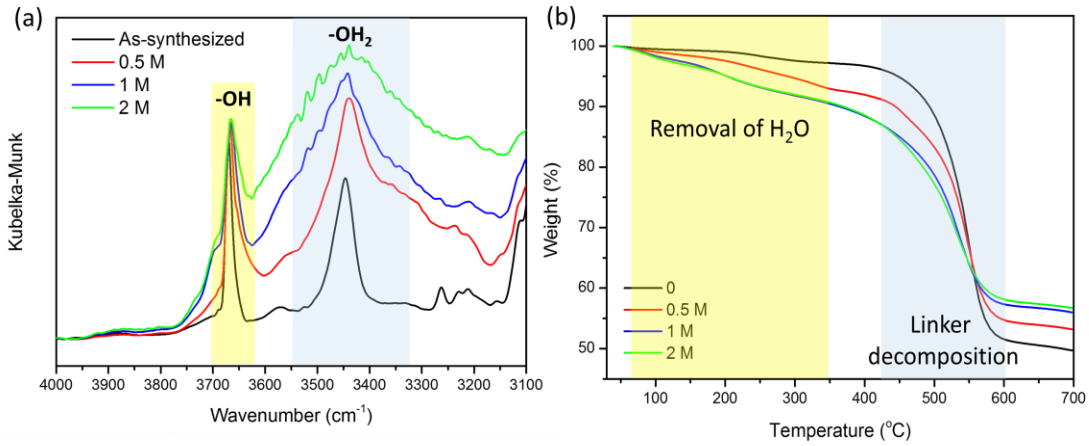

Figure 29. (a) DRIFTS spectra and (b) TGA curves for PCN-160-31% treated with different concentration of AcOH.

Diffuse reflectance infrared Fourier transform spectroscopy (DRIFTS) were performed on a SHIMADZU IR Affinity-1 spectrometer equipped with DRS-8000A diffuse reflectance attachment. For thermogravimetric analysis, about 10 mg of the sample was heated on a TGA-50 (SHIMADZU) thermogravimetric analyzer from room temperature to 700 °C at a rate of 5 °C·min^{-1} under N_2 flow of 15 mL·min^{-1}. The initial weight loss before 300 °C is attributed to the removal of the coordinated water molecules on the clusters, which is comparable to the theoretical mass percentage. TGA curves indicate thermal stability of the framework up to 450 °C, where decomposition of the framework starts (Figure 29).

3.2.8 Molecular Modeling

The missing-linker model was built by taking a stoichiometric 3 × 3 × 3 supercell of PCN-160 with face-centered cubic (**fcu**) topology and randomly removing a certain amount of linkers. We developed a customized perl script in Material Studio package to randomly delete the ligands in 3 × 3 × 3 supercell of PCN-160. The 3 × 3 × 3 supercell was chosen because it is the largest model Zeo++ package could handle.[4] API (Application Program Interface) of Material Studio was adopted to manipulate the atom, bond and fragment objects. Firstly, the ligands were detached from metal cluster by deleting the O-C bonds. Then a search for N-N bonds was made so that we can identify all the ligand fragments in the supercell. Later, a random number list was generated based on the deleting percentage of ligands. The randomly selected ligand fragments were deleted. Finally, the O-C bonds between metal cluster and ligands were added back into the supercell to restore the bonds connectivity in the system. The hydrogen on the terminal -OH/H_2O ligands were automatically added by Material Studio. Similarly, a script for metal cluster random deletion was developed. However, for metal cluster deletion, the ligands around the metal cluster were also

deleted based on the observation that terminal carboxylates could be removed under acidic condition. The major part of these scripts was listed as follow:

```
#!perl
use strict;
use Getopt::Long;
use MaterialsScript qw(:all);
my $doc = $Documents{"filename.xsd"};
my $NumberOfDeleted=48; #input: number of deleted ligands.
my $bonds = $doc->UnitCell->Bonds;
our @fragments=();
our $fragmentsnum=0;
foreach my $bond (@$bonds) {
if (($bond->Atom1->ElementSymbol eq "N") and   ($bond->Atom2->ElementSymbol eq "N")){
    my $fragmentAtoms=$bond->Atom1->Fragment->Atoms;
    $fragmentsnum=$fragmentsnum+1;
    push(@fragments,[($fragmentAtoms,$fragmentsnum)]);
 }
}
my $range = $fragmentsnum;
# building deleting list
our @randnumlist=();
our $randnumconter=0;
do{  my $random_number = int(rand($range));
     my $flag=0;
   foreach my $j(@randnumlist){
              if($random_number eq $j){$flag=1;}
            }
   if($flag eq "0"){
push(@randnumlist,$random_number);
$randnumconter=$randnumconter+1;
}
}while( $randnumconter< $NumberOfDeleted );
#check the length of randnumlist
my $ii=0;
foreach my $i (@randnumlist) {
$ii=$ii+1;
}
if ($ii eq $NumberOfDeleted){
    #delete the ligand
    foreach my $i (@randnumlist) {
       @fragments[$i]->[0]->Delete;
       print "Deleting ligand NO.:",$i,"\n";
      }
}
print "fragments number is:###",$fragmentsnum,"###","\n";
print "% of ligands had been deleted:",100*$NumberOfDeleted/$fragmentsnum,"%","\n";
#calculate bonds
$doc->CalculateBonds;
```

Based on the script above, we developed two types of defect models, namely, a missing-linker model and a missing-cluster model. The pore size distributions were simulated by the Zeo++ package.[4] The simulated pore distribution for missing cluster model provides clear evidence that

the experimentally observed mesopores originated from missing-cluster defects. The missing-linker defects alone will not lead to the formation of 2.5 nm mesopores. Therefore, the 2.5 nm mesopores are tentatively attributed to the missing-cluster defects, in which a Zr_6 cluster is removed along with linkers around it. As the missing-cluster defects locally created an eight-connected net with ReO_3 (**reo**) topology, it is also refered as **reo** defects (Figure 30-31).

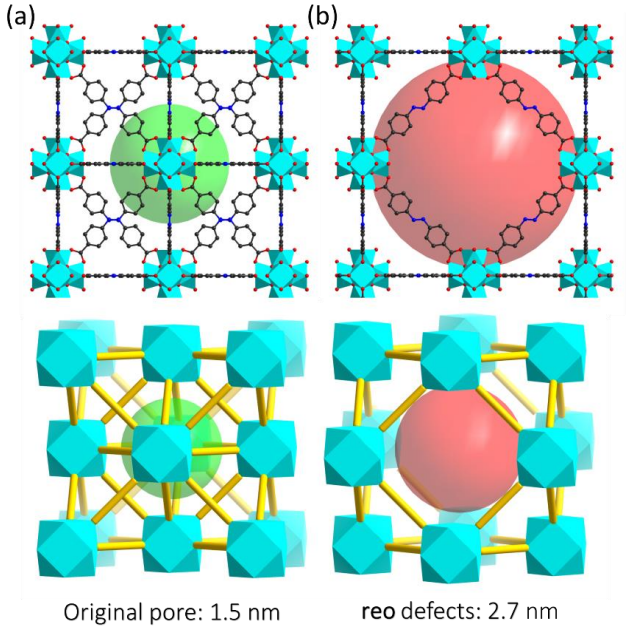

Figure 30. (a) Structure and topology of PCN-160 with **fcu** topology; (b) Structure and topology of the **reo** defect region.

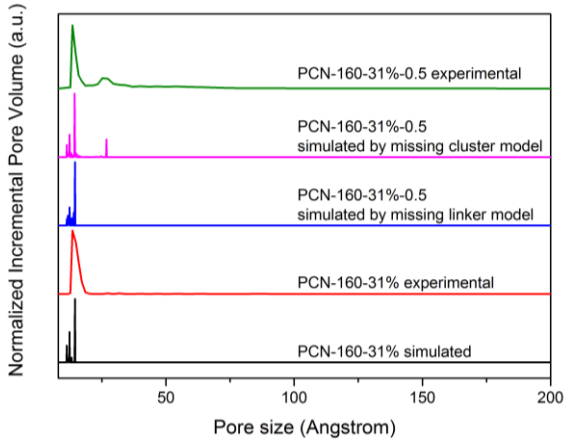

Figure 31. A comparison of experimental and simulated pore size distribution based on missing-linker model and missing-cluster model.

3.2.9 SEM and TEM

Transmission electron microscopy (TEM) experiments were conducted on a FEI Tecnai G2 F20 ST microscope (America) operated at 200 kV. Field-emission scanning electron microscopy (FESEM) images were collected on the FEI Quanta 600 field emission scanning electron microscope (America) at 20KV. A 10nm Platinum/Palladium film was sputtered on the samples before FESEM measurements (Figure 32-35).

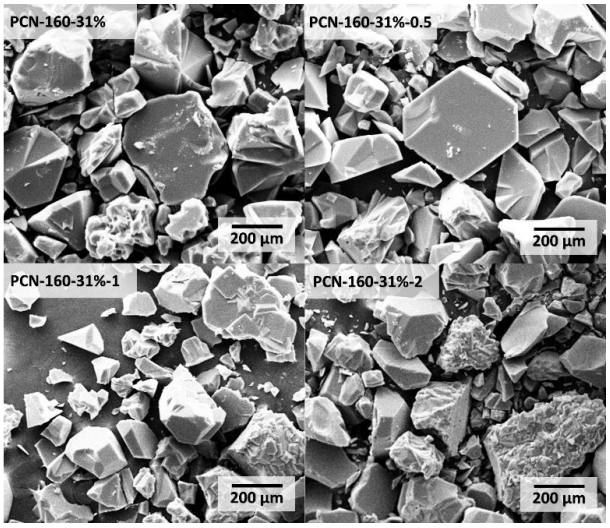

Figure 32. SEM images of PCN-160-31% treated with different concentration of AcOH (scale bar 200 µm).

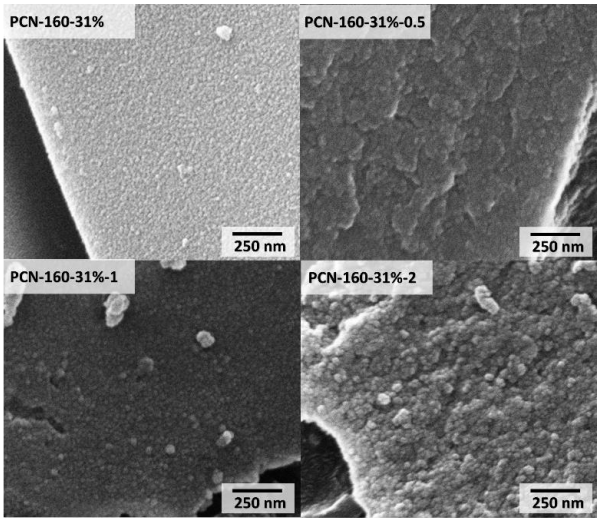

Figure 33. SEM images of PCN-160-31% treated with different concentration of AcOH (scale bar 250 nm).

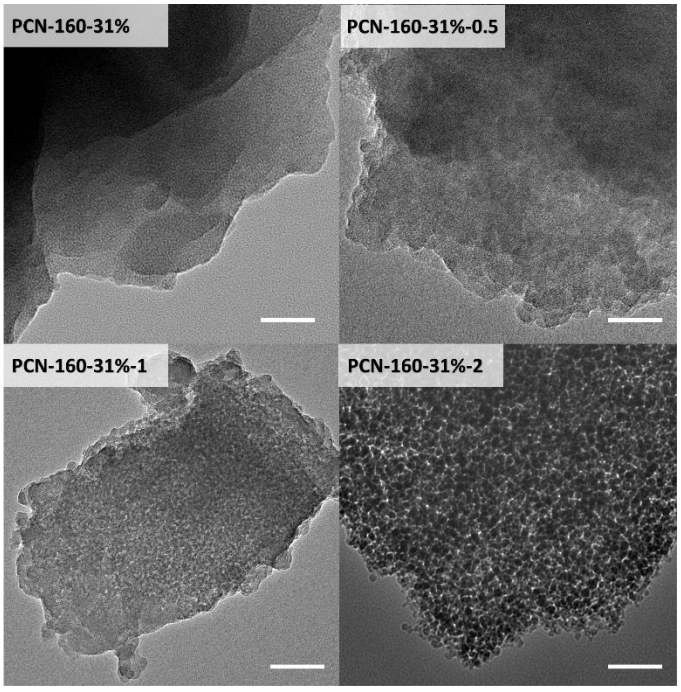

Figure 34. TEM images of PCN-160-31% treated with different concentration of AcOH (scale bar 40 nm).

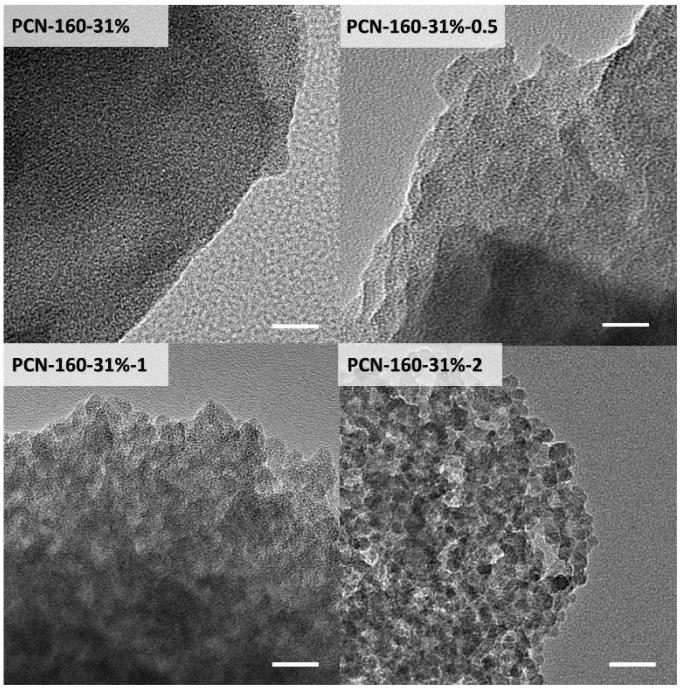

Figure 35. TEM images of PCN-160-31% treated with different concentration of AcOH (scale bar 20 nm).

3.2.10 Guest Adsorption

$Cr_2O_7^{2-}$ Adsorption. About 50 mg of dry samples were precisely weighted and used for the removal of dichromate with a concentration of 100 ppm. The dichromate aqueous solutions (20 mL) containing the adsorbents were mixed well with magnetic stirring and maintained for a certain time (from 1 to 60 min) at 25 °C. 0.1 mL of solution were sampled each time, diluted into 2 mL, and then separated from the adsorbent with a syringe filter (PTFE, 0.25 μm). The dichromate concentrations were calculated by the comparison of the UV-vis absorbance (at λ = 257 nm) (Figure 36-37).

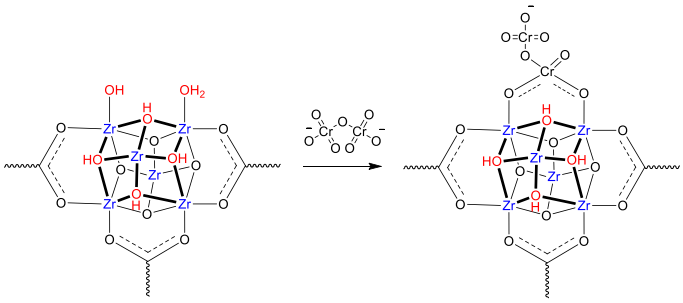

Figure 36. Proposed adsorption mechanism of $Cr_2O_7^{2-}$ ion onto PCN-160-31%-*C* by coordinated at terminal $-OH^-/H_2O$ ligands.

POM Adsorption. $Na_6K_4[Ni_4(H_2O)_2(PW_9O_{34})_2]\cdot 32H_2O$ was synthesized according to the literature.[5] About 50 mg of dry samples were precisely weighted and mixed well with 10 mL of $H_3PMo_{12}O_{40}$ in methanol/H_2O (0.25%) under magnetic stirring at 25 °C. 0.1 mL of solution were sampled each time, diluted into 2 mL, and then separated from the adsorbent with a syringe filter (PTFE, 0.25 μm). The POM concentration were calculated by the comparison of the UV-vis absorbance (at λ = 250 nm).

MOP Adsorption. $Cu_{24}(BDC\text{-}OH)_{24}(H_2O)_{24}$ (MOP) was synthesized according to the literature.[6] About 50 mg of dry samples were precisely weighted and mixed well with 10 mL of MOP in DMF solution (1%) under magnetic stirring at 25 °C. 0.1 mL of solution were sampled

each time, diluted into 2 mL, and then separated from the adsorbent with a syringe filter (PTFE, 0.25 μm). The MOP concentration were calculated by the comparison of the UV-vis absorbance (at λ = 690 nm).

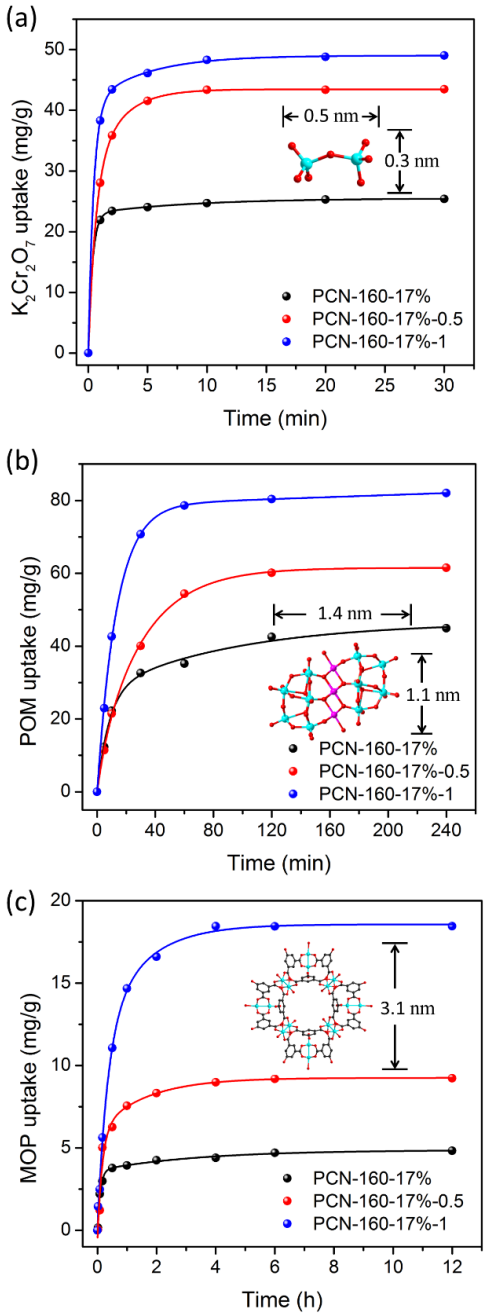

Figure 37. Adsorption kinetics of $[Cr_2O_7]^{2-}$, POM and MOP in PCN-160-17%, PCN-160-17%-0.5, and PCN-160-17%-1, respectively.

3.2.11 Enzyme Encapsulation

Creating defects in CYCU-3. Labile CBAB linkers were doped in CYCU-3 during the synthesis by using a mixture of CBAB (50mg) and AZDC (100mg) as starting materials. The linker ratio of CBAB in the product is 22%, which was determined by UV-vis spectroscopy. The samples with 22% of labile CBAB linkers was denoted as CYCU-3-22%. The crystallinity and the porosity of samples are well maintained after the doping of CBAB as proved by PXRD patterns and N_2 sorption isotherms (Figure 38).

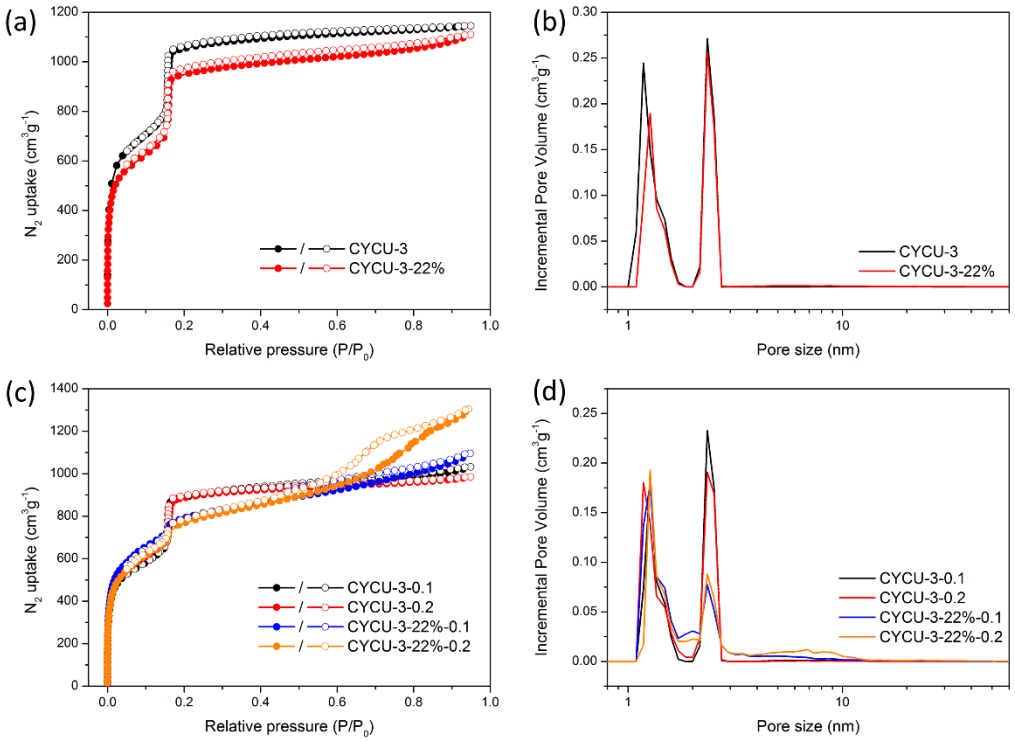

Figure 38. N_2 sorption isotherms and pore size distributions of CYCU-3 after partial substitution of linkers (a),(b) and acid treatment (c),(d).

Defects were created in CYCU-3-22% by treating with the solution of HCl in DMF at 40 ºC for 24 h. The crystallinity of the samples are maintained after acid treatment, which is confirmed by PXRD patterns. N_2 sorption isotherms and pore size distributions show the growth of mesopores

with a diameter of ~7 nm along with the decrease of small mesopore volume (3 nm in diameter). This indicates that the 3 nm mesopores were gradually extended to the ~7 nm large mesopores by acid etching. CYCU-3-22%-0.2 shows high porosity and large mesopores so that it is used for enzyme encapsulation and catalysis studies (Figure 39).

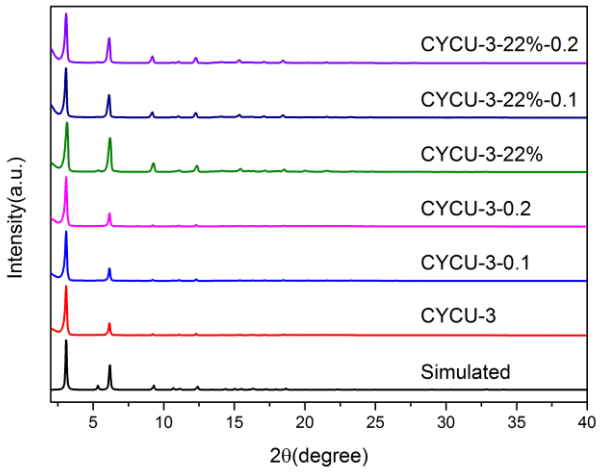

Figure 39. PXRD patterns of CYCU-3 after different treatment.

Enzyme Loading. The cytochrome c (Cyt c) solution (300 μM) were incubated with activated CYCU-3-22% and CYCU-3-22%-0.2 (10 mg) at 25 °C. The resulted enzyme loaded CYCU-3-22% and CYCU-3-22%-0.2 were denoted as Cyt c@ CYCU-3 and Cyt c@ CYCU-3D respectively where D stands for defected samples. The uptake of Cyt c was determined by UV-visible spectroscopy. The absorption of the soret band at 399 nm was proportional to the concentration of enzyme according to the Beer-Lambert Law. The loading amount of enzymes was calculated by measuring the concentration of enzymes in the supernatant and then subtracting from the free-enzyme amount added in the beginning of experiment. The enzyme uptake reached the saturation in 48 h since no more change on the soret band of supernatant was observed. The maximum loadings are 23.3 mmol/g for Cyt c@ CYCU-3 and 14.5 mmol/g for Cyt c@ CYCU-

3D. Before catalytic reaction, the solid samples were immersed in water for two days during which the solvent was decanted and freshly replenished five times to ensure full removal of any loosely bound Cyt c. N_2 sorption isotherms of CYCU-3 and CYCU-3D after enzyme loading prove that the enzyme occupies the hexagonal channels, leaving the triangular channels poised for substrates (Figure 40).

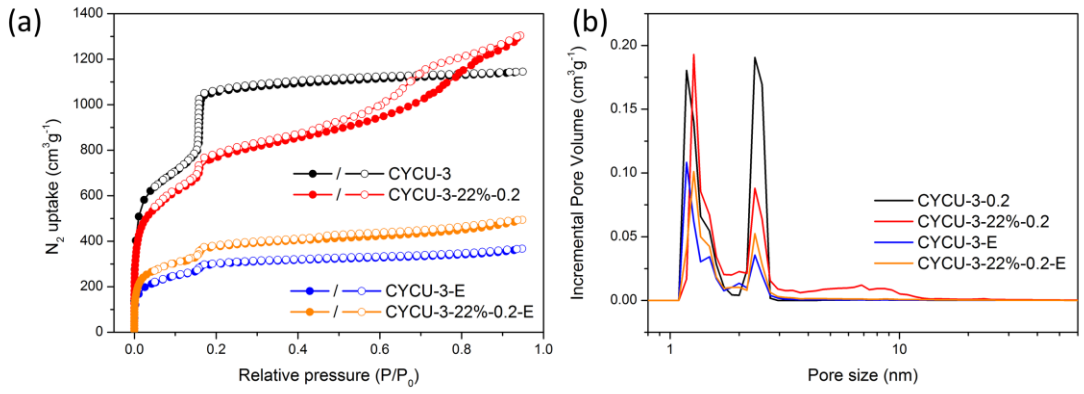

Figure 40. N_2 sorption isotherms (a) and pore size distributions (b) of CYCU-3-22% and CYCU-3-22%-0.2 before and after enzyme loading.

Kinetic Studies. Cyt c can catalyze the oxidation of o-phenylenediamine (o-PDA) and 2-2'-azino-bis(3-ethylbenzthiazoline-6-sulfonic acid) (ABTS) in the presence of H_2O_2. The products were confirmed by scanning the UV-vis absorbance on spectrophotometer and the concentrations of products were calculated by their molar extinction coefficients at respective wavelengths (16300 $M^{-1}cm^{-1}$ at 450 nm for the peroxidized product of o-PDA and 3.6×104 $M^{-1}cm^{-1}$ at 418 nm for peroxidized product of ABTS). The concentration of H_2O_2 was determined spectrophotometrically at 240 nm with $\varepsilon = 43.6\ M^{-1}cm^{-1}$. Kinetic measurements were carried out in time course mode by monitoring the absorbance change at 450 nm for o-PDA and 418 nm for ABTS. The Michealis-Menten equation was used for enzyme kinetics.

$$V_0 = \frac{V_{max}[S]}{K_m + [S]}$$

V_0 is the initial catalytic rate, V_{max} is the maximum reaction rate, which is obtained when the catalytic sites on the enzyme are saturated with substrate. [S] is the substrate concentration and K_m is the apparent Michealis-Menten constant. Lineweaver-Burk plot was employed for illustrating kinetic data and calculate the parameters by taking the reciprocal of both sides of the Michaelis–Menten equation.

The reactions were conducted in the 3ml cuvette directly. The substrate (2 mM) and Cyt c (or MOF immobilized Cyt c, 0.5 μM) were added to buffer followed with the addition of H_2O_2. After a quick shaking, the cuvette was put in the UV sample holder as quickly as possible. The data were collected using the kinetic mode and the plots of absorbance to time were obtained. The background need to be scanned before data collection with addition of water instead of H_2O_2. The specific activities for Cyt c, Cyt c@ CYCU-3 and Cyt c@ CYCU-3D were measured with 2 mM ABTS, 20 mM H_2O_2, 0.5 μM enzyme in 3 ml water at 25 °C. The specific activities were calculated by comparing the reaction rate catalyzed by each catalyst (Table 11, Figure 41-42).

Table 11. Comparison of kinetic parameters for Cyt c, Cyt c@ CYCU-3 and Cyt c@ CYCU-3D.

Catalyst	**Substrate**	K_m **(mM)**	k_{cat} **(min)**	k_{cat}/K_m	V_{max} **(mM/min)**
Cyt c	o-PDA	6.92	2.13	0.308	0.00106
Cyt c@ CYCU-3D	o-PDA	12.1	1.81	0.148	0.000905
Cyt c@ CYCU-3	o-PDA	8.75	1.41	0.161	0.000707
Cyt c	ABTS	19.9	104	5.22	0.0521
Cyt c@ CYCU-3D	ABTS	9.05	31.2	3.45	0.0156
Cyt c@ CYCU-3	ABTS	5.87	4.62	0.787	0.00231

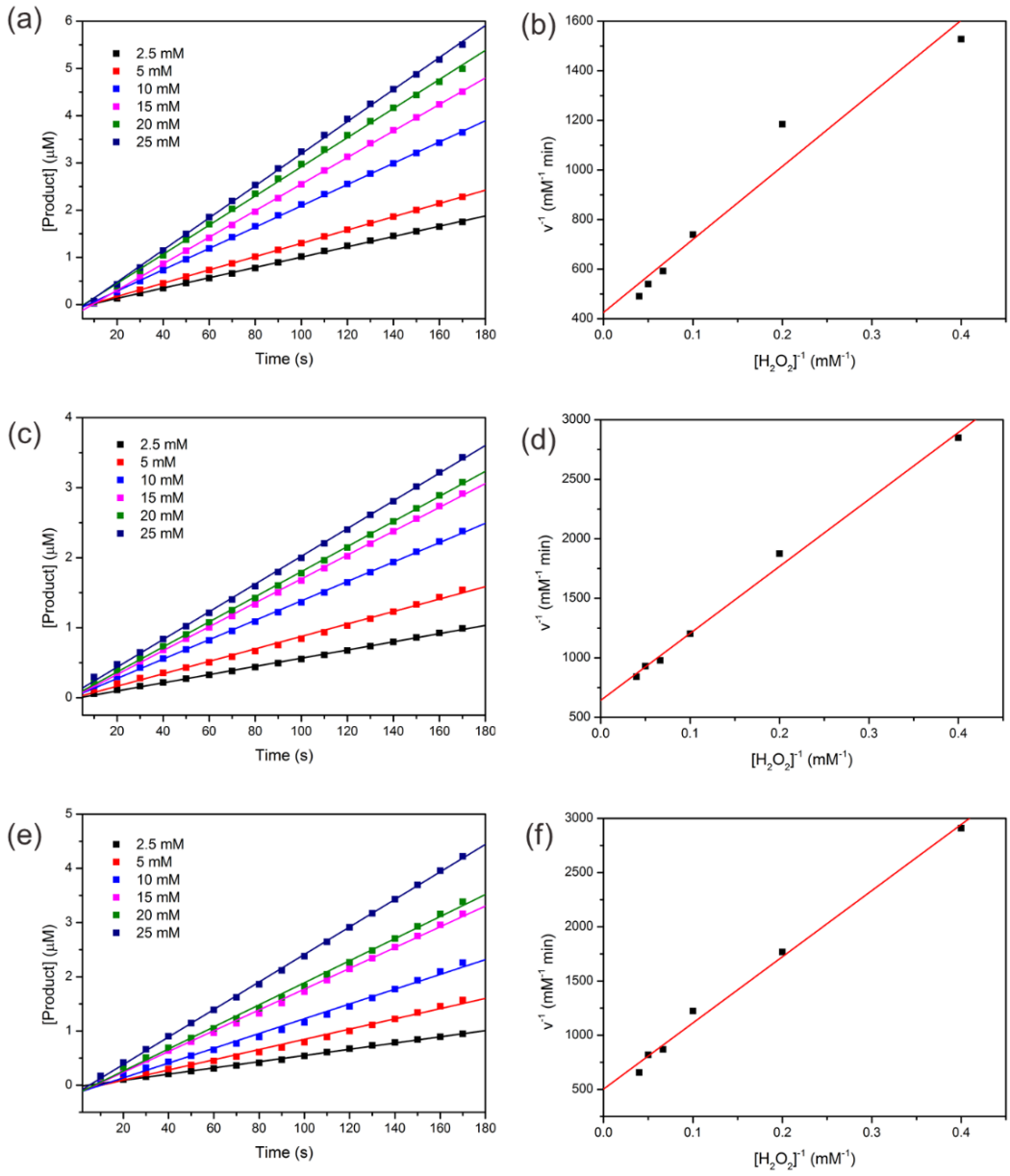

Figure 41. The initial o-PDA oxidation profile catalyzed by free Cyt c (a), Cyt c@ CYCU-3 (c) and Cyt c@ CYCU-3D (e). The concentrations of H_2O_2 range from 2.5 mM to 25 mM. Lineweaver-Burk plot of o-PDA oxidation catalyzed by free Cyt c (b), Cyt c@ CYCU-3 (d) and Cyt c@ CYCU-3D (f).

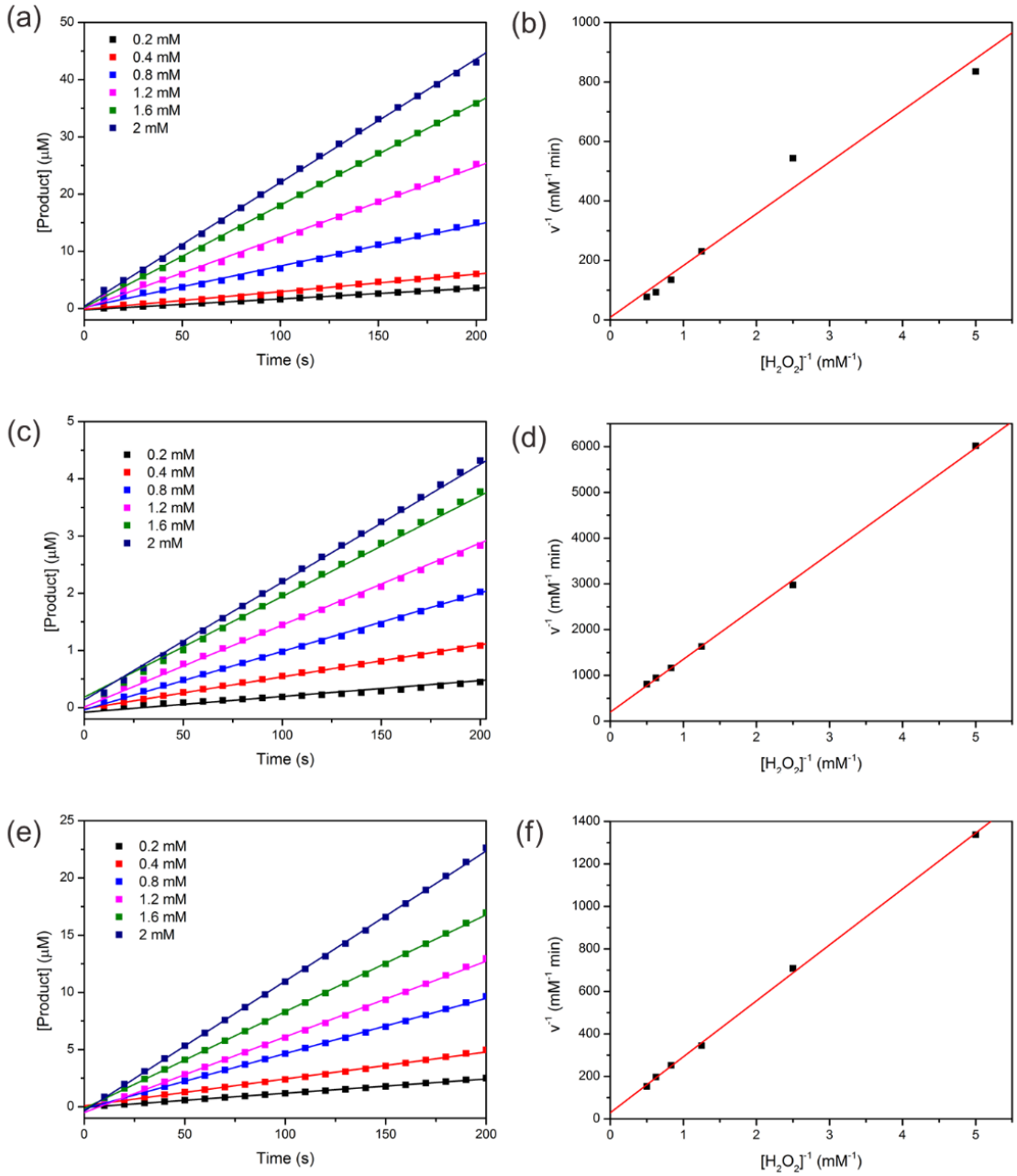

Figure 42. The initial ABTS oxidation profile catalyzed by free Cyt c (a), Cyt c@ CYCU-3 (c) and Cyt c@ CYCU-3D (e). The concentrations of H_2O_2 range from 0.2 mM to 2 mM. Lineweaver-Burk plot of ABTS oxidation catalyzed by free Cyt c (b), Cyt c@ CYCU-3 (d) and Cyt c@ CYCU-3D (f).

3.3 Results and Discussion

3.3.1 Labilizing Zr-MOFs by Linker Exchange

Zr-MOFs were firstly selected as platforms for the implementation of the linker labilization strategy because of their superior stability and strong tolerance of missing-linker defects. An imine-based linker, denoted as CBAB (4-carboxybenzylidene-4-aminobenzate), was designed as the pro-labile linker, which can be easily dissociated into 4-amino benzoic acid and 4-formylbenzoic acid in a single step through hydrolysis. The equilibrium constant of CBAB hydrolysis reaction was measured to be 0.0601 in *N*,*N*-dimethylformamide (DMF), which increased to 4.36 in 0.5 M AcOH/DMF solution (AcOH = acetic acid). An azobenzene-based linker, namely AZDC (azobenzene-4,4'-dicarboxylate), was selected as a robust linker to support the framework. As AZDC and CBAB have very similar lengths and the same connectivity, they are expected to give rise to mixed linker MOFs when combined with Zr_6 clusters. The robust AZDC linkers can support the framework, whereas the CBAB can be removed by acid treatment to increase the MOF porosity. We attempted to synthesize mixed linker Zr-MOFs starting from a mixture of AZDC and CBAB in a one-pot reaction, but to no avail. Only a Zr−AZDC MOF was obtained whereas the CBAB linker was not incorporated in the product. In fact, the synthesis of Zr-MOFs was carried out at a high temperature (120 °C) with an excess amount of carboxylic acid as a modulating reagent.[89] The CBAB presumably decomposed under such harsh conditions due to its acid sensitivity. To overcome this, postsynthetic linker exchange was adopted.

The Zr-AZDC-MOF, namely PCN-160, was synthesized as a template under solvothermal condition using trifluoroacetic acid as the modulating reagent. SCXRD revealed that PCN-160 crystallized in the cubic space group $Fm\bar{3}m$. Each individual Zr_6 cluster was connected to 12 AZDC to form a UiO type structure with face-centered cubic (**fcu**) topology. Note that Zr-AZDC

MOFs isostructural to PCN-160 have been previously reported using different synthetic methods.[104-107] The linker exchange can be carried out under relatively low temperature without acid, which maintains the intactness of the imine bond in CBAB.[108-109] Considering their similarity, the AZDC in PCN-160 is expected to be substituted by CBAB through linker exchange.

Systematic studies were performed to investigate the linker exchange process. The linker exchange was carried out by incubating the crystals of PCN-160 in the CBAB/DMF solutions at 75 °C. As AZDC possesses a distinctive UV-vis absorption peak at 432 nm, the linker exchange process can be easily monitored by UV-vis spectroscopy. The effects of incubation time and CBAB concentration in DMF solution were studied. As shown in Fig. 1a, the CBAB content in PCN-160 gradually increases as incubation time increases and levels off after 150 min. Further elongation of incubation time does not increase the CBAB content, indicating that a dynamic equilibrium is reached between the solid and the solution. The exchange ratio, defined as moles of CBAB divided by the moles of organic linkers (CBAB+AZDC) in PCN-160, was calculated based on the AZDC concentration in the solution and the weight of the MOF material, which matches well with the ^{1}H-NMR result of digested samples. Upon completion of linker exchange, the MOFs with labile CBAB linkers are denoted as PCN-160-R%, where R% stands for the exchange ratio. The exchange ratios of PCN-160 vary from 5.5% to 65%, when incubated with CBAB solutions of different concentration. A positive correlation is observed between the CBAB concentration and the exchange ratio at equilibrium state. However, the ratio of CBAB exchanged to CBAB added decreases as the CBAB concentration increases, suggesting that stronger driving forces are needed to reach higher exchange ratios (Figure 43b). The CBAB/DMF solution almost saturates at 80 mM, which means the exchange ratio can reach as high as 65% without changing the stock solution. To drive the equilibrium of the system forward, the supernatant was exchanged with fresh

saturated CBAB stock solution to remove the AZDC. Complete exchange can be realized by repeatedly exchanging the supernatant with fresh CBAB stock solution every 300 min for 4 times. Single-crystal to single-crystal transformation is realized so that the structure of the resulting MOF after linker exchange can be precisely determined by SCXRD. The resulting MOF, PCN-160-100%, also crystallized in the cubic space group $Fm\bar{3}m$ with unit cell parameters of $a = b = c =$ 29.47 Å, which is similar to that of PCN-160 ($a = b = c =$ 29.39 Å). The UV-vis and ^{1}H-NMR spectra of digested samples confirm that the AZDC is completely substituted by CBAB.

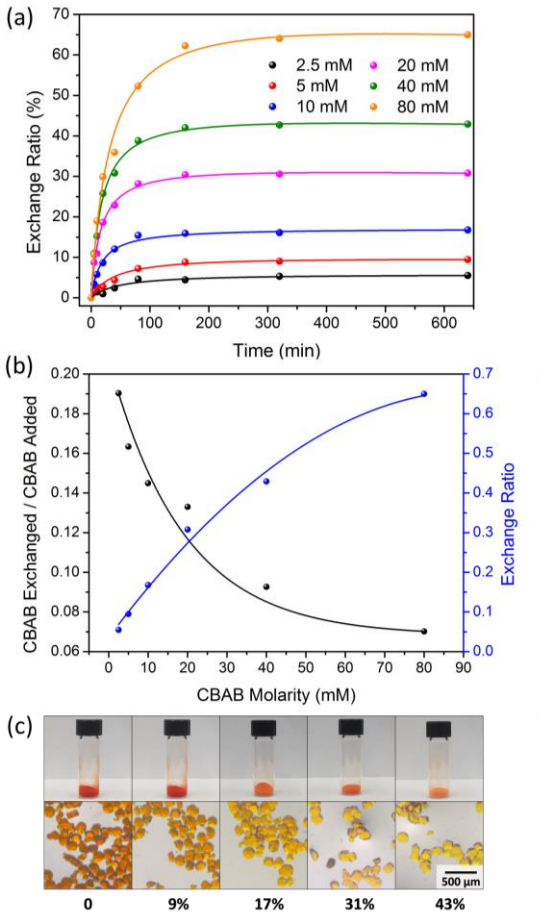

Figure 43. Linker exchange monitored by UV-vis spectra. (a) AZDC concentration in supernatant as a function of incubation time in different concentrations of CBAB solutions; (b) Relationship between CBAB exchanged/CBAB added, exchange ratio and CBAB concentration in solution; (c) Images of the PCN-160 crystals with different exchange ratios.

The supernatants after linker exchange were analyzed by ICP-MS, which showed no detectable Zr^{4+}. The weights of MOF materials were invariant before and after the linker exchange process, eliminating the possibility of dissolution or decomposition during the treatment. PCN-160-R% samples maintain single crystallinity as revealed by the PXRD patterns and the microscope images of the respective single-crystals (Figure 43c). N_2 sorption isotherms also indicate that the porosity and structural integrity of PCN-160-R% are well-retained after the linker exchange (Figure 44a). These results unambiguously show that the exchange ratio of PCN-160 can be precisely tuned with retention of framework integrity and porosity, which is essential for the linker labilization method.

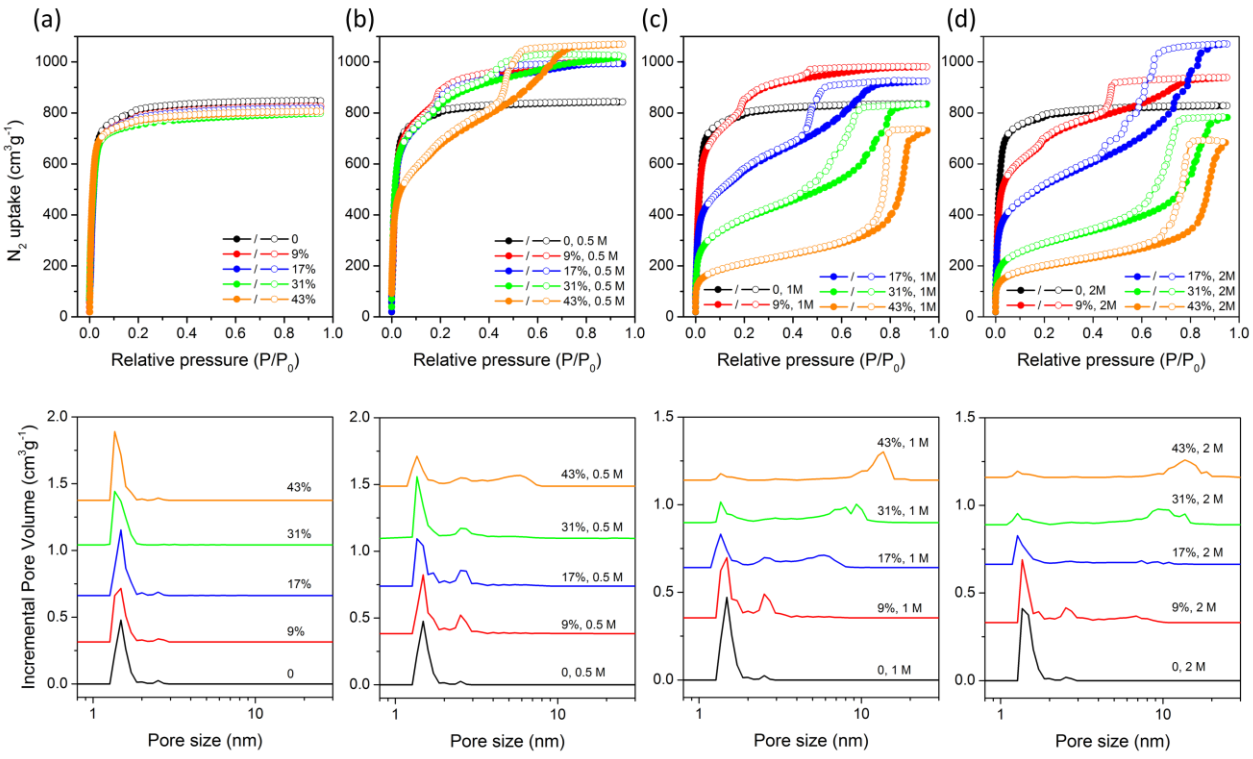

Figure 44. N_2 sorption isotherms and pore size distributions. PCN-160-R%-*C* treated with pure DMF (a), 0.5 M AcOH/DMF solution (b), 1 M AcOH/DMF solution (c), and 2 M AcOH/DMF solution (d).

3.3.2 Creating Hierarchical Pores by Linker Labilization

It is known that the CBAB linker easily dissociates into 4-amino benzoic acid and 4-formylbenzoic acid under acetic condition. The terminal benzoates are much more labile than the bridging linker, as they can be replaced by acetates or a pair of terminal –OH/H_2O ligands.[110] Therefore, we proposed that the CBAB in PCN-160 could be partially removed by acetic acid treatment to create controllable missing-linker defects. Presumably the defect concentration can be affected by (a) exchange ratio of PCN-160 and (b) AcOH concentration. Therefore, control experiments were conducted to investigate the effects of each factor. PCN-160 samples with exchange ratios varying from 0 to 43% were prepared and treated with different concentrations of AcOH/DMF solution at 40 °C for 24 h. The resulting materials are denoted as PCN-160-R%-*C*, where R% stands for exchange ratio and *C* represents the acid concentration. PXRD measurements showed that the MOF materials after acid etching possessed the same diffraction patterns as the parent PCN-160. The microscope images of the respective single-crystals demonstrated that the crystal morphology was not affected by the linker labilization process. The porosity of each sample was estimated by N_2 sorption measurements. Prior to the gas sorption measurements, the MOF materials were washed thoroughly with DMF and water to remove any remaining acetic acid, and exchanged by acetone before thermal activation at 100 °C under vacuum. The N_2 sorption isotherms at 77 K demonstrated the formation of the hierarchically structured MOF materials with both micropores and mesopores (Figure 44). In contrast to the type-I isotherm for the microporous PCN-160, type-IV isotherms were observed for PCN-160-R%-*C* samples with hysteresis loops characteristic of large constricted mesopores.

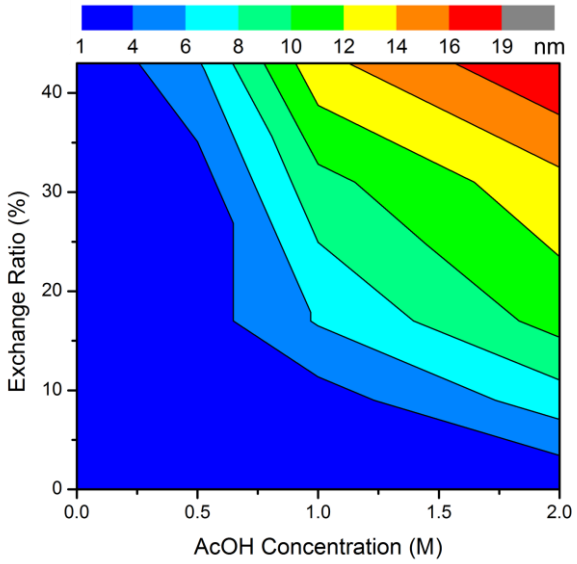

Figure 45. Control of pore size. Maximum pore size of PCN-160-R%-*C* as a function of exchange ratio and AcOH concentration.

The pore-size distribution of PCN-160-R%-*C* samples were calculated from the N_2 adsorption isotherms using a density functional theory (DFT) model. Generally, the porosities and pore sizes of these MOFs show strong dependences on both exchange ratio and AcOH concentration. When 0.5 M acetic acid was used as the etching reagent, both porosities and pore sizes increased with the exchange ratios. For example, when the exchange ratio increases from 0 to 9%, an obvious mesopore with a diameter of 2.5 nm emerges. Further increment of the exchange ratio creates a second mesopore as large as 5.4 nm. Although the pore size of the micropores (1.5 nm) is the same in all the hierarchical-pore MOFs, the pore volume of micropores decreases as the pore volume of mesopores increases, suggesting that the micropores are partially converted into mesopores through linker labilization. The MOF porosities, as indicated by the total N_2 uptake at 77 K and 1 bar, are dramatically enhanced by the linker labilization. This is attributed to the defects created by linker labilization, which increase the pore size while decreasing the material density.

The AcOH concentration also affects the porosity and pore size of hierarchical-pore MOFs. When PCN-160-31% was adopted as the starting material, the pore size of the resulting material was enlarged by increasing the AcOH concentration. The maximum pore size of PCN-160-31%-0.5 is only 2.5 nm, which is smaller than that of PCN-160-31%-1 (9.3 nm) and PCN-160-31%-2 (13.6 nm). However, the fraction of mesopores increases at the expense of a decrease in the total pore volume. The total N_2 uptake of PCN-160-31%-2 (782 cm^3 g^{-1}) decreased by 27% compared to that of PCN-160-31%-0.5 (1066 cm^3 g^{-1}). Meanwhile, a slightly broader PXRD peak and increased PXRD background were observed for PCN-160-31%-2. These results indicate that high AcOH concentration and exchange ratio create a large concentration of defects, which forms large mesopores and partially destroys the framework integrity at the same time. Therefore, the porosity of PCN-160-R%-*C* represents a delicate balance between defect concentration and framework stability. To maintain the framework integrity, the AcOH concentration can reach as high as 2 M while the exchange ratio is no more than 43%. A contour plot was generated to describe the relationship among AcOH concentration, exchange ratio and the maximum pore size (Figure 45). In general, the pore size is positively related to the AcOH concentration and exchange ratio. Therefore, the pore size of PCN-160 can be tuned by judicious control of exchange ratio and AcOH concentration, providing a versatile platform for pore size directed applications.

3.3.3 Defect Analysis

To investigate the origin of mesopores created by linker labilization, a series of experiments were performed in combination with molecular simulations. First, we seek to determine the composition change of PCN-160 before and after linker labilization. The PCN-160-31%, PCN-160-31%-0.5, PCN-160-31%-1, and PCN-160-31%-2 samples were precisely weighted, dissolved in K_2CO_3 solution and analyzed by UV-Vis spectra to determine the weight

percent of AZDC and CBAB in MOF materials. The weight percent of CBAB in PCN-160-31% decreases after acid treatment, indicating that the labile CBAB linkers are partially removed by acid etching. As a control experiment, PCN-160 was treated with AcOH under identical condition, which did not show obvious weight loss. The connection numbers of the Zr clusters in the MOF samples were calculated according to the weight percent of each linker. The Zr_6 clusters in PCN-160 and PCN-160-31% are approximately 12-connected, which are reduced to ~9-connected after acid treatment. The concentrations of CBAB and AZDC in the solution after the linker labilization process were also analyzed by UV-vis spectra. The concentration of CBAB is much higher than that of AZDC indicating the removal of labile CBAB linker under acidic conditions.

SCXRD is a powerful and ubiquitous technique to definitively elucidate structures at the molecular level. Given that PCN-160-R%-*C* could undergo linker exchange and linker labilization with retention of single crystallinity, direct evidence of the structural change can be gathered by SCXRD. Although the exact identity of defect sites is unknown, the missing linkers would most likely be replaced by a pair of –OH/H_2O groups to compensate for the charge loss from the linkers. In a Zr_6 cluster terminated by –OH/H_2O, each terminal –OH/H_2O ligand is separated as far as possible to reduce the steric hindrance and Coulomb repulsion. Hence the O−Zr−O angle is approximately 100°.[24, 29, 111] However, restricted by the O−O distance of carboxylates, the O−Zr−O bond angle in a 12-connected Zr_6 cluster is about 120°. Therefore, the obvious distinction of O from carboxylates and –OH/H_2O ligands by SCXRD allows for the direct "observation" of defects in the resolved single-crystal structure. A comparison of PCN-160-31% and PCN-160-31%-2 single-crystal structure clearly indicates the emergence of defects after AcOH etching. The terminal –OH/H_2O ligands in PCN-160-31% are almost invisible by crystallography. However, after AcOH treatment, the terminal –OH/H_2O ligands can be unambiguously differentiated from

carboxylates. The occupancies of the carboxylate linkers were refined as 75% and the terminal –OH/H_2O was refined with occupancies of 25%, in agreement with the connection number calculated from UV-vis data.

Further evidence consistent with creation of defects is provided by the diffuse reflectance infrared Fourier transform spectroscopy (DRIFTS) measurements. According to the literature, the sharp peak appearing at 3666 cm^{-1} is assigned to the terminal –OH groups and bridging μ_3-OH groups, and the broad band centered at 3446 cm^{-1} corresponds to the H_2O, which either binds to Zr^{4+} as a terminal ligand or interacts with the Zr_6 clusters through hydrogen bonds.[67, 110] In the nearly defect-free PCN-160-31%, a sharp peak appeared at 3666 cm^{-1} and a relatively weak peak was observed at 3446 cm^{-1}, corresponding to the μ_3-OH groups and lattice H_2O, respectively. After acid treatment, the –OH peak at 3666 cm^{-1} becomes broader with a shoulder appearing at 3698 cm^{-1}, which is consistent with terminal -OH groups observed for NU-1000.[110] Meanwhile, the H_2O peak becomes intense and broad, due to the presence of terminal -H_2O on the Zr_6 cluster, which in turn attracts peripheral H_2O molecules through hydrogen bonding. TGA data further confirms the creation of defects by replacing linkers with terminal –OH/H_2O. For PCN-160-31%, no obvious weight loss was observed before 300 °C, indicating a nearly defect-free structure. The acid etched samples showed a weight loss of 8% before 300 °C, which is attributed to the removal of the coordinated H_2O on the cluster and the hydrogen bonded water species in the cavity. In addition, the weight loss corresponding to the thermal decomposition of organics became smaller after acid treatment, suggesting that organic linkers were partially removed.

3.3.4 Proposed Formation Mechanism of Hierarchical Pores

With the material composition in hand, we further turned our efforts to investigate the origin of the hierarchical pores by molecular simulation. Intuitively, the CBAB and AZDC linkers

are expected to be randomly distributed in PCN-160 considering the similar length and connection of two linkers. The acid treatment partially removes CBAB, leaving random missing-linker defects. A missing-linker model was built based on this assumption, in which a stoichiometric 3 × 3 × 3 supercell of the **fcu** PCN-160 was taken and randomly selected linkers were removed. Pore size distribution was estimated by Zeo++ with N_2 as a probe (radius 1.82 Å). The maximum pore size of PCN-160 was simulated to be 1.5 nm, which matched well with the pore diameter from N_2 sorption isotherms (1.5 nm). According to the composition determined by UV-vis and ^{1}H-NMR techniques, about 25% of linkers in the PCN-160-31%-0.5 were removed by acid etching. However, the mesopores were not observed in the simulated pore size distribution even though 25% of linkers were removed from the model. These results contradicted the missing-linker model and suggested the possible existence of missing-cluster defects in PCN-160-R%-*C*. In fact, the missing-cluster defects have been observed and thoroughly studied in UiO-66.[99] The missing of Zr_6 clusters along with the linkers around them locally created an eight-connected net with ReO_3 (**reo**) topology. The model with **reo** defects was built by removing a suitable number of randomly selected Zr_6 clusters and linkers. The simulated maximum pore size (2.7 nm) corresponds to the experimentally observed 2.5 nm mesopore. Further evidence is provided by the ICP-MS data of the supernatant after acid treatment, which indicates the existence of Zr^{4+} as a result of cluster removal. Therefore, the 2.5 nm mesopore can be explained by the **reo** defect, in which a Zr_6 cluster is removed along with linkers around it.

Furthermore, multiple adsorption/desorption steps were observed for the PCN-160-31%-1, indicating that different kinds of textural mesopores coexist in the hierarchical-pore MOFs. While the 2.5 nm mesopore can be explained by the **reo** defects, the second mesopore (> 5 nm) is difficult to explain on the molecular level. Scanning electron microscope (SEM) and transmission

electron microscope (TEM) were adopted to reveal the morphology of the hierarchical-pore materials, in order to uncover the formation mechanism of the large mesopores. As expected, the PCN-160-31% crystals before acid treatment show a very smooth surface in the SEM images. SEM and TEM images of PCN-160-31%-0.5 show the appearance of mesopores as indicated by riddled edges. Different from PCN-160-31% and PCN-160-31%-0.5, PCN-160-31%-1 shows a sponge-like morphology, corresponding to the 5.4 nm mesopores from N_2 sorption isotherms. In the case of PCN-160-31%-2, a pomegranate-type structure is observed, in which the microcrystalline MOF forms nanodomains. On the basis of the above results and literature precedents,[99, 112-114] a possible mechanism for the formation of large mesopores (> 5 nm) is proposed. The linker labilization initially induces missing-linker defects by partially removal of labile CBAB linkers, which reduced the connection number of Zr_6 clusters. As a result, some Zr_6 clusters and the linkers around are removed to form missing-cluster defects (**reo** defects), corresponding to 2.5 nm mesopores (Figure 46a,b). As the defect sites are relatively labile compared to defect-free structures, further acid etching gradually dissolves the materials from the defect sites as weak points, which enlarges the mesopores while maintaining the crystallinity (Figure 46c). This explains the observation that the small mesopore volume decreases as the large mesopore emerges. A sponge-like structure is therefore obtained by enlarging the 2.5 nm mesopores. As etching of the crystalline framework proceeds, the framework becomes fragmented, resulting in the pomegranate-type of morphology. In other words, the linker labilization process partially dissolves the MOF crystals from the inside out, creating large mesopores inside the particle while leaving the particle size visually intact.

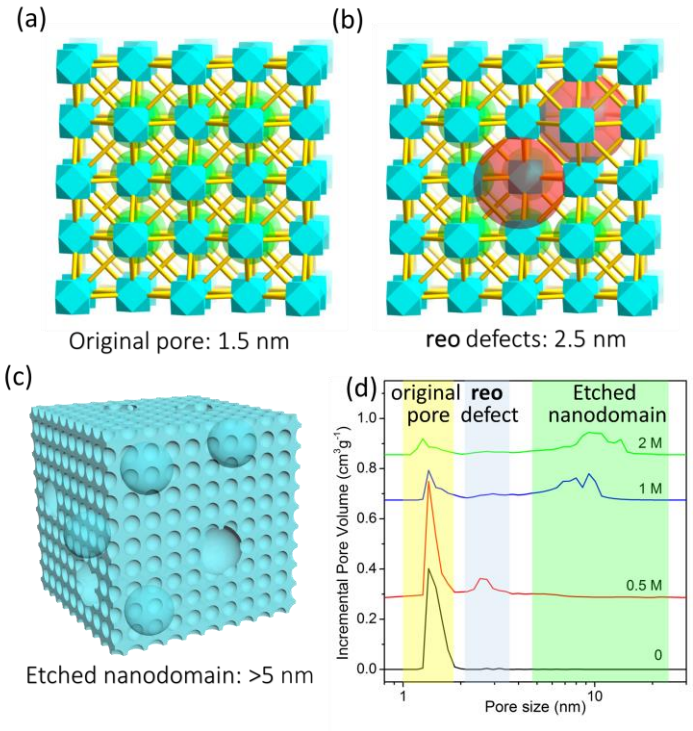

Figure 46. Schematic illustration of formation mechanism. Formation mechanism of the micropores (a), small mesopores (b), and large mesopores (c); (d) pores size distribution of PCN-160-34% treated with different amounts of acid, highlighting the origin of different pores.

Based on this mechanism, the effects of exchange ratios and acid concentrations on the pore architecture of PCN-160 can be rationalized. The exchange ratio controls the concentration of the "weak points" in MOF crystals where the crystal dissolution initiates. Meanwhile, the acid concentration affects the rate of dissolving on each weak point. With high exchange ratio and low acid concentration, the concentration of "weak points" is high whereas the dissolving rate is slow so that the formation of **reo** defects are favored. This corresponds to the observation that the mesopores with diameter of 2.5 nm were observed at low acid concentration. On the other hand, the large mesopores (> 5 nm) are usually created by the extension of small mesopores (2.5 nm) at high acid concentration. It should be noted that defects can be introduced and controlled by varying the modulating acid during the MOF synthesis.[99] However, the defect concentration and the

mesopore volume introduced in a one-pot reaction are still limited, because the relatively low stability of highly defective structures which cannot survive the harsh solvothermal reaction conditions. In contrast, linker labilization is carried out at low temperature under mild conditions, which maintained the porosity and crystallinity of MOFs to the maximum extent. Therefore, the pore sizes and pore size distributions of PCN-160 can be precisely controlled by adjusting the exchange ratios and acid concentrations, providing a versatile platform for a variety of potential applications, especially when specific pore architectures are needed.

3.3.5 Enhancing Guest Adsorption and Catalytic Performance

To check the accessibility of the created pore spaces by linker labilization, a guest uptake study was performed. PCN-160-17% (1.5 nm), PCN-160-17%-0.5 (2.5 nm), PCN-160-17%-1 (5.8 nm) with distinct maximum pore size were selected as representative examples of the hierarchical-pore MOFs. A series of guest molecules with different sizes, including $[Cr_2O_7]^{2-}$ (0.3 × 0.5 nm), $[Ni_4(H_2O)_2(PW_9O_{34})_2]^{10-}$ (polyoxometalate or POM, 1.1 × 1.4 nm), and $Cu_{24}(BDC\text{-}OH)_{24}(H_2O)_{24}$ (metal–organic polyhedron or MOP, 3.1 nm), were selected as the probe molecules. The molecular dimension of $[Cr_2O_7]^{2-}$ is much smaller than the window size of PCN-160-17%. However, the $[Cr_2O_7]^{2-}$ uptake is not only dependent on the pore volume, but also strongly affected by the defect concentration because the missing-linker sites in Zr-MOFs are reported to bind strongly with anions, such as arsenate, selenate and dichromate.[34, 115-116] The PCN-160-17%-0.5 and PCN-160-17%-1 with much higher concentration of missing-linker defects show higher dichromate uptake compared to that of PCN-160-17%, demonstrating the effect of defects. Although the micropore size (1.5 nm) in PCN-160-17% is large enough for POMs, the diffusion of POMs in the MOF cavity is limited by the small window size (0.9 nm), which is smaller than the molecular dimensions of the POM (1.1 × 1.4 nm). In contrast, the hierarchical pore architecture of PCN-160-

17%-0.5 and PCN-160-17%-1 allows quick diffusion of large molecules through mesopores which finally reach the storage sites within micropores. Therefore, the POM uptake and rate of adsorption are enhanced by linker labilization. To recognize different mesopore sizes of PCN-160-17%-0.5 and PCN-160-17%-1, the adsorption of the MOP was tested. It was found that the PCN-160-17%-1 with 9.3 nm mesopores have a much higher MOP uptake than PCN-160-17%-0.5 and PCN-160-17%, indicating the contribution of large mesopores.

The hierarchical porous architectures created by linker labilization allow for efficient diffusion and adsorption of large molecules, making them promising materials for a wide range of applications, including adsorption, separation, and catalysis. To investigate the effect of linker labilization on the catalytic performance of MOFs, we chose CYCU-3 as a platform.[117] CYCU-3 is a robust MOF constructed from 1D Al−O chains connected by linear AZDC linkers. It features a hierarchical micro-mesopore architecture with hexagonal channels (3.0 nm in diameter) and triangular channels (1.5 nm in diameter). The large hexagonal channels are suitable for enzyme encapsulation and the triangular channels allow for efficient substrate diffusion.[118-120] However, the walls of the channels in CYCU-3 are too condensed to allow any substrate diffusion between neighboring channels. Therefore, the accessibility of the immobilized enzymes are largely suppressed.[121-122] We propose that linker labilization can creates defects on the walls of the channels in CYCU-3, which act as widows that connects the channels throughout the crystal to facilities the diffusion of reactants and products.

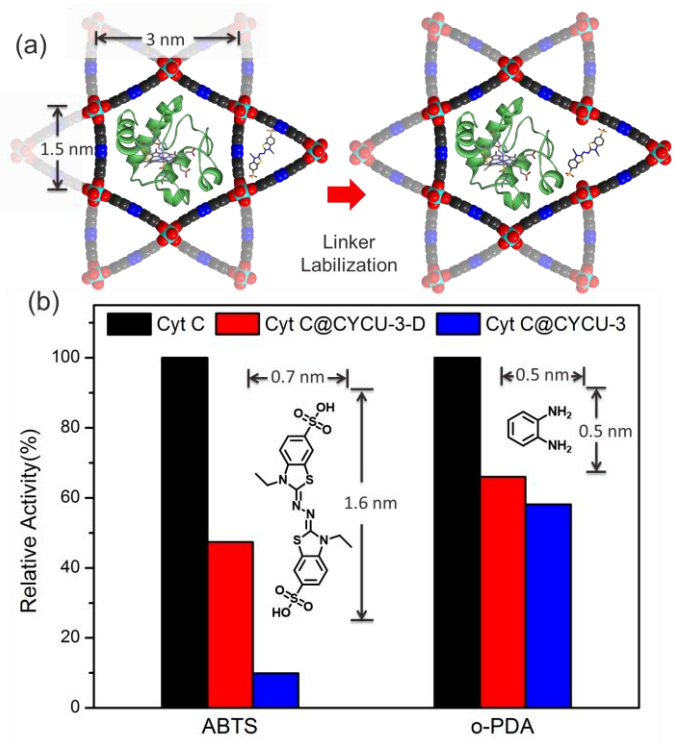

Figure 47. Enhancing activity of immobilized enzyme. (a) Illustration of the accessibility of enzymes in CYCU-3 and CYCU-3D; (b) Relative activity of Cyt c, Cyt c@CYCU-3 and Cyt c@CYCU-3D for the oxidation of ABTS and o-PDA.

Linker labilization was carried out on CYCU-3 by replacing 22% of the AZDC linkers with labile CBAB linkers and subsequently removing the labile linkers by treating with 0.2 mM HCl in DMF to create a defected MOF (CYCU-3D). N_2 sorption isotherms of CYCU-3D indicate the growth of mesopores with a diameter of ~7 nm along with the decrease of small mesopore volume (3 nm in diameter). This is consistent with the observation in PCN-160 system that the large mesopores were created by the extension of small mesopores through acid etching. Cytochrome c (Cyt c) with a molecular dimension of 2.6 × 3.2 × 3.3 nm were immobilized in CYCU-3 and CYCU-3D by treating the activated MOF crystals with aqueous solution of Cyt c (300 μM) at 25 °C. The uptake of Cyt c was determined by UV-vis spectroscopy, which shows a

maximum loading of 23.3 mmol·g^{-1} for CYCU-3 and 14.5 mmol·g^{-1} for CYCU-3D after 48 h. Pore size distributions CYCU-3 and CYCU-3D after enzyme loading suggests that the enzyme occupies the hexagonal channels, leaving the triangular channels poised for substrates.

Before catalytic reaction, the solid samples were immersed in water for two days during which the solvent was decanted and freshly replenished five times to ensure full removal of any loosely bound Cyt c. UV-vis spectroscopy reveal that no detectable enzyme leaching in water within two days after washing. To evaluate the accessibility of Cyt c after immobilization in different MOFs, the oxidation of o-phenylenediamine (o-PDA) and 2,2'-azino-bis(3-ethylbenzothiazoline-6-sulphonic acid) (ABTS) catalyzed by Cyt c were performed. The molecular size of o-PDA (0.5 × 0.5 nm) is relatively small so that it could diffuse in the hexagonal channels to reach the active sites of encapsulated enzymes. Therefore, the Cyt c immobilized in CYCU-3 and CYCU-3D both show similar k_{cat}, K_m, and V_{max} values to the free enzyme, indicating a comparable catalytic performance. However, the catalytic activity of Cyt c immobilized in CYCU-3 dramatically decreased for bulky substrates. As shown in Figure 47, the relative activity for ABTS oxidation is reduced by 90% when Cyt c was encapsulated in CYCU-3, which may be caused by the diffusion control. Considering the sizes of ABTS (0.7 × 1.6 nm) and Cyt c, the hexagonal channels are expected to be blocked by the encapsulated Cyt c, leaving no space for the diffusion of ABTS. The ABTS cannot access the enzyme from the triangular channels as the walls of the channels are too condensed. Therefore, the diffusion of ABTS in CYCU-3 are largely restricted, which in turn results in the low activity of the encapsulated Cyt c. However, the activity of Cyt c in CYCU-3 increased almost 5 times after linker labilization. The Cyt c immobilized in CYCU-3D shows dramatically enhanced k_{cat} and V_{max} compared with the ones in CYCU-3, highlighting the beneficial effect of hierarchical porous structure on the catalytic performance. The

defects created by linker labilization not only creates large mesopores (7 nm in diameter) but also forms windows on the wall of the channels, allowing for efficient substrate diffusion between neighboring channels. Therefore, the substrates can reach the active center of Cyt C through the triangular channels even though the hexagonal channels are not accessible. This result corroborates well with the findings by Hupp, Farha and coworkers in which they demonstrated the critical role of the hierarchical structure of NU-1000 for enzyme encapsulation applications.[121] The hierarchical pore architecture created by linker labilization represents an integration of micropores, mesopores and windows that connect them throughout the crystal, which allows binding of the enzyme and diffusion of substrates.

3.4 Conclusions

In conclusion, a linker labilization method was developed to increase the porosity and pore size of microporous MOFs by creating crystal defects controllably. MOFs were constructed with various amount of pro-labile linkers, which were partially removed by acid etching to create mesopores with tunable sizes. The maximum pore size by N_2 sorption measurements is tuned from 1.5 nm to 18 nm by judicious control of pro-labile-linker content and acid concentration. Experiments in combination with molecular simulations revealed the formation mechanism of the mesopores. The beneficial effect of hierarchical porous structure on the adsorption properties and catalytic performances was demonstrated. We believe linker labilization may provide a feasible and versatile method to enlarge MOF pore size, which promises potential applications in guest adsorption/separations, heterogeneous catalysis, drug delivery, and sensing.

4. MIXED-LINKER MOFS CONSTRUCTED BY LINKER INSTALLATION*

4.1 Introduction

As an inorganic and organic hybrid material, MOF is epitomized by its tunable structure and function through judicious selection of metal nodes, organic linkers, and the combination of the two.[123-125] Placing two or more functionalities having synergistic effect of various kinds within one framework is particularly interesting for its potential applications in many aspects.[6] A ubiquitous approach to introduce multifunctionalities into MOFs is one-pot synthesis with mixed linkers.[80, 126-127] One of the representative works is MTV-MOFs (multivariate MOFs), conducted by Yaghi and coworkers, in which up to eight linear linkers having the same length but distinct functionalities were introduced into one framework.[42] It suggests that linkers of similar length and connectivity tend to be incorporated into one mixed-linker framework, rather than a mechanical mixture of single-linker MOFs. The apportionment of functionalities is crucial for the functions of MTV-MOFs. For example, these properly juxtaposed functional groups can potentially mimic the delicate enzyme system.[44] Further efforts were made to elucidate the spatial appointment of functional groups by solid state NMR and molecular simulation. However, it is still a challenge to locate the exact position of each component due to the disordered distribution of functional groups.[45]

---

*Reproduced in part with permission from: Yuan, S.; Chen, Y.-P.; Qin, J.-S.; Lu, W.; Zou, L.; Zhang, Q.; Wang, X.; Sun, X.; Zhou, H.-C. "Linker installation: engineering pore environment with precisely placed functionalities in zirconium MOFs", *J. Am. Chem. Soc.* **2016**, *138*, 8912-8919. Copyright 2016 American Chemical Society; Yuan, S.; Zou, L.; Li, H.; Chen, Y.-P.; Qin, J.; Zhang, Q.; Lu, W.; Hall, M. B.; Zhou, H.-C. "Flexible zirconium metal-organic frameworks as bioinspired switchable catalysts", *Angew. Chem. Int. Ed.*,**2016**, 55, 10776-10780. Copyright 2016 by Wiley-VCH Verlag GmbH & Co. KGaA, Yuan, S.; Lu, W.; Chen, Y.-P.; Zhang, Q.; Liu, T.-F.; Feng, D.; Wang, X.; Qin, J.; Zhou, H.-C. "Sequential linker installation: precise placement of functional groups in multivariate metal–organic frameworks". *J. Am. Chem. Soc.* **2015**, *137*, 3177-3180. Copyright 2015 American Chemical Society.

One way to control the arrangement of functionalities is to use linkers with different symmetry and/or connectivity.[128-132] If topology compatibility is satisfied, ordered arrangement of different linkers becomes feasible. In this case, functional groups can be addressed by single crystal X-ray crystallography. Recently, this goal has been exemplified by copolymerizing multiple topologically distinct linkers to produce isoreticular sets of MOFs with systematically modulated pore architectures.[96] However, some potential limitations remain with this strategy. First, it is extremely difficult to introduce more than two linkers simultaneously into one framework, as the linkers of distinct size and connectivity tend to form different domains instead of one uniform phase.[133] In addition, it requires extra efforts to maintain the integrity of certain sensitive functional groups under the harsh solvothermal conditions (i.e. functional group protection and deprotection).[134] Moreover, this approach so far is only sufficiently attested for soft Lewis acidic metal species (M^{2+}).[42, 129-132, 135-136] The resulting structures usually exhibit relatively weak chemical stability, which limits their applications.

In one-pot synthesis, the competition between kinetically-favored and thermodynamically-favored products makes it exceedingly challenging to achieve mixed-linker MOF products. This promotes us to develop stepwise synthetic routes to sequentially introduce functionalities in robust Zr-MOFs and therefore control their positions and distributions. We developed a new method, linker installation, to precisely place different functionalities into Zr-MOFs under mild conditions.[29] In this method, a Zr-MOF constructed from 8-connected $Zr_6O_4(OH)_8(H_2O)_4$ clusters was selected as a matrix. Linear carboxylate linkers with various functionalities were post-synthetically installed into the matrix by replacing the terminal OH^-/H_2O ligands of adjacent $Zr_6O_4(OH)_8(H_2O)_4$ clusters.[103, 110] Since linkers with different lengths were installed in pre-designed positions in the MOF structure, multiple functional groups were therefore precisely

placed at defined location in the MOF cavity. This methodology provides a powerful tool to construct multivariate MOFs with precisely positioned functionalities in desired proximity, which would otherwise be difficult to achieve.[22, 24, 29]

4.2 Experimental Section

4.2.1 Materials and Instrumentation

L2 to L12, H_2TPDC (2',5'-dimethylterphenyl-4,4''-dicarboxylic acid), H_2BDDC (4,4'-(1,3-butadiyne-1,4-diyl)bis(3-methylbenzoic acid)) and H_2BPYDC (BPYDC = 2,2'-bipyridne-5,5'-dicarboxylic acid) were prepared according to the literature (Scheme 2).[29, 137-144] All other reagents and solvents were commercially available and used as received. Powder X-ray diffraction (PXRD) measurements were carried out on a BRUKER D8-Focus Bragg-Brentano X-ray Powder Diffractometer equipped with a Cu sealed tube (λ = 1.54178 Å) at 40 kV and 40 mA. Nuclear magnetic resonance (NMR) data were collected on a Mercury 300 spectrometer. Gas sorption measurements were conducted on a Micrometritics ASAP 2020 system. ICP-MS data were analyzed with a Perkin Elmer NexION® 300D ICP-MS system.

Scheme 2. Linkers with different substituents used in this work.

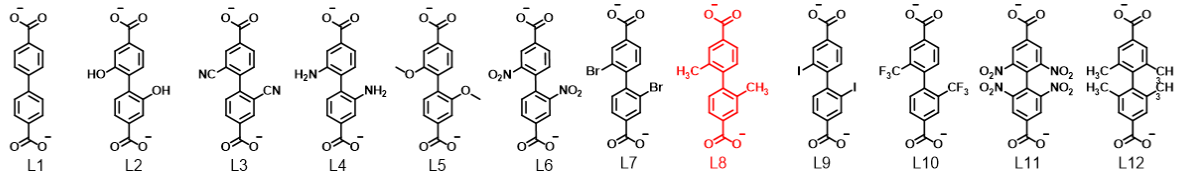

4.2.2 Linker Syntheses

Synthesis of H_2Me_2-BPDC (L8). Methyl 4-iodo-3-methylbenzoate (5.0 g, 18.1 mmol) and copper powder (20.0 g, 314.7 mol) were well mixed under argon atmosphere. The resulting mixture was heated up to 250 °C overnight. After cooled down, the reaction mixture was extracted

with chloroform (30 mL × 3). The combined extracts were evaporated to dryness. Flash chromatography with ethyl acetate/hexanes (5%–10%) as eluent afforded dimethyl 2,2'-dimethylbiphenyl-4,4'-dicarboxylate (1.2 g, 3.8 mmol, 42.5%). ^{1}H NMR ($CDCl_3$, 300 MHz) δ: 7.97 (d, 2H), 7.91 (dd, 2H), 7.16 (d, 2H), 3.94 (s, 6H), 2.08 (s, 6H) ppm. Dimethyl 2,2'-dimethylbiphenyl-4,4'-dicarboxylate (1.0, 3.3 mmol) was suspended in a mixture of THF/MeOH (50 mL, v/v = 1/1, THF = tetrahydrofuran, MeOH = methanol), to which an aqueous solution of 2 N KOH (20 mL) was added. The resulting mixture was stirred and refluxed overnight. After cooled to room temperature, organic solvents were evaporated, and the remaining aqueous solution was acidified with 1M HCl to give a precipitate, which was collected by filtration, washed with water, and dried in the oven to produce 0.7 g of 2,2'-dimethylbiphenyl-4,4'-dicarboxylic acid (H_2Me_2-BPDC) with a yield of 77.3%. ^{1}H NMR (DMSO-d_6, 300 MHz) δ: 12.96 (brs, 2H), 7.91 (d, 2H), 7.83 (dd, 2H), 7.21 (d, 2H), 2.04 (s, 6H) ppm. These values are in good agreement with the literature (Scheme 3).[145]

Scheme 3. Synthesis of H_2Me_2-BPDC.

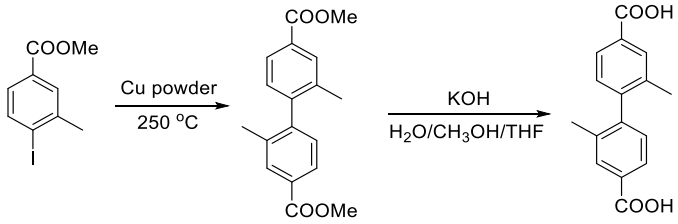

Synthesis of $H_2(CF_3)_2$-BPDC (L10). 4-iodo-3-(trifluoromethyl)benzonitrile (5.0 g, 16.8 mmol) and copper powder (20.0 g, 314.7 mol) were well mixed under argon atmosphere. The resulting mixture was heated up to 250 °C overnight. After cooled down, the reaction mixture was extracted with chloroform (30 mL × 3). The combined extracts were evaporated to dryness. Flash chromatography with ethyl acetate/hexanes (5%–10%) as eluent afforded 2,2'-

bis(trifluoromethyl)-[1,1'-biphenyl]-4,4'-dicarbonitrile (1.8 g, 5.3 mmol, 63.1%). 2,2'-bis(trifluoromethyl)-[1,1'-biphenyl]-4,4'-dicarbonitrile (1.8 g, 5.3 mmol) was suspended in a mixture of THF/MeOH (50 mL, v/v = 1/1), to which an aqueous solution of 2 N KOH (20 mL) was added. The resulting mixture was stirred and refluxed overnight. After cooled to room temperature, organic solvents were evaporated, and the remaining aqueous solution was acidified with 1N HCl to give a precipitate, which was collected by filtration, washed with water, and dried in the oven to produce 1.3 g of $H_2(CF_3)_2$-BPDC with a yield of 64.9%. ^{1}H NMR (DMSO-d_6, 300 MHz) δ: 13.65 (brs, 2H), 8.29 (d, 2H), 8.25 (dd, 2H), 7.58 (d, 2H) ppm (Scheme 4).

Scheme 4. Synthesis of $H_2(CF_3)_2$-BPDC.

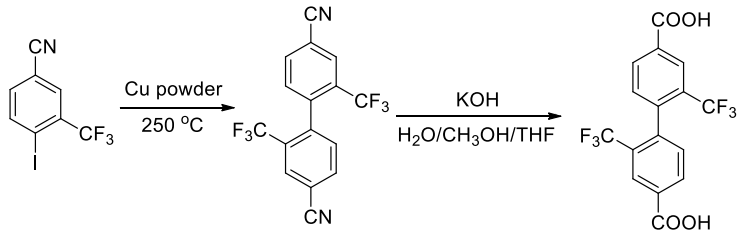

Synthesis of H_2Me_4-BPDC (L12). Ferric chloride (145.8, 0.9 mol) was added to 250 ml mesitylene (216 g, 1.8 mol) in a 500 mL flask under nitrogen protection. The hydrogen chloride was generated rapidly. After 4 h, the reaction mixture was poured into ice. The organic phase was separated by filtration, washed with water, and dried over anhydrous sodium sulfate. The crude bimesityl was collected at 75–140 °C by fractional distillation. After the distillate was cooled down, the crystals which precipitated were collected by filtration. Then the crystals were recrystallized with acetone to afford colorless crystals (44 g, 0.183 mol) with a yield of 20.3%. Cobaltous acetate (15 g, 60.2 mmol) was added into 200 ml of acetic acid in a 500 ml three-necked round-bottom flask equipped with a thermometer, condenser, dropping funnel, and magnetic stirrer. 16 ml of 39 % peracetic acid were added slowly to the flask by the dropping funnel. The

color of the reactants changed from red (Co^{2+}) to green (Co^{3+}) in an exothermic reaction. Then bimesityl (10 g, 41.6 mmol) were added by dropping funnel. After this, the dropping funnel was replaced with a gas dispersion tube. Oxygen was introduced at 145 ml/min at room temperature. The reaction mixture was maintained at 100 ^{o}C for 5 hours. Then the mixture was cooled to ambient temperature. The mixture was poured into 1 L water, the precipitate was collected, washed with more water, and then dissolved in 200 ml of ether. The ether solution was extracted with a 5% aqueous solution of sodium hydrogen carbonate, and the aqueous solution was acidified with hydrochloric acid. The precipitate was crude product. The crude product was re-dissolved in 100 ml ether. The extraction of the ether solution with sodium hydrogen carbonate and the acidification was repeated to afford pure H_2Me_4-BPDC (4.3 g, 14.4 mmol) with a yield of 34.7%. ^{1}H NMR (DMSO-d_6, 300 MHz) δ: 12.85 (brs, 2H), 7.75 (s, 4H), 1.86 (s, 12H) ppm. These values are in good agreement with the literature (Scheme 5).[143]

Scheme 5. Synthesis of H_2Me_4-BPDC.

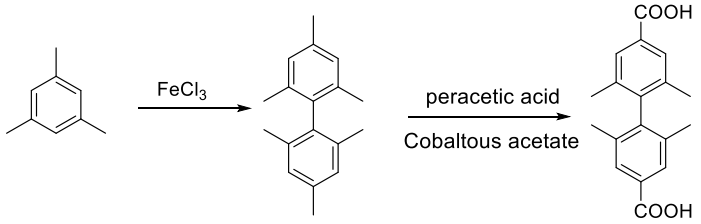

Synthesis of H_2Me-BPDC. Ethylene glycol dimethyl ether (DME, 200 mL) was bubbled with nitrogen for about one hour before introduced into nitrogen-protected solid mixture of methyl 4-iodo-3-methylbenzoate (5.0 g, 18.1 mmol), 4-methoxyl carbonylphenylboronic acid (3.9 g, 21.7 mmol)**,** potassium carbonate (7.5 g, 54.25 mmol) and tetrakis (triphenylphosphine) palladium (0.3 g, 0.26 mmol). The mixture was allowed to reflux for 3 days under nitrogen protection. After cooling to room temperature, the solvent was evaporated to dryness. The residue was washed with

a large amount of water followed by acetone. After removing the solvent, the residue was purified with column chromatography (silica gel, CH_2Cl_2) to give the ester as a white solid (3.6 g). Dimethyl 2-dimethylbiphenyl-4,4'-dicarboxylate (3.0, 10.6 mmol) was suspended in a mixture of THF/MeOH (50 mL, v/v = 1/1,) and 30 mL aqueous solution of 2 N KOH. The resultant mixture was stirred and refluxed overnight. After cooled to room temperature, organic solvents were removed, and the remaining solution was acidified with 1 M HCl to give a precipitate, which was collected and washed with water. Dried in the oven to produce 2.2 g of H_2Me-BPDC with a yield of 81.1%. ^{1}H NMR (DMSO-d_6, 75 MHz) δ: 13.04 (brs, 2H), 8.02 (d, 2H), 7.90 (s, 1H), 7.83 (dd, 1H), 7.50 (d, 2H), 7.35 (d, 1H), 2.28 (s, 3H) ppm. These values are in good agreement with the literature (Scheme 6).[145]

Scheme 6. Synthesis of H_2Me-BPDC.

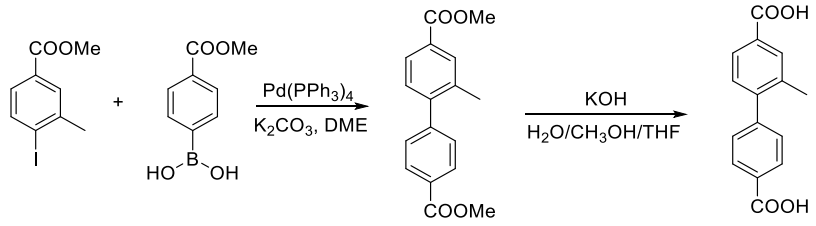

4.2.3 MOF Syntheses

Synthesis of PCN-700-$(NO_2)_2$. $ZrCl_4$ (200 mg), L6 (100 mg), trifluoroacetic acid (1 mL) and DMF (20 mL) were charged in a Pyrex vial. The mixture was heated in 100 ºC oven for 7 days. After cooling down to room temperature, the colorless crystals of PCN-700-$(NO_2)_2$ were harvested (yield: 65%).

Synthesis of PCN-700-Me_2. $ZrCl_4$ (200 mg), L8 (100 mg), trifluoroacetic acid (1.0 mL) and DMF (20 mL) were charged in a Pyrex vial. The mixture was heated in 120 ºC oven for 3

days. After cooling down to room temperature, the colorless crystals of PCN-700-Me_2 were harvested (yield: 68%).

Synthesis of PCN-700-$(CF_3)_2$. $ZrCl_4$ (200 mg), L10 (100 mg), trifluoroacetic acid (1.0 mL) and DMF (20 mL) were charged in a Pyrex vial. The mixture was heated in 120 ºC oven for 3 days. After cooling down to room temperature, the colorless crystals of PCN-700-$(CF_3)_2$ were harvested (yield: 58%).

Synthesis of PCN-700-$(NO_2)_4$. $ZrCl_4$ (200 mg), L11 (100 mg), trifluoroacetic acid (1 mL) and DMF (20 mL) were charged in a Pyrex vial. The mixture was heated in 100 ºC oven for 3 days. After cooling down to room temperature, the colorless crystals of PCN-700-$(NO_2)_4$ were harvested (yield: 60%).

Synthesis of PCN-700-Me_4. $ZrCl_4$ (200 mg), L12 (100 mg), trifluoroacetic acid (1.0 mL) and DMF (20 mL) were charged in a Pyrex vial. The mixture was heated in 120 ºC oven for 3 days. After cooling down to room temperature, the colorless crystals of PCN-700-Me_4 were harvested (yield: 71%).

Syntheses of Compounds 1-6. Compounds **1-6** were synthesized by the linker installation of PCN-700-Me_2 with H_2FA (fumaric acid), H_2BDC (terephthalic acid), H_2NDC (2,6-naphthalene-dicarboxylic acid), H_2BPDC (4,4'-biphenyldicarboxylate), H_2TPDC and H_2BDDC respectively through an acid and base reaction. Generally, crystals of PCN-700-Me_2 (100 mg) were treated with the solution of linear linkers in DMF (0.03 M, 40 mL) at 75 ºC for 24 h. The crystals were collected by filtration and washed with fresh DMF 3 times (yield: 96%).

Syntheses of Compounds 7-11. Compounds **7-11** were synthesized by sequential treatment of PCN-700-Me_2 crystals with different linear linkers. In a typical synthetic condition, PCN-700-Me_2 crystals were treated with the solution of a certain linear linker in DMF (0.03 M,

40 mL) at 75 ºC for 24 h. The crystals were collected by filtration and further treated with the solution of a secondary linker DMF (0.03 M, 40 mL) at 75 ºC for 24 h. The resulting crystals were collected by filtration and washed with fresh DMF three times (yield: 93%).

Syntheses of PCN-700-BPYDC(Cu). Crystals of PCN-700-Me_2 (100 mg) were treated with the solution of BPYDC in DMF (0.03 M, 40 mL) at 75 ºC for 24 h. The crystals of PCN-700-BPYDC were collected by filtration and washed with fresh DMF and acetonitrile. Crystals of PCN-700-BPYDC (100 mg), CuI (100 mg) and acetonitrile (40 mL) were charged in a Pyrex vial. The mixture was heated in 75 ºC oven for 24 h. The red-brown crystals of PCN-700-BPYDC(Cu) were harvested by filtration (yield: 91%).

Syntheses of PCN-700-BPYDC(Cu)-TPDC-R_2. Crystals of PCN-700-Me_2 (100 mg) were sequentially treated with the solution of BPYDC and TPDC-R_2 in DMF (0.03 M, 40 mL) at 75 ºC for 24 h. The crystals of PCN-700-BPYDC-TPDC-R_2 were collected by filtration and washed with fresh DMF and acetonitrile. Crystals of PCN-700-BPYDC-TPDC-R_2 (100 mg), CuI (100 mg) and acetonitrile (40 mL) were charged in a Pyrex vial. The mixture was heated in 75 ºC oven for 24 h. The red-brown crystals of PCN-700-BPYDC(Cu)-TPDC-R_2 were harvested by filtration and washed thoroughly by DMF and acetonitrile (yield: 90%).

4.2.4 ^{1}H-NMR Digestion Experiments

The composition of linkers in these MOFs were characterized by ^{1}H-NMR digestion experiments. The activated samples (around 5 mg) were digested by 10 M HCl aqueous solution and dried in 100 ºC oven. The solid was dissolved in about 0.5 mL DMSO-d_6 for ^{1}H NMR spectroscopy. The PXRD and ^{1}H-NMR spectra are presented below (Figures 48-59).

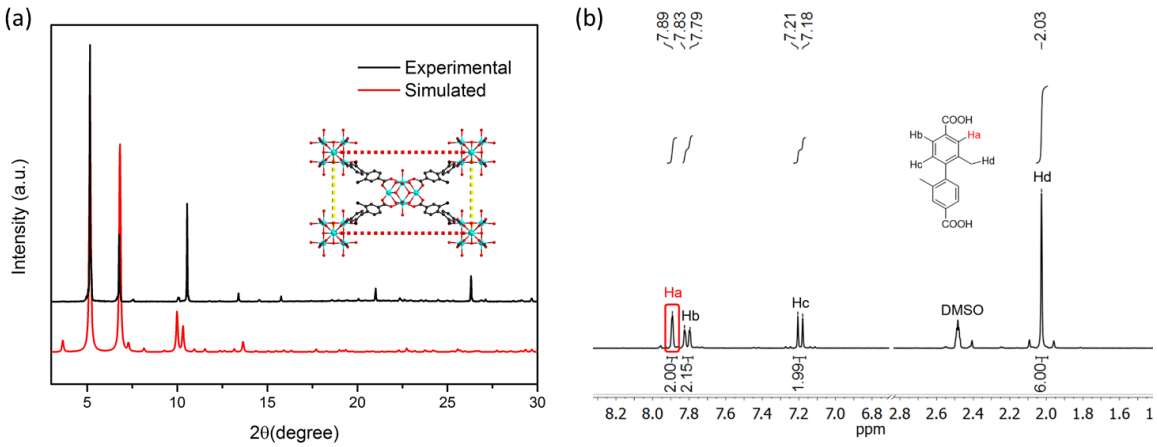

Figure 48. (a) PXRD patterns and (b) ^{1}H-NMR spectrum of PCN-700.

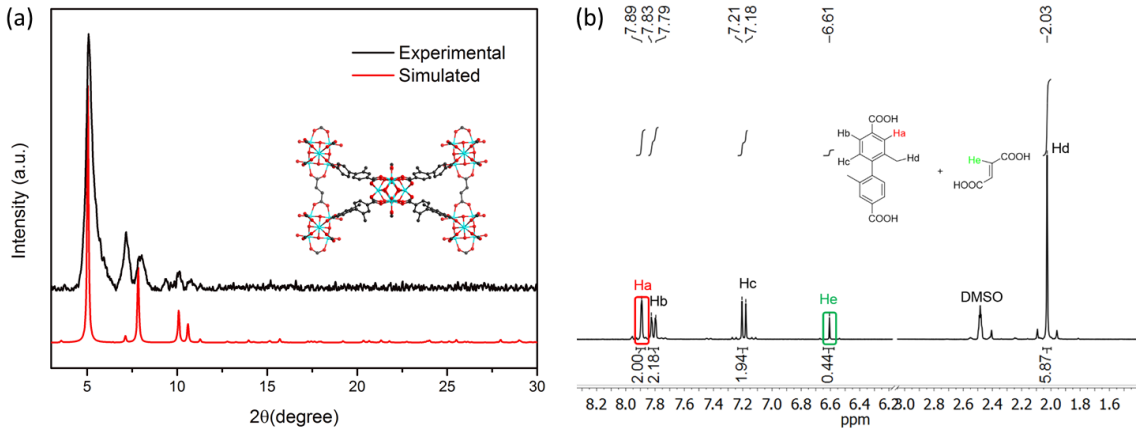

Figure 49. (a) PXRD patterns and (b) ^{1}H-NMR spectrum of compound 1.

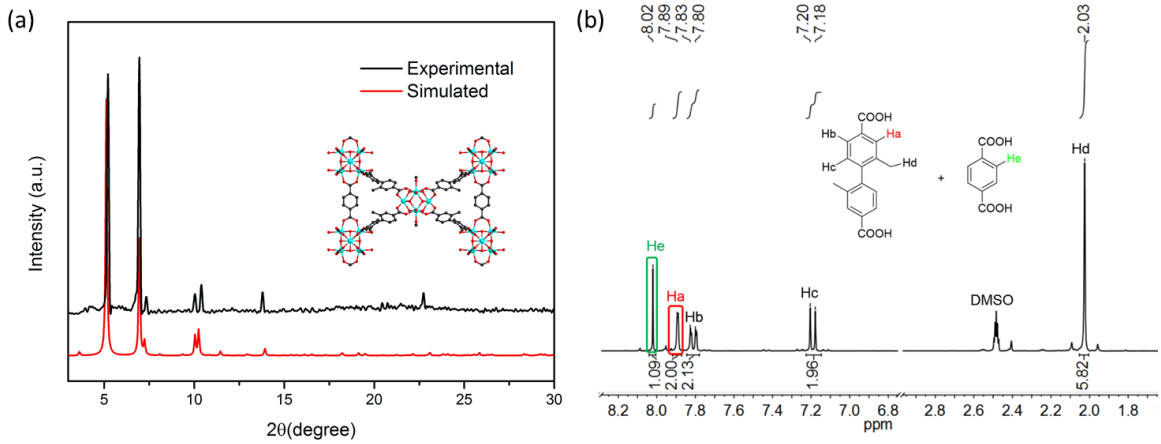

Figure 50. (a) PXRD patterns and (b) ^{1}H-NMR spectrum of compound 2.

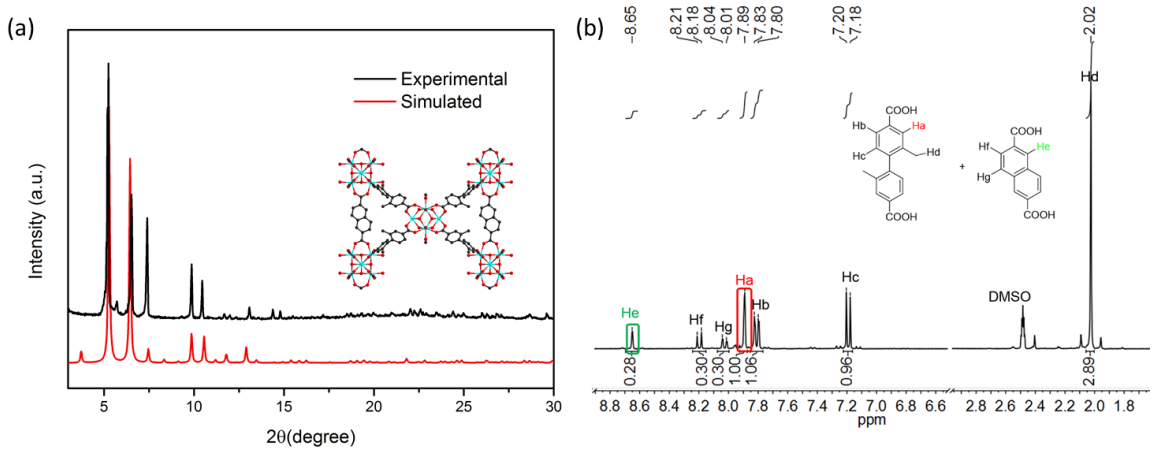

Figure 51. (a) PXRD patterns and (b) ^{1}H-NMR spectrum of compound 3.

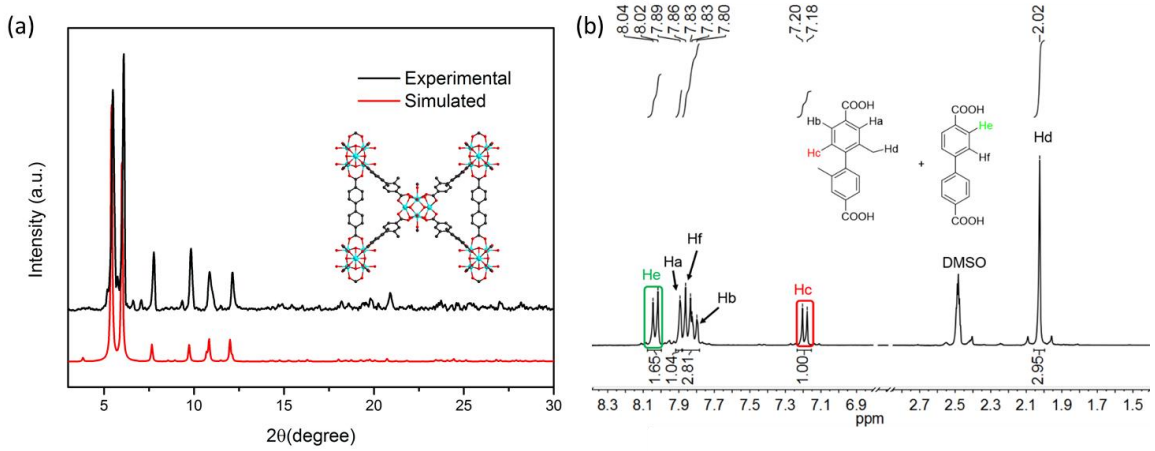

Figure 52. (a) PXRD patterns and (b) ^{1}H-NMR spectrum of compound 4.

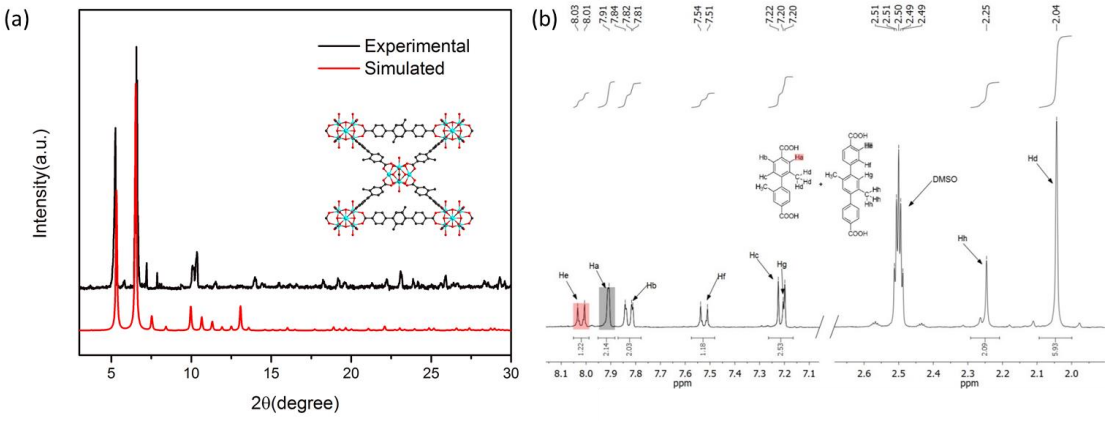

Figure 53. (a) PXRD patterns and (b) ^{1}H-NMR spectrum of compound 5.

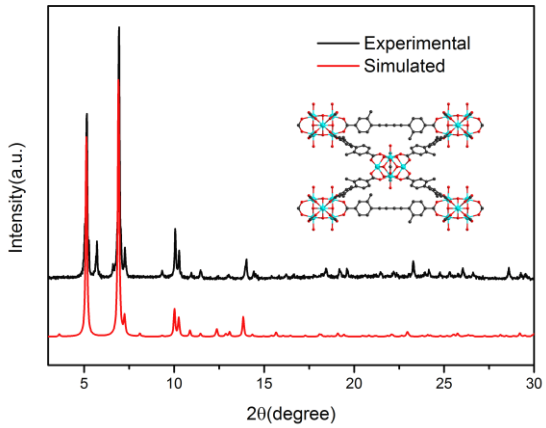

Figure 54. (a) PXRD patterns of compound 6.

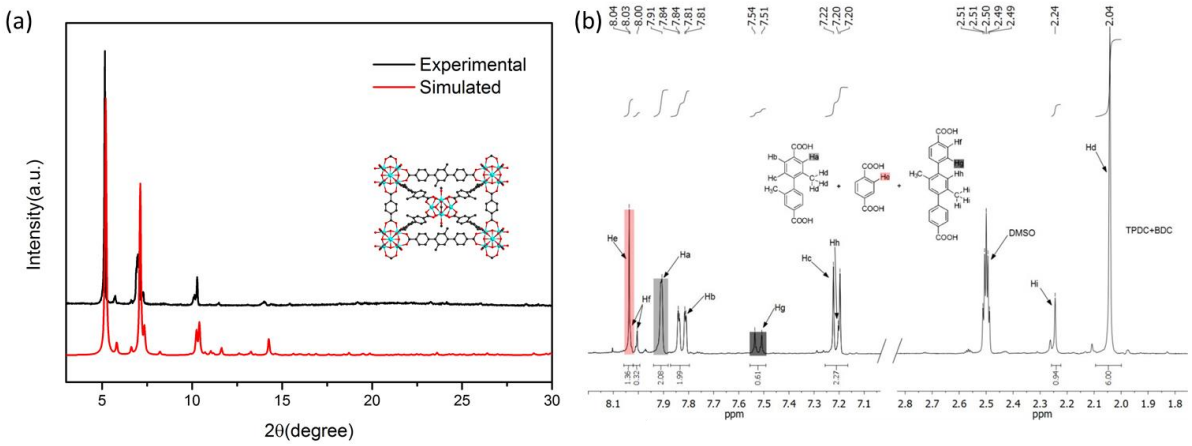

Figure 55. (a) PXRD patterns and (b) ^{1}H-NMR spectrum of compound 7.

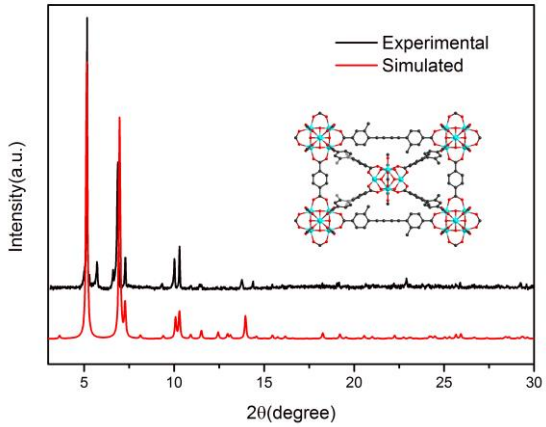

Figure 56. (a) PXRD patterns of compound 8.

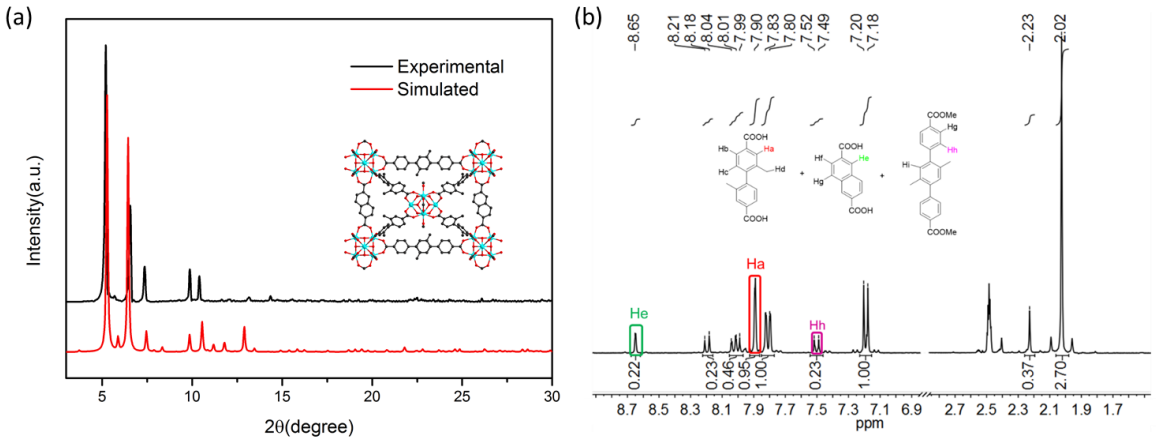

Figure 57. (a) PXRD patterns and (b) ^{1}H-NMR spectrum of compound 9.

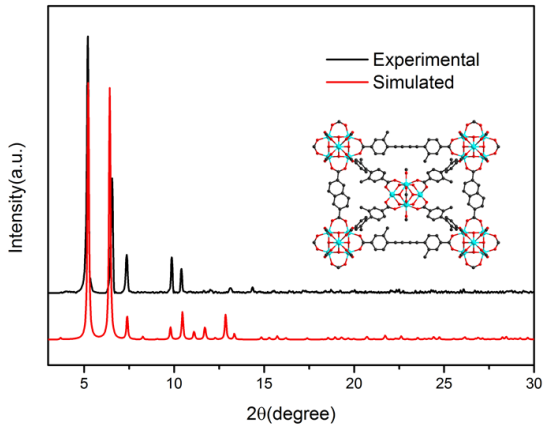

Figure 58. (a) PXRD patterns of compound 10.

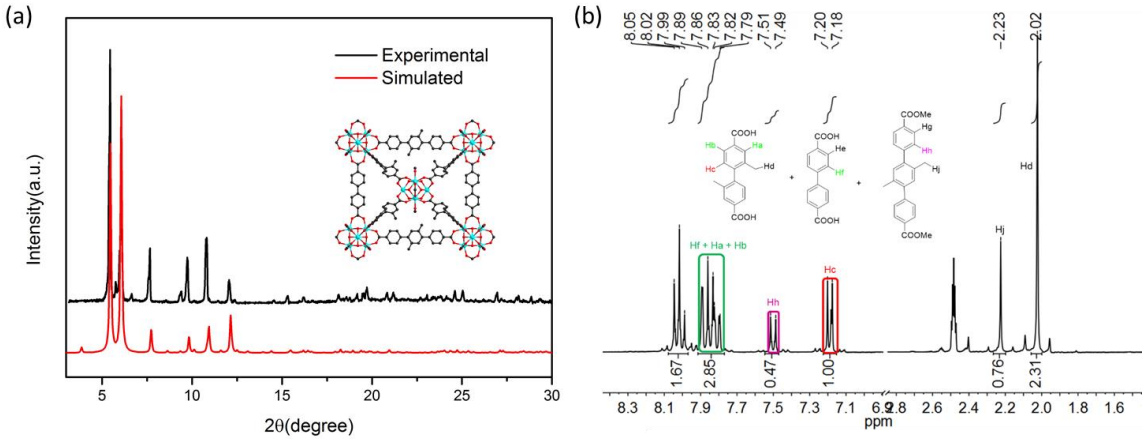

Figure 59. (a) PXRD patterns and (b) ^{1}H-NMR spectrum of compound 11.

4.2.5 Single Crystal X-Ray Crystallography

All as-synthesized crystals were taken from the mother liquid without further treatment, transferred to oil and mounted into a loop for single crystal X-ray data collection. All the activated crystals were synthesized and transferred to oil and mounted into a loop for single crystal X-ray data collection. Diffraction was measured on a Bruker Smart Apex diffractometer equipped with a Mo-Kα sealed-tube X-ray source (λ = 0.71073 Å, graphite monochromated) and a low temperature device (110 K). The data frames were recorded using the program APEX2 and processed using the program *SAINT* routine within APEX2. The data were corrected for absorption and beam corrections based on the multi-scan technique as implemented in *SADABS*. The structures were solved by direct method using *SHELXS* and refined by full-matrix least-squares on F^2 using *SHELXL* software.[146]

Refinement Details of PCN-700-(OMe)$_2$. Diffraction frames were integrated in Tetragonal P by APEX2 and determined with the R(sym) of 0.082 by *XPREP*. *XPREP* suggested that *P*4$_2$/*mmc* was the best centrosymmetric space group (CFOM = 28.83), as was well-transformed to obtain Fourier peaks by direct method (RE = 0.270). After reasonable restraints on the ligand geometry, the thermal parameters of the OMe groups were found larger than usual. The OMe groups were modelled on the two sides of the phenyl rings (60.56% for O_1C_1 group and 39.44% for $O_{1B}C_{1B}$ group). We obtained that R_1 [I > 2σ(I)] value is 0.1951 before *SQUEEZE* routine and 0.0651 after *SQUEEZE* routine of *PLATON*. The squeezed void volume was 5311 Å^3, equivalent to 61.7% of the unit cell.

Refinement Details of PCN-700-Me$_2$. Diffraction frames were integrated in Tetragonal P by APEX2. *XPREP* agreed that the R(sym) was 0.102 for this highest symmetric Bravais lattice. Based on statistics of systematic absence, *P*4$_2$/*mmc* was the best choice with lowest CFOM factor,

as was well-transformed to get Fourier peaks by direct method. All atoms were easily found after using *SHELXS.* No any geometry restraints were applied for the structure refinement. We obtained that R1 value is 0.0953 before *SQUEEZE* routine and 0.0417 after *SQUEEZE* routine of *PLATON*. The squeezed void volume was 6070 $Å^3$, equivalent to 68.6% of the unit cell.

Refinement Details of PCN-700-I_2. Diffraction frames were integrated in Tetragonal P by APEX2 and determined with the R(sym) of 0.615 by *XPREP*. Based on the previous experience on the isostructural PCN-700, *P*4_2/*mmc* was directly chosen. It was well-transformed to get Fourier peaks by direct method using *SHELXS.* After reasonable restraints on the ligand geometry, the thermal parameters of the iodine groups were found unacceptable, suggesting splitting the whole ligand into two parts (50%-50% for part A and B respectively). Furthermore, there is only one iodine group on each phenyl ring; the occupancy of the iodine group should be half for each symmetrical side as well. We obtained that R_1 [I > 2σ(I)] value is 0.1802 before *SQUEEZE* routine and 0.0800 after *SQUEEZE* routine of *PLATON*. The squeezed void volume was 5461 $Å^3$, equivalent to 62.2% of the unit cell.

Refinement details of PCN-700-$(NO_2)_2$. Diffraction frames were integrated in Tetragonal P by APEX2 and determined with the R(sym) of 0.147 by *XPREP*. *XPREP* suggested that 4_2 screw axis and *c*-glide planes should be taken based on statistics of systematic absence. *P*4_2*/mmc* was the best centrosymmetric space group (CFOM = 38.7), as was well-transformed to obtain Fourier peaks by direct method (RE = 0.268). After reasonable restraints on the ligand geometry, the thermal parameters of the two NO_2 groups were found larger than usual, suggesting splitting the whole ligand into two rotating parts (47.88% and 52.12% respectively). We obtained that R_1 [I > 2σ(I)] value is 0.0718 before *SQUEEZE* routine and 0.0506 after *SQUEEZE* routine of *PLATON*. The squeezed void volume was 5968 $Å^3$, equivalent to 66.6% of the unit cell.

Refinement details of PCN-700-$(NO_2)_4$. Diffraction frames were integrated in Tetragonal P by APEX2 and determined with the R(sym) of 0.309 by *XPREP*. *XPREP* suggested that 4_2 screw axis and *c*-glide planes should be taken based on statistics of systematic absence. *P*4_2/*mmc* was the best centrosymmetric space group (CFOM = 60.68), as was well-transformed to obtain Fourier peaks by direct method (RE=0.372). After reasonable restraints on the ligand geometry, the thermal parameters of the four NO_2 groups were found unacceptable, suggesting splitting each NO_2 functional group into two parts (the first pair of NO_2 groups, 58.97% for $N_1O_1O_2$ and 41.03% for $N_1O_{1B}O_{2B}$; the second pair of NO_2 groups, 64.07% for $N_2O_3O_4$ and 35.93% for $N_2O_{3B}O_{4B}$). We obtained that R_1 [I > 2σ(I)] value is 0.1637 before *SQUEEZE* routine and 0.0889 after *SQUEEZE* routine of *PLATON*. The squeezed void volume was 6247 $Å^3$, equivalent to 63.2% of the unit cell.

Refinement details of PCN-700-Me_4. Diffraction frames were integrated in Tetragonal P by APEX2. *XPREP* agreed that the *R*(sym) was 0.289 for this highest symmetric Bravais lattice. Based on statistics of systematic absence, *P*4_2/*mmc* was the best choice with lowest CFOM factor. It was well-transformed to get Fourier peaks by direct method using *SHELXS*. We obtained that R_1 [I > 2σ(I)] value is 0.1172 before *SQUEEZE* routine and 0.0582 after *SQUEEZE* routine of *PLATON*. The squeezed void volume was 6027 $Å^3$, equivalent to 66.9% of the unit cell.

Refinement details of PCN-700-$(CF_3)_2$. Diffraction frames were integrated in Tetragonal P by APEX2, and *XPREP* also agreed this Bravais lattice (*R*(sym) = 0.197). Based on our previous experience on the isostructural PCN-700, *P*4_2/*mmc* was selected to describe the structure. Most atoms were easily found by direct method and needed restraints on the geometry of the ligands. The squeezed void volume was 5967 $Å^3$, equivalent to 64.4% of the unit cell.

Refinement details of 1. Diffraction frames were integrated in Tetragonal P by APEX2. *XPREP* suggested that 4_2 screw axis and n- and c-glide planes should be taken based on statistics

of systematic absence. $P4_2/ncm$ was the best centrosymmetric space group, as is well-transformed to obtain Fourier peaks by direct method (RE = 0.248). We also tried the lowest CFOM options, $P\bar{4}$ and $P4/m$, but the initial solutions were too poor to precede further refinements. By careful restraints of the ligand geometry and the corresponding atomic displacement parameters, R_1 [I > 2σ(I)] is 0.1121 before *SQUEEZE* treatment and 0.0616 after *SQUEEZE* treatment. The squeezed void volume was 9643 $Å^3$, equivalent to 62.0% of the unit cell.

Refinement Details of 2. Diffraction frames were integrated in Tetragonal P by APEX2, and *XPREP* also agreed this Bravais lattice (R(sym)=0.130). It suggested that 4_2 screw axis and c-glide plane should be taken based on statistics of systematic absence, and $P4_2/mmc$ was the best candidate with lowest CFOM factor (34.18). All atoms were easily found by direct method. After several geometry restraints of the ligands, C8 showed huge thermal ellipsoids; thus, a split disorder part C8' was modeled in the equivalent symmetry position with occupancy of 50%. We obtained that R1 is 0.1051 before *SQUEEZE* treatment and 0.0565 after *SQUEEZE* treatment. The squeezed void volume was 5656 $Å^3$, equivalent to 63.8% of the unit cell.

Refinement Details of 3. Diffraction frames were integrated in Tetragonal P by APEX2. *XPREP* suggested that $P4_2/mmc$ be the best centrosymmetric space group (COM = 36.13), similar to those ligand-installed analogues. In this structure, NDC possesses highly disorders and we left it isotropic to avoid non-positive definite. By careful restraints of the ligand geometry and the atomic displacement parameters, R_1 value is 0.0962 before *SQUEEZE* treatment and 0.0497 after *SQUEEZE* treatment. The squeezed void volume was 6353 $Å^3$, equivalent to 67.4% of the unit cell.

Refinement details of 4. Diffraction frames were integrated in Tetragonal P by APEX2. Based on our previous experience on the isostructural PCN-700, $P4_2/mmc$ was selected to describe

the structure. The value of R_{int} is greater than 0.25 might be caused by the impaired crystal soaking in the BPDC solution. All the ligands were exchanged, rather than installation. By careful restraints of the ligand geometry and the corresponding atomic displacement parameters, R_1 value is 0.1195 before *SQUEEZE* treatment and 0.1064 after *SQUEEZE* treatment. The squeezed void volume was 7487 $Å^3$, equivalent to 73.4% of the unit cell.

Refinement Details of 5. Diffraction frames were integrated in Tetragonal P by APEX2, and *XPREP* also agreed this Bravais lattice (R(sym)=0.279). It suggested that 4_2 screw axis and c-glide plane should be taken based on statistics of systematic absence. *P*4_2/*mmc* was the best candidate with lowest CFOM factor (48.36) to get Fourier peaks. Most of the Fourier peaks for the frameworks were clear and intense; excluding those for the central phenyl rings of Me_2-TPDC ligands, which can be constructed by C16 and C17 with symmetry operation. Since the central phenyl rings only possess two methyl groups rather than four, the occupancy of the methyl groups (C19) needed to be set half (50% -CH_3 and 50% -H). The same logic was applied to the hydrogen (H17B) riding on the phenyl ring. After fixing geometry of the ligands, R1 value is 0.1441 without *SQUEEZE* treatment and 0.0802 with *SQUEEZE* treatment. The squeezed void volume was 5836 $Å^3$, equivalent to 63.6% of the unit cell.

Refinement details of 6. Diffraction frames were integrated in Tetragonal P by APEX2 and determined with the R(sym) of 0.172 by *XPREP*. *XPREP* suggested that *P*4_2*/mmc* be the best centrosymmetric space group (COM=48.01), similar to those ligand-modified analogues. In this structure, the chemical formula is $[Zr_6\ O_8\ (O_4)_{0.5}]\ [C_{16}\ H_{12}\ O_4]_4\ [C_{20}\ H_{12}\ O_4]_{0.5}$; that is, half a BDDC ligand ($C_{20}\ H_{12}\ O_4$) were installed in the PCN-700 framework. Note that when the BDDC ligand is absent, O-containing ligand will coordinate to the Zr_6 clusters (occupancy of 50%). By careful restraints of the ligand geometry and the atomic displacement parameters, R_1 value is 0.1243

before *SQUEEZE* treatment and 0.0772 after *SQUEEZE* treatment. The squeezed void volume was 5757 $Å^3$, equivalent to 64.5 % of the unit cell.

Refinement Details of 7. Diffraction frames were integrated in Tetragonal P by APEX2. *XPREP* suggested that 2_1 screw axis and n-glide plane should be taken based on statistics of systematic absence. *P*4_2*/mnm* was the best centrosymmetric space group, as is well-transformed to obtain Fourier peaks by direct method. We also tried the lowest CFOM options, $P\bar{4}$ and *P*4/*m*, but the initial solutions were too poor to precede further refinements. Note that the μ_3-O and OH^- on the eight faces of the Zr octahedral clusters (denoted as O1S O1S' O2S O2S') were refined as 50% and 50% to keep the neutral charge balance. In order to eliminate the flat thermal ellipsoids on these sites, isotropic ADP refinement were reasonably adopted for the 3-fold symmetric positions, O1S O1S' O2S O2S'. By careful restraints of the ligand geometry and the corresponding atomic displacement parameters, R1 value is 0.1490 before *SQUEEZE* treatment and 0.0950 after *SQUEEZE* treatment. The squeezed void volume was 10721 $Å^3$, equivalent to 62.2% of the unit cell.

Refinement Details of 8. Diffraction frames were integrated in Tetragonal P by APEX2 and determined with the R(sym) of 0.196 by *XPREP*. *XPREP* suggested that *P*4_2*/mmc* be the best centrosymmetric space group (COM = 61.07), similar to those ligand-modified analogues. In this structure, the chemical formula is $[Zr_6\ O_8\ (O_4)_{0.5}]\ [C_{16}\ H_{12}\ O_4]_4\ [C_8\ H_4\ O_4]\ [C_{20}\ H_{12}\ O_4]_{0.5}$; that is, one BDC ligand ($C_8\ H_4\ O_4$) and half a BDDC ligand ($C_{20}\ H_{12}\ O_4$) were installed in the PCN-700 framework. Note here, we left BDDC ligands isotropic to avoid non-positive definite. By careful restraints of the ligand geometry and the atomic displacement parameters, R_1 value is 0.1267 before *SQUEEZE* treatment and 0.0831 after *SQUEEZE* treatment. The squeezed void volume was 5436 $Å^3$, equivalent to 62.0 % of the unit cell.

Refinement details of 9. Diffraction frames were integrated in Tetragonal P by APEX2 and determined with the R(sym) of 0.313 by *XPREP*. *XPREP* suggested low CFOM options, $P\bar{4}$ and *P*4/*m*. The heavy Zr atoms were clearly present, but the coordinates of the ligand positions were too poor to precede further refinements. Checked with *Platon Addsym* unit, the symmetry of the Zr_6 clusters suggested the space group be changed to $P4_2/mnm$. In this space group, the chemical formula is described as $(Zr_6\ O_8\ O_2)\ (C_{16}\ H_{12}\ O_4)_4\ (C_{12}\ H_6\ O_4)\ (C_{22}\ H_{16}\ O_4)_{0.5}$; that is, one NDC ligand ($C_{12}\ H_6\ O_4$) and half a TPDC ligand ($C_{22}\ H_{16}\ O_4$) were installed in the PCN-700 framework. In this structure, NDC possesses highly disorders and the TPDC only has two methyl groups on its central phenyl ring, which was modelled as four with occupancy of 50%. By careful restraints of the ligand geometry and the atomic displacement parameters, R_1 value is 0.1824 before *SQUEEZE* treatment and 0.1160 after *SQUEEZE* treatment. The squeezed void volume was 12273 $Å^3$, equivalent to 65.0 % of the unit cell.

Refinement details of 10. Diffraction frames were integrated in Tetragonal P by APEX2 and determined with the R(sym) of 0.107 by *XPREP*. *XPREP* suggested that $P4_2/mmc$ be the best centrosymmetric space group (COM = 92.41), similar to those ligand-modified analogues. In this structure, the chemical formula is $[Zr_6\ O_8]\ [C_{16}\ H_{12}\ O_4]_4\ [C_{12}\ H_6\ O_4]\ [C_{20}\ H_{12}\ O_4]$; that is, one NDC ligand ($C_8\ H_4\ O_4$) and one BDDC ligand ($C_{20}\ H_{12}\ O_4$) were installed in the PCN-700 framework. In this structure, NDC and BDDC possess highly disorder nature and we left it isotropic to avoid non-positive definite. Note that the BDDC ligand suffered bending force upon installation (the occupancy was set half for each part). The value of R_{int} is greater than 0.25 might be caused by the impaired crystal soaking twice in the NDC and BDDC solution. By careful restraints of the ligand geometry and the atomic displacement parameters, R_1 value is 0.3478 before *SQUEEZE* treatment

and 0.1263 after *SQUEEZE* treatment. The squeezed void volume was 5897 $Å^3$, equivalent to 61.4 % of the unit cell.

Refinement details of 11. Diffraction frames were integrated in Tetragonal P by APEX2. Based on our previous experience on the isostructural PCN-700, $P4_2/mmc$ was selected to describe the structure. The value of R_{int} is greater than 0.25 might be caused by the impaired crystal soaking in the BPDC solution. 80% of the ligands in the original host framework were exchanged with BPDC ligands, rather than pure BPDC installation. In this structure, the chemical formula is $[Zr_6 O_8] [C_{14} H_8 O_4]_{4*0.8} [C_{14} H_8 O_4] [C_{22} H_{16} O_4]$. By careful restraints of the ligand geometry and the corresponding atomic displacement parameters, R_1 value is 0.1532 before *SQUEEZE* treatment and 0.1025 after *SQUEEZE* treatment. The squeezed void volume was 7153 $Å^3$, equivalent to 68.9% of the unit cell.

Refinement details of PCN-700-BPYDC(Cu)-TPDC. Diffraction frames were integrated in Tetragonal P by APEX2 and determined with the R(sym) of 0.052 by *XPREP*. *XPREP* suggested that $P4_2/mmc$ be the best centrosymmetric space group (COM=26.66), similar to previous ligand-modified analogues. In this structure, the chemical formula is $[Zr_6 O_8] [C_{16} H_{12} O_4]_4 [C_{12} N_2 H_6 O_4 (Cu_{0.53} I_{0.27} N_{0.27})] [C_{22} H_{16} O_4]$; that is, one BPYDC ligand and one TPDC ligand ($C_{22} H_{16} O_4$) were installed in the PCN-700 framework. The Cu(I) ions were attached to the BPYDC ligands post-synthetically with an occupancy of 53%. The Cu(I) ions were coordinated to BPYDC ligands on both symmetrical positions with occupancy of 50%. Each Cu(I) was coordinated with one iodine ion and one acetonitrile (only N1S shown in the structure). By careful restraints of the ligand geometry and the corresponding atomic displacement parameters, R_1 value is 0.1304 before *SQUEEZE* treatment and 0.0815 after *SQUEEZE* treatment. The squeezed void volume was 6067 $Å^3$, equivalent to 60.5% of the unit cell. Note that the μ_3-O and OH^- on the eight faces of the Zr

octahedral clusters should be refined as 50% and 50% to keep the neutral charge balance. This was ignored for clarity and simplicity.

For all structures, *PLATON* addsym unit were performed twice to check the most suitable space group: one is to check the heavy atom moiety, the other is to check the final structure. After all ligands were fixed with reasonable geometry, the enormous thermal ellipsoids were refined with the help of EADP restrains. All non-hydrogen atoms were refined with anisotropic displacement parameters during the final cycles, whereas organic hydrogen atoms were located with isotropic displacement parameters set to 1.2 × U_{eq} of the attached atoms. The strong Q peaks were contributed to scattering of disordered solvent molecules, which were removed by using the *SQUEEZE* routine of *PLATON*; structures were then refined again using the data generated (Figure 60, Table 12).

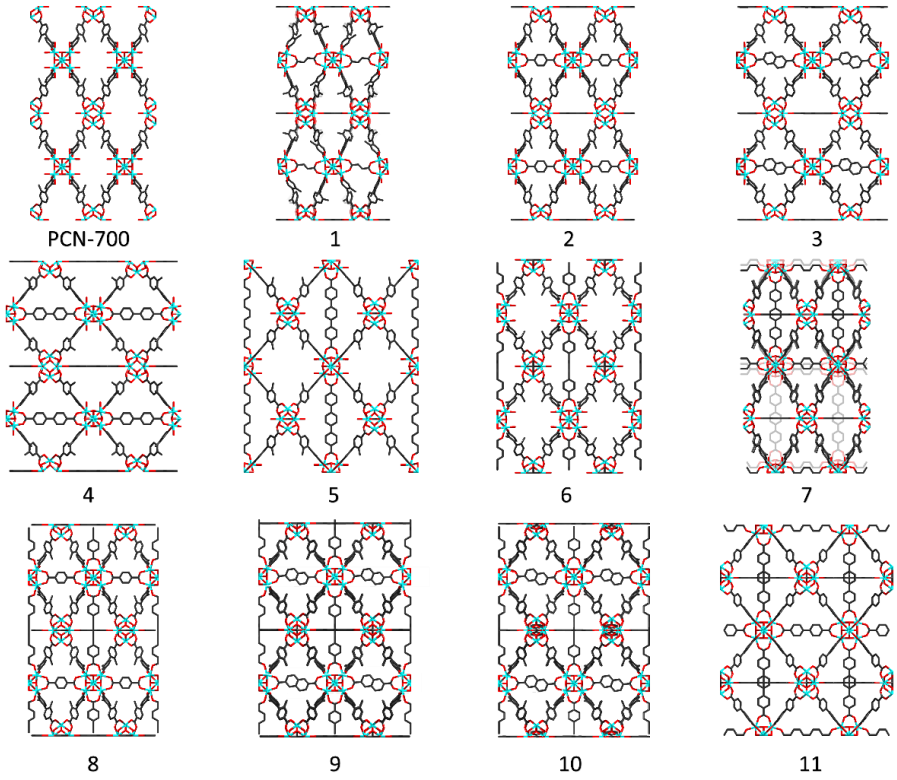

Figure 60. The crystal structures of PCN-700 and compounds **1-11** viewed along *a*-axis.

Table 12. Crystal data and structure refinements

Name	PCN700-$(OMe)_2$	PCN-700-I_2	PCN-700-$(NO_2)_2$	PCN700-$(NO_2)_4$
Empirical formula	$C_{64}H_{48}O_{40}Zr_6$	$C_{56}H_{24}I_8O_{32}Zr_6$	$C_{56}H_{24}N_8O_{48}Zr_6$	$C_{56}H_{16}N_{16}O_{64}Zr_6$
Formula weight	2004.34	2771.27	2124.15	2484.17
Temperature/K	110(2)	110(2)	110(2)	110(2)
Crystal system	Tetragonal	Tetragonal	Tetragonal	Tetragonal
Space group	$P4_2/mmc$	$P4_2/mmc$	$P4_2/mmc$	$P4_2/mmc$
a/Å	24.263(4)	24.35(3)	24.250(5)	23.024(2)
b/Å	24.263(4)	24.354	24.250(5)	23.024(2)
c/Å	14.615(3)	14.797(16)	15.232(3)	18.6484(19)
α/°	90.00	90.00	90.00	90.00
β/°	90.00	90.00	90.00	90.00
γ/°	90.00	90.00	90.00	90.00
Volume/Å^3	8604(3)	8776(13)	8958(3)	9885.5(17)
Z	2	2	2	2
ρ_{calc} g/cm^3	0.774	1.049	0.788	0.835
μ/mm^{-1}	0.393	1.786	0.384	0.361
F(000)	1984	2560	2080	2432
Wavelength (Å)	0.71073	0.71073	0.71073	0.71073
2Θ range for data collection/°	4.68 to 51.98	3.74 to 52.00	3.76 to 48.52	3.54 to 52.00
Completeness	99.2%	99.3%	99.4%	99.8%
Reflections collected	22231	38616	79525	67631
Independent reflections	4577	4690	3956	5275
R_{int}	0.0800	0.2957	0.1280	0.2396
Data	4577	4690	3956	5275
Restraints	59	64	46	109
Parameters	112	147	177	136
GOF on F^2	1.007	1.002	1.001	1.008
R_1 [I > 2σ(I)][a]	0.0651	0.0800	0.0506	0.0889
wR_2 [I > 2σ(I)][b]	0.1488	0.1450	0.1044	0.1925
R_1 (all data)[a]	0.0852	0.2289	0.0780	0.1483
wR_2 (all data)[b]	0.1539	0.1665	0.1138	0.2107
Residue peak / hole (eÅ^{-3})	0.909 / -0.670	0.597 / -1.068	0.430 / -0.486	1.181 / -1.721

Table 12. Continued.

Name	Compound **6** (PCN-700-BDDC)	Compound **8** (PCN-700-BDC-BDDC)	Compound **9** (PCN-700-NDC-TPDC)
Empirical formula	$C_{74}H_{54}O_{32}Zr_6$	$C_{82}H_{58}O_{32}Zr_6$	$C_{87}H_{62}O_{32}Zr_6$
Formula weight	2002.49	2102.60	2166.69
Temperature/K	110(2)	110(2)	110(2)
Crystal system	Tetragonal	Tetragonal	Tetragonal
Space group	$P4_2/mmc$	$P4_2/mmc$	$P4_2/mnm$
a/Å	24.378(10)	24.288(11)	33.505(13)
b/Å	24.378	24.288	33.505
c/Å	15.017(6)	14.859(7)	16.824(7)
α/°	90.00	90.00	90.00
β/°	90.00	90.00	90.00
γ/°	90.00	90.00	90.00
Volume/Å^3	8925(5)	8766(6)	18887(11)
Z	2	2	4
ρ_{calc} g/cm^3	0.745	0.797	0.762
μ/mm^{-1}	0.375	0.384	0.358
F(000)	1988	2092	4320
Wavelength (Å)	0.71073	0.71073	0.71073
2Θ range for data collection/°	3.18 to 49.00	3.22 to 51.98	3.64 to 52.00
Completeness	95.5%	99.0%	99.9%
Reflections collected	30878	32486	88526
Independent reflections	3903	4670	9863
R_{int}	0.1335	0.1519	0.2094
Data	3903	4670	9863
Restraints	83	46	161
Parameters	105	108	186
GOF on F^2	1.002	1.008	1.001
R_1 [I > 2σ(I)][a]	0.0772	0.0831	0.1160
wR_2 [I > 2σ(I)][b]	0.1700	0.1862	0.2652
R_1 (all data)[a]	0.1316	0.1441	0.1803
wR_2 (all data)[b]	0.1794	0.1984	0.2882
Residue peak / hole (eÅ^{-3})	0.915 / -1.175	1.969 / -1.330	3.992 / -2.836

Table 12. Continued.

Name	Compound **10** (PCN-700-NDC-BDDC)	Compound **11** (PCN-700-BPDC-TPDC)	PCN-700-BPYDC(Cu)-TPDC
Empirical formula	$C_{96}H_{66}O_{32}Zr_6$	$C_{80.8}H_{49.6}O_{28.8}Zr_6$	C_{98} H_{70} $Cu_{0.53}$ $I_{0.27}$ $N_{2.27}$ O_{32} Zr_6
Formula weight	2278.81	2028.52	2405.90
Temperature/K	110(2)	110(2)	110(2)
Crystal system	Tetragonal	Tetragonal	Tetragonal
Space group	$P4_2/mmc$	$P4_2/mmc$	$P4_2/mmc$
a/Å	23.900(3)	23.33(4)	23.0867(9)
b/Å	23.900	23.332	23.087
c/Å	16.817(2)	19.07(3)	18.8049(8)
α/°	90.00	90.00	90.00
β/°	90.00	90.00	90.00
γ/°	90.00	90.00	90.00
Volume/Å^3	9606.5(18)	10381(23)	10022.9(6)
Z	2	2	2
ρ_{calc} g/cm^3	0.788	0.649	0.797
μ/mm^{-1}	0.354	0.322	3.188
F(000)	2276	2010	2399
Wavelength (Å)	0.71073	0.71073	1.54184
2Θ range for data collection/°	3.40 to 50.00	3.90 to 52.00	3.82 to 158.32
Completeness	78.5%	99.8%	99.1%
Reflections collected	3629	97194	60375
Independent reflections	3629	5531	5832
R_{int}	0.0000	0.3369	0.0685
Data	3629	5531	5832
Restraints	231	52	85
Parameters	137	102	155
GOF on F^2	1.012	1.004	1.002
R_1 [I > 2σ(I)][a]	0.1263	0.1025	0.0815
wR_2 [I > 2σ(I)][b]	0.2823	0.1844	0.1899
R_1 (all data)[a]	0.1614	0.2678	0.0964
wR_2 (all data)[b]	0.2946	0.2288	0.1966
Residue peak / hole (eÅ^{-3})	1.254 / -1.028	1.265 / -0.649	2.565 / -1.174

[a] $R_1 = \Sigma||F_o| - |F_c||/\Sigma|F_o|$.

[b] $wR_2 = |\Sigma w(|F_o|^2 - |F_c|^2)|/\Sigma|w(F_o^2)^2|^{1/2}$.

4.3 Results and Discussion

4.3.1 Topology Guided Design of MOF Matrix

In order to obtain the prototype MOF, a topology-guided linker design strategy is adopted.[93, 147] The combination of Zr_6 cluster and linear linker usually gives rise to an **fcu** net in which the Zr_6 cluster is fully connected by linkers, leaving no room for further linker installation.[148] To address this, a **bcu** net is selected as target topology for the prototype MOF.[149] A **bcu** net is composed of 8-connected cubic nodes which can be viewed as a deduction from an **fcu** net by deleting four linkers in the equatorial plane of the octahedral Zr_6 cluster (Figure 61). These uncoordinated sites in **bcu** net are well poised for subsequent linker installation. However, the reactions between Zr^{4+} ions and linear linkers such as BDC, BPDC and TPDC always yield a 12-connected **fcu** net (UiO-66, UiO-67 and UiO-68 respectively) under solvothermal conditions because high-connected network is thermodynamically favored compared to the low-connected ones. It has been well demonstrated that the MOF topology could be tuned by the linker configuration; therefore we expect that a **bcu** structure could be obtained through judicious linker design.[139, 150] We reason that the **bcu** net could be realized if the two carboxylate groups of the linker twist off the coplanar position (Figure 62b). As shown in Figure 62c, the two carboxylate groups of the linker are required to be in the same plane in order to form a 12-connected **fcu** structure. With the twisted linker, a **bcu** net (Figure 62f) should be expected as opposed to an **fcu** net (Figure 62e). To verify our hypothesis, two methyl groups were introduced at 2 and 2' positions of BPDC linker. Since the dihedral angle of biphenyl rings in BPDC is known to be directly related to the size and nature of substituents on the 2 and 2' positions, the Me_2-BPDC (2,2'-dimethylbiphenyl-4,4'-dicarboxylate) is expected to provide two off-plane carboxylate groups.[139]

As expected, reaction of H_2Me_2-BPDC and $ZrCl_4$ in *N*,*N*-dimethylformamide (DMF) at 120 °C yielded crystals of desired MOF with 8-connected topology, designated as PCN-700.

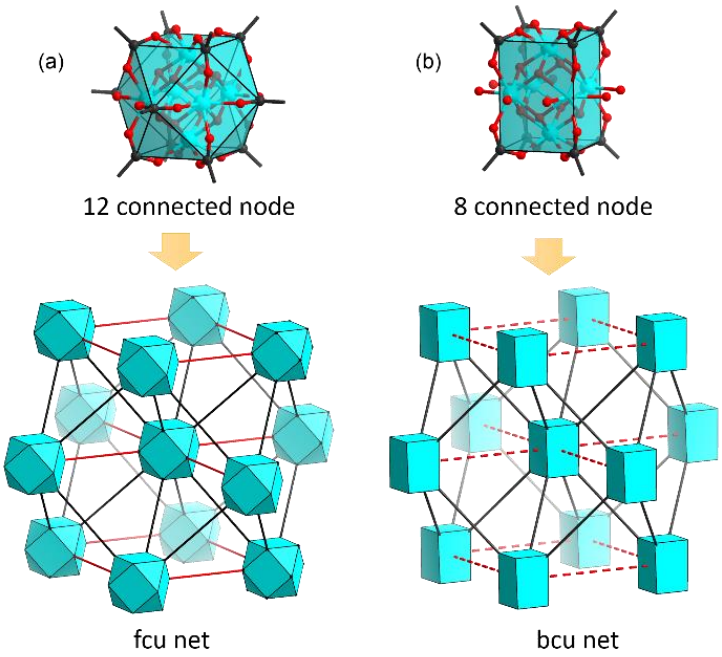

Figure 61. (a) **fcu** net formed by 12-connected nodes; (b) **bcu** net formed by 8-connected nodes.

4.3.2 Control MOF Structures by Linker Design

A challenge encountered in the synthesis of PCN-700 is the formation of competing phases, known as the UiO structures, with the desired PCN-700 product. When combined with linear linkers such as BPDC, Zr_6 clusters can form an **fcu** net (UiO-67 structure) or a **bcu** net (PCN-700 structure) depending on the configuration of linkers. In the **fcu** net, two carboxylates of each linker adopt a coplanar configuration, whereas the two carboxylates are perpendicular to each other in the **bcu** net. Considering the fact that the formation of Zr–carboxylate bond is an exothermic process, the fcu net, with 12-connected Zr_6 clusters, is believed to be thermodynamically more favorable than the 8-connected **bcu** net.[151] However, the coplanar configuration is kinetically unfavorable if bulky substituents are introduced on the 2- and 2'-positions of BPDC. The steric

hindrance of substituents will force the two phenyl rings as well as the carboxylates into a perpendicular arrangement (Figure 62b), which would increase the energy barrier of **fcu** nets formation, since the two carboxylates are required to be coplanar (Figure 62a). Therefore, we assume that a **bcu** net could be obtained as a kinetically controlled product if bulky substituents are introduced on the phenyl rings of the linkers. The competitive formation of UiO-67 structure and PCN-700 structure represents the competition between thermodynamics and kinetics.

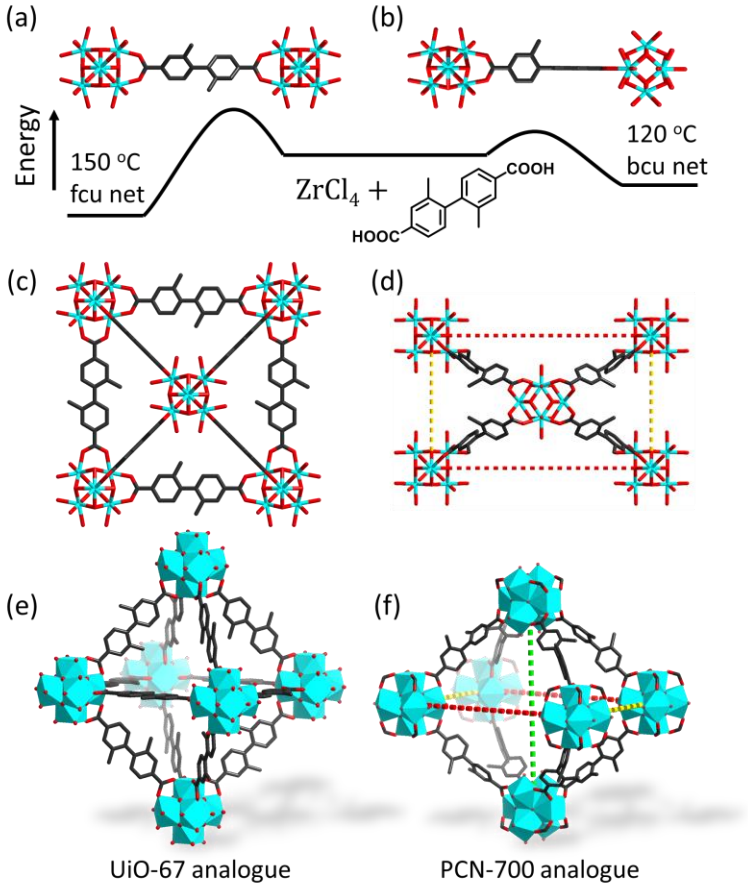

Figure 62. Kinetic control in the synthesis of PCN-700: (a) Linker conformation in **fcu** nets; (b) linker conformation in **bcu** nets; (c) UiO-67 and (d) PCN-700 structures viewed along *a*-axis; cages of (e) UiO-67 and (f) PCN-700 structures.

To verify our hypothesis, twelve linkers with different substituents (L1 to L12) were synthesized and reacted with $ZrCl_4$ at different temperatures. The products were characterized by powder X-ray diffraction and compared with the simulated patterns of UiO-67 and PCN-700 respectively. As shown in Figure 63, a phase diagram can be summarized to describe the products from different linkers under variable temperatures. As expected, the resulting MOF structures are strongly dependent on the level of steric hindrance and the number of substituents. In general, PCN-700 is the dominant phase if bulky substituents are introduced on the linkers, and vice versa. Empirically, the steric hindrance of substituents on each linker needs to be larger than that of L5 in order to form PCN-700 isostructures. It should be noted that the "steric argument" cannot explain all the experimental results. As long as steric effect is concerned, L7 is more likely to give PCN-700 structure than L5 concerning that the bromo group is bulkier than methoxy group. However, the employment of L5 give rise to PCN-700 structure while L7 only result in UiO-67 structure under identical synthetic condition. This is tentatively attributed to the stronger interaction between methoxy groups which favors the perpendicular conformation. As a result, L7 do not fit in the phase diagram. Meanwhile, the temperature also affects the final products as it controls the balance between kinetic and thermodynamic products. The PCN-700 phase, as a kinetic product, is favored at relatively low temperature. For example, the L6 would give rise to pure PCN-700 phase at 80 °C and 100 °C while a mixture of UiO-67 and PCN-700 phases would be generated if the reaction is carried out at 120 °C. When the reaction temperature is further elevated to 140 °C, only UiO-67 phase can be obtained. Therefore, pure PCN-700 isostructural product can be synthesized by rational design of the linkers and judicious control of reaction conditions, which steers the system toward the PCN-700 phases and away from the competing UiO-67 phases.

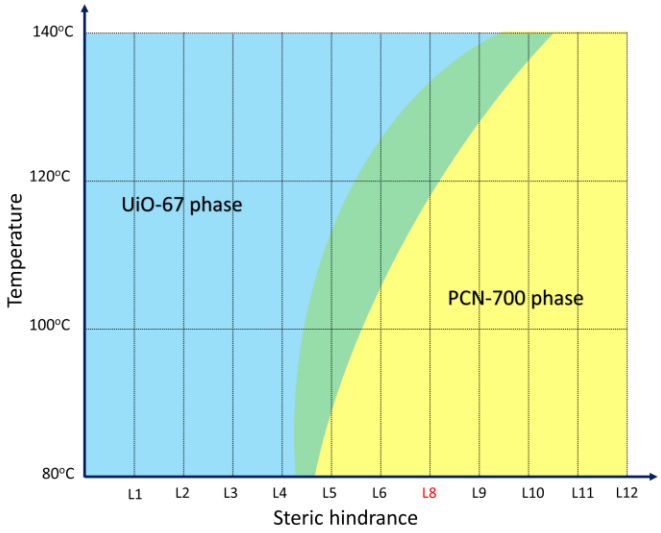

Figure 63. Phase diagram showing the products with different linkers under different temperatures.

L8 linker was selected from twelve linkers to construct the matrix for linker installation studies. Obviously, L1-L5 and L7 are not suitable for linker installation purposes as they tend to form UiO-67 phases under solvothermal conditions. L6 gave rise to pure PCN-700 phase at 100 °C with low yield. Intuitively, L9-L12 would be adequate for linker installation studies as they form PCN-700 phase at a wide range of temperatures. However, it should be noted that increasing the steric hindrance of substituents on the linker will decrease the MOF porosity and flexibility as further proved by N_2 adsorption studies. Obviously, a rigid and less porous structure is not suitable for the installation of different linkers. The structure constructed from L8 possesses a delicate balance between enough steric effects and sufficient space. Hence, L8 was chosen as a representative example for the further investigation of linker installation.

4.3.3 Flexibility of PCN-700 Series

The framework needs to be flexible to accommodate linear linkers with different lengths. Therefore, the flexibility of PCN-700 series was investigated. Flexible behaviors of MOFs are

usually triggered by the removal or introduction of guest molecules. Bearing this in mind, we carried out successive single-crystal X-ray diffraction analyses (SC-XRD) analyses on PCN-700-Me_2 during desolvation to generate "snapshots" of the breathing process.

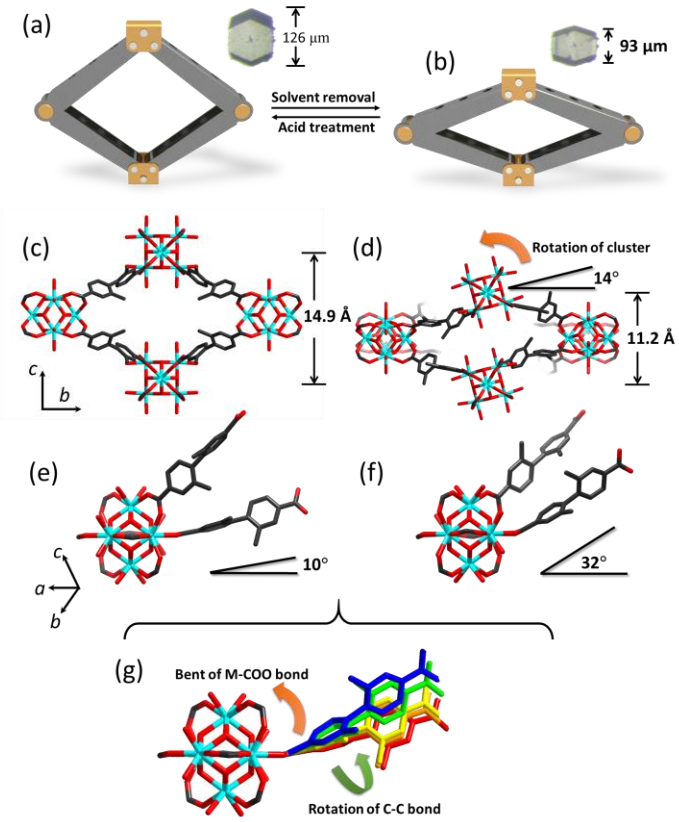

Figure 64. (a) and (b) Graphic representations of PCN-700-Me_2 before and after desolvation. Inserted photos are microscopic images of the respective single crystals. (c) and (d) Structures of PCN-700-Me_2 before and after desolvation. (e) and (f) Linker conformation before and after desolvation. (g) An overlap of structural conformations during desolvation.

Crystallographic data clearly shows that PCN-700-Me_2 exhibits a scissor-jack-like behavior, shrinking along *c*-direction by tweaking the metal–linker conjunction angle (Figure 64a). A significant decrease in the length of *c*-axis (from 14.92 Å to 11.24 Å) and a slight increase in the length of *a*/*b*-axis (from 24.35 Å to 24.84 Å) are observed upon guest removal. The flexible Zr–carboxylate connection, acting as a hinge, is primarily responsible for the breathing behavior.

As shown in Figure 64e and f, PCN-700-Me_2 undergoes a large conformational change that is associated with the bending of Zr–O–C angle (from 133° to 130°) and, more intuitively, the varying of dihedral angle between the equatorial plane of O–Zr–Zr–O and the plane of carboxylate (from 10° to 32°). The bending of Zr–carboxylate bond affords a closer packing along *c*-direction, which gives rise to a shrinkage of the *c*-axis. A closer investigation indicates that the breathing motion of PCN-700-Me_2 is a collective result. Along with the bending of Zr–carboxylate bond, we also observed rotation of the C–C bond between two phenyl rings, which alleviates the steric hindrance within the structure by arranging the two methyl groups on adjacent linkers as far apart as possible. As a collateral effect of the rotation of C–C bond, Zr_6 clusters tilt about 14° (Figure 64d). An overlap of different conformations during desolvation (Figure 64g) underlines the fact that the bending of Zr–carboxylate junction and the conformational change of the organic linker together account for the breathing behavior of PCN-700-Me_2.

Table 13. Tuning the breathing amplitude by different linkers.

Linker	Topology	In DMF			Without solvent			Δ*c*/ %	Δ*V*/ %
		c / Å	*a* / Å	*V* / Å^3	*c* / Å	*a* / Å	*V* / Å^3		
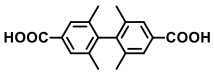 H_2Me_4-BPDC	**bcu**	15.36	24.22	9008	14.08	24.08	8170	9.09	10.3
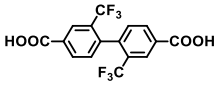 $H_2(CF_3)_2$-BPDC	**bcu**	15.00	24.40	8930	12.09	24.67	7352	24.1	21.5
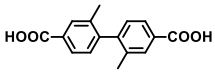 H_2Me_2-BPDC	**bcu**	14.92	24.35	8844	11.24	24.84	6933	32.7	27.6
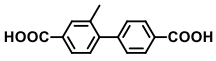 H_2Me-BPDC	**fcu**	-	-	-	-	-	-		

It should be noted that the axial breathing amplitude of PCN-700-Me_2 is much larger than the volumetric breathing amplitude. The nearly uniaxial breathing behavior can be directly observed on a real crystal under optical microscope. One particular PCN-700-Me_2 crystal was measured with a length of 126 μm along *c*-axis, which shrank to 93 μm (Figure 64a and b) upon desolvation (*c*-direction is determined by Apex 2). These values match very well with unit cell parameters determined by SC-XRD. Such high elasticity in macroscopic single crystals is rarely observed to the best of our knowledge.[152]

The SC-XRD investigation of the breathing mechanism manifests the structure-property correlations, which further enable us to judiciously modulate the flexibility of the PCN-700 system. Since PCN-700-Me_2 undergoes unit-cell dimensional contraction along *c*-axis, which involves a rotation of the C–C bond between phenyl rings, we speculate that the framework flexibility can be tuned by changing substituents on phenyl rings of the linker. To tune the breathing amplitude, linkers with different substituents were synthesized, and designated as H_2Me_4-BPDC (2,2',6,6'-tetramethylbiphenyl-4,4'-dicarboxylic acid), $H_2(CF_3)_2$-BPDC (2,2'-bis(trifluoromethyl)-biphenyl-4,4'-dicarboxylatic acid), and H_2Me-BPDC (2-methylbiphenyl-4,4'-dicarboxylic acid) (Table 13). As expected, H_2Me_4-BPDC and $H_2(CF_3)_2$-BPDC give rise to MOFs with increased structural rigidity because of the elevated steric hindrance. Among this series, PCN-700-Me_4 exhibits the highest degree of rigidity while only small changes along *c*-axis (15.4 Å to 14.1 Å) and unit cell volume (9008 $Å^3$ to 8170 $Å^3$) were observed upon desolvation (Table 1). Intuitively, linkers with less bulky substituents tend to form more flexible MOF structures, as demonstrated in MIL-53 and MIL-88 systems.[153-154] However, this is not the case in PCN-700 system. The substituents on the phenyl rings are required to be bulky enough to induce two off-plane carboxylate groups. As far as steric hindrance is concerned, H_2Me-BPDC is expected to

generate an even more flexible MOF than PCN-700-Me_2. However, only an **fcu** net (UiO-67 analogue) was obtained by using H_2Me-BPDC. By far, PCN-700-Me_2 is the most flexible one that we obtained with the **bcu** topology.

Scheme 7. Chemical equation representing linker installation process.

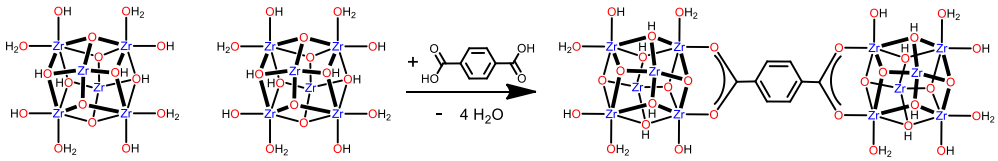

4.3.4 Sequential Linker Installation

To carry out linker installation, PCN-700 crystals were sequentially exposed to a solution of H_2BDC and H_2Me_2-TPDC in DMF at 75 °C for 24 h. The carboxylate linkers can react with the terminal OH^-/H_2O ligands on $Zr_6O_4(OH)_8(H_2O)_4$ clusters pf PCN-700 through an acid-base reaction. The afforded crystals were washed with fresh DMF before X-ray single crystal diffraction data collection. The existence and position of BDC and Me_2-TPDC are unambiguously observed in the crystallographically resolved structure. The resultant structure, designated as compound 7, crystallizes in *P*4_2/*mnm* space group. Interestingly, the unit cell of compound 7 is doubled compared to the prototype MOF (PCN-700) due to the asymmetric distribution of Me_2-TPDC linker which eliminates a mirror plane passing though the Zr_6 cluster. In compound 7, each Zr_6 cluster is 11-connected to eight Me_2-BPDC, two BDC, and one Me_2-TPDC linkers. The overall composition can be formulized as $Zr_6O_4(OH)_5(H_2O)$(Me_2-BPDC)$_8$$BDC_2$($Me_2$-TPDC), which has been further confirmed by ^{1}H-NMR.

It should be noted that the sequence of the installation is crucial for the success of linker installation process. As shown in Figure 65, starting with short linker, the BDC will occupy all the

small pockets (pocket B) with an O···O distance of 7.0 Å, leaving the large pockets (pocket A') unoccupied. Pocket A' has an O···O distance of 16.5 Å, which is slightly longer than the size of Me_2-TPDC (15.2 Å). Further incorporated Me_2-TPDC will only occupy every other pocket A' and stretch the rest pocket A' to 17.4 Å (pocket A''). As a result, a MOF with three linkers of different lengths is obtained. However, if the Me_2-TPDC linkers are installed first, they will occupy all the pockets A and meanwhile stretch the pocket B to 8.2 Å (pocket B'). Therefore, it is impossible to lock BDC into these elongated pockets (pocket B') since the length of BDC is only 7.0 Å.

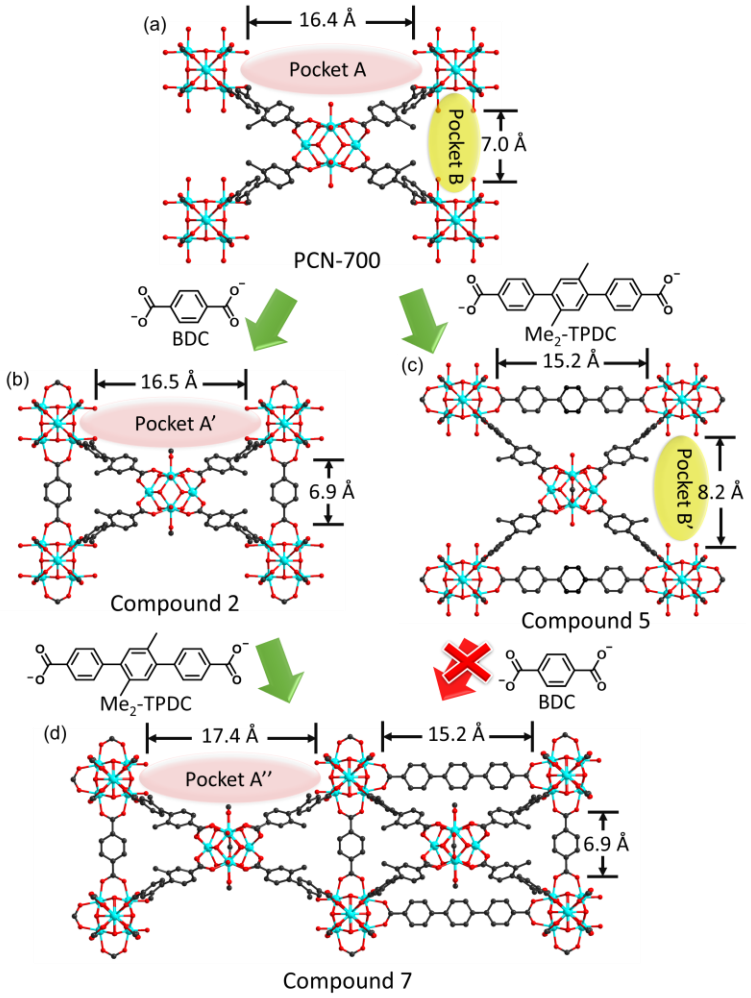

Figure 65. Single crystal structures of (a) PCN-700, (b) compound 2, (c) compound 5, (d) compound 7 resulted from linker installation of PCN-700.

4.3.5 Geometrical Prediction of Linker Installation

Previously, we have demonstrated that BDC (1,4-benzenedicarboxylate) and TPDC (2',5'-dimethylterphenyl-4,4"-dicarboxylate) can be sequentially installed into PCN-700 by reacting with terminal OH^-/H_2O ligands through an acid-base reaction.[29] PCN-700 structure shows high degree of flexibility which can adapt to the post-synthetically installed linkers. This inspires us to explore other possible combinations of linear linkers that can be installed into PCN-700.

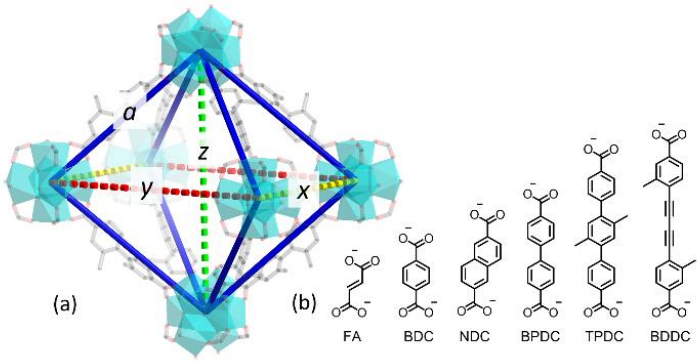

Figure 66. (a) Illustration of the octahedral cage in PCN-700; (b) linear linkers used for linker installation

Geometrical analysis is used to predict the possible combinations. A cage is taken from PCN-700 and simplified as an octahedron (Figure 66a). There are three pockets in each cage for accommodation of linear linkers, the lengths of which are denoted as *x*, *y* and *z*. The length of the original linker L8 in PCN-700, denoted as α, can be measured directly from the single crystal structure. For simplicity, the above lengths are obtained by measuring the distance between the centers of adjacent clusters. The length α is a constant (α = 18.9 Å), while *x*, *y*, and *z* are variables. An equation can be deduced from the geometrical calculation which describes the relationship between α, *x*, *y*, and *z* (Equation **1**).

$$4\alpha^2 = x^2 + y^2 + z^2 \quad \text{(Equation 1)}$$

By solving this equation, we are able to predict possible combinations of linkers that can be installed into PCN-700. Mathematically, there are infinite solutions for a ternary quadric equation. In reality, however, the length of *x*, *y* and *z* are limited by existing organic linkers. Considering the size of pockets in PCN-700, six linear linkers with different lengths were selected (Figure 66b), namely FA (fumarate), BDC (1,4-benzenedicarboxylate), NDC (2,6-napthalene dicarboxylate), BPDC (4,4'-biphenyldicarboxylate), TPDC and BDDC (4,4'-(1,3-butadiyne-1,4-diyl)bis(3-methylbenzoate)), respectively. Taking this into consideration, eleven combinations of these linkers can be installed into PCN-700 according to Equation 1, which are summarized in Table 14.

Table 14. Geometrically predicted combinations of linkers that could be installed in PCN-700.

	Length (Å)										
Number	1	2	3	4	5	6	7	8	9	10	11
x	9.1	15.4	16.8	18.9	19.0	15.7	15.4	15.4	16.8	16.8	18.9
y	25.9	24.4	23.9	23.1	23.1	24.3	23.1	24.4	23.1	24.0	23.1
z	25.9	24.4	23.9	23.1	23.1	24.3	25.6	24.4	24.8	24.0	23.1
x	FA	BDC	NDC	BPDC	-	-	BDC	BDC	NDC	NDC	BPDC
y					TPDC	BDDC	TPDC	BDDC	TPDC	BDDC	TPDC
z					TPDC	BDDC		BDDC		BDDC	TPDC

To prove our prediction, linker installation process was carried out by soaking PCN-700 crystals in the solution of linear linkers at 70 °C for 24 h. The afforded crystals were washed with fresh DMF before single crystal X-ray diffraction data collection. Single crystal to single crystal transformation is realized, hence the positions of subsequently installed linkers are unambiguously observed in the crystallographically resolved structure (Figure 67). All of the predicted MOFs are

experimentally obtained and confirmed by single crystal X-ray diffraction and powder X-ray diffraction analysis. The pristine PCN-700 structure crystallizes in tetragonal crystal system with the $P4_2/mmc$ space group. Each $Zr_6O_4(OH)_8(H_2O)_4$ cluster is connected to eight L8 linkers, giving rise to a **bcu** net. Compound **1** to **6** are formed by installation of FA, NDC, BDC, BPDC, TPDC, and DBBC into PCN-700, respectively, which contains two different linear linkers and 10-connected $Zr_6O_4(OH)_6(H_2O)_2$ clusters. Those MOFs are formulated as $Zr_6O_4(OH)_6(H_2O)_2(L8)_4L$ (L = FA, BDC, BPDC, TPDC, or DBBC) and their structures can be simplified as **bct** nets.

Sequential treatment of PCN-700 crystals with different linkers of appropriate lengths leads to the installation of two linkers. For example, installation of BPDC to PCN-700 gives rise to compound **3** which can further transform into compound **11** when treated with TPDC solution. Compound **7** to **11** are composed of three different linear linkers including one pristine linker from the framework and two post-synthetically inserted ones. They can be classified into two groups depending on the connection number of Zr_6 clusters. Compounds **7** and **9** contain 11-connected $Zr_6O_4(OH)_5(H_2O)$ clusters and possess **ela** topology. Their overall compositions can be formulated as $Zr_6O_4(OH)_5(H_2O)(L8)_4LL'_{0.5}$ (L = BDC or NDC; L' = TPDC). In these compounds, two pockets are occupied in an octahedral cage, leaving one pocket empty. The size of the unoccupied pocket doesn't match with any linkers thus no linker is installed during the treatment. Compound **8**, **10** and **11** contain 12-connected $Zr_6O_4(OH)_4$ cluster, can be formulated as $Zr_6O_4(OH)_4(L8)_4LL'$ (L = BDC, NDC, or BPDC; L' = TPDC or DBBC). The overall structure can be simplified into a 12-connected net with a point symbol of $\{3^{24}.4^{28}.5^{13}.6\}$.[155] In these compounds, the size of two linkers perfectly matches with the size of pockets in PCN-700 so that all the pockets in the octahedral cage are occupied. Mathematically, the size of the linkers in compounds **8**, **10** and **11** satisfy Equation **1** and $y = z$ simultaneously. The composition of compound **1** to **11** was determined by

single crystal X-ray diffractions and confirmed by ^{1}H-NMR of digested samples. Linker installation is necessary for the synthesis of compound **1** to **11.** We attempt to synthesize mixed linker Zr-MOFs starting from a combination of L8 and other linear linkers through a one-pot synthetic approach; however, a mixture of PCN-700 and UiO phases are usually obtained. In the one-pot synthesis, the competitive formation of different products makes it exceedingly challenging to achieve mixed linker MOFs.

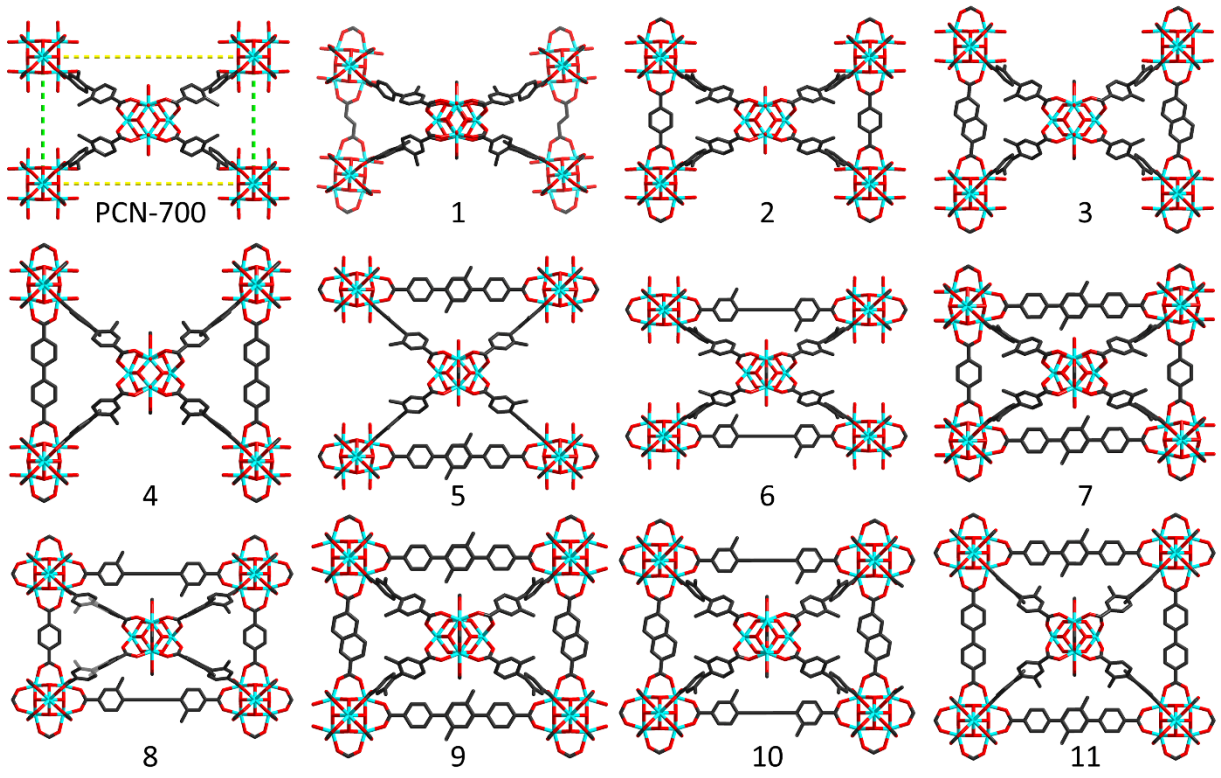

Figure 67. Single crystal structures of eleven geometrically predicted MOFs resulted from linker installation of PCN-700.

The flexibility of PCN-700 plays an important role in linker installation. The unit cell parameters along *c* axis vary from 11.8 Å to 19.1 Å in different compounds, allowing for structural adaptation corresponding to the installed linkers. The installed linkers also possess certain flexibility, which ensures the installation of two linkers even though their lengths do not strictly

match with the calculation. For example, the lengths of BDDC are 16.4 and 16.1 Å in compounds **7** and **10**, respectively, so that BDDC can pair with both BDC and NDC. In light of the ubiquity of linker installation method, a variety of promising applications can be envisioned in PCN-700 platform.

4.3.6 Engineering the Pore Environment by Linker Installation

Linker installation is a unique strategy to control the MOF porosity by incorporation of different linkers or a combination thereof. The installed linkers affect the shape and size of MOF cavities which in turn influence their sorption properties. Furthermore, linkers can be precisely placed at determined channels within the crystalline lattice, and thus the opening and closing of each cavity can be controlled. Consequently, an engineered pore architecture can be realized.[46-47]

The N_2 adsorption measurements were carried out for PCN-700 and compound **1** to **11** in order to investigate the influence of different linkers on the MOF porosity (Figure 68a and b). The N_2 sorption isotherms indicate that the porosity of PCN-700 is well maintained and precisely controlled during linker installation. The lengths of the installed linkers along *a*-axis directly correlate to the MOF porosity as proved by the total N_2 uptake. The channel size along *a*-axis is precisely controlled by the size of installed linkers. The length of FA (4.95 Å) is shorter than the distance between adjacent Zr_6 clusters in pristine PCN-700-Me_2 (6.98 Å) so that the installation of FA squeezes the structure. The installation of BDC linker did not change the unit cell parameter by a large amount, whereas the NDC and BPDC open up the MOF cavity along *a*-axis. With gradually increased length of linear linkers, the N_2 total uptake increased from 328 (compound **1**) to 638 cm^3g^{-1} (compound **3**). With installed linkers occupying the free space inside the MOF cavity, compound **1** to **11** seems to have reduced porosity and decreased N_2 uptake. However, a carful overview of the structures of each compound reveals that the MOF porosity could increase

by careful selection of linkers. A linker with proper length can open up the MOF cavity along *b* direction which results in a dramatic swell in unit cell volume and therefore increase of porosity. For example, the N_2 uptake of PCN-700 is enhanced by 33.4% after BPDC installation, meanwhile the cell volume increased by 17.4%. The installation of TPDC and BDDC does not further increase the pore volume as they occupy different cavities compared with BPDC. Therefore, the installation of BPDC resulted in the largest enhancement of porosity.

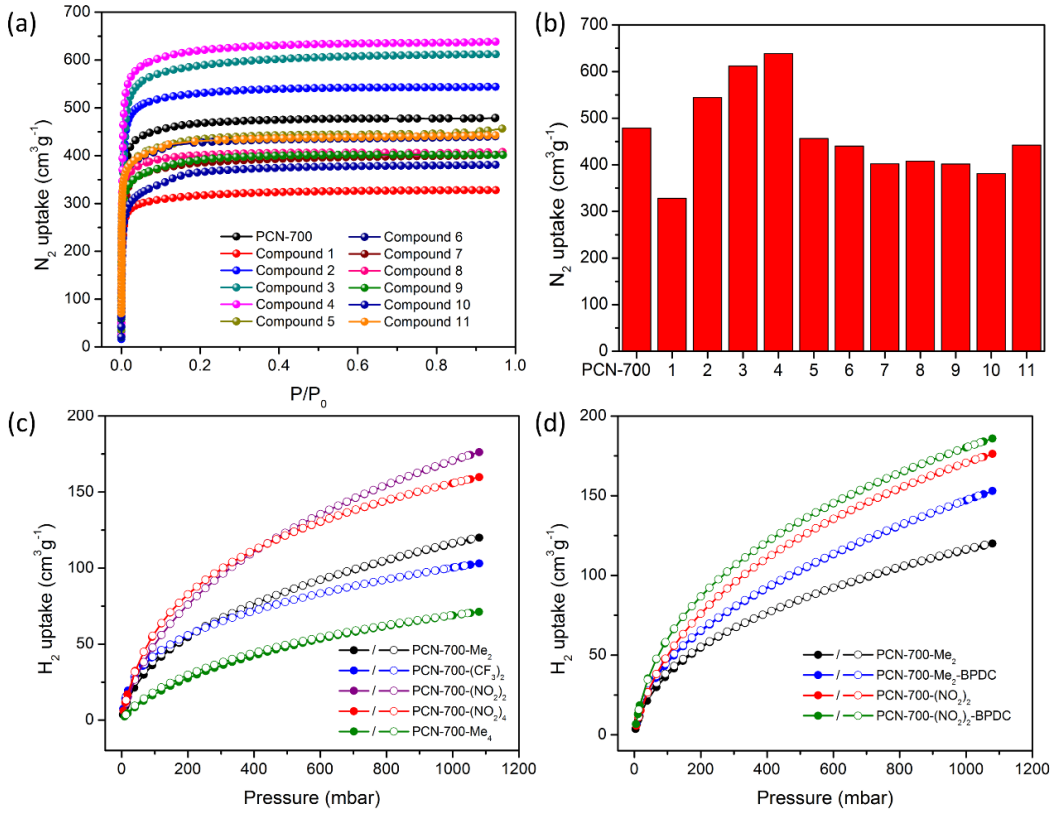

Figure 68. (a) N_2 adsorption isotherms of PCN-700 and compounds **1-11** at 77 K; (b) a comparison of total N_2 uptake of PCN-700 and compounds **1-11** demonstrating the control of pore volume by linker installation; (c) H_2 adsorption-desorption isotherms of PCN-700 decorated with different functional groups at 77 K; (d) H_2 adsorption-desorption isotherms of PCN-700 with different functional groups and installed linkers at 77 K showing the synergistic effect of linker installation and linker functionalization.

The pore environment of PCN-700 can be decorated by functionalized linkers. The H_2 adsorption isotherms illustrate the beneficial effect of different functional groups on the pore environments and therefore the MOF properties. For example, the replacement of methyl groups with nitro groups on the primary linker of PCN-700 increases its H_2 adsorption capacities by 47% (Figure 68c). Systematic variation of the pore volume and decoration of pore environment have synergistic effect on the adsorption behavior. A certain combination of linkers (PCN-700-$(NO_2)_2$-BPDC) display increases in their H_2 adsorption capacities of 57% compared to that of the parent framework (PCN-700-Me_2) (Figure 68d).

4.3.7 Size-selective Catalytic System Built through Linker Installation

PCN-700 demonstrates a nearly ideal platform for systematic modulation of pore volume and pore environment by judicious selection of linkers. This leads to a highly tunable multifunctional MOF system which is capable of complex functional behavior. Herein, we show that a size-selective catalytic system for aerobic alcohol oxidation reaction can be built in PCN-700 through the sequential installation of BPYDC(Cu) (Figure 69b) and TPDC-R_2 (Figure 69c). The BPYDC(Cu) moiety act as the catalytic active center while the TPDC-R_2 with different substituents, controls the selectivity of substrates (Figure 69a). Two components within the cavity of PCN-700 work synergistically as a size-selective catalyst for the aerobic alcohol oxidation (Scheme 8).

Conversion of alcohols to aldehydes and ketones is among the most important and widely used class of oxidation reactions in organic chemical synthesis and industry.[30, 156-158] The aerobic alcohol oxidation promoted by (bpy)Cu catalyst, has been reported in the literature as a particularly versatile and effective method (bpy = 2,2'-bipyridine).[159-160] The immobilization of the (bpy)Cu

catalyst in MOFs offers several advantages over the homogeneous systems, such as easy catalyst separation and recovery, regeneration, and handling. In addition, the well-defined pores of MOF catalysts may favor shape and size selectivity which is difficult to realize in homogeneous catalysts. For catalytic applications, PCN-700 provides unique advantages since its pore size can be tuned by the installation of different linkers, giving rise to a controllable size-selective catalytic system. This incentivizes us to immobilize (bpy)Cu catalyst in PCN-700 and, at the same time, tune the size-selectivity via linker installation.

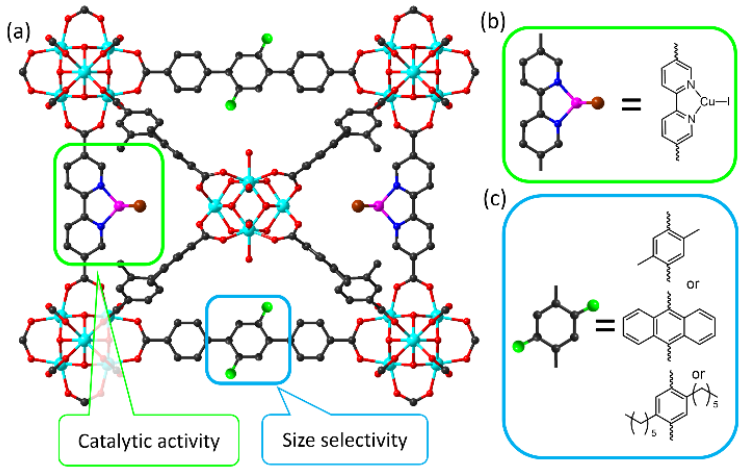

Figure 69. (a) The size-selective catalytic system for aerobic alcohol oxidation reaction built in PCN-700 through linker installation; (b) and (c) Structure of catalytic center and size selective moiety. Coordinated CH_3CN on the Cu is removed for clarity.

The PCN-700-BPYDC(Cu)-TPDC system was assembled *via* stepwise linker installation and metalation. First, the BPYDC and TPDC-R_2 were sequentially installed by treating PCN-700 crystals with solutions of BPYDC and TPDC-R_2 in DMF at 75 °C. PCN-700-BPYDC-TPDC-R_2 bears open bipyridine sites that readily react with CuI in acetonitrile to form the metalated framework. The single crystal structure of PCN-700-BPYDC(Cu)-TPDC-R_2 clearly shows the existence and position of BPYDC(Cu) and TPDC-R_2 components within the framework. The

coordination environment of Cu^+ is clearly determined in the single crystal structure, which provides direct structure evidence of the catalytic center. According to the crystal structure, the Cu^+ center is chelated by a bipyridine group and further coordinated with an N from acetonitrile and an I^- ion as counterion. PCN-700 is an inherent crystalline platform allowing for the metalations to occur quantitatively without appreciable loss of crystallinity, thereby enabling examination of the catalytic center by single-crystal X-ray diffraction. The Cu^+ center is arranged around the 1D channel along *c*-axis whereas the TPDC-R_2 controls the accessibility of the Cu^+ center by partially blocking the channels. Therefore, the size-selectivity of the whole material can be tuned by changing the size of substituents on the TPDC-R_2 linker. To evaluate our hypothesis, the TPDC-R_2 linker was functionalized by methyl group, phenyl group and hexyl group, respectively, which is expected to result in different selectivity towards the substrates.

Scheme 8. Aerobic oxidation of alcohol by using BPYDC(Cu) functionalized PCN-700.[a]

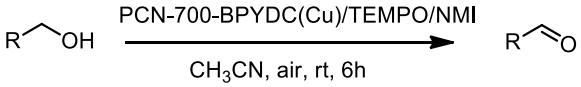

The catalytic performance of PCN-700-BPYDC(Cu)-TPDC-R_2 system in the oxidation of various alcohols with different molecular sizes were evaluated. As shown in Figure 70, alcohols were converted to corresponding aldehyde in good yields and high selectivity for homogenous reference, regardless of the molecular size. The yield of benzaldehyde catalyzed by PCN-700-BPYDC(Cu) is as high as the homogeneous reference, suggesting the high accessibility and activity of the (bpy)Cu moiety within the MOF cavity. Indeed, the size of benzyl alcohol (~4.3 Å) is much smaller than the channel size of PCN-700-BPYDC(Cu) (~14 Å), which allows for efficient diffusion of the substrate. The increase of the aromatic rings on alcohol decreases yields of the

corresponding aldehydes under the same condition, showing a clear size-selectivity. The 9-anthracenemethanol shows a relative low yield (24%) catalyzed by PCN-700-BPYDC(Cu), perhaps resulted from the large molecular size (9.2 Å) which limits the diffusion rate of substrate and the accessibility of catalytic centers.

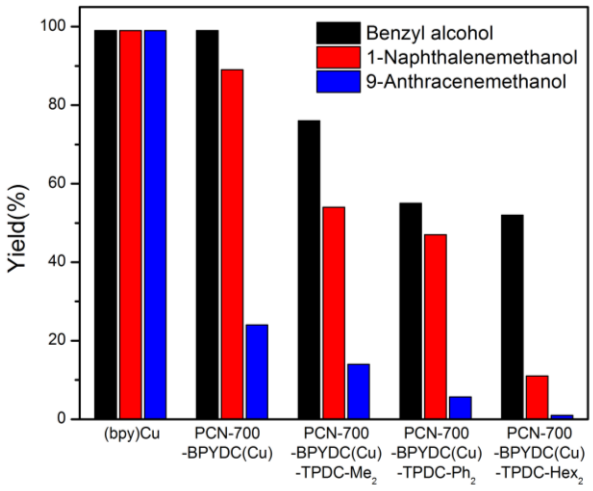

Figure 70. Size selective alcohol aerobic oxidation using PCN-700 installed with different linkers. Reaction condition: alcohol (0.5 mmol), catalyst (0.005 mmol based on Cu), TEMPO (0.05 mmol), N-methylimidazole (NMI, 0.05 mmol), CH_3CN (5.0 mL), ambient air, room temperature, 6 h. Yields were determined by ^{1}H-NMR analysis and calculated based on the ratios of product/(product + starting material).

By installation of TPDC with different functional groups into PCN-700-BPYDC(Cu), the size-selectivity can be fine-tuned. The TPDC partially blocks the channel along the *c*-axis, which affects the diffusion of substrate as well as the accessibility of the Cu^+ center. By increasing the size of substituents on TPDC linker, the yields of the alcohol conversion are dramatically decreased, especially for bulky substrates (Figure 70). With TPDC-Hex_2 installed, the 9-anthracene alcohol is almost excluded by the small MOF cavity, which explains the lowest yield (<1%). The guest-selective alcohol oxidation reaction suggested that the catalytic reaction

occurred exclusively in MOF cavity, whereas the external surface of the MOF crystal was only responsible for very limited conversion of alcohols. Based on the experimental result and literature, a simplified mechanism is proposed for the aerobic alcohol oxidation reaction catalyzed by PCN-700-BPYDC(Cu). To evaluate the recyclability, PCN-700-BPYDC(Cu) catalyst was simply separated from the mixture at the end of the reaction by centrifuge and reused for the next reaction. The catalytic activity was well-maintained after three cycles. PCN-700 can be functionalized with various catalysts by judicious selection of chelating linkers and metal precursor, allowing the development of heterogeneous catalysts with unprecedented degree of control. PCN-700 system also serves as an inherent crystalline platform, possibly facilitating the observation of catalytic center and reaction intermediates by single-crystal X-ray diffraction to gather fundamental insight into metal-catalyzed reactions.

4.4 Conclusions

In summary, we present a comprehensive study on the linker installation method. First, kinetic analysis is adopted to construct a MOF with inherent missing linker sites, namely PCN-700. Twelve linkers with different substituents are designed to study the size effect of functional groups on the linkers. Guided by the geometrical analysis, linkers with different lengths and combinations thereof were sequentially installed into a parent PCN-700, giving rise to eleven new MOFs, and each bearing up to three different functional groups in predefined positions. The pore environments of the PCN-700 system were engineered by tuning the sizes and functionalities of installed linkers. Systematic variation of the pore volume and decoration of pore environment resulted in synergistic effects including an enhancement of H_2 uptake to 57%. Besides, a size-selective catalytic system for aerobic alcohol oxidation is built in PCN-700 through linker installation, which shows high activity and tunable size-selectivity. These results highlight the

unique potential of the linker installation method to decorate pore environment of MOF with multiple functional groups in a highly designed manner. In light of the ubiquity of Zr-MOFs with coordinately unsaturated Zr_6 clusters, we believe that linker installation is a versatile strategy to synthesize stable MOFs with unprecedented multi-functionality.

5. HETEROMETAL EXPANSION OF ZR-MOFS BY CLUSTER METALATION*

5.1 Introduction

Transition metal cluster complexes have been widely studied for their structures, bonding interactions and applications in catalysis and magnetism.[161-162] Recently, heterometallic multinuclear clusters have attracted increasing attention due to the interesting ligand dynamics and synergistic effects between different metal species.[163-165] Compared to the conventional metal oxide mixtures, the stoichiometry of metal species in heterometallic clusters can be controlled on the atomic scale. However, when deposited onto porous supports, aggregation of these nanoclusters often occurs at elevated temperatures.[166] Thus, it is urgent to discover new materials with well-separated nanoclusters and controllable stoichiometry of metal species on the molecular level. In this sense, metal-organic frameworks (MOFs) constructed with isolated metal clusters and organic struts are ideal candidates for the employment of heterometallic clusters.[10, 75, 167] Divalent-metal-containing MOFs have been extensively studied for their exceptional porosity and potential applications in gas storage/separation, catalysis and magnetics.[8-10, 123, 168-169] However, their practical applications are hampered by their sensitivity to ambient moisture.[170] Therefore, researchers in recent years have been concentrating on the development of Zr-MOFs, which tend to possess much greater stability due to the strength of the Zr-O bonds and high connectivity of the Zr_6 clusters.[16, 171-172] The exceptional chemical stability of Zr-MOFs has made them a suitable

*Reproduced in part with permission from: Yuan, S.; Chen, Y. P.; Qin, J.; Lu, W.; Wang, X.; Zhang, Q.; Bosch, M.; Liu, T. F.; Lian, X.; Zhou, H. C., Cooperative Cluster Metalation and Ligand Migration in Zirconium Metal‐Organic Frameworks. *Angew. Chem. Int. Ed.* **2015,** *54* (49), 14696-14700. Copyright 2015 by Wiley-VCH Verlag GmbH & Co. KGaA.

platform for the investigation of various applications.[110, 173-175] Yet, the underlying functionality of Zr-MOFs is less diversified as opposed to low-valent metal based MOFs. First, the open metal sites in many Zr-MOFs are not accessible to guest molecules, which hurts their potential in gas storage applications, as open metal sites are deemed to be a significant contributor to the gas adsorption enthalpy.[176] Second, multiple redox states are responsible for many catalytic properties; the catalytic reactions driven by Zr-MOFs are largely restricted within Lewis acid catalysis because of the redox inert nature of Zr^{4+}.[177] In addition, the diamagnetic property of Zr^{4+} also limits its magnetic applications.

Efforts have been made to functionalize Zr-MOFs with other transition metals by incorporating the active metal species on the nodes of Zr-MOFs. An intuitive approach is to directly construct a MOF from a bimetallic cluster which contains zirconium as structural support and other transition metals as active sites. The one pot synthesis of bimetallic M-Zr-MOFs (M = 3d metal) has been attempted extensively in our lab, but to no avail. As an alternative approach, bimetallic MOFs can be realized by post-synthetic metal exchange or metalation of Zr_6 cluster. Cohen and coworkers reported a titanium-containing analogue of UiO-66 (Ti-UiO-66) synthesized by post-synthetic metal exchange of Zr^{4+} with Ti^{4+}, which was later on revealed to exhibit photocatalytic activity.[109, 178-180] The Hupp group demonstrated that the -OH ligands on the Zr_6 nodes of UiO-66 can be metalated with redox-active V^{5+} ions to produce V-UiO-66 for catalysis.[58] However, despite all these efforts, it is still an elusive goal to obtain the precise structural information of post-incorporated metals because of the disordered distributions and low occupancy of the post-synthetically incorporated metal ions.

Single-crystal X-ray diffraction (SCXRD) is a powerful and ubiquitous technique to definitively elucidate structures at the molecular level.[181-182] It has been widely used to determine

static structures as well as provide direct evidence of consecutive chemical transformations. Utilizing this technique, Doonan and coworkers have recently been able to solve the precise coordination environments of metals on metallo-linkers in MOFs.[183] This prompted us to study the cluster transformation during the metalation in a crystalline Zr-MOF matrix *via* SCXRD. Herein, we report the synthesis of two bimetallic MOFs by performing post-synthetic cluster metalation on PCN-700, a Zr-MOF with 8-connected $Zr_6O_4(OH)_8(H_2O)_4$ clusters. SCXRD unambiguously shows that a $Zr_6M_4O_8(OH)_8(H_2O)_8$ (M = Co, Ni) cluster is formed as a result of the reaction between M^{2+} (M = Co, Ni) and OH^-/H_2O ligands on the $Zr_6O_4(OH)_8(H_2O)_4$ cluster. Interestingly, ligand migration is observed concurrently with cluster metalation, in which the ligand dissociates itself from the vertex zirconium atom and bonds to the post-incorporated metal. Single crystallinity is preserved throughout the process so that the structural transformation is recorded by successive SCXRD measurements. This is the first time that a zirconium-containing bimetallic MOF with precisely defined structure has been reported. As post-synthetic cluster metalation could occur on Zr_6 clusters with reduced connectivity, we believe that it will be a general strategy to synthesize bimetallic MOFs containing isolated heterometallic clusters with well-defined structures and metal contents. We anticipate that cluster metalation will offer broad opportunities for a variety of applications including catalysis, gas adsorption, and magnetics. This work also sheds light on the possible mechanism of the cluster transformation process, which is of great importance for the design of functionalized MOFs with high chemical stability.

5.2 Experimental Section

5.2.1 Materials and Instrumentation

All reagents and solvents were commercially available and used as received. Powder X-ray diffraction (PXRD) was carried out with a BRUKER D8-Focus Bragg-Brentano X-ray Powder

Diffractometer equipped with a Cu sealed tube (λ = 1.54178) at 40 kV and 40 mA. Nuclear magnetic resonance (NMR) data were collected on a Mercury 300 spectrometer. Gas sorption measurements were conducted on a Micrometritics ASAP 2020 system.

5.2.2 MOF Syntheses

Synthesis of PCN-700. $ZrCl_4$ (100 mg), H_2Me_2-BPDC (100 mg), trifluoroacetic acid (1.0 ml) and DMF (30 mL) were charged in a Pyrex vial. The mixture was heated in 120 ºC oven for 72 h. After cooling down to room temperature, the colorless crystals of PCN-700 were harvested (105 mg, yield: 68%).

Synthesis of PCN-800(Ni). PCN-700 (50 mg), $Ni(NO_3)_2 \cdot 6H_2O$ (500 mg) and DMF (18 mL) were charged in a Pyrex vial. The mixture was heated in 85 ºC oven for 48 h. The pale green crystals of PCN-800(Ni) were collected by filtration and washed with fresh DMF three times. (55 mg, yield: 92%). Alternatively, a mixture of PCN-700 (50 mg), $Ni(NO_3)_2 \cdot 6H_2O$ (500 mg), DMF (18 mL), and Et_3N (0.1 mL) was heated in 85 ºC oven for 6 h. The pale green crystals of PCN-800(Ni) were collected and washed with fresh DMF three times (56 mg, yield: 94%).

Synthesis of PCN-800(Co). PCN-700 (50 mg), $Co(NO_3)_2 \cdot 6H_2O$ (500 mg) and DMF (18 mL) were charged in a Pyrex vial. The mixture was heated in 85 ºC oven for 48 h. The purple crystals of PCN-800(Co) were collected by filtration and washed with fresh DMF three times. (56 mg, yield: 94%). Alternatively, a mixture of PCN-700 (50 mg), $Co(NO_3)_2 \cdot 6H_2O$ (500 mg), DMF (18 mL), and Et_3N (0.1 mL) was heated in 85 ºC oven for 6 h. The purple crystals of PCN-800(Co) were collected and washed with fresh DMF three times (57 mg, yield: 95%).

Synthesis of PCN-800(In). PCN-700 (50 mg), $InCl_3$ (500 mg) and DMF (18 mL) were charged in a Pyrex vial. The mixture was heated in 85 ºC oven for 48 h. The colorless crystals of PCN-800(In) were collected by filtration and washed with fresh DMF three times. (58 mg, yield:

97%). The Zr/In ratio was determined by SEM-EDX (1.69) and ICP-MS (1.73) which matched the theoretical ratio (1.50).

Capture of Intermediate. The intermediates during the single crystal to single crystal transformation process were captured by sequential sampling over the reaction time. PCN-700 crystals (200 mg), $Ni(NO_3)_2 \cdot 6H_2O$ (2 g) and DMF (72 mL) were charged in a Pyrex vial. The mixture was heated in 85 ºC oven and sampled at 2, 6, 12, 24, and 48h. The samples are designated as **Compound 2, 3, 4, 5** and **6**, respectively. Each time, about 40 mg of sample was taken out along with around 15 mL of solution. The samples were washed with fresh DMF three times and characterized by single crystal X-ray diffraction analysis, powder X-ray diffraction analysis, energy dispersive X-ray analysis, and inductively coupled plasma mass spectrometry.

5.2.3 Single Crystal X-Ray Crystallography

All crystals were taken from the mother liquid without further treatment, transferred to oil and mounted into a loop for single crystal X-ray data collection. Diffraction was measured on a Bruker D8 Venture or D8 Quest diffractometer equipped with a Cu-Kα (λ = 1.54184 Å, graphite monochromated) or Mo-Kα sealed-tube X-ray source (λ = 0.71073 Å, graphite monochromated). The raw frame data were processed using SAINT and SADABS to yield the reflection data file.[1] The structure was solved using the charge-flipping algorithm, as implemented in the program *SUPERFLIP*[2] and refined by full-matrix least-squares techniques against F_o^2 using the SHELXL program[3] through the OLEX2 interface.[4] The hydrogen atoms from the linkers were placed geometrically and refined using a riding model. The refinement of the framework was performed by ignoring the contribution of the disordered solvent molecules. The region containing the disordered electron density was identified by considering the van der Waals radii of the atoms constituting the ordered framework. Platon SQUEEZE[5] was used and .fab file was created

containing partial structure factors representing the SQUEEZE region. The appropriate partial structure factors were used for input to SHELXL with the ABIN instruction. The ABIN instruction reads *h, k, l, A* and *B* from the file name fab, where *A* and *B* are the real and imaginary components of a partial structure factor.[3]

Refinement Details of 2. Diffraction frames were integrated in Tetragonal P by APEX2, and *XPREP* also agreed this Bravais lattice (R(sym)=0.135). It suggested that 4_2 screw axis and *c*-glide plane should be taken based on statistics of systematic absence, and $P4_2/mmc$ was the best candidate with lowest CFOM factor (38.50). All atoms were easily found by direct method, building a PCN-700 framework. The strong residues were assigned as O1S, O2S, O3S and Ni1, which form an octahedral geometry with O4. The occupancy of the octahedral additional unit was refined to converge with the occupancy of 11.95% (12% in CIF for simplicity); understandably there are total 0.48 Ni attached to one Zr_6 cluster. Note that the neighboring two octahedral units are symmetric disorders of the Ni attachment. When one Ni1 group is present, the other Ni1 group symmetrically generated close to it must disappear. We obtained that R1 is 0.1168 before *SQUEEZE* treatment and 0.0739 after *SQUEEZE* treatment. The squeezed void volume was 5563 $Å^3$, equivalent to 63.6% of the unit cell.

Refinement Details of 3. Similar to structure **2**, $P4_2/mmc$ was the best candidate with lowest CFOM factor (36.35) to describe this structure. The electron density was intense to construct a PCN-700 framework. After appropriate geometry restraints to the ligands (Me_2-BPDC), it showed relatively huge thermal ellipsoids; thus, a split ligand was included in the model with occupancy of 80.04% for the one coordinated to the Zr_6 cluster and 19.96% for the other one coordinated to the attached Ni1S unit (set 80% and 20% in final refinement for simplicity). The Ni1S accompanying O11S was connected to O1S and O2S on the Zr_6 cluster and partially

coordinated by the second disorder part of the ligand. The occupancy of the Ni1S unit (Ni1S+O11S) was refined toward 24%. On the other hand, the Ni2S accompanying O22S, O23S, and O24S also form an octahedral geometry with O2S, similar to the situation of structure **2**. The occupancy of the Ni2S unit (Ni2S+O22S+O23S+O24S) was refined toward 6.4%, making the size of the thermal ellipsoids comparable to that of the Ni1S unit. Accordingly, there are total 1.22 Ni attached to one Zr_6 cluster. Note that the Ni1S unit and the Ni2S unit should not be present at the same time. We made a hypothesis that Ni2S unit is the initial state and the Ni1S unit is the final state of the metal attachment process.

After fixing geometry of the ligands and the two attached Ni parts, R1 value is 0.1564 without *SQUEEZE* treatment and 0.0926 with *SQUEEZE* treatment. The squeezed void volume was 5420 $Å^3$, equivalent to 58.0% of the unit cell.

Refinement Details of 4. Similar to structure **3**, the space group $P4_2/mmc$ was selected to describe this structure. After fixing geometry of the ligands (Me_2-BPDC), two disorder parts of the ligand was modelled with occupancy of 65.74% for the one coordinated to the Zr_6 cluster and 34.26% for the other one coordinated to the attached Ni3 unit. The Ni3 accompanying O7S was connected to O1S and O2S on the Zr_6 cluster and partially coordinated by the second disorder part of the ligand. The occupancy of the Ni3 unit (Ni3+O7S) was refined toward 44.92%. Accordingly, there are total 1.84 Ni attached to one Zr_6 cluster.

With the help of EADP restraints to all disorder parts of the ligand, we obtained that R1 is 0.2064 before *SQUEEZE* treatment and 0.1020 after *SQUEEZE* treatment. The squeezed void volume was 5628 $Å^3$, equivalent to 60.2% of the unit cell.

Refinement Details of 5. Differing from the structures described above, *XPREP* suggested that 4_2 screw axis and *n*-glide plane should be taken based on statistics of systematic absence, and

*P*4$_2$/*n* was the only candidate. All atoms were roughly found by direct method. After that, *PLATON* addsym unit were performed to find the additional symmetry in the structure and suggest the new space group be *P*4$_2$/*ncm*. The attached Ni unit (Ni4+O26S) was supposed to fully coordinate with O23S and O24S on the Zr_6 cluster and completely coordinated by the first disorder part of the ligand (O1, O2, C1~C18). Accordingly, there are total 4 Ni attached to one Zr_6 cluster. The two disorder parts of the ligand were modelled with occupancy of 45.91% and 54.09% respectively. However, we did not split the O20S into two disorder parts because there is the carboxylate disorder occupying the same position (O11'). The atom O20S should rotate around the Zr2-Zr2 axis of the Zr_6 octahedral cluster, thus leading to higher ADP max/min ratio.

With the help of geometry restraints and EADP control to all disorder parts of the ligand, we obtained that R1 is 0.2372 before *SQUEEZE* treatment and 0.1177 after *SQUEEZE* treatment. The squeezed void volume was 11042 $Å^3$, equivalent to 58.9% of the unit cell.

Refinement Details of 6 (PCN-800(Ni)). Diffraction frames were integrated in Tetragonal P by APEX2, and *XPREP* also agreed this Bravais lattice (R(sym)=0.091). $P\bar{4}$ was selected to describe this structure (lowest CFOM factor 14.92). After most atoms were easily found by direct method, *PLATON* addsym unit were performed to find the additional symmetry, suggesting the new space group be *P*4$_2$/*mmc*. Similar to **5**, the attached Ni unit (Ni3+O13) was supposed to fully coordinate with O15 and the ligand (Me_2-BPDC), showing reasonable thermal ellipsoids compared with that of Zr atoms.

The resulting R1 value is 0.1795 before *SQUEEZE* treatment and 0.0816 after *SQUEEZE* treatment. The squeezed void volume was 6060 $Å^3$, equivalent to 66.6% of the unit cell.

For all structures, *PLATON* addsym unit were performed to find the additional symmetry. All ligands were fixed with reasonable geometry; the enormous thermal ellipsoids were refined

with the help of EADP restrains. All non-dangling and non-hydrogen atoms were refined with anisotropic displacement parameters during the final cycles, whereas organic hydrogen atoms were located with isotropic displacement parameters set to 1.2 × U_{eq} of the attached atoms. The strong Q peaks were contributed to scattering of disordered solvent molecules, which were removed by using the *SQUEEZE* routine of *PLATON*; structures were then refined again using the data generated (Table 15).

Table 15. Crystal data and structure refinements.

Reaction Time	**0**	**2 h**	**6 h**	**12 h**
Name	**1 (PCN-700)**	**2**	**3**	**4**
CCDC	1036874	1062331	1062332	1062333
Formula	Zr_6 C_{64} H_{56} O_{32} $Zr_6O_8(OH)_8$ $(Me_2\text{-BPDC})_4$	$Ni_{0.48}$ Zr_6 C_{64} H_{48} $O_{33.92}$ $[Ni_4O_{16}]_{0.12}[Zr_6O_8(O)_8]$ $(Me_2\text{-BPDC})_4$	$Ni_{1.22}$ Zr_6 C_{64} H_{48} $O_{33.99}$ $[Ni_4O_4]_{0.24}[Ni_4O_{16}]_{0.06}$ $[Zr_6O_8(O)_8](Me_2\text{-BPDC})_4$	$Ni_{1.84}$ Zr_6 C_{64} H_{48} $O_{33.84}$ $[Ni_4O_4]_{0.46}[Zr_6O_8(O)_8]$ $(Me_2\text{-BPDC})_4$
Formula weight	1884.41	1935.16	1979.44	2013.81
Shape	Blocky	Cube	Cube	Cube
Color	Colorless	Colorless	Colorless	Colorless
Crystal System	Tetragonal	Tetragonal	Tetragonal	Tetragonal
Space Group	$P4_2/mmc$	$P4_2/mmc$	$P4_2/mmc$	$P4_2/mmc$
a, b(Å)	24.348(14)	24.413(5)	24.77(3)	24.77(3)
c (Å)	14.918(9)	14.683(4)	15.25(2)	15.25(2)
α,β,γ (º)	90.000	90.000	90.000	90.000
V (Å^3)	8844(7)	8751(3)	9352(18)	9352(18)
Z	2	2	2	2
T (K)	110(2)	110(2)	110(2)	110(2)
$d_{calcd.}$ (g/cm^3)	0.708	0.734	0.703	0.715
μ(mm^{-1})	0.376	0.432	0.476	0.537
F(000)	1872	1914	1956	1988
θ_{max} [deg]	25.98	27.49	26.00	26.00
Completeness	100.0%	99.8%	99.8%	99.7 %
Collected reflections	69047	59588	82307	62498
Unique reflections	4753	5455	5012	5003
Parameters	138	107	104	121
Restraints	0	1	30	44
R_{int}	0.0962	0.1293	0.1440	0.2560
$R1$ [I > 2σ(I)]	0.0417	0.0739	0.0926	0.1020
$wR2$ [I > 2σ(I)]	0.0910	0.1768	0.2570	0.2050
$R1$(all data)	0.0644	0.1077	0.1334	0.2601
$wR2$ (all data)	0.0961	0.1864	0.2832	0.2389
GOF on F^2	1.001	0.992	1.004	1.004
$\Delta\rho_{max}$/ $\Delta\rho_{min}$ [e·Å^{-3}]	0.544 / -0.440	1.263 /-2.242	1.460 /-0.963	0.987 / -0.819

Table 15. Continued.

Reaction Time	**24 h**	**48 h**	**48 h**
Name	**5**	**6 (PCN-800(Ni))**	**PCN-800(Co)**
CCDC	1062334	1062335	1062336
Formula	$Ni_4\ Zr_6\ C_{64}\ H_{48}\ O_{40}$ $[Zr_6\ Ni_4\ O_{24}]$ $(Me_2\text{-}BPDC)_4$	$Ni_4\ Zr_6\ C_{64}\ H_{48}\ O_{40}$ $[Zr_6\ Ni_4\ O_{24}]$ $(Me_2\text{-}BPDC)_4$	$Co_4\ Zr_6\ C_{64}\ H_{48}\ O_{40}$ $[Zr_6\ Co_4\ O_{24}]$ $(Me_2\text{-}BPDC)_4$
Formula weight	2239.18	2239.18	2240.06
Shape	Cube	Cube	Cube
Color	Light green	Light green	Purple
Crystal System	Tetragonal	Tetragonal	Tetragonal
Space Group	$P4_2/ncm$	$P4_2/mmc$	$P4_2/mmc$
a, *b*(Å)	34.869(8)	24.558(10)	24.66(4)
c (Å)	15.417(3)	15.079(6)	15.15(2)
α,β,γ (º)	90.000	90.000	90.000
V (Å^3)	18745(6)	9094(5)	9213(19)
Z	4	2	2
T (*K*)	110(2)	110(2)	110(2)
$d_{calcd.}$ (g/cm^3)	0.793	0.818	0.808
μ(mm^{-1})	0.750	0.773	0.715
F(000)	4416	2208	2200
θ_{max} [deg]	26.00	26.63	25.99
Completeness	99.9 %	72.9%	96.1%
Collected reflections	140615	28548	36409
Unique reflections	9436	3792	4760
Parameters	242	98	82
Restraints	80	19	3
R_{int}	0.1582	0.0876	0.2024
*R*1 [I > 2σ(I)]	0.1177	0.0816	0.1008
*wR*2 [I > 2σ(I)]	0.2875	0.1820	0.2106
*R*1 (all data)	0.1714	0.1605	0.2487
*wR*2 (all data)	0.3063	0.1983	0.2333
GOF on F^2	1.266	1.008	1.000
$\Delta\rho_{max}$/ $\Delta\rho_{min}$ [e·Å^{-3}]	1.306 / -1.746	1.451 / -0.868	0.745 / -0.903

5.2.4 Materials Characterization

Powder X-ray Diffraction. The structural transformation of PCN-700 is substantiated by powder X-ray diffraction. PCN-700 samples are immersed in a DMF solution of $Ni(NO_3)_2$ at 85 °C for 2, 6, 12, 24 ,and 48 h. The powder X-ray diffraction patterns of bulk materials are well matched with the simulated ones from single crystal X-ray diffraction data (Figures 71-76).

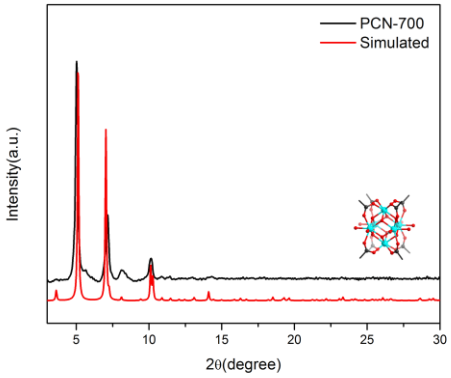

Figure 71. Powder X-ray diffraction (PXRD) patterns of PCN-700 (**Compound 1**). Insert shows the structure of cluster determined by single crystal X-ray diffraction analysis.

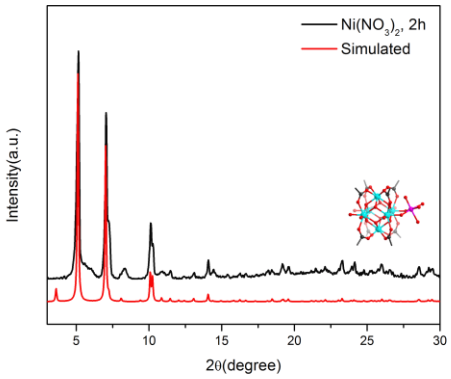

Figure 72. Powder X-ray diffraction (PXRD) patterns of PCN-700 after exposing to a DMF solution of $Ni(NO_3)_2$ at 85 °C for 2 h (**Compound 2**). Insert shows the structure of cluster determined by single crystal X-ray diffraction analysis.

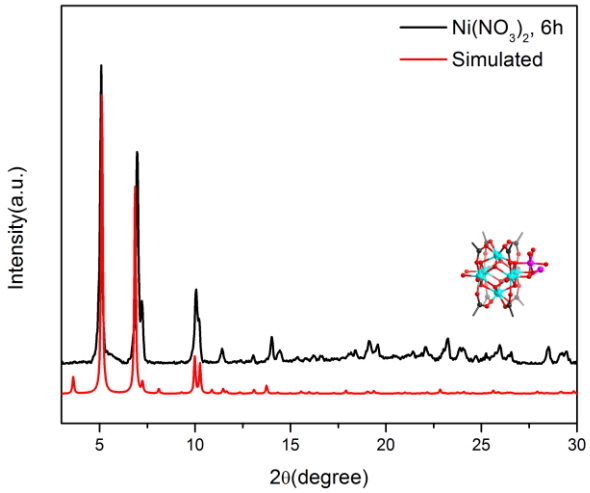

Figure 73. Powder X-ray diffraction (PXRD) patterns of PCN-700 after exposing to a DMF solution of $Ni(NO_3)_2$ at 85 °C for 6 h (**Compound 3**). Insert shows the structure of cluster determined by single crystal X-ray diffraction analysis.

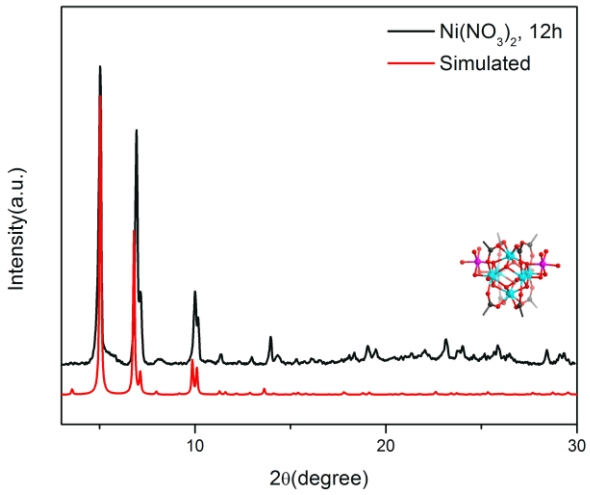

Figure 74. Powder X-ray diffraction (PXRD) patterns of PCN-700 after exposing to a DMF solution of $Ni(NO_3)_2$ at 85 °C for 12 h (**Compound 4**). Insert shows the structure of cluster determined by single crystal X-ray diffraction analysis.

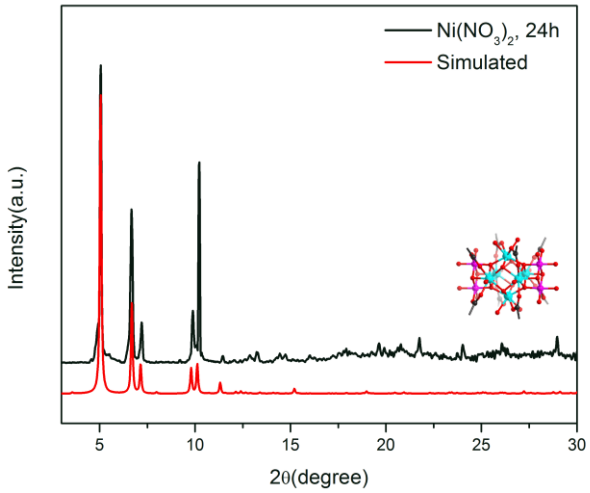

Figure 75. Powder X-ray diffraction (PXRD) patterns of PCN-700 after exposing to a DMF solution of $Ni(NO_3)_2$ at 85 °C for 24 h (**Compound 5**). Insert shows the structure of cluster determined by single crystal X-ray diffraction analysis.

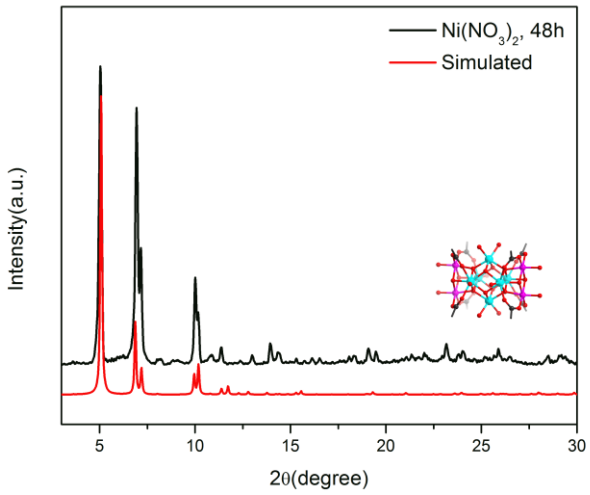

Figure 76. Powder X-ray diffraction (PXRD) patterns of PCN-700 after exposing to a DMF solution of $Ni(NO_3)_2$ at 85 °C for 48 h (PCN-800(Ni)). Insert shows the structure of cluster determined by single crystal X-ray diffraction analysis.

N_2 Sorption Isotherm. Before gas sorption experiment, as-synthesized sample was washed with *N*,*N*-Dimethylmethanamide (DMF) and immersed in acetone for three days, during which the solvent was decanted and freshly replenished three times. The solvent was removed under vacuum at 120 ^{o}C, yielding porous material. Gas sorption measurements were then conducted using a Micrometritics ASAP 2020 system (Figures 77-82).

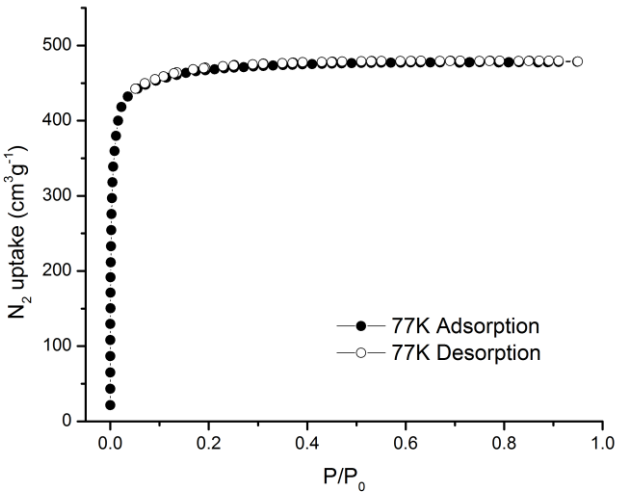

Figure 77. The N_2 sorption isotherms of PCN-700 at 77 K.

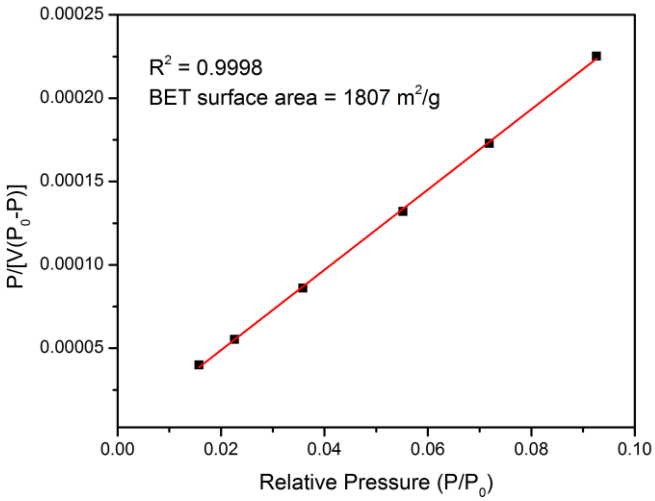

Figure 78. Plot of the linear region on the N_2 isotherm of PCN-700 for the BET equation.

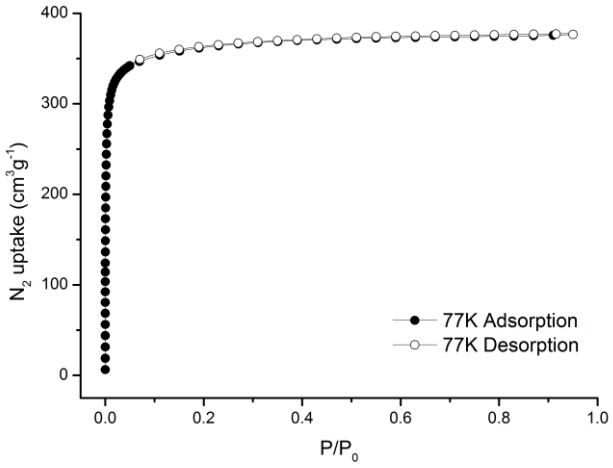

Figure 79. The N_2 sorption isotherms of PCN-800(Ni) at 77 K.

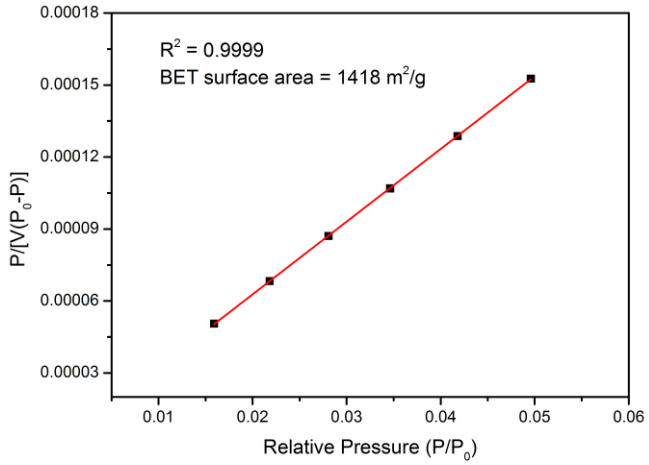

Figure 80. Plot of the linear region on the N_2 isotherm of PCN-800(Ni) for the BET equation.

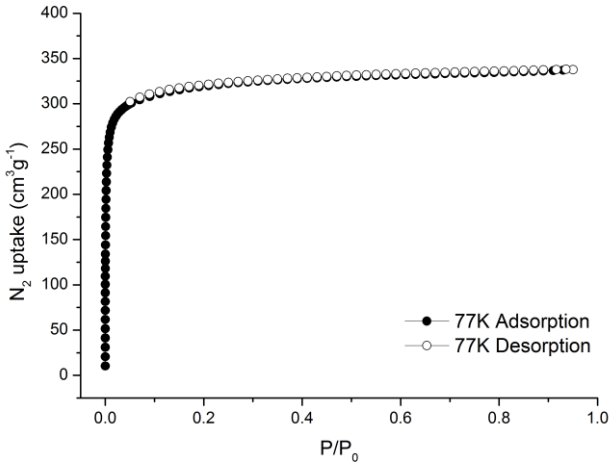

Figure 81. The N_2 sorption isotherms of PCN-800(Co) at 77 K.

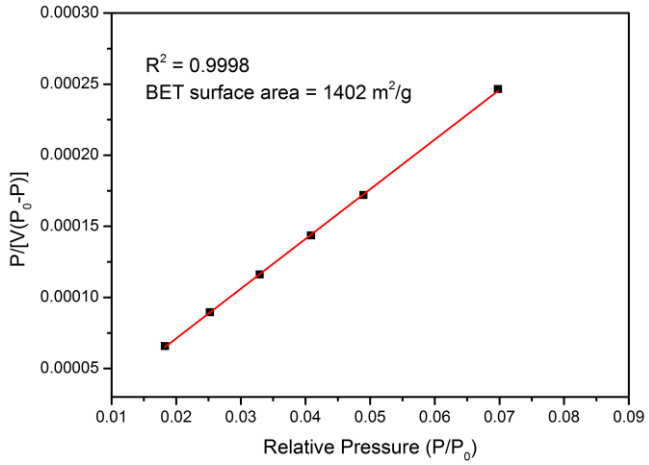

Figure 82. Plot of the linear region on the N_2 isotherm of PCN-800(Co) for the BET equation.

Thermogravimetric Analysis. PCN-700 and PCN-800(Ni) samples were activated before thermogravimetric measurement (Figure 83). For thermogravimetric analysis, about 10 mg of the sample was heated on a TGA Q500 thermogravimetric analyzer from room temperature to 700 °C at a rate of 2 °C·min^{-1} under N_2 flow of 15 mL·min^{-1}. The initial weight loss before 300 °C (8.987% for PCN-700 and 14.24% for PCN-800(Ni)) is attribute to the removal of the coordinated water molecule on the cluster which is comparable to the theoretical mass percentage (calc. 7.615% for

PCN-700 and 8.088% for PCN-800(Ni)). Both of the TGA curves indicate no mass loss before 500 °C, where decomposition of the framework starts. The mass loss corresponding to the thermal decomposition of organics is 40.33 % for PCN-700 and 55.47 % for PCN-800(Ni), which match well with the calculation (calc. 45.30% for PCN-700 and 53.32% for PCN-800(Ni)).

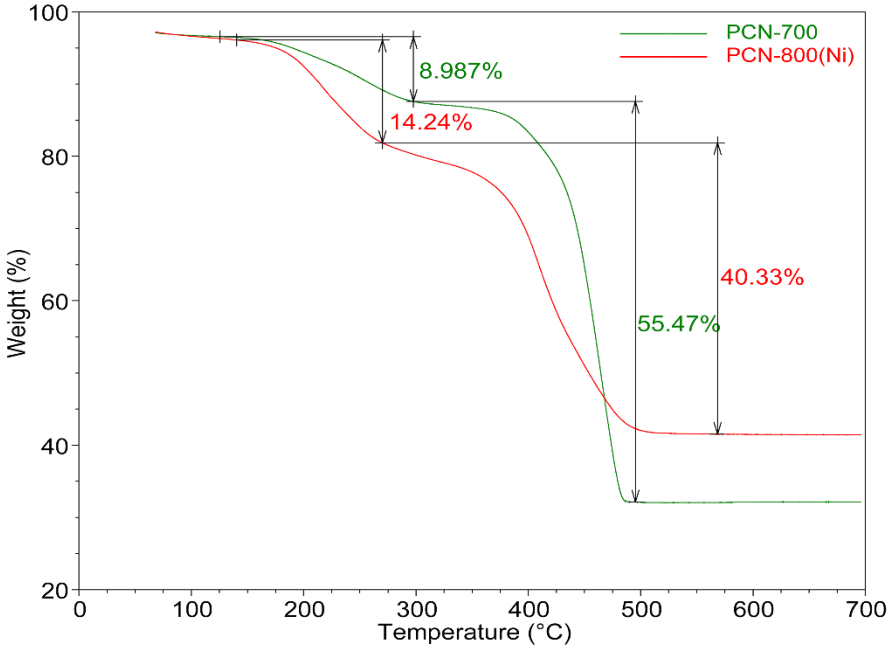

Figure 83. Thermogravimetric (TG) analyses of PCN-700 and PCN-800(Ni).

SEM/EDX Analysis. Instrumental information of SEM/EDX: Images and analyses of SEM/EDX were taken by FEI Quanta 600 FE-SEM. The Quanta 600 FEG is a field emission scanning electron microscope capable of generating and collecting high-resolution and low-vacuum images. It is equipped with a motorized x-y-z-tilt-rotate stage, providing the following movements: x = y = 150 mm (motorized); z = 65 mm (motorized); Tilt +70 degrees to –5 degrees (motorized); Source: Field emission gun assembly with Schottky emitter source. Voltage: 200 V to 30 kV. Beam Current: >100 nA.

ICP Analysis. Samples were prepared in triplicate with weights of around 3 mg. Each sample was dissolved in J.T. Baker Ultrex® II Ultrapure 70% nitric acid at 70°C for 12 hours. Samples were then diluted to 150x in 1% nitric acid and 18.2 MΩ water from Millipore Milli-Q® water purification system. Calibration standards were prepared from certified reference standards from RICCA Chemical Company. Samples were further analyzed with a Perkin Elmer NexION® 300D ICP-MS. Resulting calibration curves have minimum R^2=0.9999. Additionally, in order to maintain accuracy, quality control samples from certified reference standards and internal standards were utilized. The individual results of the triplicate samples were averaged to determine the metal ratios (Table 16).

Table 16. SEM-EDX and ICP data for compound 1~6 and PCN-800(In)

Name	**1**	**2**	**3**	**4**	**5**	**6**
Reaction time (h)	0	2	6	12	24	48
Cluster composition based on SCXRD	Zr_6	$Zr_6Ni_{0.5}$	$Zr_6Ni_{1.22}$	$Zr_6Ni_{1.84}$	Zr_6Ni_4	Zr_6Ni_4
Ni% based on SCXRD (%)	0	7.69	16.9	23.5	40.0	40.0
Cluster composition based on EDX	Zr_6	$Zr_6Ni_{0.56}$	$Zr_6Ni_{1.34}$	$Zr_6Ni_{1.54}$	$Zr_6Ni_{3.67}$	$Zr_6Ni_{3.77}$
Ni% based on EDX (%)	0	8.53	18.2	20.4	38.0	38.6
Cluster composition based on ICP	Zr_6	$Zr_6Ni_{0.51}$	$Zr_6Ni_{1.23}$	$Zr_6Ni_{1.80}$	$Zr_6Ni_{3.24}$	$Zr_6Ni_{3.86}$
Ni% based on ICP(%)	0	7.85	17.0	23.0	35.1	39.1

Catalytic Acetaldehyde Cyclotrimerization. A mixture of acetaldehyde (1 mmol) and catalyst (1 mol% In^{3+} in respect to acetaldehyde) was charged in a Pyrex vial. The mixture was stirred at room temperature for 4 h. The solvent phase was decanted and monitored by ^{1}H NMR ($CDCl_3$, 300 MHz). PCN-800(In) efficiently catalyze acetaldehyde cyclotrimerization into

paraldehyde at room temperature with conversion of 76% and selectivity up to 99% within 2 h. For comparison, no detectable amount of product was observed for pristine PCN-700 under the same condition. We further increase the reaction temperature to 100 ^{o}C for 2 h, only a small amount of crotonaldehyde as the aldol condensation product of acetaldehyde was observed (yield: ~3%). The crystallinity was maintained throughout the catalysis (Figures 84-85).

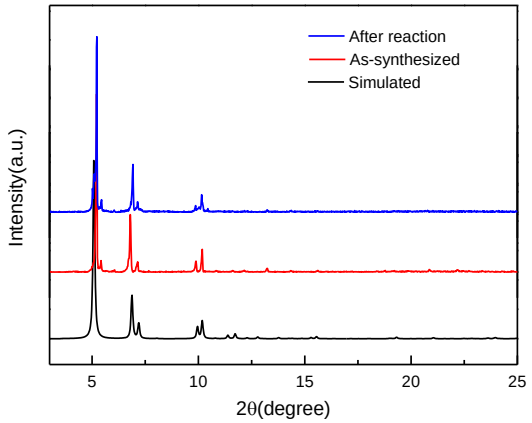

Figure 84. Powder X-ray diffraction (PXRD) patterns of PCN-800(In) before and after catalytic reaction.

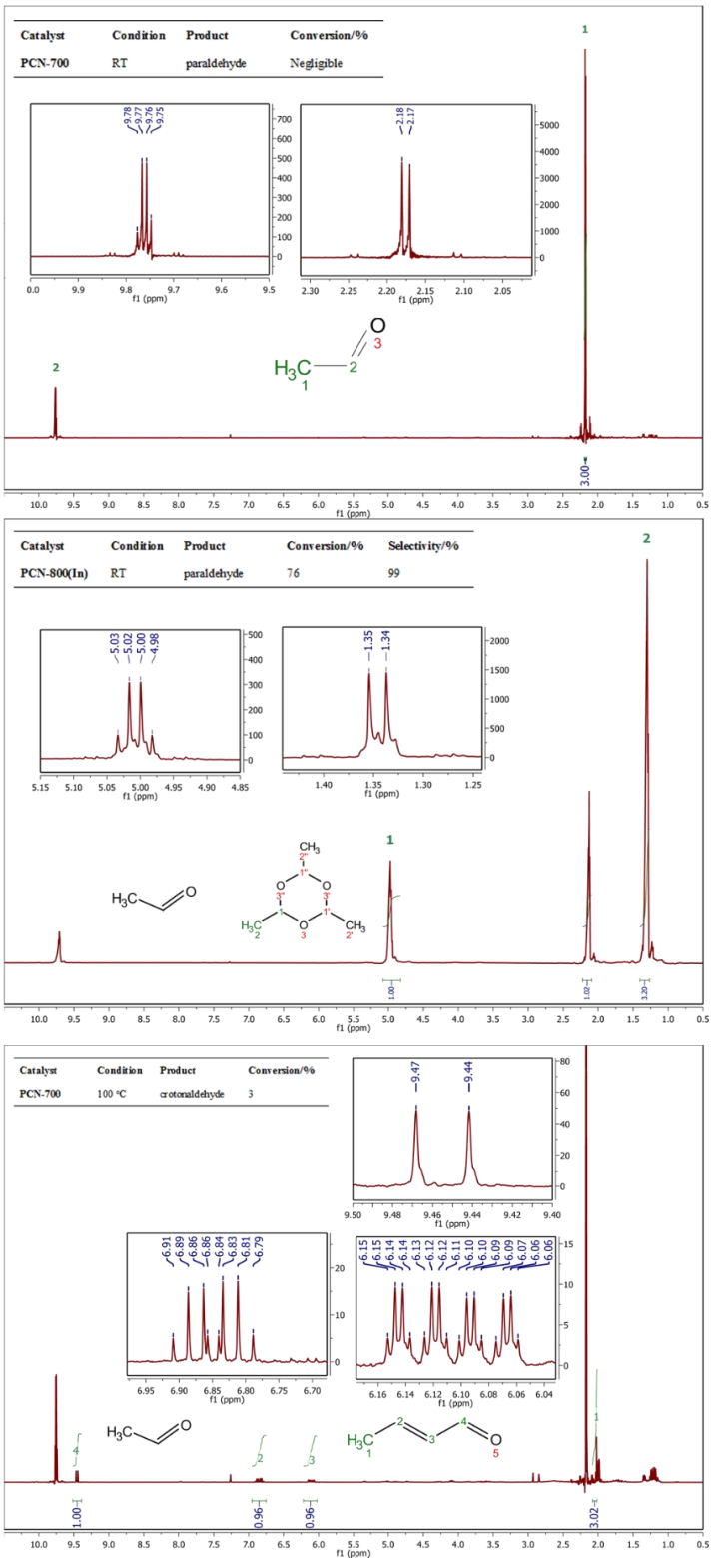

Figure 85. Acetaldehyde transformations products by ^{1}H NMR spectroscopy.

5.3 Results and Discussion

5.3.1 Cluster Metalation of PCN-700

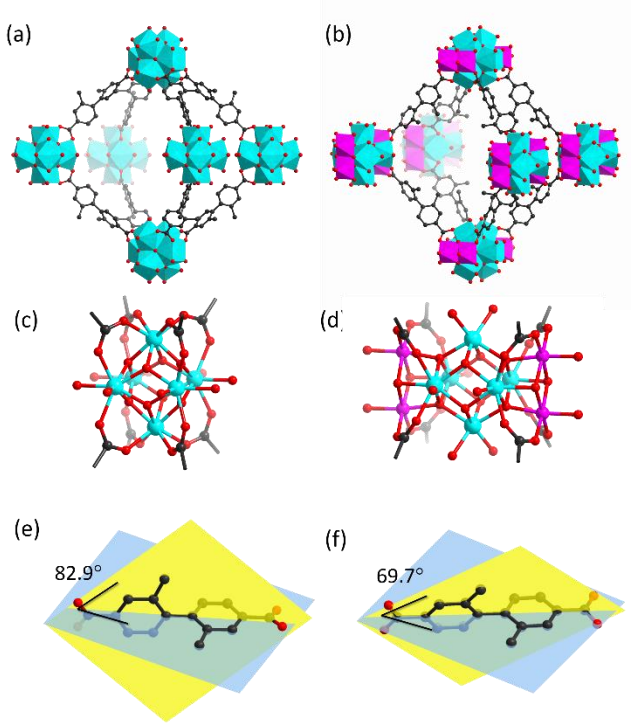

Figure 86. (a) The structure of PCN-700; (b) the structure of PCN-800(Ni); (c) the Zr_6 cluster in PCN-700; (d) the Zr_6Ni_4 cluster in PCN-800(Ni) showing the incorporated Ni and migrated carboxylate ligands; (e) the ligand conformation in PCN-700; (f) the ligand conformation in PCN-800. Color scheme: pink, Ni; blue, Zr; red, O; and black, C; H atoms are omitted for clarity.

A Zr-MOF, PCN-700, was chosen as a scaffold structure to build bimetallic MOFs (Figure 86a).[29] PCN-700 matches up with four criteria for post-synthetic cluster metalation studies. First, as opposed to the 12-connected Zr-cluster in UiO series MOFs, the $Zr_6O_4(OH)_8(H_2O)_4$ cluster in PCN-700 is 8-connected with carboxylate ligands, leaving eight terminal $-OH^-/H_2O$ ligands poised for post-synthetic metalation (Figure 86c). Second, the reactive terminal $-OH^-/H_2O$ ligands are directly exposed to the channels which facilitates metal ion diffusion and thus the metalation reaction. Third, PCN-700 possesses a certain degree of structural flexibility, which endows the

framework with structural adaptability during the metalation. In addition, PCN-700 is robust enough to maintain crystallinity during the metalation under solvothermal conditions, which enables us to employ single crystal X-ray crystallography to monitor the transformation process. Overall, the reduced connectivity, accessibility, flexibility, and high stability make PCN-700 an optimal platform for implementing the post-synthetic cluster metalation strategy.

To carry out the post-synthetic cluster metalation, PCN-700 crystals were exposed to a DMF (*N*,*N*-Dimethylformamide) solution of $Ni(NO_3)_2$ at 85 °C for 48 h. The shape and size of PCN-700 crystals were maintained throughout the modification, indicating a single crystal to single crystal transformation rather than dissolution and reformation of the crystals. The resultant product, designated as PCN-800(Ni), crystalizes in the $P4_2/mmc$ space group. Although it exhibits the identical topology to PCN-700 (Figure 86b), the metal nodes and the ligand conformation have undergone dramatic changes. Each Ni^{2+} reacts with two terminal -H_2O ligands and one μ_3-OH ligand in a Zr_6 cluster to afford a new Zr_6Ni_4 cluster. Interestingly, a ligand migration is concurrently observed during the cluster metalation which involves the dissociation of Zr-carboxylate bond and formation of Ni-carboxylate bond. As a result, the carboxylate ligand migrates from Zr_6 clusters to the expanded Zr_6Ni_4 clusters and bridges a Ni^{2+} and a Zr^{4+} (Figure 86c, d). Each Ni^{2+} is 6-coordinated with one μ_4-O, two μ_3-OH, one terminal -H_2O, and two O from carboxylates, completing an octahedral geometry. Two kinds of crystallographically independent Zr^{4+} ions exist within the Zr_6Ni_4 cluster. The coordination environments of four equivalent Zr^{4+} ions on the equatorial plane are intact during the cluster metalation and ligand migration, whereas two Zr^{4+} ions at axial positions become 6-coordinated with two μ_4-O, two μ_3-O, and two terminal -H_2O. The Zr-O and Ni-O distance, ranging from 2.03 Å to 2.25 Å and 1.94 Å to 2.07 Å, respectively, falls within the normal range.[172, 184] In stark contrast to other metal exchanged or

metalated Zr-MOFs (i.e. Ti-UiO-66 and V-UiO-66),[58, 109] PCN-800(Ni) is formed through the cleavage of Zr-carboxylate bonds and generation of Ni-carboxylate bonds. Consequently, PCN-800(Ni) is a fundamentally new structure with well-defined Zr_6Ni_4 clusters. To the best of our knowledge, the bimetallic zirconium-containing MOF with distinct metal positions has never been reported before.

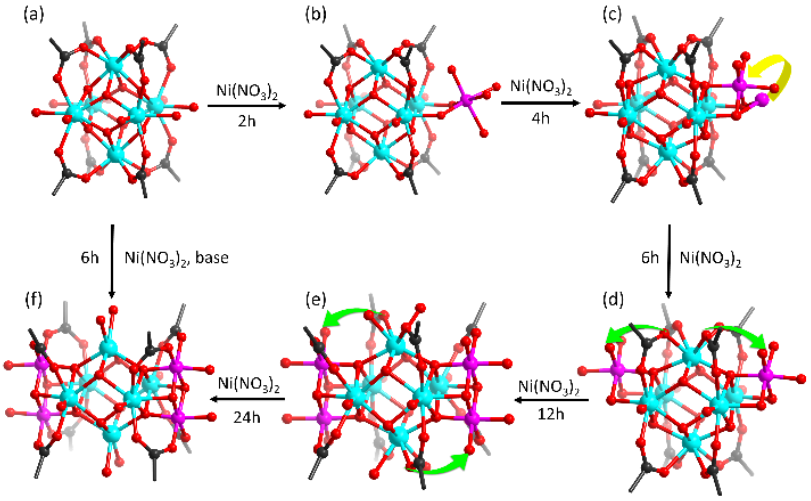

Figure 87. Cluster transformation during the cluster metalation and ligand migration; the yellow and green arrows illustrate the metal and ligand migrations, respectively.

5.3.2 Structural Transformation Monitored by SC-XRD

Given that PCN-700 could undergo cluster metalation and ligand migration with retention of single crystallinity, we turned our efforts to obtaining SCXRD data for the intermediates during the transformation process. Single crystals of PCN-700 were immersed in a DMF solution of $Ni(NO_3)_2$ at 85 °C and sampled every 2, 4, 6, 12, and 24h. The samples were analyzed by single crystal X-ray diffraction which gave snapshots of the structure transformation process. The SCXRD data clearly reveals a cooperative cluster metalation and ligand migration process. As shown in Figure 87b, the Ni^{2+} ions first attach to two terminal -H_2O. The four disordered Ni^{2+} are

observed on each Zr_6 clusters with occupancy of 12.5%, indicating that 0.5 Ni^{2+} is coordinated to each Zr_6 cluster on average. With increased soaking time, the attached Ni^{2+} further coordinates with μ_3-OH so that each Ni^{2+} is chelated by a μ_3-O and two terminal -OH ligands (Figure 87c). An intermediate is observed in which 20% of Ni^{2+} is attached to terminal -OH ligands and 80% of Ni^{2+} is chelated by a μ_3-O and two terminal -OH ligands (Figure 87c). The ligand migration process occurs along with the cluster metalation. When 1.15 Ni^{2+} is incorporated in each Zr_6 cluster at 6h, only a negligible amount of ligand migrates. At 12h, the occupancy of Ni^{2+} reaches 46% (corresponding to 1.84 Ni^{2+} per Zr_6 cluster) and ligand migration becomes obvious. The site occupancy of Ni^{2+} reaches almost 100% after 24h, meanwhile, we are able to observe an intermediate in which half of the ligand migrates. At this stage, the unit cell is doubled compared to PCN-700 because of the decreased symmetry upon ligand migration. Eventually, when the ligand migration completes, the unit cell goes back to its original state. As a result, a MOF based on $Zr_6Ni_4O_8(OH)_8(H_2O)_8$ clusters is generated. The structural transformation of bulk material was characterized by powder X-ray diffraction. It is observed that the peaks at around 7 and 10 degree gradually splits with the incorporation of Ni because of the reduced symmetry, which matches well with the simulations. The bulk materials at each transformation stage have same composition as the single crystal structure indicates, which was substantiated by energy dispersive X-ray analysis and inductively coupled plasma mass spectrometry.It should be noted that the cluster metalation by 3d metal cations have been previously reported in isolated Zr_6 cluster in which the robust Zr_6 clusters remained during the transformation whereas the -OH and carboxylate ligands changed their coordination modes to accommodate the post-incorporated metals. The resulting heterometallic clusters can also be characterized by SCXRD, but the transformation process remains unclear because of the difficulties in capturing the intermediates.[184] In this work, however,

the crystalline MOF provides a perfect platform to enable us to, for the first time, structurally elucidate the intermediate clusters by SCXRD and therefore garner fundamental insights into the metalation process.

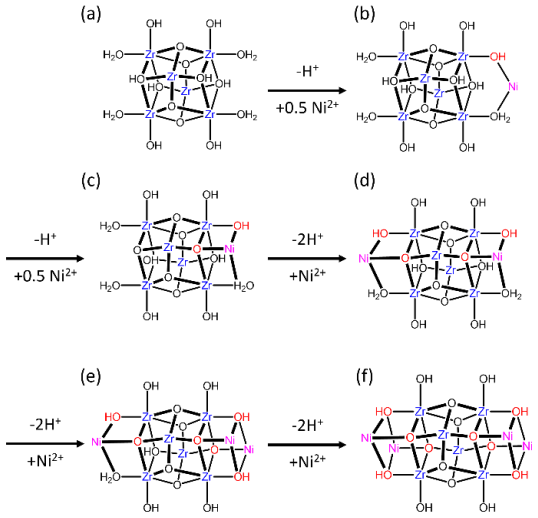

Figure 88. The scheme of clusters metalation showing the incorporation of Ni; red mark indicates the deprotonated ligands.

5.3.3 Deprotonation Mechanism

We propose that the deprotonation of terminal -H_2O and μ_3-OH ligands on Zr_6 clusters is directly correlated to the metalation. According to previous research, $Zr_6(\mu_3\text{-}O)_4(\mu_3\text{-}OH)_4(OH)_4(OH_2)_4(COO)_8$ is the preferred form for 8-connected Zr_6 clusters (Figure 88a).[185] The terminal -H_2O is first deprotonated and coordinated to Ni^{2+} ions (Figure 88b). Then, the μ_3-OH is deprotonated and coordinated to the same Ni^{2+}, so that this Ni^{2+} is fixated by two μ_3-OH and one μ_4-O (Figure 88c). Overall, four terminal -H_2O ligands are deprotonated to form four μ_3-OH, meanwhile four μ_3-OH ligands are deprotonated into μ_4-O. The eight negative charges from deprotonation are balanced by four post-incorporated Ni^{2+} (Figure 88f). DMF is known to gradually decompose into dimethyl amine at high temperature in the presence of transition metal

ions, which we believe is responsible for the deprotonation of terminal -H_2O and μ_3-OH ligands, and thus favors the metalation process. To corroborate our hypothesis, Et_3N or NaOH was added during the post-synthetic cluster metalation in the hope to speed up the deprotonation process of terminal -H_2O and μ_3-OH ligands, therefore accelerate the metalation process. As expected, with the addition of Et_3N or NaOH to the solution, PCN-800(Ni) can be synthesized in 6 h.

The flexibility of PCN-700 plays an important role in the ligand migration. The conformation of the ligand can undergo dramatic change, allowing the carboxylate group to dissociate from Zr^{4+} and associate with the post-incorporated Ni^{2+}. The torsion angle of the linker, defined by two methylphenyl planes, changed from 82.9° in PCN-700 to 69.7° in PCN-800(Ni), as shown in Figure 1e and 1f. Adaptation of ligand conformation and coordination to meet the coordination environment of inserted metal ions has rarely been reported.[186] The bulk material maintains its crystallinity after the transformation process as supported by powder X-ray diffraction patterns and N_2 gas adsorption-desorption isotherms. As a proof-of-concept of the general applicability of this method, $Co(NO_3)_2$ was used instead of $Ni(NO_3)_2$ under the same conditions, which gave rise to a isostructural bimetallic MOF based on Zr_6Co_4 clusters, designated as PCN-800(Co).

5.3.4 Catalysis

The cluster metalation is a powerful tool to functionalize Zr-MOFs for a variety of applications including chemical catalysis. The acetaldehyde cyclization was selected as a model reaction, which is an industrially attractive process that can lead to many different products (Scheme 9). As $InCl_3$ was known as a homogeneous catalyst for cyclotrimerization of aldehydes[187], we synthesized PCN-800(In) by performing cluster metalation on PCN-700. As a heterogeneous catalyst, PCN-800(In) efficiently catalyze acetaldehyde cyclotrimerization at room temperature

under solvent-free condition with conversion of 76% and selectivity up to 99% within 2 h (Table 17). For comparison, no detectable amount of product was observed for pristine PCN-700 under the same condition.

Scheme 9. MOF-catalyzed acetaldehyde transformations

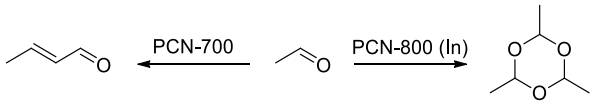

Table 17. Acetaldehyde transformations catalyzed by different MOFs

Entry	Catalyst	Condition	Product	Conversion/%	Selectivity/%
1	$InCl_3$	RT	paraldehyde	78	99
2	PCN-800(In)	RT	paraldehyde	76	99
3	PCN-700	RT	paraldehyde	Negligible	-
4	PCN-700	100 °C	crotonaldehyde	3	-

5.4 Conclusions

In summary, we report for the first time the synthesis of bimetallic MOFs based on Zr_6M_4 (M = Co, Ni) cluster through cooperative cluster metalation and ligand migration. The bimetallic cluster evolution is monitored by successive single crystal X-ray diffraction analyses, which provide fundamental insights into the metalation process. Given that the cluster metalation could be applied to Zr-MOFs with reduced connectivity, we expect it to be a general and facile strategy to functionalize Zr-MOFs with other metals. In light of the structural diversity and high chemical stability of Zr-MOFs, this strategy will allow for the functionalization of Zr-MOFs for a variety of promising applications.

6. RETROSYNTHESIS OF MULTI-COMPONENT MOFS*

6.1 Introduction

Crystal engineering of metal−organic frameworks (MOFs) has allowed the construction of complex structures at atomic precision, but has yet to reach the same level of sophistication as organic synthesis. The synthesis of complex MOFs with multiple organic and/or inorganic components is ultimately limited by the lack of control over framework assembly in a "one-pot" reaction. Indeed, the competitive assembly of multiple components usually ends up with a thermodynamically favored MOF as the main product, which impedes the incorporation of multi-components into a kinetic product. Retrosynthetic analysis is a concept to approach the synthesis of complex organic molecules by transforming a target molecule into simpler precursors and sequentially applying a set of known chemical reactions to assemble them together (Figure 89a). Inspired by the concept of retrosynthesis utilized to construct complex organic molecules and natural products[188], we proposed that MOFs as porous solid materials could be rationally designed and synthesized in multistep synthetic approaches[189]. Therein, kinetic analysis, an analog of retrosynthetic analysis, allowed us to conceptually break down a predicted MOF structure into available metal precursors and ligands (i.e., synthons). The synthons were subsequently assembled into the designed MOF structure step by step under kinetic control using known post-synthetic modification methods[34,35], which circumvent the undesirable thermodynamic sink. In other words, we use labile coordination bonds to sequentially "layer-on" molecular elaborations to a robust

*Reproduced in part with permission from: Yuan, S.; Qin, J.-S.; Li, J.; Huang, L.; Feng, L.; Fang, Y.; Lollar, C.; Pang, J; Zhang, L.; Sun, D.; Alsalme, A.; Cagin, T.; Zhou, H.-C. Retrosynthesis of multi-component metal−organic frameworks, *Nat. Commun.* **2018**, *9*, 808. Copyright 2018 Nature Publishing Group.

framework, which eventually formed the designed multi-component coordination assemblies (Figure 89b). As a proof of concept, four quaternary MOFs were assembled under the kinetic guidance, each composed of up to three different metals and two different linkers in a predetermined array within the crystal lattice. Furthermore, to demonstrate the utility of such a retrosynthetic design, a cooperative bimetallic catalytic system was constructed in a MOF by the sequential incorporation of a Fe-porphyrin and a Cu-pyridyl moiety.[28]

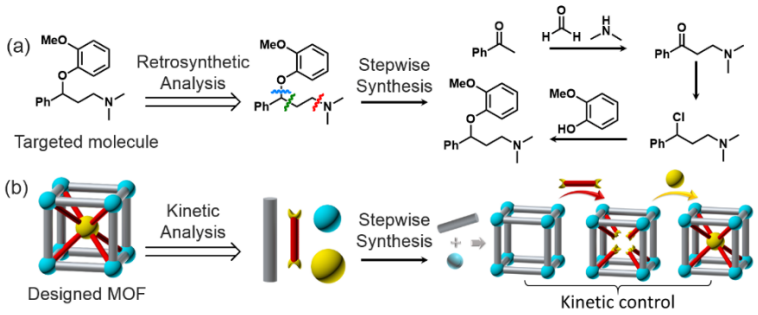

Figure 89. Retrosynthesis of (a) organic molecules and (b) multi-component MOFs.

6.2 Experimental Section

6.2.1 Materials and Instrumentation

All commercial chemicals were used without further purification unless otherwise mentioned. Powder X-ray diffraction (PXRD) was carried out with a BRUKER D8-Focus Bragg−Brentano X-ray powder diffractometer equipped with a Cu sealed tube (λ = 1.541 78) at 40 kV and 40 mA. Single Crystal X-ray Diffraction (SC-XRD) was measured on a Bruker D8 Venture or D8 Quest diffractometer equipped with a Cu-Kα (λ = 1.54184 Å, graphite monochromated) or Mo-Kα sealed-tube X-ray source (λ = 0.71073 Å, graphite monochromated). Elemental analyses for C, H and N were carried out on a German Elementary Vario EL III instrument. Thermogravimetric analyses (TGA) were conducted on a TGA-50 (SHIMADZU) thermogravimetric analyzer. Gas sorption measurements were conducted using a Micrometritics

ASAP 2420 system at various temperatures. NMR data were collected on a Mercury 300 spectrometer. Ultraviolet–visible absorption spectra were recorded on a Shimadzu UV-2450 spectrophotometer. ICP-MS data were collected with a Perkin Elmer NexION 300D ICP-MS. Field-emission SEM images were collected on the FEI Quanta 600 field-emission SEM (America) at 20 KV.

6.2.2 Ligand Syntheses

Scheme 10. Synthetic route for TCPP ligands.

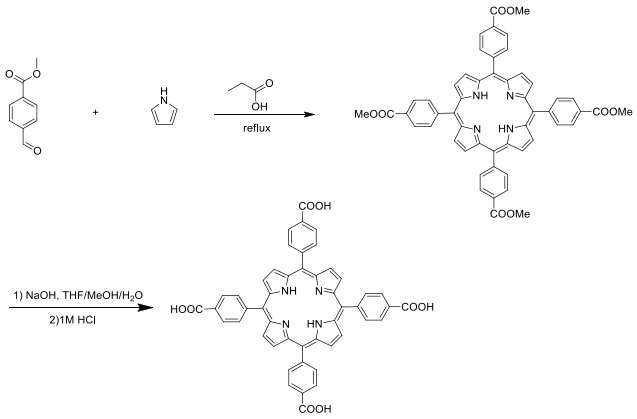

5,10,15,20-Tetrakis(4-methoxycarbonylphenyl)porphyrin (TPPCOOMe). In a 500-mL three necked flask, methyl *p*-formylbenzoate (6.9 g, 0.042 mol) was dissolved in propionic acid (100 mL). Pyrrole was then added dropwise (3.0, 0.043 mol) and the solution was refluxed for 12 h. After the reaction mixture was cooled down to room temperature, precipitates were collected by suction-filtration and washed with methanol, ethyl acetate and THF. After dried in the oven, purple solid was obtained as pure product. (1.9 g, 2.24 mmol, 21% yield). 1H NMR (300 MHz, $CDCl_3$) δ 8.81 (s, 8H), 8.43 (d, 8H), 8.28 (d, 8H), 4.11 (s, 12H), -2.83 (s, 2H).

Tetrakis(4-carboxyphenyl)porphyrin (TCPP). The obtained ester (0.75 g) was stirred in THF (25 mL) and MeOH (25 mL) mixed solvent, to which a solution of NaOH (2.40 g, 60.00 mmol) in H_2O (25 mL) was introduced. This mixture was refluxed for 12 h. After cooling down

to room temperature, THF and MeOH were evaporated. Additional water was added to the resulting water phase and the mixture was heated until the solid was fully dissolved, then the homogeneous solution was acidified with 1M HCl until no further precipitate was detected. The precipitate was collected by filtration, washed with water and dried in vacuum. FTIR (KBr): ν= 3444 (m), 3034 (w), 2634 (w), 1702 (s), 1614 (s), 1570 (m), 1404 (s), 1311 (m), 1277 (s), 1204 (m), 1180 (m), 1106 (m), 1004 (s), 862 (m), 799 (s), 770 (s), 721 (m) cm^{-1} (Scheme 10).

6.2.3 MOF Syntheses

Synthesis of PCN-224. PCN-224 was synthesized on the basis of previous reports with slight modifications[190]. $ZrCl_4$ (30 mg), H_4TCPP (10 mg), benzoic acid (600 mg) and DMF (3 mL) were charged in a Pyrex vial. The mixture was heated in a 120 ºC oven for 24 h. After cooling to room temperature, cubic dark purple crystals of PCN-224 were harvested. The as-synthesized PCN-224 was washed thoroughly with DMF, water, and 1 M HCl in DMF to remove dangling ligands on Zr_6 clusters. Anal. Calcd (%) for PCN-224: C, 44.04; H, 2.62; N, 4.28%. Found: C, 50.34; H, 3.10; N, 3.64%.

Synthesis of PCN-224(Ni). PCN-224(Ni) was synthesized by the metalation of PCN-224(No Metal). The crystals of PCN-224 were incubated in the solution of $Ni(NO_3)_2$ at 100 ºC for 24 h. After cooling to room temperature, cubic dark red crystals of PCN-224(Ni) were harvested and washed thoroughly with DMF (10 mg, yield: 70%). Alternatively, large single crystals of PCN-224(Ni) can be synthesized from Ni-TCPP. A DMF (3 mL) solution of $ZrCl_4$ (30 mg), Ni-TCPP (10 mg) and benzoic acid (600 mg) were charged in a Pyrex vial. The mixture was heated in a 120 ºC oven for 24 h. After cooling to room temperature, cubic dark red crystals of PCN-224(Ni) were harvested. As PCN-224(Ni) single crystals show strong X-ray diffraction, they were used for the structural characterization of the single crystal to single crystal transformation process.

Anal. Calcd (%) for PCN-224(Ni): C, 42.22; H, 2.36; N, 4.10%. Found: C, 45.43; H, 3.13; N, 4.48%.

Synthesis of PCN-224(Ni)-INA. PCN-224(Ni) (10 mg), INA (30 mg) and DMF (4 mL) were charged in a Pyrex vial. The mixture was heated in an 80 ºC oven for 24 h resulting in the coordination of INA to the Zr_6 cluster of PCN-224(Ni).

Synthesis of PCN-201(Ni)-Cu. After the synthesis of PCN-224(Ni)-INA, the supernatant was decanted, and CuI (30 mg) and MeCN (4 mL) were added. The mixture was heated in a 65 ºC oven for 24 h to generate the crystals of PCN-201(Ni)-Cu. The crystals of PCN-201(Ni)-Cu were collected by centrifugation and washed 3 times with aliquots of DMF. Anal. Calcd (%) for PCN-201(Ni)-Cu: C, 39.75; H, 2.44; N, 5.15%. Found: C, 30.38; H, 3.11; N, 2.22%.

Synthesis of PCN-201(Ni)-Ni. After the synthesis of PCN-224(Ni)-INA, the supernatant was decanted and $NiCl_2$ (30 mg) and DMF (4 mL) were added. The mixture was heated in a 65 ºC oven for 24 h to generate the crystals of PCN-201(Ni)-Ni. The crystals of PCN-201(Ni)-Ni were collected by centrifugation and washed 3 times with aliquots of DMF. Anal. Calcd (%) for PCN-201(Ni)-Ni: C, 42.10; H, 2.58; N, 5.45%. Found: C, 39.59; H, 3.58; N, 5.03%.

Synthesis of PCN-224(Ni)-DCDPS. PCN-224(Ni) (10 mg), DCDPS (30 mg) and DMF (4 mL) were charged in a Pyrex vial. The mixture was heated in an 80 ºC oven for 24 h resulting in the coordination of DCDPS to the Zr_6 cluster of PCN-224(Ni).

Synthesis of PCN-202(Ni)-Hf. After the synthesis of PCN-224(Ni)-DCDPS, to the solution was added $HfCl_4$ (30 mg) and acetic acid (0.1 mL). The mixture was heated in an 80 ºC oven for 24 h. The crystals of PCN-202(Ni)-Hf were collected by centrifugation and washed 3 times with aliquots of DMF. Anal. Calcd (%) for PCN-202(Ni)-Hf: C, 44.00; H, 2.72; N, 2.28%. Found: C, 45.82; H, 3.45; N, 4.68%.

Synthesis of PCN-202(Ni)-Zr. After the synthesis of PCN-224(Ni)-DCDPS, to the solution was added $ZrCl_4$ (30 mg) and acetic acid (0.1 mL). The mixture was heated in an 80 ºC oven for 24 h. The crystals of PCN-202(Ni)-Zr were collected by centrifugation and washed 3 times with fresh DMF. Anal. Calcd (%) for PCN-202(Ni)-Zr: C, 45.61; H, 2.82; N, 2.36%. Found: C, 46.98; H, 3.50; N, 3.82%.

Synthesis of PCN-201(Fe)-Cu. The synthesis of PCN-201(Fe)-Cu is similar to that of PCN-201(Ni)-Cu except that $FeCl_2$ was used for the metallation of PCN-224. The black crystals of PCN-201(Fe)-Cu were collected by centrifugation and washed 3 times with aliquots of DMF. Anal. Calcd (%) for PCN-201(Fe)-Cu: C, 39.15; H, 2.40; N, 5.07%. Found: C, 37.77; H, 3.48; N, 5.02%.

6.2.4 Single Crystal X-Ray Crystallography

All crystals were taken from the mother liquid without further treatment, transferred to oil and mounted into a loop for single crystal X-ray data collection. Diffraction was measured on a Bruker D8 Venture or D8 Quest diffractometer equipped with a Cu-Kα (λ = 1.54184 Å, graphite monochromated) or Mo-Kα sealed-tube X-ray source (λ = 0.71073 Å, graphite monochromated). The raw frame data were processed using SAINT and SADABS to yield the reflection data file.[1] The structure was solved using the charge-flipping algorithm, as implemented in the program *SUPERFLIP*[2] and refined by full-matrix least-squares techniques against F_o^2 using the SHELXL program[3] through the OLEX2 interface.[4] The hydrogen atoms from the linkers were placed geometrically and refined using a riding model. The refinement of the framework was performed by ignoring the contribution of the disordered solvent molecules. The region containing the disordered electron density was identified by considering the van der Waals radii of the atoms constituting the ordered framework. Platon SQUEEZE[5] was used and .fab file was created

containing partial structure factors representing the SQUEEZE region. The appropriate partial structure factors were used for input to SHELXL with the ABIN instruction. The ABIN instruction reads *h, k, l, A* and *B* from the file name fab, where *A* and *B* are the real and imaginary components of a partial structure factor (Table 18).[3]

Refinement Details for PCN-201(Ni)-Cu. Due to the weak diffractions at high Bragg angle, several atoms show unusual isotropic thermal parameters,thus several restraints were applied to ensure a reasonable refinement. In details, SIMU restraints were also used for organic ligands with large thermal motion (O2 C9 C10 C12 N2 C11 C1 C2 O1 C4 C3 C3 C4 C6 C5 C6 C7 C8 N1 C5 Ni1). FLAT was used to ensure the planarity of some part of ligand. DFIX was used to fix the C9-C10 to 1.55 Å, C10-C11 and C11-C12 to 1.35 Å.

Refinement Details for PCN-201(Ni)-Ni. Due to the weak diffractions at high Bragg angle, several atoms show unusual isotropic thermal parameters, thus several restraints were applied to ensure a reasonable refinement. In details, SIMU restraints were also used for organic ligands with large thermal motion (O3 O4 O1 O2 C9 C10 C11 N2 C12C9 C10 C11 N2 C12 O1 C1 C2 C3 C4 C5 C6 C8 C7 N1). FLAT was used to ensure the planarity of some part of ligand (O2 C9 C10 C11 N2 C12). DFIX was used to fix the C12-C11, C10-C11, N2-C12 to 1.35 \%A, N2-C11,C10-C12 to 2.35 \%A, C9-C10 1.55 \%A.

Refinement Details for PCN-202(Ni)-Hf. Due to the weak diffractions at high Bragg angle, several atoms show unusual isotropic thermal parameters, thus several restraints were applied to ensure a reasonable refinement. In details, SIMU restraints were also used for organic ligands with large thermal motion (O1 C1 C3 C2 C4 C6 C7 C8 C5 N4 O3 C9 C10 C11 C12 C13 S4 C14 C15 C16 C17 C18 O5). FLAT was used to ensure the planarity of some part of ligand (C10 C11 C12 C13 C9 and C13 C12_$1 C11_$1 C10 C11 C12 C9 S4, EQIV $1 +X,+Z,+Y). DFIX

was used to fix the C1-O1, O5-C18, O3-C9 to 1.25 \%A; C14-C15, C15-C16, C16-C17, C11-C12, C12-C13, C10-C11 to 1.35 \%A; C15-C17, C14-C16, C11-C13, C10-C12 to 2.35 \%A; C17-C18,C9-C10 to 1.55 \%A; C14-S4, C13-S4 to 1.85 \%A; C10-O3 to 2.5 \%A.

Refinement Details for PCN-202(Ni)-Zr. Due to the weak diffractions at high Bragg angle and not good crystal quality, several atoms show unusual isotropic thermal parameters, thus several restraints were applied to ensure a reasonable refinement. In details, SIMU restraints were also used for organic ligands with large thermal motion (S1 O1 O4 C9 > C18). FLAT was used to ensure the planarity of some part of ligand (S1 C9 C10 C11 C12 C13). DFIX was used to fix the C14-C15, C13-C12, C11-C12,C10-C11,C9-C10 to 1.35 \%A, C13-C11,C10-C12 to 2.35 \%A, S1-C12 2.70 \%A.

Refinement Details for PCN-224(Ni)-DCDPS. Due to the weak diffractions at high Bragg angle and not good crystal quality, several atoms show unusual isotropic thermal parameters, thus several restraints were applied to ensure a reasonable refinement. In details, SIMU restraints were also used for organic ligands with large thermal motion (O4 S1 C10 C10 C11 C12 C13 O5 C9). FLAT was used to ensure the planarity of some part of ligand (C10 C11 C12 C13 C9). DFIX was used to fix the C13-C12, C11-C12, C10-C11 to 1.35 \%A, C9-C10 to 1.55 \%A, C13-C11, C10-C12 to 2.35 \%A, C13-S1 to 1.9 \%A, S1-O5 to 1.45 \%A; O5-C13 to 2.6 \%A.

Refinement Details for PCN-224(Ni)-INA., Due to the weak diffractions at high Bragg angle, several atoms show unusual isotropic thermal parameters, thus several restraints were applied to ensure a reasonable refinement. In details, SIMU restraints were also used for organic ligands with large thermal motion (N2 C12 C11 C10 C9 O2). FLAT was used to ensure the

planarity of some part of ligand (C10 N2 C12 C11). DFIX was used to fix the C12-C11, C10-C11, N2-C12 to 1.35 \%A, N2-C11,C10-C12 to 2.35 \%A.

Table 18. Crystal data and structure refinements.

Compound	**PCN-201(Ni)-Cu**	**PCN-201(Ni)-Ni**	**PCN-202(Ni)-Zr**
CCDC	**1544109**	**1544110**	**1544113**
Empirical formula	$C_{144}H_{80}N_{16}O_{42.67}Cu_4I_4Ni_2Zr_8$	$C_{144}H_{80}N_{16}O_{42.67}Ni_6Cl_4Zr_8$	$C_{912}H_{480}N_{48}O_{320}S_{24}Ni_{12}Zr_{60}$
Formula weight	4325.84	3940.72	24176.57
Temperature/K	173(2)	173(2)	173(2)
Crystal system	cubic	cubic	cubic
Space group	*Im*-3*m*	*Im*-3*m*	*Im*-3*m*
a/Å	38.3126(7)	38.3070(10)	38.418(5)
b/Å	38.3126	38.307	38.418
c/Å	38.3126	38.307	38.418
α/°	90	90	90
β/°	90	90	90
γ/°	90	90	90
Volume/Å^3	56237(3)	56213(4)	56705(20)
Z	6	6	1
ρ_{calc}/(g cm^{-3})	0.766	0.698	0.708
μ/mm^{-1}	4.965	2.611	0.420
F(000)	12608.0	11720.0	11968.0
Radiation	CuKα (*λ* = 1.54184 Å)	CuKα (*λ* = 1.54184 Å)	MoKα (*λ* = 0.71073 Å)
2Θ range for data collection/°	5.65 to 149.232	5.652 to 137.724	4.24 to 54.976
Reflections collected	93526	47618	596037
Independent reflections	5368 [R_{int}= 0.1027, R_{sigma}= 0.0352]	4826 [R_{int}= 0.0491, R_{sigma}= 0.0269]	6036 [R_{int}= 0.1519, R_{sigma}= 0.0257]
Data/restraints/parameters	5368/85/151	4826/51/141	6036/83/174
Goodness-of-fit on F^2	1.050	1.432	2.071
Final R indexes [I>=2σ (I)]	R_1= 0.0748, wR_2= 0.2131	R_1=0.1008, wR_2= 0.3002	R_1= 0.1510, wR_2= 0.3926
Final R indexes [all data]	R_1= 0.0918, wR_2= 0.2400	R_1= 0.1177, wR_2= 0.3348	R_1= 0.2143, wR_2= 0.4882
Largest diff. peak/hole / e Å^{-3}	0.81/-0.92	1.66/-0.86	4.77/-2.39

Table 18. Continued.

Compound	**PCN-202(Ni)-Hf**	**PCN-224(Ni)-INA**	**PCN-224(Ni)-DCDPS**
CCDC	**1544112**	**1544108**	**1544111**
Empirical formula	$C_{960}H_{480}N_{48}O_{304}S_{24}Ni_{12}Hf_{12}Zr_{48}$	$C_{864}H_{480}N_{96}O_{256}Ni_{12}Zr_{48}$	$C_{912}H_{480}N_{48}O_{304}S_{24}Ni_{12}Zr_{48}$
Formula weight	25544.29	21384.49	22825.93
Temperature/K	173(2)	173(2)	100(2)
Crystal system	cubic	cubic	cubic
Space group	*Im*-3*m*	*Im*-3*m*	*Im*-3*m*
a/Å	38.3665(8)	38.2762(6)	38.364(10)
b/Å	38.3665	38.2762	38.364
c/Å	38.3665	38.2762	38.364
α/°	90	90	90
β/°	90	90	90
γ/°	90	90	90
Volume/Å^3	56475.1(13)	56077(3)	56462(43)
Z	1	1	1
ρ_{calc}/(g cm^{-3})	0.751	0.633	0.671
μ/mm^{-1}	3.374	2.147	2.362
F(000)	12512.0	10640.0	11360.0
Radiation	CuKα (*λ* = 1.54184 Å)	CuKα (*λ* = 1.54184 Å)	CuKα (*λ* = 1.54184 Å)
2Θ range for data collection/°	5.642 to 149.372	5.656 to 135.388	5.642 to 148.862
Reflections collected	137606	42607	143603
Independent reflections	5379 [R_{int}= 0.0502, R_{sigma}= 0.0139]	4649 [R_{int}= 0.0403, R_{sigma}= 0.0240]	5370 [R_{int}= 0.1153, R_{sigma}= 0.0356]
Data/restraints/parameters	5379/87/136	4649/11/112	5370/18/121
Goodness-of-fit on F^2	2.577	1.353	1.865
Final R indexes [I>=2σ (I)][a]	R_1= 0.1804, wR_2= 0.4467	R_1= 0.1054, wR_2= 0.2979	R_1= 0.1510, wR_2= 0.4063
Final R indexes [all data][b]	R_1= 0.2021, wR_2= 0.5135	R_1= 0.1255, wR_2= 0.3308	R_1= 0.1937, wR_2= 0.4598
Largest diff. peak/hole / e Å^{-3}	6.35/-5.66	2.00/-0.76	1.99/-1.02

[a] $R_1 = \Sigma||F_o| - |F_c||/\Sigma|F_o|$.
[b] $wR_2 = |\Sigma w(|F_o|^2 - |F_c|^2)|/\Sigma|w(F_o^2)^2|^{1/2}$.

6.2.5 Materials Characterization

Topology Analysis. To better understand the structure of PCN-202(Ni)-Hf, topology analyses were carried out using TOPOS 4.0.[3] The disordered DCDPS linker appears as a "tritopic" linker because of the 2-fold disorder. Topologically, the 12-connected metal clusters can be regarded as a cuboctahedron nodes and tetratopic TCPP linkers can be viewed as square nodes. If the 2-fold disordered DCDPS linker is regarded as a 3-connected triangle node, the overall structure can be simplified into a 3,4,12,12 connected net with a point symbol of $\{4^{24}.6^{36}.8^{6}\}_5\{4^{3}\}_{12}\{4^{4}.6^{2}\}_6$.

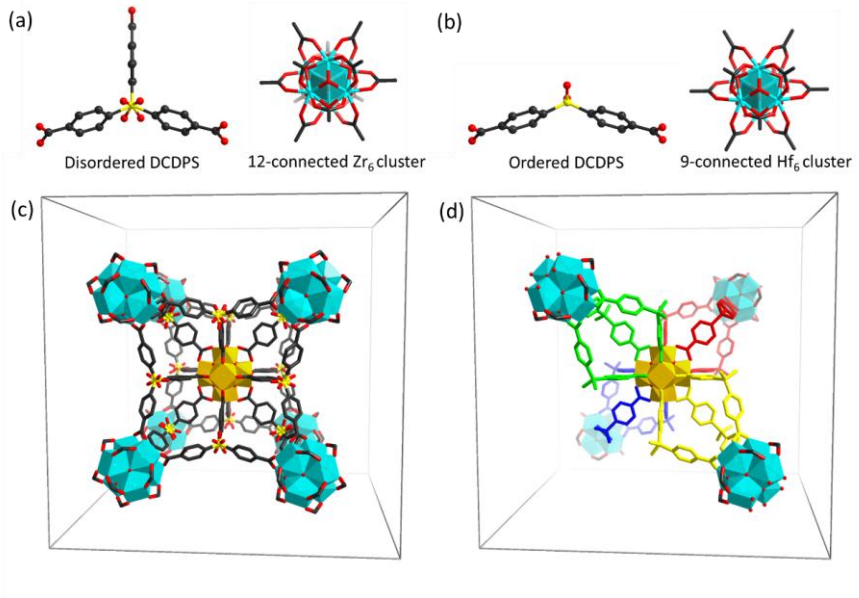

Figure 90. (a) and (c) Crystal structure of PCN-202(Ni)-Hf with disorder. (b) and (d) simulated structure of PCN-202(Ni)-Hf without disorder.

To eliminate the disorder of the DCDPS linker, we simulated an ordered structure of PCN-202(Ni)-Hf by reducing the space group from *Im*-3*m to I*-43*m*. The reduced space group with lower symmetry will eliminate the positional disorder of DCDPS linker by removing the mirror plan passing through its center. It should be noted that we attempted to refine the crystal structure of PCN-202(Ni)-Hf with a lower symmetry space group such as *I*-43*m*. However, the disorder is not

eliminated, suggesting an inherent disorder of PCN-202(Ni)-Hf. In the simulated structure, each DCDPS linker is 2-connected to a Zr_6 cluster and a Hf_6 cluster. Therefore, each Zr_6 cluster is 9 connected to 6 TCPP and 3 DCDPS respectively, while each Hf_6 cluster is 12 connected to DCDPS linkers. Three pairs of DCDPS linkers bridges a pair of Zr_6 and Hf_6 cluster so that topologically they regarded as one edge. Consequently, Zr_6 clusters are simplified into a 5-connected hexagonal pyramid nodes while Hf_6 clusters are reduced into 4-connected tetrahedron nodes. The overall structure is simplified into a 4,4,7-connected net with point symbol of $\{4^4.6^2\}_6\{4^6.6^{15}\}_4\{6^6\}$. Note that the topology of ordered structure is dependent on the space groups that are chosen to eliminate the disorder. Different topologies might result if other space groups are selected to simplify the structure (Figures 910-91).

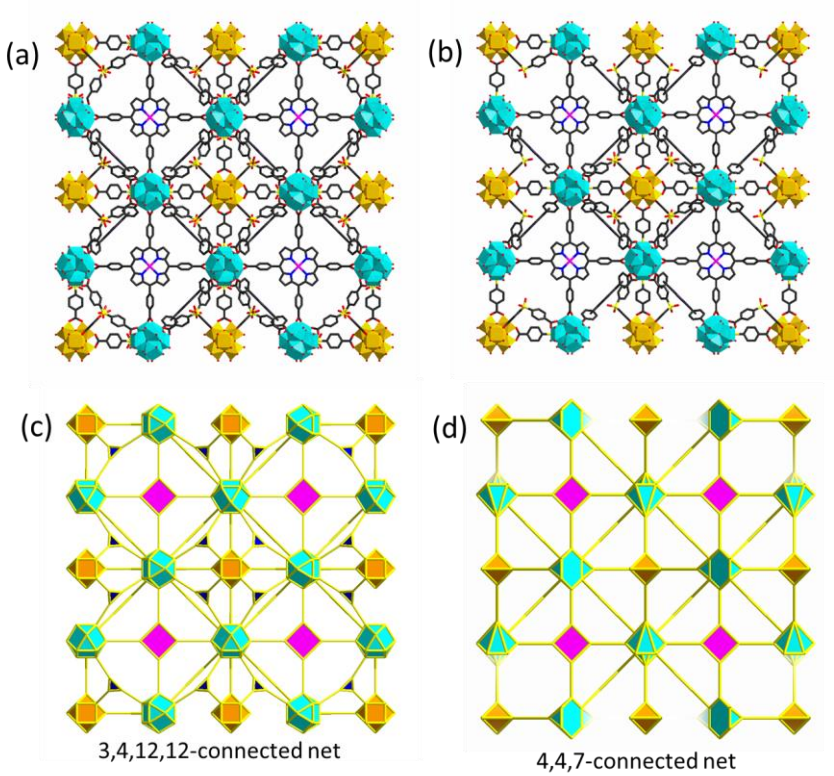

Figure 91. (a) Crystal structure of PCN-202(Ni)-Hf with disorder. (b) simulated structure of PCN-202(Ni)-Hf without disorder. (c) Building units and their simplified topological elements. (d) and (e) topology of PCN-202(Ni)-Hf with and without disorder.

PXRD Patterns. Powder X-ray diffraction (PXRD) was carried out with a BRUKER D8-Focus Bragg-Brentano X-ray Powder Diffractometer equipped with a Cu sealed tube (λ = 1.54178) at 40 kV and 40 mA. The experimental PXRD patterns were compared with the simulated ones based on single crystal structures (Figures 92-95).

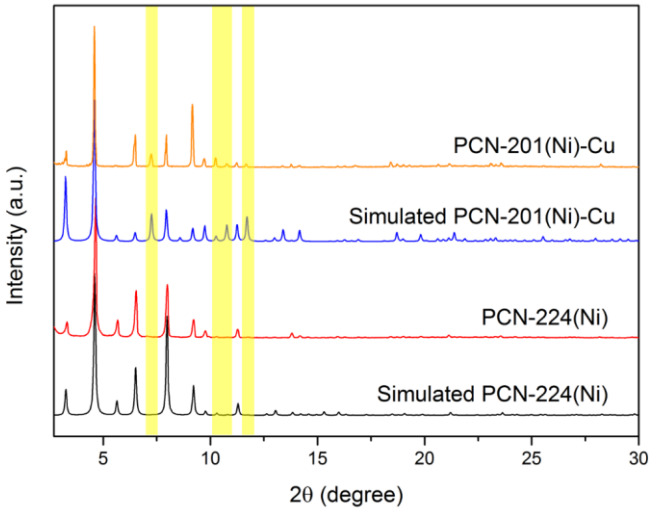

Figure 92. A comparison of powder X-ray diffraction (PXRD) patterns for PCN-201(Ni)-Cu and PCN-224(Ni).

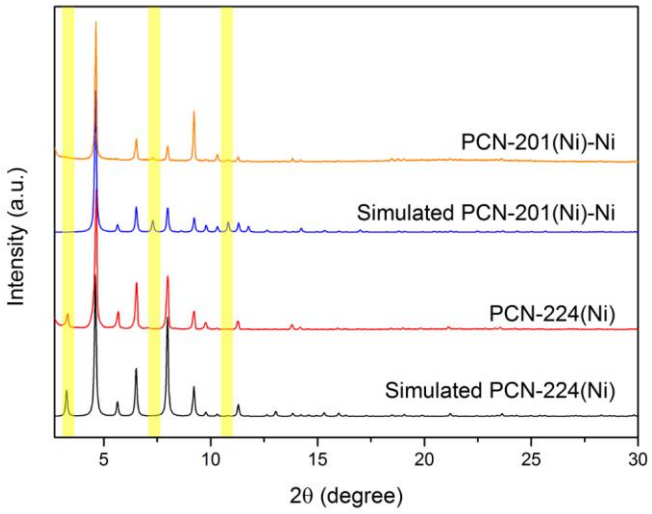

Figure 93. A comparison of PXRD patterns for PCN-201(Ni)-Ni and PCN-224(Ni).

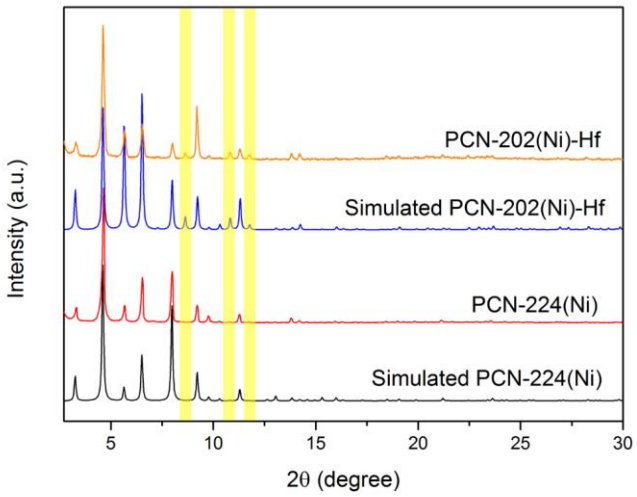

Figure 94. A comparison of PXRD patterns for PCN-202(Ni)-Hf and PCN-224(Ni).

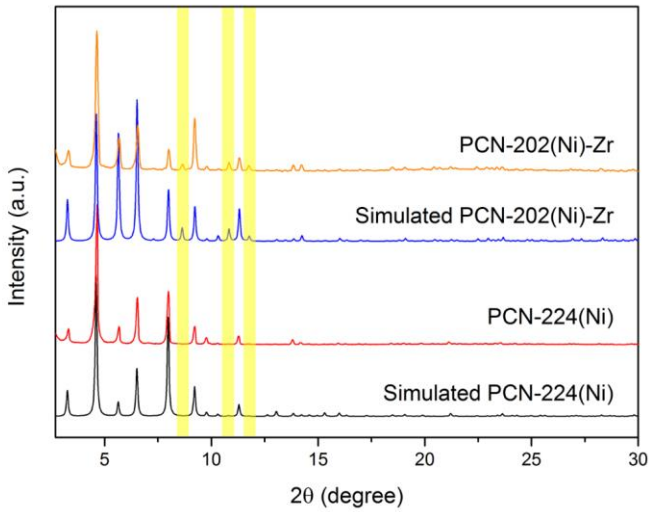

Figure 95. A comparison of PXRD patterns for PCN-202(Ni)-Zr and PCN-224(Ni).

Gas Sorption Isotherm. Before gas sorption experiments, as-synthesized sample was washed with *N*,*N*-Dimethylmethanamide (DMF) and immersed in acetone for 3 days, during which the solvent was decanted and freshly replenished three times. The solvent was removed under vacuum at 100 ^{o}C, yielding porous material. Gas sorption measurements were then conducted using a Micrometritics ASAP 2020 system (Figures 96-101).

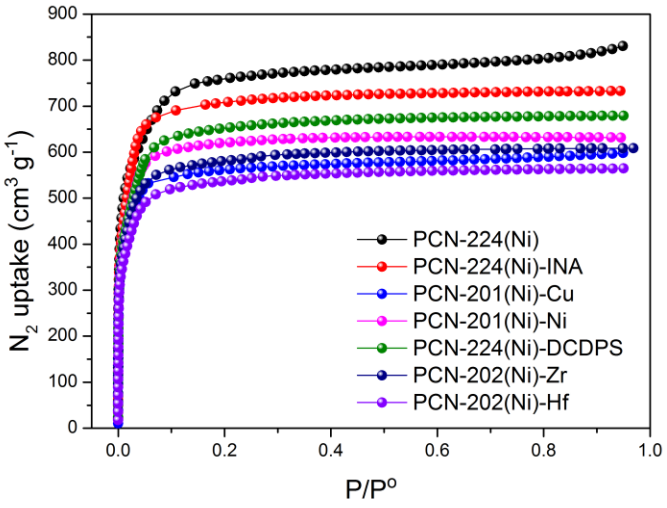

Figure 96. N_2 adsorption isotherms of PCN-224(Ni), PCN-224(Ni)-INA, PCN-201(Ni)-Ni, PCN-201(Ni)-Cu, PCN-224(Ni)-DCDPS, PCN-202(Ni)-Zr, and PCN-202(Ni)-Hf at 77 K.

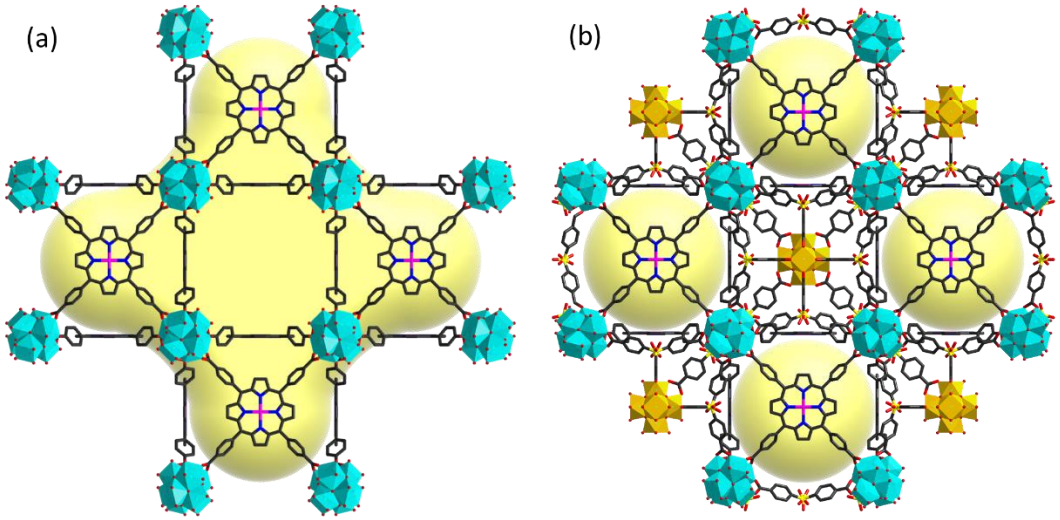

Figure 97. The mesopores of PCN-224(Ni) are separated into micropores in PCN-202(Ni)-Zr as shown from single crystal structures.

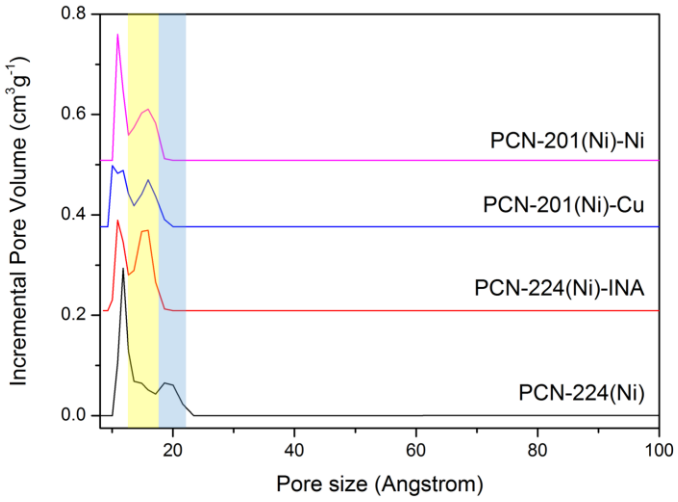

Figure 98. DFT pore size distribution of PCN-224(Ni), PCN-224(Ni)-INA, PCN-201(Ni)-Ni, and PCN-201(Ni)-Cu calculated from N_2 isotherms at 77 K.

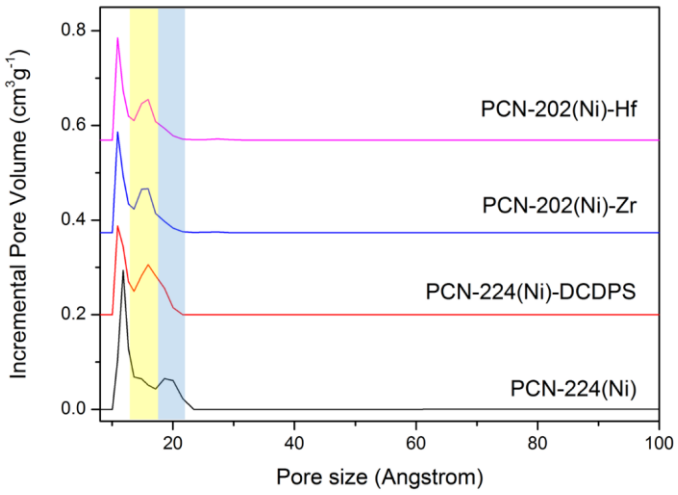

Figure 99. DFT pore size distribution of PCN-224(Ni), PCN-224(Ni)-DCDPS, PCN-202(Ni)-Zr, and PCN-202(Ni)-Hf calculated from N_2 isotherms at 77 K.

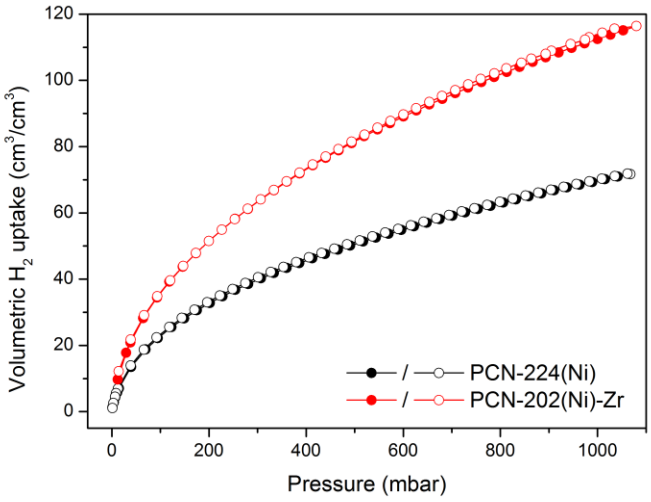

Figure 100. Volumetric H_2 uptake of PCN-224(Ni) and PCN-202(Ni)-Zr at 77 K.

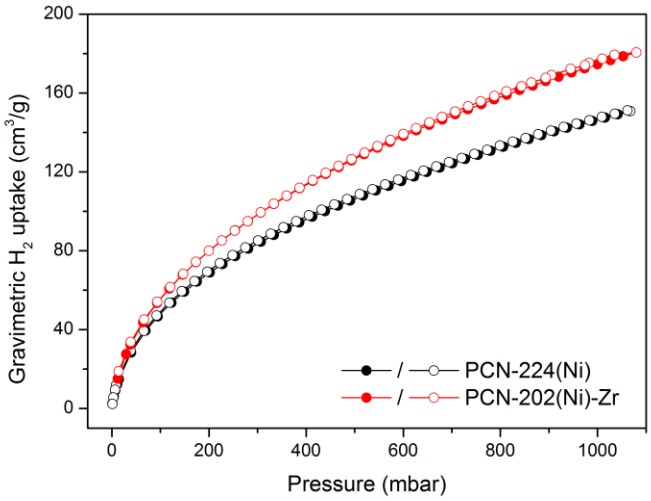

Figure 101. Gravimetric H_2 uptake of PCN-224(Ni) and PCN-202(Ni)-Zr at 77 K.

^{1}H NMR spectroscopy. For ^{1}H NMR spectroscopy of digested MOF samples, the activated samples (around 5 mg) were dissolved with saturated K_2CO_3 aqueous solution (1 mL), neutralize by 10 M HCl aqueous solution, and dried in a 100 ^{o}C oven. The solid was then dissolved in about 0.5 mL DMSO-d_6 for ^{1}H NMR analysis. For the catalytic reactions, the MOF catalyst was

immediately separated from the reaction system after 10 min. About 100 µL of reaction supernatant was sampled, dissolved in 1 mL of dimethyl sulfoxide-d_6 and then measured by ^{1}H NMR. It took about 20 min before the spectrum was recorded (Figures 101-105, Table 19).

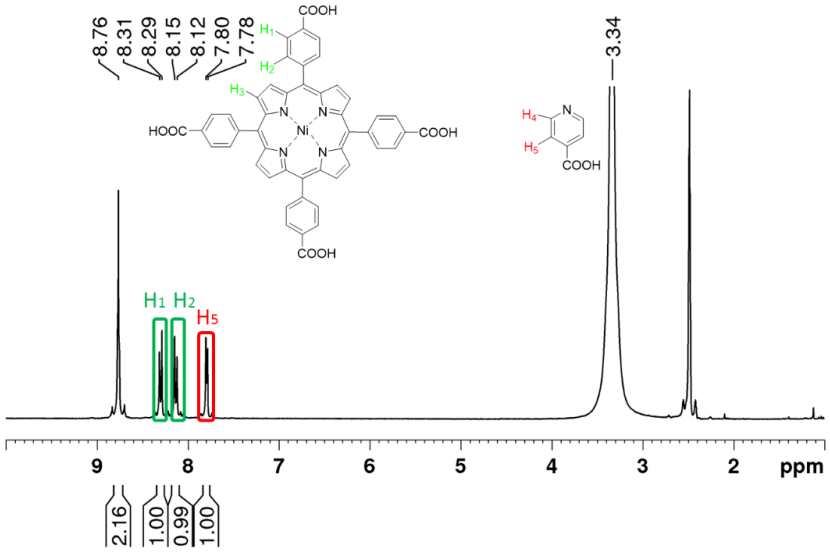

Figure 102. ^{1}H NMR spectroscopy of digested PCN-201(Ni)-Cu**.**

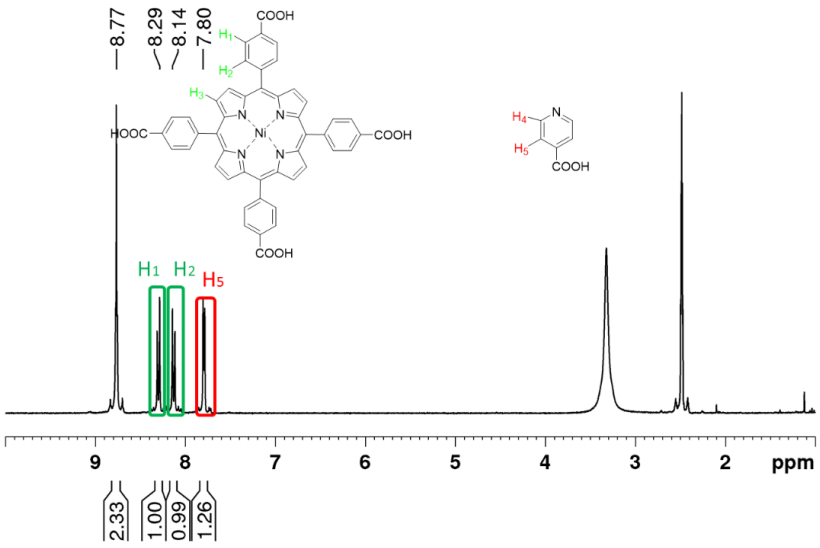

Figure 103. ^{1}H NMR spectroscopy of digested PCN-201(Ni)-Ni**.**

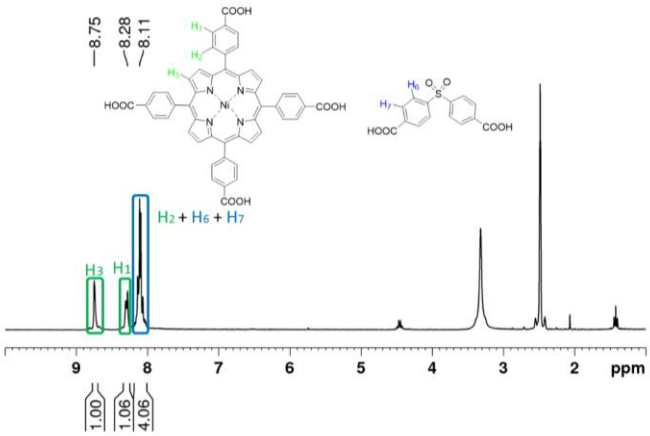

Figure 104. [1]H NMR spectroscopy of digested PCN-202(Ni)-Hf**.**

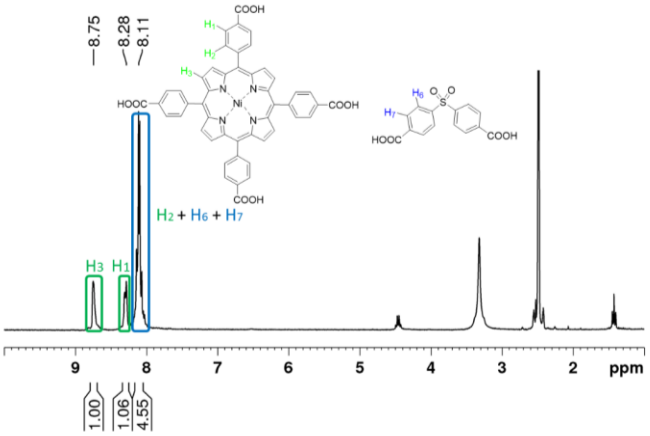

Figure 105. [1]H NMR spectroscopy of digested PCN-202(Ni)-Zr**.**

Table 19. Compositional analysis of PCN-224(Ni), PCN-201(Ni)-Cu, PCN-201(Ni)-Ni, PCN-202(Ni)-Hf, PCN-202(Ni)-Zr and PCN-201(Fe)-Cu by [1]H-NMR.

	Formula	**Theoretical**	**Experimental**
PCN-224(Ni)	$[Zr_6O_4(OH)_8(H_2O)_4]_4$ $(Ni\text{-}TCPP)_6$	—	—
PCN-201(Ni)-Cu	$[Zr_6O_4(OH)_4]_4(CuI)_{12}$ $(Ni\text{-}TCPP)_6(INA)_{24}$	TCPP:INA = 1:4	TCPP:INA = 1:4.00
PCN-201(Ni)-Ni	$[Zr_6O_4(OH)_4]_4(NiCl_2)_{12}$ $(Ni\text{-}TCPP)_6(INA)_{24}$	TCPP:INA = 1:4	TCPP:INA = 1:5.04
PCN-202(Ni)-Hf	$[Zr_6O_4(OH)_4]_4[Hf_6O_4(OH)_4]$ $(Ni\text{-}TCPP)_6(DCDPS)_{12}(HDPDCS)_6(OH)_6(H_2O)_6$	TCPP:DCDPS = 1:3	TCPP:DCDPS = 1:3.55
PCN-202(Ni)-Zr	$[Zr_6O_4(OH)_4]_4[Zr_6O_4(OH)_4]$ $(Ni\text{-}TCPP)_6(DCDPS)_{12}(HDPDCS)_6(OH)_6(H_2O)_6$	TCPP:DCDPS = 1:3	TCPP:DCDPS = 1:3.06
PCN-201(Fe)-Cu	$[Zr_6O_4(OH)_4]_4(CuI)_{12}$ $(FeCl\text{-}TCPP)_6(INA)_{24}$	TCPP:INA = 4:1	TCPP:INA = 4.81:1

SEM/EDX Analysis. Instrumental information of SEM/EDX: Images and analyses of SEM/EDX were taken by FEI Quanta 600 FE-SEM. The Quanta 600 FEG is a field emission scanning electron microscope capable of generating and collecting high-resolution and low-vacuum images. It is equipped with a motorized x-y-z-tilt-rotate stage, providing the following movements: $x = y = 150$ mm (motorized); $z = 65$ mm (motorized); Tilt +70 degrees to –5 degrees (motorized); Source: Field emission gun assembly with Schottky emitter source. Voltage: 200 V to 30 kV. Beam Current: >100 nA (Table 20).

Table 20. Compositional analysis of PCN-224(Ni), PCN-201(Ni)-Cu, PCN-201(Ni)-Ni, PCN-202(Ni)-Hf, PCN-202(Ni)-Zr and PCN-201(Fe)-Cu by ICP-MS.

	Formula	**Theoretical**	**Experimental**
PCN-224(Ni)	$[Zr_6O_4(OH)_8(H_2O)_4]_4$ $(Ni\text{-}TCPP)_6$	Zr:Ni = 4:1	Zr:Ni = 3.7:1
PCN-201(Ni)-Cu	$[Zr_6O_4(OH)_4]_4(CuI)_{12}$ $(Ni\text{-}TCPP)_6(INA)_{24}$	Zr:Ni:Cu = 4:1:2	Zr:Ni:Cu = 3.7:1:1.4
PCN-201(Ni)-Ni	$[Zr_6O_4(OH)_4]_4(NiCl_2)_{12}$ $(Ni\text{-}TCPP)_6(INA)_{24}$	Zr:Ni = 4:3	Zr:Ni = 3.8:3
PCN-202(Ni)-Hf	$[Zr_6O_4(OH)_4]_4[Hf_6O_4(OH)_4]$ $(Ni\text{-}TCPP)_6(DCDPS)_{12}(HDPDCS)_6(OH)_6(H_2O)_6$	Zr:Ni:Hf = 4:1:1	Zr:Ni:Hf = 3.5:1:0.91
PCN-202(Ni)-Zr	$[Zr_6O_4(OH)_4]_4[Zr_6O_4(OH)_4]$ $(Ni\text{-}TCPP)_6(DCDPS)_{12}(HDPDCS)_6(OH)_6(H_2O)_6$	Zr:Ni = 5:1	Zr:Ni = 5.5:1
PCN-201(Fe)-Cu	$[Zr_6O_4(OH)_4]_4(CuI)_{12}$ $(FeCl\text{-}TCPP)_6(INA)_{24}$	Zr:Fe:Cu = 4:1:2	Zr:Fe:Cu = 3.8:0.7:2

ICP-MS Analysis. Samples were prepared in triplicate with weights of around 3 mg. Each sample was dissolved in J.T. Baker Ultrex® II Ultrapure 70% nitric acid at 70 °C for 12 hours. Samples were then diluted to 150x in 1% nitric acid and 18.2 MΩ water from Millipore Milli-Q® water purification system. Calibration standards were prepared from certified reference standards from RICCA Chemical Company. Samples were further analyzed with a Perkin Elmer NexION® 300D ICP-MS. Resulting calibration curves have minimum $R^2 = 0.9999$. Additionally, in order to maintain accuracy, quality control samples from certified reference standards and internal

standards were utilized. The individual results of the triplicate samples were averaged to determine the metal ratios.

Thermogravimetric Analysis. All the MOF samples were activated before thermogravimetric measurement. For thermogravimetric analysis, about 10 mg of the sample was heated on a TGA Q500 thermogravimetric analyzer from room temperature to 800 °C at a rate of 5 °C·min^{-1} under N_2 flow of 15 mL·min^{-1}. The result of thermogravimetric analyses for all the samples were shown in Figure 106 and Figure 107. The TGA curves of PCN-224(Ni) and PCN-202(Ni)-Zr were compared in Figure 108. The initial weight loss before 185 °C (5.755% for PCN-224(Ni) and 2.956% for PCN-202(Ni)-Zr) is attributed to the removal of the water molecule in the pores. The weight loss from 185 °C to 265 °C is attributed to the removal of coordination water on the cluster, which is comparable to the theoretical mass percentage (calc. 7.244% for PCN-224(Ni) and 1.125% for PCN-202(Ni)-Zr). It should be pointed out that the terminal H_2O/OH^- groups on the Zr_6 clusters in PCN-224(Ni) is replaced by carboxylate groups from DCDPS linkers to form PCN-202(Ni)-Zr so that the H_2O content in PCN-224(Ni) is much higher than that in PCN-202(Ni)-Zr. This matched well with the experimental data. The decomposition of the framework starts at around 400 °C for PCN-224(Ni) and 450 °C for PCN-202(Ni)-Zr. The mass loss corresponding to the thermal decomposition of organics is 46.18% for PCN-224(Ni) and 65.80% for PCN-202(Ni)-Zr, which match well with the calculation (calc. 49.98% for PCN-224 and 68.51% for PCN-202(Ni)-Zr). PCN-202(Ni)-Zr shows higher thermal stability compared to PCN-224(Ni) possibly because of the higher connection number of Zr_6 clusters (Figures 106-108).

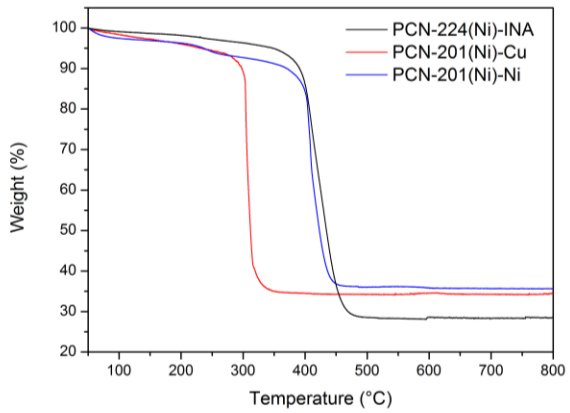

Figure 106. Thermogravimetric analyses (TGA) of PCN-224(Ni)-INA, PCN-201(Ni)-Cu and PCN-201(Ni)-Ni.

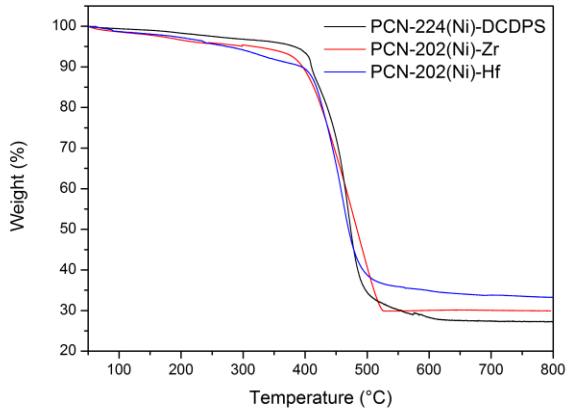

Figure 107. Thermogravimetric analyses of PCN-224(Ni)-DCDPS, PCN-202(Ni)-Hf and PCN-202(Ni)-Zr.

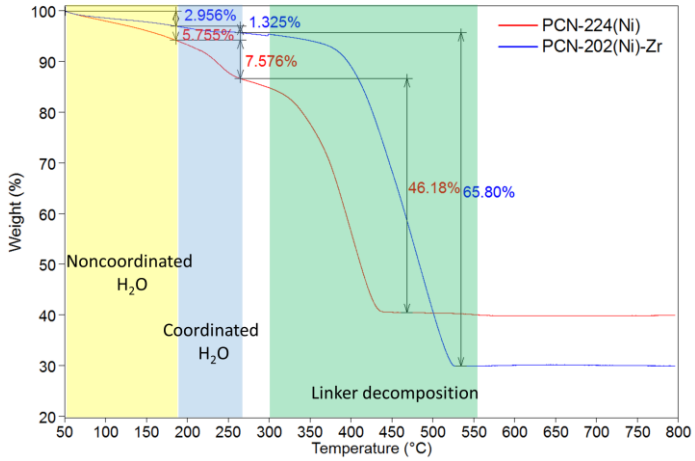

Figure 108. A comparison of TGA curves for PCN-224(Ni) and PCN-202(Ni)-Zr.

Single-crystal to Single-crystal Transformation Studies. To show that PCN-224 undergoes single crystal to single crystal transformation to generate PCN-202(Ni)-Hf, control experiments was conducted. The crystal of PCN-224(Ni) were observed by microscope during the modification process, which shows no change of crystal size or crystal shape (Figure 109). The solution is colorless throughout the treatment of DCDPS and $HfCl_4$, indicating no dissolution of PCN-224(Ni). For comparison, the DMF solution containing 1 mg TCPP has a dark red color. The supernatant was separated and analyzed by UV, which eliminate the existence of TCPP (Figure 111). The microscopic images of crystals for PCN-224(Ni), PCN-201(Ni)-Cu, PCN-201(Ni)-Ni, PCN-202(Ni)-Hf, PCN-202(Ni)-Zr, and PCN-201(Fe)-Cu were also compared in Figure 110 which show almost identical size. These experimental results confirm that the formation of PCN-202(Ni)-Hf from PCN-224(Ni) is a single crystal to single crystal transformation process instead of a dissolution-recrystallization process (Figures 109-111).

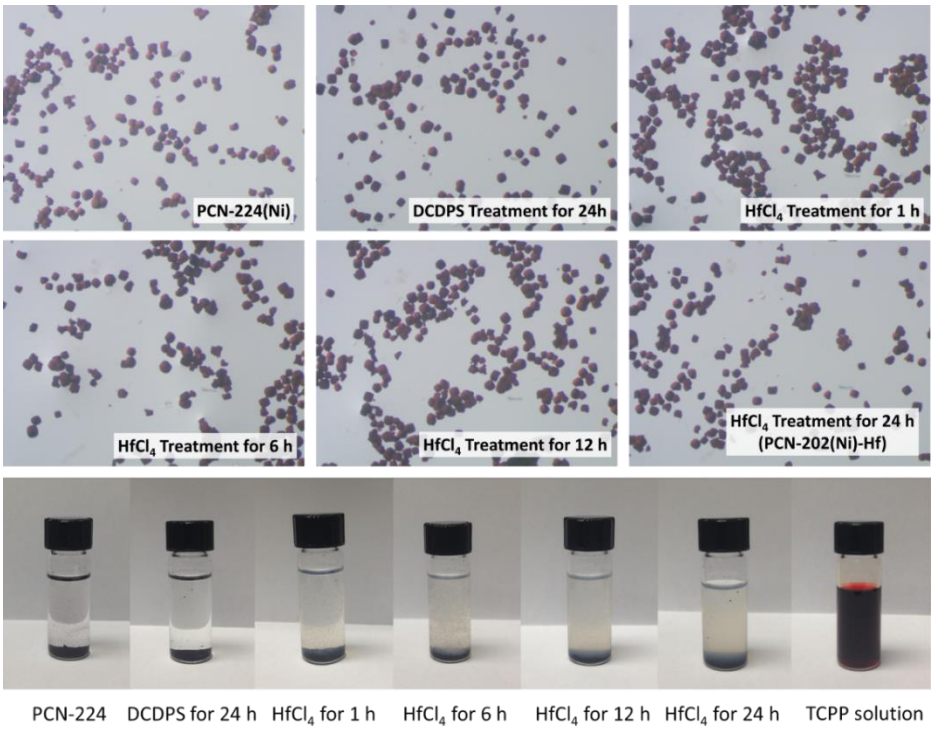

Figure 109. Photos of crystals during the formation of PCN-202(Ni)-Hf.

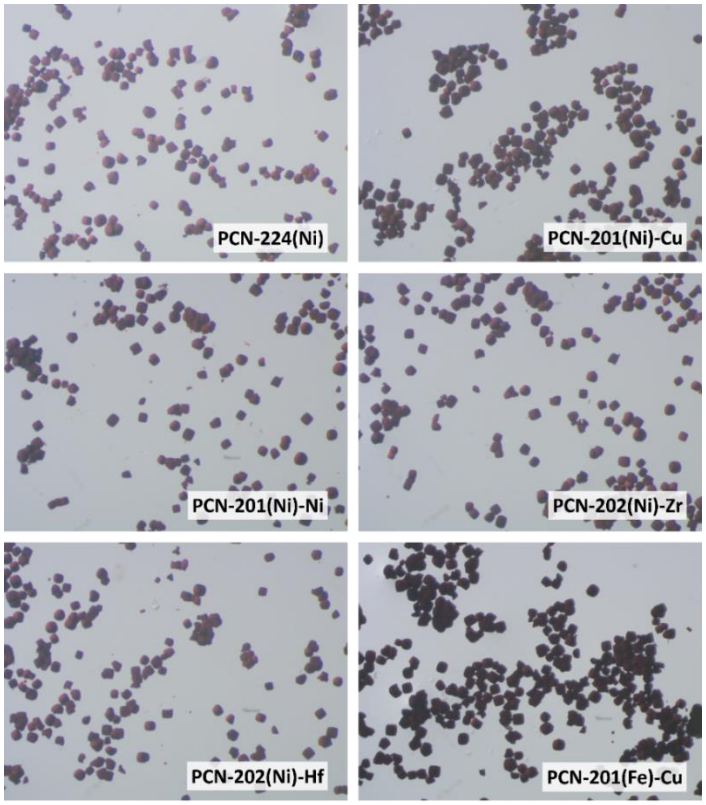

Figure 110. Microscopic images of PCN-224(Ni), PCN-201(Ni)-Cu, PCN-201(Ni)-Ni, PCN-202(Ni)-Zr, PCN-202(Ni)-Hf, and PCN-201(Fe)-Cu.

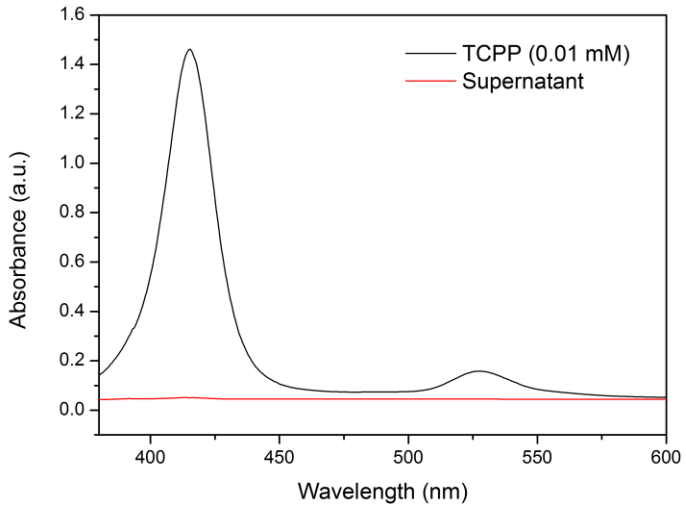

Figure 111. UV spectrum of TCPP solution and the supernatant during the synthesis of PCN-202(Ni)-Zr.

6.3 Results and Discussion

6.3.1 Kinetic Analysis

Chemists approach the synthesis of complex organic molecules by identifying simpler molecules that can be modified rationally or linked through covalent bonds by sequentially applying a set of known chemical reactions[189]. Organic synthesis takes robust covalent bond as its base, which allows for further modification of functional groups or connection with other moieties without breaking the molecular backbone. Researchers have thus developed and applied numerous chemical reactions that together form a reaction library. The idea of MOF retrosynthesis conceptually parallels the retrosynthetic analysis used for organic synthesis: organic linkers and metal clusters are sequentially linked by coordination bonds to form pre-designed MOF structures. However, fundamental differences between organic molecules and MOFs might hamper the realization of MOF retrosynthesis. Unlike covalently linked organic molecules, MOFs are mostly composed of relatively labile coordination bonds, which could break when multiple modification reactions are performed post-synthetically. To address this, we proposed a kinetic analysis for the design and construction of multi-component MOFs. First, the proposed MOF structure is broken down into available organic linkers and metal clusters. Second, the organic linkers and metal clusters as synthons are sequentially assembled under kinetic guidance. In order to maintain the structural integrity of the MOF during multi-step reactions, the most robust coordination bond, which usually requires harsh solvothermal reaction conditions, is formed initially. Other synthons are subsequently anchored onto the framework by labile coordination bonds formed under relatively mild condition. The whole process is controlled by kinetics so that different components can be precisely placed at designated positions within the crystal lattice while maintaining the structural intactness of the MOF backbone to the maximum extent. Therefore, multi-component

MOFs as kinetic products could be isolated by circumventing the undesirable thermodynamic sink in a "one-pot" reaction. Since previous studies have demonstrated the feasibility of post-synthetic incorporation of two essential parts of MOFs, organic linkers and inorganic metal clusters[24, 57], we have reason to believe that multi-component MOFs can be synthesized by sequential installation of linkers and metal clusters in a prototype MOF through a series of known chemical reactions.

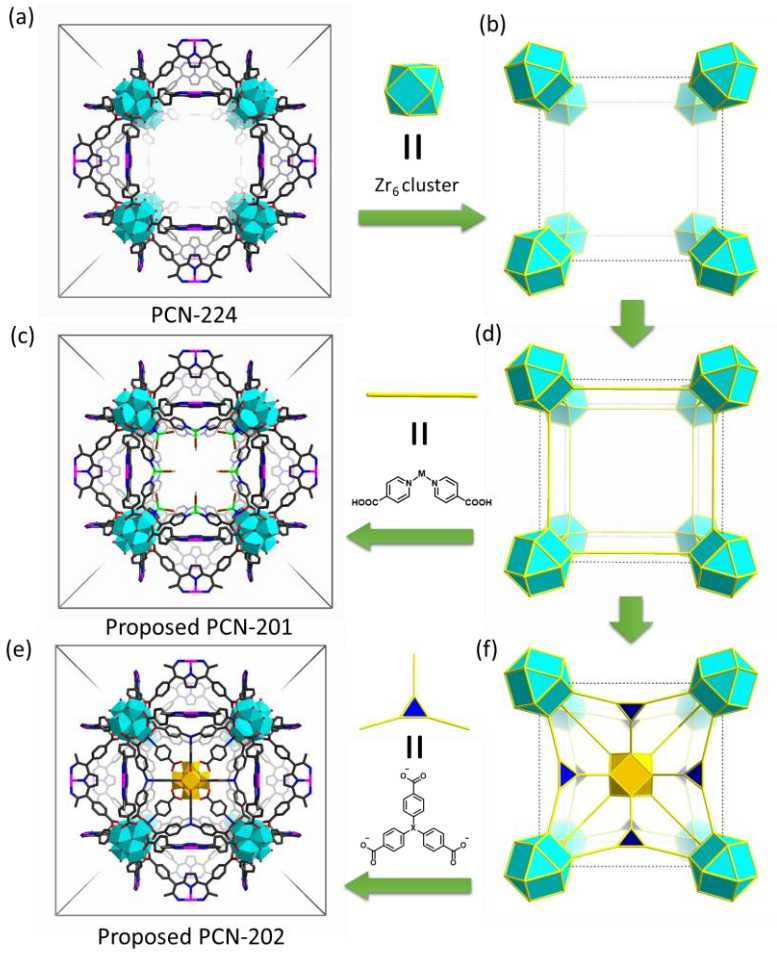

Figure 112. Design of multi-component MOFs based on PCN-224 prototype. (a) The unit cell of PCN-224 and (b) the cubic cage confined by 8 clusters. (c) The unit cell of proposed structure PCN-201 and (d) the topological representation of PCN-201 with linear metal-INA fragments incorporated. (e) The unit cell of proposed structure PCN-202 and (f) the topological representation of PCN-202 with a tritopic linker and 12-connected cluster incorporated.

We initially sought for a parent MOF that could be used as a scaffold for the incorporation of organic and inorganic components. To be used for such purposes, three criteria need to be satisfied: i) There must exist binding sites for the installation of hetero-linkers or clusters, ii) large cavities to provide sufficient space for the subsequent incorporation of metal–organic moieties, and iii) high chemical stability to ensure the structural intactness during multiple modification reactions. Following an analysis of reported MOFs, we found that a zirconium-MOF, PCN-224, fulfilled all three criteria[190]. First, PCN-224 is constructed from 6-connected Zr_6 clusters, leaving six pairs of terminal H_2O/OH^- groups poised for the binding of carboxylates. Studies have shown that Zr_6 clusters with unsaturated connectivity readily coordinate with carboxylate ligands by replacing the terminal H_2O/OH^- groups *via* acid and base reactions[29, 110]. Second, PCN-224 is highly porous with a large cavity (approximately 2 nm in diameter), which is sufficient for further installation of organic linkers and incorporation of inorganic clusters. Third, the high chemical stability of PCN-224 ensures its structure intactness during harsh modification conditions. Therefore, PCN-224 is selected as an ideal candidate for the incorporation of secondary linkers and metal clusters.

The PCN-224 structure contains a large cubic cage confined by eight Zr_6 clusters (Figure 112a). Three pairs of terminal H_2O/OH^- from each Zr_6 cluster are exposed to the inner wall of the cage (Figure 112b). Noticeably, terminal H_2O/OH^- groups from each pair of neighboring Zr_6 clusters can be connected by bent ditopic fragments (Figure 112d). Thus, a metal-isonicotinate (M-INA) fits the space ideally. As shown in Figure 112c, a model, namely PCN-201, was built by installing M-INA between each pair of adjacent Zr_6 clusters. A careful examination of the PCN-224 structure indicates that the terminal H_2O/OH^- groups from each pair of neighboring Zr_6 clusters can be bridged by tritopic linkers, thereby forming a cube in which each linker acts as an

edge (Figure 112f). The cube contains 12 edges, each with a dangling carboxylate pointing towards the cubic center, so that a 12-connected inorganic SBU will fit into the center. Considering the lengths of linkers and size of clusters, we proposed that the combination of a tritopic organic linker and a 12-connected inorganic SBU would fit the cubic cage of PCN-224, thus forming a new MOF named PCN-202 (Figure 112e).

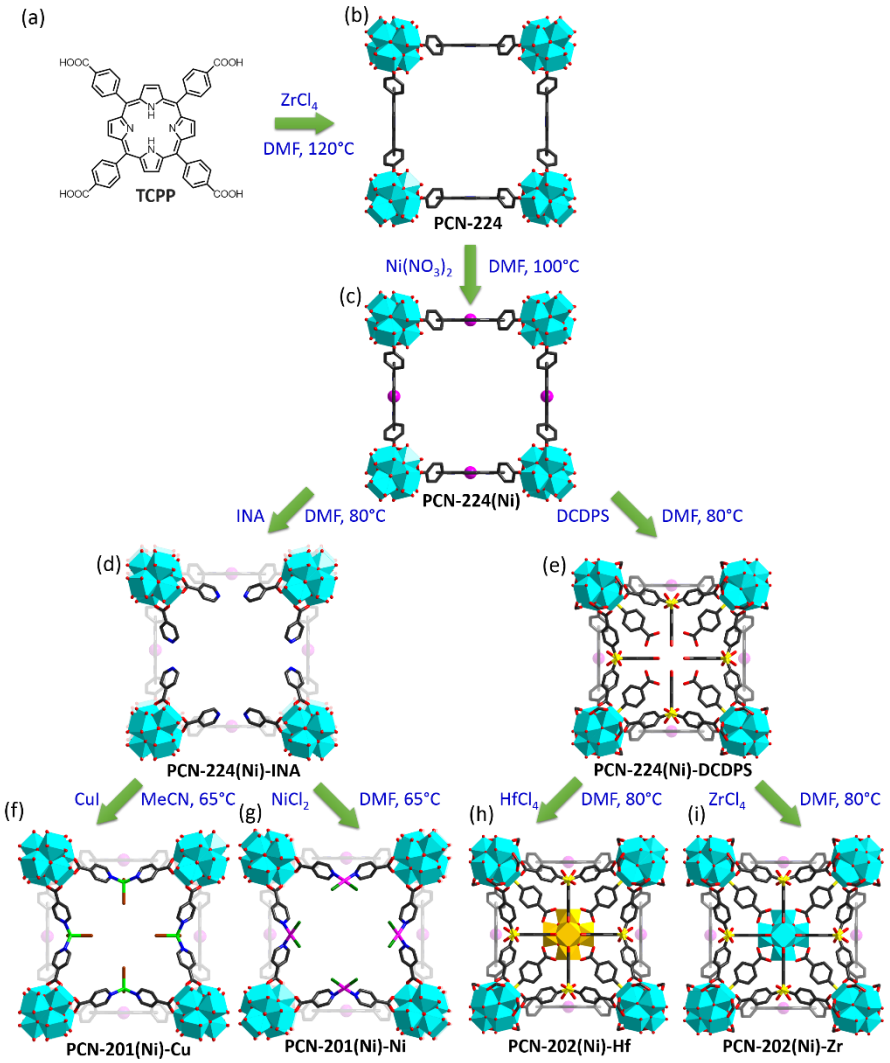

Figure 113. Synthetic approaches of multi-component MOFs. (a) TCPP linker (b) PCN-224, (c) PCN-224(Ni), (d) PCN-224(Ni)-INA, (e) PCN-224(Ni)-DCDPS, (f) PCN-201(Ni)-Cu, (g) PCN-201(Ni)-Ni, (h) PCN-202(Ni)-Hf, and (i) PCN-202(Ni)-Zr.

6.3.2 Retrosynthesis of Multi-Component MOFs

Guided by kinetic considerations, the robust PCN-224 was initially synthesized by the reaction of $ZrCl_4$ and TCPP (TCPP = tetrakis(4-carboxyphenyl)porphyrin) at 120 °C with benzoic acid as the modulating reagent (Figure 113a and b). The crystals of PCN-224 were washed with water and 1 M HCl/DMF solution to remove dangling ligands on the Zr_6 clusters and the weakly bonded Zr^{4+} on the porphyrin center. The vacant porphyrin center readily chelated transition metals with +2 or +3 oxidation states. Because of the chelating effect, the metalloporphyrin became robust enough to survive further modification reactions. As a proof of concept, the porphyrin center of PCN-224 was metallated with Ni^{2+} by incubating PCN-224 crystals in $Ni(NO_3)_2$/DMF solution (70 mM) at 100 °C overnight (Figure 113c). The single crystal structure clearly indicated the existence of Ni^{2+} at the center of the porphyrin linker. The crystals of PCN-224(Ni) were further treated with the INA solution in DMF (30 mM) resulting in the selective binding of INA to the coordinatively unsaturated sites of Zr_6 clusters through carboxylates (Figure 113d). According to the hard and soft acids and bases theory, the carboxylate group will bind to the coordinatively unsaturated sites of Zr_6 clusters by replacing the terminal H_2O/OH^- groups leaving the pyridyl moiety open. A pair of pyridyl groups from neighboring Zr_6 clusters forms a vacant bipyridyl moiety allowing the binding of most transition metal ions under proper conditions. As a proof of concept, a Cu^+ or a Ni^{2+} ion was installed into the PCN-224(Ni)-INA to form PCN-201(Ni)-Cu and PCN-201(Ni)-Ni respectively. The Cu^+ ions were installed in PCN-224(Ni)-INA by reacting with CuI solution in MeCN (70 mM) at 65 °C (Figure 113f). Similarly, the bipyridyl moiety of PCN-224(Ni)-INA was metallated with Ni^{2+} by treating with $NiCl_2$ solution in DMF (70 mM) at 65 °C (Figure 113g). PCN-201(Ni)-Cu and PCN-201(Ni)-Ni were characterized by single crystal X-ray diffraction (SC-XRD), which clearly showed the existence and coordination environment

of the subsequently incorporated Cu^{+} and Ni^{2+}. According to the crystal structure, the Cu^{+} center was chelated by two pyridyl groups from INA ligands and further coordinated with a solvent and an I^{-} counterion, thereby achieving a tetrahedral geometry. On the other hand, Ni^{2+} formed a square planar coordination environment by coordinating with two pyridyl groups from INA ligands and two Cl^{-} as counterions.

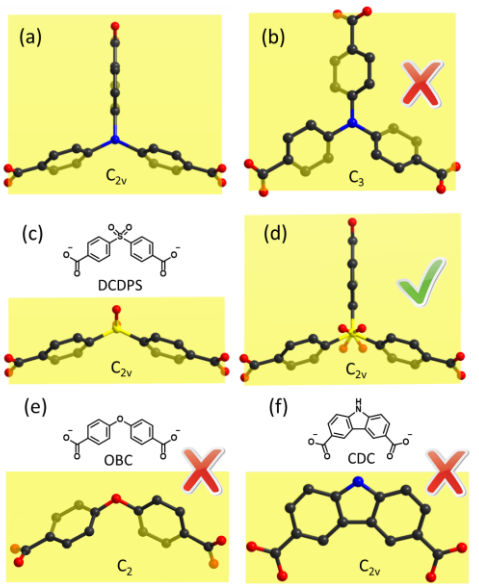

Figure 114. (a) TPA conformation in the proposed structure, (b) TPA conformation in its free state, (c) DCDPS conformation in its free state, (d) disordered DCDPS linker, (e) and (f) conformation and symmetry of OBC and CDC.

Similar experiments were carried out to synthesize the proposed structure of PCN-202 using tritopic linkers, TPA (4,4′,4″-Tricarboxytriphenylamine) for example, but to no avail. We reason that the formation of the proposed structure required TPA in an unfavorable conformation. In order to fit the pore environment of PCN-224, TPA needs to adopt a C_{2v} symmetry with each phenyl ring perpendicular to the equatorial plane as shown in Figure 114a. However, TPA molecules tend to exhibit a C_3 symmetry (Figure 114b), which is not compatible with the PCN-224 structure. To solve this problem, we employed DCDPS (4,4′-dicarboxydiphenyl sulfone) as a

linker instead of TPA. Although DCDPS is a ditopic linker with a bent conformation (Figure 114c), it crystallographically appears as a triangular linker if it is disordered (Figure 114d). Each phenyl ring of DCDPS was perpendicular to the equatorial plane, which ideally matched the pore environment of PCN-224. Compared to TPA, DCDPS is a semi-flexible linker that can adjust its conformation to a certain extent. This will ensure the successful coordination of DCDPS to the cavity of PCN-224 even if the linker length and bond angle do not exactly match the pore environment.

Crystals of PCN-224(Ni) were treated with a DMF solution of DCDPS (30 mM, 15 mL) at 75 °C for 24 h (Figure 114e). As shown by the crystal structure, DCDPS was coordinated on the vacant sites of Zr_6 clusters by replacing terminal H_2O/OH^- groups. Given the flexible conformation of the dangling DCDPS and the disorder caused by the framework symmetry, it is difficult to precisely determine the occupancy of DCDPS in this intermediate structure by crystallography. Based on the ^{1}H-NMR data of the digested samples, the DCDPS:TCPP ratio is about 4:1 which equals to 6 DCDPS on each Zr_6 clusters. This result indicates that all terminal H_2O/OH^- groups are replaced by a dangling DCDPS with only one coordinated carboxylate group. After the DCDPS treatment, a solution of $HfCl_4$ (100 mM) and AcOH (400 mM) in DMF (5 mL) was added. The mixture was heated at 80 °C for 24 h to afford crystals of PCN-202(Ni)-Hf (Figure 114h). PCN-202(Ni)-Zr was also assembled under similar synthetic conditions except that $ZrCl_4$ was used instead of $HfCl_4$ (Figure 114i). The crystal structure of PCN-202(Ni)-Hf and PCN-202(Ni)-Zr showed the same backbone structure as PCN-224(Ni) with Hf_6 (or Zr_6) clusters in the pore center and DCDPS bridging the neighboring Hf_6 (or Zr_6) clusters. It should be noted that the conformation of the linkers was important for the formation of PCN-202. Two other linkers, OBC and CDC, with C_2 and C_{2v} symmetry respectively, have also been attempted to construct PCN-202 structures

(OBC = 4,4′-oxybisbenzoate, CDC = 3,6-carbazoledicarboxylate). Although they have approximately the same size with DCDPS, the dihedral angles between the carboxylate group and the equatorial plane (~40° for OBC and 0° for CDC) are not suitable for the PCN-202 structure. Therefore, they did not give rise to PCN-202 under identical synthetic condition.

The SC-XRD data unambiguously showed the stepwise incorporation of organic linkers and formation of metal clusters, which ruled out the possibility of MOF dissolution and recrystallization. Furthermore, microscopic observation of the crystal during modification showed no change in crystal size or shape. Moreover, the solution was colorless throughout the treatment with DCDPS and $HfCl_4$ solution, thereby indicating no dissolution of PCN-224(Ni) which would release dark red TCPP. The supernatant was further separated and analyzed by UV and ICP, which eliminated the possible existence of TCPP or Zr^{4+} that could be generated by the decomposition of PCN-224(Ni). Such results confirmed that the formation of PCN-201 and PCN-202 from PCN-224(Ni) was a single crystal to single crystal transformation process instead of a dissolution-recrystallization process.

The formation process of PCN-201 and PCN-202 was carried out under rigorous kinetic control. The assembly of all the components in a “one-pot” reaction always ends up with thermodynamically favored PCN-224 as the main product whereas other labile components were excluded from the product. The sequence of each process was also designed by kinetic considerations which were essential for the formation of the targeted structure. For example, if the porphyrin center was initially unoccupied, Cu-porphyrin would form during the treatment with CuI solution, which could hardly be replaced by other metals given the strong chelating effect of porphyrin. The sequence of linker installation and cluster incorporation was also critical for the final structure. When the CuI and INA were simultaneously introduced to the reaction system, Cu-

INA-based coordination polymers were immediately formed as impurities. Likewise, if $HfCl_4$ and DCDPS were added simultaneously, those two components tend to form a gel in the solution instead of an ordered structure in the MOF cavity. Furthermore, the one-pot synthesis of PCN-201 and PCN-202 were attempted starting from a mixture of organic linkers and metal salts, which did not give rise to desired products. Indeed, the self-assembly of organic linkers and metal cations in a one-pot reaction is essentially a black box. Different combinations of metal cations and ligands make it exceedingly difficult to control the product. More importantly, the formation condition of different metal–organic species in a multi-component MOF requires different solvents, temperatures and metal-ligand ratios, which are almost impossible to satisfy in a one-pot reaction. Indeed, MeCN as solvent favors the dissolution of CuI and the formation of CuI-based MOFs but disfavors the crystallization of Zr-based MOFs. Meanwhile, the synthesis of Zr-based MOFs usually requires an excess amount of acid as modulating reagent, which prohibits the formation of CuI or Ni-based MOFs. The multistep synthesis with kinetic considerations allows the integration of different metal SBUs into one framework by avoiding the undesired thermodynamic sink. The successful synthesis of PCN-201 and PCN-202 highlights the power of kinetic analysis for the construction of multi-component MOFs.

6.3.3 Structure Description

PCN-201(Ni)-Cu and PCN-202(Ni)-Hf represent rare cases of quaternary MOFs composed of up to three different metals and two different linkers, each compartmentalized in a predetermined array within the crystal lattice. For clarity, the structures of PCN-201(Ni)-Cu and PCN-202(Ni)-Hf were described and compared with their parent PCN-224(Ni). PCN-201(Ni)-Cu crystallized in the cubic space group *Im*-3*m*. Crystallographically, it contains a 12-connected Zr_6 cluster, a pair of Cu^+ bridged INA (Cu-INA_2), and a metalloporphyrin linker with Ni^{2+} in the center.

Each Zr_6 cluster was connected by six adjacent TCPP linkers forming the scaffold structure (PCN-224) which can be simplified into a 4,6-connected net with **she** topology (Figure 115a and e). Each Cu-INA_2 moiety bridges the neighboring Zr_6 cluster to fulfill the structure of PCN-201(Ni)-Cu. Topologically, the 12-connected metal clusters can be regarded as cuboctahedron nodes and tetratopic TCPP linkers can be viewed as square nodes (Figure 115d). The Cu-INA_2 moiety was treated as a linear linker for clarity. The overall structure was analyzed to be a 4,12-connected net with a point symbol of $\{3^{12}.4^{18}.5^{24}.6^{12}\}_2\{3^4.4^2\}_3$ determined by TOPOS 4.0 (Figure 115b and f)[155]. The new topology was named as **tam** and included in the reticular chemistry structure resource (RCSR) database[191].

Single-crystal X-ray analysis revealed that PCN-202(Ni)-Hf also crystallized in the cubic space group *Im*-3*m* (Figure 5c). It contains a 12-connected Zr_6 cluster, a 12-connected Hf_6 cluster, a disordered DCDPS linker and a Ni^{2+} centered metalloporphyrin linker. Each component is precisely located at a predetermined position within the periodic lattice. It has the same backbone structure as PCN-224(Ni), which is formed by the connection of 6-connected Zr_6 clusters and tetratopic TCPP linkers. The DCDPS is 2-fold disordered in the crystal lattice so that it appears as a 3-connected linker. Crystallographically, twelve "tritopic" DCDPS linkers bridged eight neighboring Zr_6 clusters into a cube with side lengths of ~2 nm. Each "tritopic" DCDPS linker on the edge of the cube is connected to a pair of Zr_6 clusters, thereby leaving a dangling carboxylate pointing towards the cube center. The twelve dangling carboxylates form a natural pocket for a 12-connected cluster, which ideally accommodates a Hf_6 cluster. Topologically, the 12-connected metal cluster can be regarded as cuboctahedron nodes and tetratopic TCPP linkers can be viewed as square nodes (Figure 5d). The DCDPS linker is 2-fold disordered in the structure so that it is regarded as a 3-connected triangle node for simplicity. The overall structure can be simplified into

a 3,4,12,12-connected net with a point symbol of $\{4^{24}.6^{36}.8^{6}\}_5\{4^{3}\}_{12}\{4^{4}.6^{2}\}_6$, namely **amu** (Figure 115g).

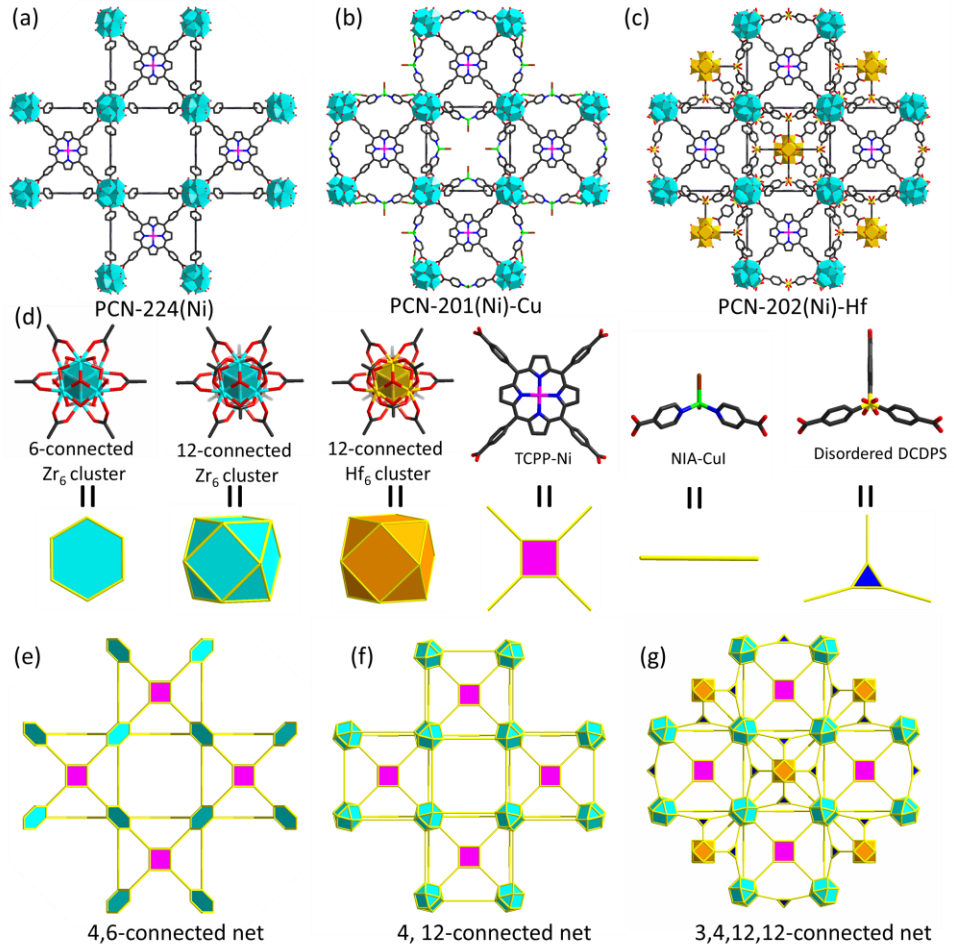

Figure 115. Structure of PCN-224(Ni), PCN-201(Ni)-Cu and PCN-202(Ni)-Hf. (a), (b), and (c) Crystal structures of PCN-224(Ni), PCN-201(Ni)-Cu and PCN-202(Ni)-Hf, (d) building units and their simplified topological elements, (e), (f), and (g) topologies of PCN-224(Ni), PCN-201(Ni)-Cu and PCN-202(Ni)-Hf.

To clarify the connection of the disordered DCDPS linker, we simulated an ordered structure of PCN-202(Ni)-Hf by reducing the space group from *Im*-3*m* to *I*-43*m*. The reduced space group will eliminate the disorder of the DCDPS linker by removing the mirror plan passing through its center. In the simulated structure, each DCDPS linker is 2-connected to a Zr_6 cluster and a Hf_6

cluster. Therefore, each Zr_6 cluster is 9-connected to six TCPP and three DCDPS respectively, while each Hf_6 cluster is 12-connected to DCDPS linkers. Three pairs of DCDPS linkers bridge a pair of Zr_6 and Hf_6 clusters so that they are topologically simplified into an edge. Consequently, Zr_6 clusters are regarded as 5-connected hexagonal pyramid nodes while Hf_6 clusters are reduced into 4-connected tetrahedron nodes. The overall structure is simplified into a 4,4,7-connected net with a point symbol of $\{4^4.6^2\}_6\{4^6.6^{15}\}_4\{6^6\}$, namely **hcz**. Note that the topology of ordered structure depends on the space group that is chosen to eliminate the disorder. Different topologies might have resulted if other space groups were selected to simplify the structure.

6.3.4 Stability and Porosity

Based on the single crystal structure, ^{1}H-NMR and elemental analysis data, the formula of PCN-201(Ni)-Cu, PCN-201(Ni)-Ni, PCN-202(Ni)-Hf and PCN-202(Ni)-Zr were determined as $(Zr_6O_4(OH)_4)_4(CuI)_{12}TCPP_6INA_{24}$, $(Zr_6O_4(OH)_4)_4(NiCl_2)_{12}TCPP_6$ INA_{24}, $(Zr_6O_4(OH)_4)_4$ $(Hf_6O_4(OH)_4)TCPP_6DCDPS_{12}HDCDPS_6(OH)_6(H_2O)_6$, and $(Zr_6O_4(OH)_4)_5$ $TCPP_6DCDPS_{12}$ $HDCDPS_6(OH)_6(H_2O)_6$, respectively. Their compositions were further confirmed by EDX, ICP-MS experiments. Elemental mapping at the microstructural level by SEM with EDS showed a uniform distribution of metals and ligands throughout the crystal, indicating a homogeneous crystalline material. The incorporation of hetero-metal-clusters and organic linkers slightly changed the X-ray diffraction of the material as recognized on powder X-ray diffraction (PXRD) patterns. New peaks emerge at 7.2, 10.7 and 11.7 degrees (2θ) in the PXRD pattern of PCN-201(Ni)-Cu, which matched well with simulations. In the PXRD of PCN-201(Ni)-Ni, the peak at 3.3 degrees disappears, while two additional peaks appear at 7.3 and 10.9 degrees. The PXRD patterns of PCN-202(Ni)-Zr and PCN-202(Ni)-Hf are almost identical and differ from PCN-224(Ni) at 8.6, 10.8 and 11.8 degrees.

PCN-224(Ni), PCN-201(Ni)-Cu, PCN-201(Ni)-Ni, PCN-202(Ni)-Hf and PCN-202(Ni)-Zr were also analyzed by TGA. The initial weight loss before 185 °C is attributed to the removal of the water molecules in the pores, whereas the removal of coordinated water on the Zr_6 cluster corresponds to the weight loss from 185 to 265 °C. PCN-224(Ni) shows much higher weight loss than other samples before 265 °C due to the water removal from Zr_6 clusters (7.576% for PCN-224(Ni) and ~1% for other samples). Presumably, the terminal H_2O/OH^- groups on the Zr_6 clusters are replaced by carboxylate groups in PCN-201(Ni)-Cu, PCN-201(Ni)-Ni, PCN-202(Ni)-Hf and PCN-202(Ni)-Zr so that the water content in PCN-224(Ni) is far greater than other MOFs. The decomposition of PCN-201(Ni)-Cu starts at 300 °C, whereas other MOFs do not show obvious mass loss until 400 °C. This is tentatively attributed to the redox active Cu that catalyzes the oxidative decomposition of the framework. The further weight losses corresponding to the thermal decomposition of organic fragments match well with the calculation.

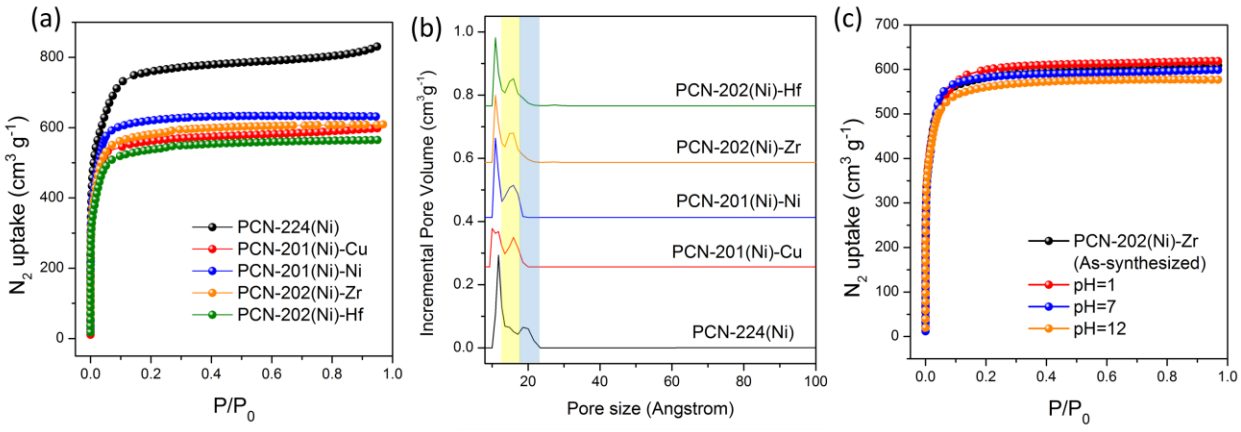

Figure 116. Gas sorption measurements for PCN-224(Ni) and its derivatives. (a) N_2 adsorption isotherms of PCN-224(Ni) and its derivatives at 77 K. (b) Pore size distributions of PCN-224(Ni) and its derivatives calculated from N_2 adsorption isotherms. (c) N_2 adsorption isotherms of PCN-202(Ni)-Zr upon treatments in pH = 1, 7 and 12 aqueous solutions.

The N_2 adsorption isotherms of PCN-201(Ni)-Cu, PCN-201(Ni)-Ni, PCN-202(Ni)-Hf and PCN-202(Ni)-Zr were measured and show a clear decrease of N_2 total uptake compared with PCN-224(Ni), corresponding to the cavity filled by subsequently introduced linkers and clusters (Figure 116a). More importantly, the large cavity observed in the crystal structure of PCN-224(Ni) with a diameter of ~2 nm was occupied by metal–organic species so that a decrease in the pore diameter was observed by the pore size distributions derived from N_2 isotherms (Figure 116b). The subsequently incorporated component significantly changed the pore environment, which in turn affected the gas adsorption properties. Indeed, the volumetric H_2 adsorption capacity of PCN-202(Ni)-Zr increased by 64% compared to the parent framework PCN-224(Ni).

The stabilities of PCN-201(Ni)-Cu, PCN-201(Ni)-Ni, PCN-202(Ni)-Hf and PCN-202(Ni)-Zr were also tested. By virtue of the robust Zr (or Hf)-carboxylate bond, PCN-202(Ni)-Hf and PCN-202(Ni)-Zr show high stability in aqueous solution with pH ranging from 1 to 12 (Figure 116c). The PXRD patterns and N_2 isotherms verified the intactness of frameworks after the stability test. ^{1}H-NMR and ICP results of digested MOF samples further confirmed that the composition of materials remained unaffected by the acid or base treatment. Interestingly, PCN-201(Ni)-Cu and PCN-201(Ni)-Ni also show good water stability although the labile Cu-pyridyl or Ni-pyridyl are often believed to be water sensitive. This phenomenon indicated that the robust MOF backbone could reinforce the labile moieties in the structure, which has been previously observed in multicomponent MOFs composed of different inorganic SBUs[192]. It should be noted that the growth of a secondary metal node on the installed linker stabilized the dangling linkers by reinforcing them. For example, the dangling INA or DCDPS ligands on PCN-224(Ni)-INA and PCN-224(Ni)-DCDPS can be easily removed by water treatment. However, once the ligand bound with metals to form PCN-201(Ni)-Ni and PCN-202(Ni)-Hf, the entire structure became water

stable. The reinforcement effect suggests the possibility of incorporating catalytically active metal clusters into a robust MOF by stepwise synthesis, which is otherwise difficult to realize since some active metal clusters are often too labile to support a stable framework.

6.3.5 Cooperative Bimetallic Catalysis

The retrosynthesis of multi-component MOFs affords a new level of control over MOF structures and their related properties, which leads to highly tunable multifunctional MOF systems. Herein, we demonstrate that a cooperative bimetallic catalytic system can be constructed in PCN-201(Fe)-Cu by introducing Fe-porphyrin and Cu-pyridyl simultaneously. The Fe-porphyrin and Cu-pyridyl moieties cooperate as a Lewis acid and a nucleophile activator, respectively, leading to improved catalytic activity towards three-component, one-pot Strecker reactions.

Cooperative multimetallic activation is a common feature in enzyme catalysis[193]. In many enzymes, two or more metal centers in the active site are able to activate both nucleophilic and electrophilic reactants leading to improved kinetics and higher selectivity. Inspired by these natural systems, researchers are now developing dual activation catalysts[194]. For example, the combination of Lewis acids and Lewis bases in a single catalytic system has been applied in cycloaddition reactions between ketene enolates and various electrophiles, cyanosilylation of ketones, Corey–Chaykovsky epoxidation, and catalytic Strecker-type reactions[195-196]. The Strecker reaction is a versatile way of preparing α-aminonitriles through the attack of a nitrile group to an imine group[197]. The resulting α-aminonitriles can be hydrolyzed to obtain α-amino acids or used as intermediates in the preparation of nitrogen-containing heterocycles[198-199]. The three-component, one-pot Strecker reaction goes through *in situ* imine formation and cyano group addition, which relies on the activation of both nucleophile and electrophile[200]. When mononuclear catalysts are used, such double activation is revealed by second order reaction kinetics illustrating that two catalyst nuclei

are involved in the transition state. Therefore, catalysts containing multiple metal centers in an appropriate proximity and arrangement can result in cooperative reaction pathway and better reactivity than the related monometallic systems[201]. In this context, multi-component MOFs represent a convenient path to incorporate multiple catalytic sites in a predetermined array defined by the crystal lattice, which will lead to promising cooperative catalytic effects in a solid state material[202-203]. Coupling two catalytic sites in a MOF offers several additional advantages over homogeneous systems, including easy catalyst separation and recovery, regeneration, and handling.

PCN-201(Fe)-Cu as a cooperative bimetallic catalytic system was assembled *via* stepwise linker installation and metalation. First, PCN-224(Fe) was synthesized by the metalation of PCN-224 with $FeCl_2$ at 100 °C. The Cu-INA fragments were subsequently assembled in PCN-224(Fe) to generate PCN-201(Fe)-Cu. PCN-201(Fe)-Cu is iso-structural to PCN-201(Ni)-Cu except for the Fe^{3+} on the porphyrin center. The catalytic performance of the PCN-201(Fe)-Cu system in three-component, one-pot Strecker reactions is evaluated using benzaldehyde, aniline, and TMSCN (trimethylsilyl cyanide). A catalytic amount of PCN-201(Fe)-Cu leads to the quantitative formation of the α-aminonitrile with a turnover frequency (TOF) of 6000 h^{-1}. For comparison, the catalytic activities of two reference MOF catalysts, as PCN-201(Ni)-Cu and PCN-224(Fe) have also been examined under similar experimental conditions. PCN-201(Ni)-Cu contains the Cu-pyridyl sites, whereas the Lewis acidic Fe-porphyrin center was replaced by inert Ni-porphyrin. PCN-224(Fe) has Lewis acidic Fe-porphyrin centers, while Cu-pyridyl moieties are absent. Neither the individual catalyst nor the combination of the two were found to display a catalytic activity anywhere close to that of PCN-201(Fe)-Cu, indicating the cooperative effect of two catalytically active sites (i.e. Cu-pyridyl and Fe-porphyrin sites).

Table 21. Catalyst performance of PCN-201(Fe)-Cu in the three-component Strecker reaction.[a]

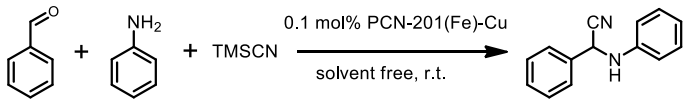

Entry	Catalyst	Substrate	Time (min)	Temprature (°C)	Yield (%)
1	PCN-201(Fe)-Cu	Benzyl aldehyde	10	25	99 ± 1[b]
2	PCN-201(Ni)-Cu	Benzyl aldehyde	10	25	21 ± 8[b]
3	PCN-224(Fe)	Benzyl aldehyde	10	25	24 ± 5[b]
4	PCN-201(Ni)-Cu and PCN-224(Fe) mixture	Benzyl aldehyde	10	25	68 ± 12[b]
5	PCN-201(Fe)-Cu	4-Methylbenzyl aldehyde	10	50	99
6	PCN-201(Fe)-Cu	4-Methoxybenzaldehyde	10	25	92
7	PCN-201(Fe)-Cu	4-Chlorobenzyl aldehyde	10	50	96
8	PCN-201(Fe)-Cu	4-Bromobenzyl aldehyde	10	50	82
9	PCN-201(Fe)-Cu	4-Cyanobenzyl aldehyde	10	50	81
10	PCN-201(Fe)-Cu	4-Nitrobenzyl aldehyde	10	50	68
11	PCN-201(Fe)-Cu	2-Furyl aldehyde	10	25	93
12	PCN-201(Fe)-Cu	Thiophene 2-carboxaldehyde	10	25	82
13	PCN-201(Fe)-Cu	Benzyl aldehyde	10	50	99
14	PCN-201(Fe)-Cu	Benzyl aldehyde	60	25	99
15[b]	PCN-201(Fe)-Cu	Benzyl aldehyde	10	25	96

[a] Reaction conditions: Generally, aldehyde (1 mmol), aniline (1 mmol), TMSCN (1 mmol), and catalyst (0.1 mol% based on Cu or 0.05 mol% based on Fe) were placed in a 4 mL vial and stirred at room temperature for 10 min. Yields were determined by ^{1}H NMR analysis and calculated based on the ratios of product/(product + starting material). [b] Values are mean ± standard error of three repeated experiments. [c] Recycled for 3 times.

Indeed, previous research has shown that the formation of the α-aminonitrile requires the activation of both the imine group and TMSCN, each interact with one of the metal centers. PCN-201(Fe)-Cu represents an integration of high valence Fe^{III} and low valence Cu^{I} centers, which simultaneously activates the electrophiles and nucleophiles. It should be emphasized that the PCN-201(Fe)-Cu is not a simple mixture of the Cu and Fe MOF catalysts. The catalytic performance of a physical mixture of PCN-201(Ni)-Cu and PCN-224(Fe) is much lower than that of PCN-201(Fe)-Cu, which provides strong evidence to the bimetallic cooperative mechanism. For the physical mixture of PCN-201(Ni)-Cu and PCN-224(Fe), reaction intermediates formed at Fe^{III} center in PCN-224(Fe) need to diffuse to the Cu^{I} sites in PCN-201(Ni)-Cu to fulfill the reaction cycle, which slow down the reaction rate. The ordered framework structure of PCN-201(Fe)-Cu affords the periodic arrangement and prearranged proximity of the Fe^{III} and Cu^{I} centers within a cavity, resulting in a cooperative effect and improved catalytic activity.

Encouraged by these results, we explored the substrate scope of PCN-201(Fe)-Cu. As shown in Table 1, different aldehydes were converted to corresponding α-aminonitriles in good yields. A broad substrate scope of substrates bearing electron-rich and electron-deficient functional groups was tolerated. To show the heterogeneous nature of catalysis, hot filtration experiment was conducted by removing the MOF catalyst after 1 min and no further increase of yield was observed within 10 min. To evaluate the recyclability, PCN-201(Fe)-Cu catalyst was simply separated from the mixture at the end of the reaction by centrifugation, washed with acetone, and reused for the next round of reaction. The catalytic activity and crystallinity were well-maintained after three cycles (Table 21). Based on the current work and findings in the literature, a reaction pathway for the Strecker reactions catalyzed by PCN-201(Fe)-Cu was proposed (Scheme 11).[200] First, the aldehyde and amine readily undergo a condensation reaction to form the Schiff base, which could

be further promoted by Lewis acidic Fe^{III} species. The resulting Schiff base as electrophile was further activated by the Fe-porphyrin sites. Meanwhile, the Cu-pyridyl moiety activates the nucleophilic TMSCN by binding to the cyano group. Close proximity ensures the efficient contact of nucleophile and electrophile to form the product. Therefore, PCN-201(Fe)-Cu represents a rare example of cooperative bimetallic catalytic systems built in multi-component MOFs. The stepwise retrosynthesis of multi-component MOFs allowed the placement of different catalysts in a predetermined array within a solid state porous material, which enables the discovery of novel cooperative catalysts with an unprecedented degree of control.

Scheme 11. Proposed mechanism for the three-component Strecker reaction catalyzed by PCN-201(Fe)-Cu.

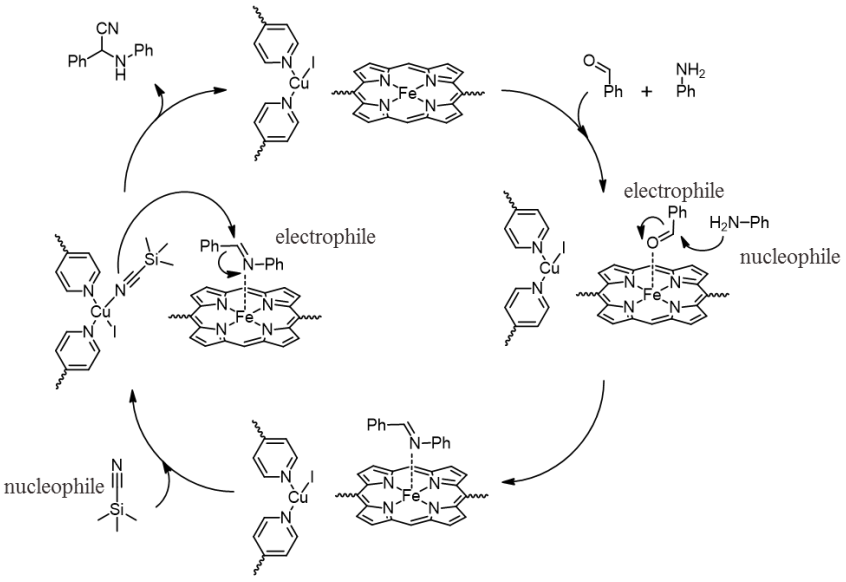

6.4 Conclusions

In conclusion, we demonstrated a “kinetic analysis” method to guide the retrosynthesis of multi-component MOFs. Four complex MOFs with multiple metal–organic domains were constructed in a stepwise manner involving the sequential application of available modification

reactions including linker installation and cluster incorporation under kinetic considerations. To demonstrate the utility of retrosynthesis, a corporative bimetallic catalyst was built in a MOF by the sequential incorporation of two collaborative metal sites. Although many challenges still remain in MOF retrosynthesis, especially in building a reaction library analogous to the large and diverse organic reaction library, the intrinsic designability of MOFs and the fast evolving MOF synthetic methodologies suggest that such a lofty goal is eventually achievable[133, 204].

7. SUMMARY AND PERSPECTIVE*

7.1 Project Summary

Before this work, most multi-component MOFs are prepared through self-assembly of metal ions and organic ligands under solvothermal conditions in a "one-pot" reaction. Although this facile method has led to the discovery of a handful of new structures, the lack of control over the reaction pathway has inherently limited the rational design of multi-component MOFs. Indeed, numerous combinations of metal ions and organic ligands could exist during the "one-pot" synthesis of a multi-component MOF which makes it exceedingly challenging to predict the product. In addition, competitive assembly of metal ions and organic ligands usually results in a thermodynamically favored MOF as main product, which impedes the incorporation of multi-components into a kinetic product. In particular, the incorporation of labile functional groups or metal species by "one-pot" synthesis is difficult considering the harsh solvothermal conditions. The growing gap between MOF design and synthesis has become a critical limitation.

The work in the dissertation has pushed the envelope of MOF synthesis. Under the guidance of kinetic analysis, a series of stepwise synthetic methods were developed to take control over MOF formation. The stepwise synthetic routs allow rational design and construction of multi-component MOFs with heterometals or mixed-linkers. As representative examples, four synthetic methods were introduced to illustrate the potential merits of kinetic analysis. In chapter 2, cluster

*Reproduced in part with permission from: Yuan, S.; Qin, J.-S.; Lollar, C. T.; Zhou, H.-C., Stable Metal–Organic Frameworks with Group 4 Metals: Current Status and Trends. *ACS Cent. Sci.*, **2018**, *4*, 440-450. Copyright 2018 American Chemical Society. Yuan, S.; Qin, J.-S.; Li, J.; Huang, L.; Feng, L.; Fang, Y.; Lollar, C.; Pang, J; Zhang, L.; Sun, D.; Alsalme, A.; Cagin, T.; Zhou, H.-C. Retrosynthesis of multi-component metal−organic frameworks, *Nat. Commun.* **2018**, *9*, 808. Copyright 2018 Nature Publishing Group.

augmentation was explored using preformed bimetallic clusters as starting materials to control the structure of obtained bimetallic MOFs.[35] Chapter 3 presented linker labilization method to create defective MOFs controllably by partially removal of labile linkers.[17] The created defects not only expand the pore sizes, but also act as chemical handles to further anchor organic ligands and metals into MOFs.[31, 34] Using defective MOFs as platforms, linker installation and cluster metalation methods were developed to precisely place functionalized organic linkers or redox active transition metals in a defective MOF matrix, which are discussed in Chapter 4 and 5.[19, 24, 29] Each method represent a step closer to the "total synthesis" of MOFs. Together, a synthetic toolkit is formed, through which a target coordination architecture can be retrosynthetically designed and stepwise synthesized (Figure 117).[28] Using the synthetic toolkit, we have synthesized a series of multi-component MOFs with targeted structures and synergistic properties, which were otherwise unforeseeable to prepare. Our work was also followed up by many research groups within and without the MOF field, leading to exciting results in gas storage, separation, energy harvesting, and catalysis. These works will not only entail significant breakthroughs in the methodology of MOF synthesis, but also promote the understanding of basic scientific principles by shedding light on a wide variety of related areas, including metal-cluster chemistry and chemical kinetics.

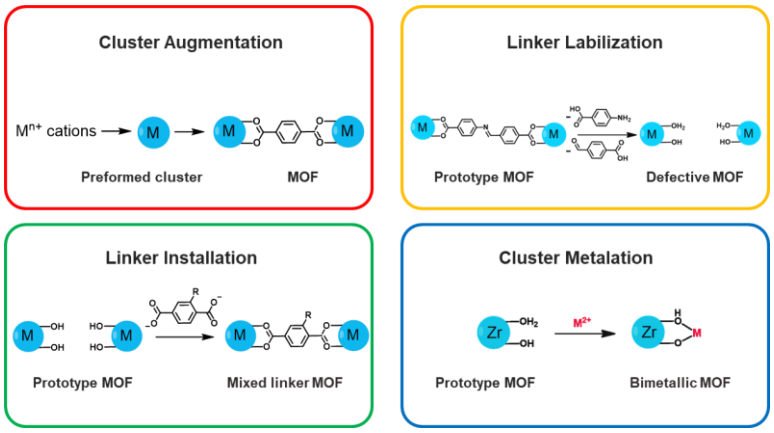

Figure 117. Schematic representation of synthetic methods for multi-component MOFs.

7.2 Outlook: The Future of MOFs

In 1995, Yaghi firstly proposed the concept of MOFs and demonstrated their applications as tunable porous platforms. Since then, MOFs have attracted intense research interest for more than two decades. A large number of new framework structures have been discovered leading to numerous advances in the basic science and applications. Now, MOFs are not only a class of materials, but also a broad concept that includes the fields as diverse as organic chemistry, inorganic chemistry, surface science, heterogenous catalysis, crystal engineering, semiconductor physics, molecular biology, etc. The associated research and applications are equally diverse, including gas storage, separation, chemical sensing, catalysis, energy harvesting, and biomedicine.[123]

Quests for advanced functionalities in MOFs inevitably requires more complex structures and pore environments. The simple MOF structures based on single metal and organic linker are far from enough to satisfy the requirements. Constructing complex MOFs from multiple components is a pathway to achieve sophisticated applications. We propose that the next generation of MOFs should be multi-component MOFs combining synergistic functional groups with controlled sequences in an ordered framework structure. The multi-component MOFs can be achieved by different approaches. They can be synthesized from heterometals (Chapter 2 and 5), mixed linkers (Chapter 4 and 6), or derived from existing MOFs by creating defects (Chapter 3). In addition, hybridization of MOFs with other materials to form composites is another pathway to realize complex functions. Overall, pushing the boundaries of complexity in MOFs by various methods will propel the MOF field into future.

7.2.1 Anisotropic MOFs: Multi-Components Arranged in Sequence

MTV-MOF is a successful example of multi-component MOFs with mixed-linkers.[42] This method involves the co-assembly of a set of organic linkers that share the same backbone but different functional groups. These linkers will be uniformly distributed within the same framework without phase separation. However, the randomly distributed linkers and functional groups have posed a challenge for the structural characterization. X-ray diffraction techniques, a powerful technique to determine MOF structures, do not show the sequence of functional groups because of the substitutional disorder of linkers. To map the multiple functional groups within an MTV-MOF, solid state NMR in combination with molecular modelling techniques need to be adopted. However, it is still a challenge to precisely locate the position of each component due to their disordered distribution.

One way to combat disorder is to use anisotropic MOFs with low symmetry as a matrix. A set of linkers with different symmetry and/or connectivity can be placed at predetermined positions within an anisotropic lattice. These linkers can be easily differentiated from each other by single-crystal X-ray crystallography so that the position of the functional group on each linker can be precisely located. To this end, asymmetric linkers are preferred to reduce the overall symmetry of the frameworks. In a recent work by Telfer and co-workers, mixed-linker MOFs with three crystallographically distinct linkers were synthesized, namely MUF-7 and MUF-77 (Figure 118b).[46] MUF-77 can be regarded as a derivative of previously reported MOF-205 by replacing the medium sized NDC linkers by a longer BPDC and a shorter BDC linker (Figure 118a). It was observed that the truxene-based linker (HETT) favored the formation of MUF-77. What has been overlooked is the effect of low-symmetric HETT linker. Replacing benzenetribenzoate linker (BTB, *D3* symmetry) with HETT (*C3* symmetry) eliminates the C_2 axis passing though the linker,

which in turn reduced the symmetry of the framework. In *P m-3n* space group, the lengths of linear linkers are required to be identical, whereas two linkers with different lengths can be accommodated in *P m-3* space group. In other words, the low-symmetric linkers tend to form anisotropic MOFs with multiple linkers arranged in crystallographically determined sequences. A greater exploration of asymmetric ligands, either in respect to their geometry, functional group position or type of coordinating groups, will leads to the discovery of more multi-component framework architectures.

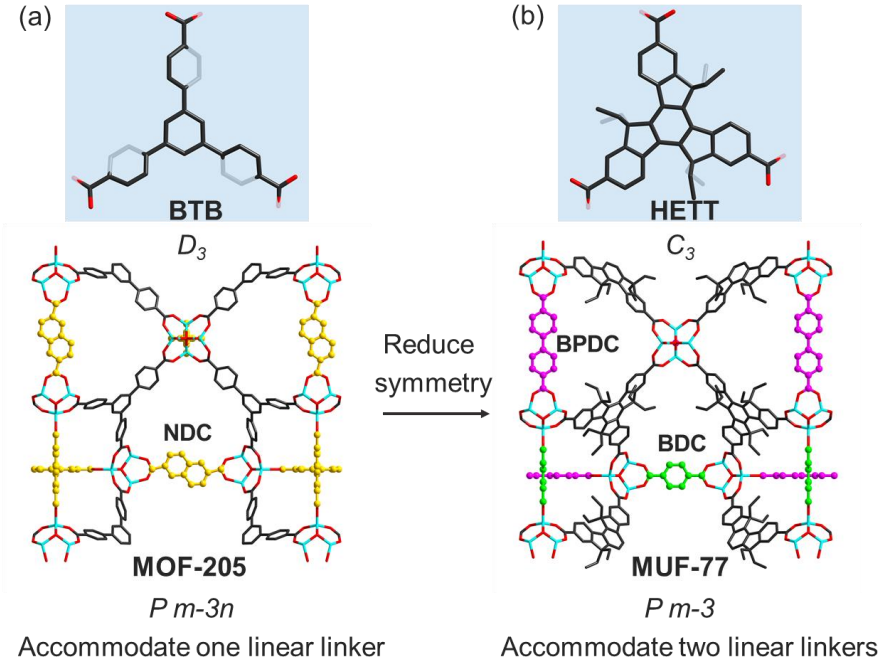

Figure 118. Structures of MOF-205 formed by high-symmetric linkers (a) and MUF-77 formed by low-symmetric linkers (b).

7.2.2 Defective MOFs: Imperfection Leads to Emerging Properties

Theoretically, defects exist ubiquitously in all the crystalline materials. Even the most carefully grown single crystals of MOFs should contain different types of defects. Although often

being overlooked, defects may dictate the performance of MOFs in some cases. Currently, most researches regard MOFs as perfect crystals, and the studies of defects is still in their nascent stage.

Recent development of Zr-MOFs brings new opportunity to defect engineering of MOFs. Zr-MOFs exhibit remarkable tolerance towards a high concentration of defects without suffering from severe loss of crystallinity or stability.[66-67] The concentration of defects can be adjusted by control of synthetic conditions such as the metal to ligand ratio, reaction time, and temperature.[100-102] However, the highly defective MOFs are unfavored in a solvothermal synthesis because of their low chemical stability. To address the limitation of one-pot method, linker labilization method was developed to introduce high concentration of defects postsynthetically.[17] In this method, two linkers with the same length but different chemical stability was adopted to synthesize a mixed-linker Zr-MOF. Defects were subsequently created by the removal of labile linkers through chemical etching or thermolysis to introduce missing linker defects. Along this line, a series of methods will be developed to introduce defects into MOFs for a specific applications.

Besides the creation of defects, another challenge lies in the characterization of local structures on defect sites. Similar to the mixed-linker MOFs with disordered ligands, X-ray diffraction techniques cannot provide clear structural evidence of defects. But the defects in zeolites has been well-investigated, which may provide useful knowledge for the study of defective MOFs. Characterization techniques used for zeolites can be adopted to MOF research including HRTEM, confocal fluorescence microscopy, and pair distribution function (PDF). Admittedly, the detection of defects of MOFs can be more challenging compared to zeolites considering the limited stability of MOFs under electron beam. However, the development of characterization techniques for electron beam-sensitive materials will promote the development of this field.

7.2.3 MOF Composites: Hybridization Brings New Opportunity

Hybridization of MOF crystals and other materials can enhance the performance or create novel functions. The porous structures of MOFs provide an opportunity to alter the properties by the inclusion of guest molecules within their pores. Synergistic properties can emerge which are different from either host or guest individually. A representative example is the 7,7,8,8-tetracyanoquinododimethane (TCNQ) incorporated HKUST-1 with an electrical conductivity of 7 S m^{-1}, which is significantly higher than both TCNQ and HKUST-1. The hybridization of MOF and organic polymer is another promising direction. The polymer@MOF composites show enhanced chemical stability and mechanical processability. On the other hand, hybridization with inorganic matter such as porous metal oxides allow the hierarchized spatial structure in which micro, meso, and macro pores coexist. Considering the unlimited tunability of MOFs, new MOF-composites with emergent properties are waiting to be explored.

7.2.4 MOF Retrosynthesis: Challenges and Opportunities

Form previous discussion, it is clear that the future of MOF chemistry lies in the combination of multiple components and functions within a complex framework structure. Despite the bright future of multi-component MOFs, the gap between material design and synthesis has impeded the realization of the beautiful design. Indeed, the structural and compositional compilation of multi-component MOFs has made them exceedingly difficult to synthesize. The complexity of multi-component MOFs is limited ultimately by the lack of control during the framework assembly in a one-pot reaction.

Inspired by the concept of retrosynthesis utilized to construct complex organic molecules and natural products, we proposed that MOFs as porous solid materials could be rationally designed and synthesized in multi-step synthetic approaches. Kinetic analysis, an analog of

retrosynthetic analysis, allowed us to conceptually break down a predicted MOF structure into available metal precursors and ligands (i.e., synthons). The synthons were subsequently assembled into the designed MOF structure step by step under kinetic control using known post-synthetic modification methods, which circumvent the undesirable thermodynamic sink. In other words, we use labile coordination bonds to sequentially layer-on molecular elaborations to a robust framework, which eventually formed the designed multi-component coordination assemblies. Although many challenges still remain in MOF retrosynthesis, especially in building a synthetic toolkit analogous to the large and diverse organic reaction library, the intrinsic designability of MOFs and the fast-evolving MOF synthetic methodologies suggest that such a lofty goal is eventually achievable.

7.3 Future Work

The development of multi-component MOFs will promote the understanding of basic scientific principles in other related areas. Binary transition metal oxides have been studied extensively for their applications in energy storage and catalysis.[205-206] The surface properties of metal oxides, including morphologies, surface terminations, and electronic structures, play critical roles in heterogeneous catalysis and electrocatalysis. However, characterization of active centers on the surface remains a challenge due to the low concentration of active species and limited surface area of metal oxides particles. In this respect, MOFs provide an opportunity to model the metal oxide surface for structural characterization and mechanistic studies.[123] MOFs represent a naturally self-assembled superlattice of metal oxide nanoparticles separated by organic linkers. It can be perceived as a bridge between heterogeneous and homogeneous systems. Each metal oxide cluster is exposed to the cavity within the porous framework and therefore is accessible by substrates, which reassembles the homogeneous catalysts. As crystalline solids, MOFs also allow

facile structural characterization by X-ray diffraction techniques to reveal the active sites. Multi-component MOFs with desired metal and organic species can be designed using the synthetic toolkit developed in my previous work. Therefore, my future work will use multi-component MOFs as models of binary metal oxide catalysts to provide insight into the structure and behavior of active surface species (Figure 119).

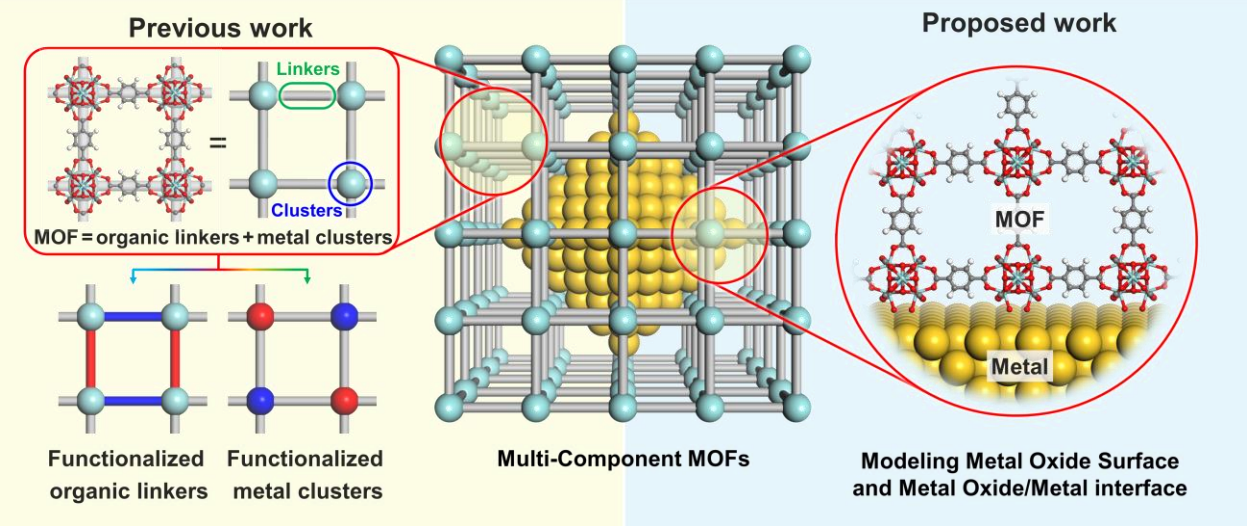

Figure 119. A summary of previous work on the synthesis of multi-component MOFs and the proposed work to model binary metal oxide surface by multi-component MOFs.

7.3.1 Modeling Binary Metal Oxide Catalysts

The unraveled structural tunability of MOFs promises the construction of various bimetallic MOFs that mimic the binary metal oxide catalysts. For example, PCN-700 allows the replacement of Zr^{4+} by Ce^{4+} without altering the framework structure.[207] The [Ce_6] cluster in PCN-700(Ce) bears a close resemblance to CeO_2, which can be regarded as ultra-small CeO_2 nanoparticles. In addition, almost all the first-row transition metals can be attached on the [Ce_6] cluster, forming [Ce_6M_4] cluster (Figure 120a). It is also possible to incorporate different metals

simultaneously on a [Ce_6] cluster by cluster metalation. As a proof of concept, the copper-substituted ceria, a known CO oxidation catalyst, will be modeled by the incorporation of Cu onto the [Ce_6] cluster of PCN-700(Ce).[208-209] The coordination environment of Cu can be clearly determined by SCXRD, providing a well-defined structural model for mechanistic studies. The porous framework act as an inherent support to isolate [Ce_6Cu_4] nanoparticles, which promises a highly active binary catalytic system surpassing the classic copper-substituted ceria catalyst for CO oxidation.

7.3.2 Developing Ternary Metal/MOF catalysts

Embedding metal nanoparticles into MOFs will maximize the metal/metal-oxide interface. More importantly, the created metal/metal-oxide interface is accessible to substrates owing to the porous nature of MOFs, which is crucial for many catalytic processes. In other words, nanoparticles embedded in MOFs should possess the highest accessible metal/metal-oxide interface area among any materials. The metal/metal-oxide interface is crucial for many catalytic reactions such as CO oxidation on Au/CeO_2,[210] and hydrogenation of CO_2 on Cu/ZnO.[211] As a proof of concept, the Au/CuO–CeO_2 catalyst will be mimicked by the incorporation of Cu onto the Ce_6 cluster and Au nanoparticles in the cavity of UiO-66-Ce simultaneously (Figure 120b). The porous framework act as an inherent support to isolate Au/CuO–CeO_2 nanoparticles, which promises a highly active ternary catalytic system. Furthermore, this method allows the incorporation of labile metal–oxo clusters into a stable framework. For example, the Cu/ZnO interface can promotes hydrogenation of CO_2 to produce methanol, but the Zn–oxo based MOFs are too labile to survive the catalytic reactions. To solve this dilemma, Zn–oxo clusters will be attached on the Zr_6 cluster of UiO-66-Zr. The robust Zr–oxo clusters form a stable framework

while the Zn–oxo clusters and Cu nanoparticles act as active sites (Figure 120c). Consequently, three components work cooperatively as a ternary catalyst for CO_2 hydrogenation.

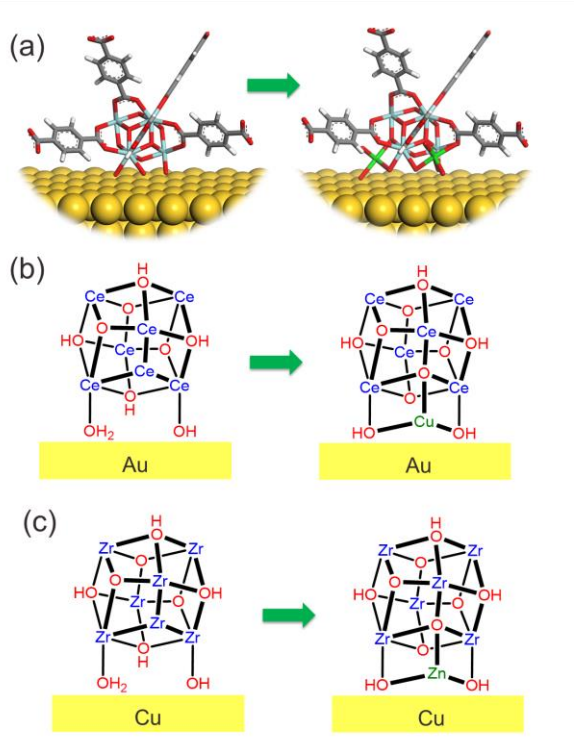

Figure 120. (a) Structural representation of cluster metalation of MOFs. Schematic representation of (b) Au/CuO–UiO-66-Ce and (c) Cu/ZnO–UiO-66-Zr constructed by cluster metalation.

The proposed work provided a few possible examples that take advantage of porous crystalline MOFs. Considering the diversity of metal oxides and the unlimited tunability of MOF platforms, many exciting researches are waiting to be explored. Eventually, a general method will be developed to model the metal oxide catalysts using MOFs for both mechanistic studies and practical applications.

REFERENCES

1 Batten Stuart, R.; Champness Neil, R.; Chen, X.-M.; Garcia-Martinez, J.; Kitagawa, S.; Öhrström, L.; O'Keeffe, M.; Paik Suh, M.; Reedijk, J., Terminology of Metal–Organic Frameworks and Coordination Polymers (Iupac Recommendations 2013). In *Pure Appl. Chem.*, 2013; Vol. 85, p 1715.

2 Farha, O. K.; Eryazici, I.; Jeong, N. C.; Hauser, B. G.; Wilmer, C. E.; Sarjeant, A. A.; Snurr, R. Q.; Nguyen, S. T.; Yazaydın, A. Ö.; Hupp, J. T., Metal–Organic Framework Materials with Ultrahigh Surface Areas: Is the Sky the Limit? *J. Am. Chem. Soc.* **2012,** *134* (36), 15016-15021.

3 Eddaoudi, M.; Moler, D. B.; Li, H.; Chen, B.; Reineke, T. M.; O'Keeffe, M.; Yaghi, O. M., Modular Chemistry: Secondary Building Units as a Basis for the Design of Highly Porous and Robust Metal−Organic Carboxylate Frameworks. *Acc. Chem. Res.* **2001,** *34* (4), 319-330.

4 Tranchemontagne, D. J.; Mendoza-Cortes, J. L.; O'Keeffe, M.; Yaghi, O. M., Secondary Building Units, Nets and Bonding in the Chemistry of Metal-Organic Frameworks. *Chem. Soc. Rev.* **2009,** *38* (5), 1257-1283.

5 Furukawa, H.; Cordova, K. E.; O'Keeffe, M.; Yaghi, O. M., The Chemistry and Applications of Metal-Organic Frameworks. *Science* **2013,** *341* (6149), 1230444.

6 Lu, W.; Wei, Z.; Gu, Z.-Y.; Liu, T.-F.; Park, J.; Park, J.; Tian, J.; Zhang, M.; Zhang, Q.; Gentle Iii, T.; Bosch, M.; Zhou, H.-C., Tuning the Structure and Function of Metal-Organic Frameworks Via Linker Design. *Chem. Soc. Rev.* **2014,** *43* (16), 5561-5593.

7 Moghadam, P. Z.; Li, A.; Wiggin, S. B.; Tao, A.; Maloney, A. G. P.; Wood, P. A.; Ward, S. C.; Fairen-Jimenez, D., Development of a Cambridge Structural Database Subset: A Collection of Metal–Organic Frameworks for Past, Present, and Future. *Chem. Mater.* **2017,** *29* (7), 2618-2625.

8 Makal, T. A.; Li, J. R.; Lu, W.; Zhou, H. C., Methane Storage in Advanced Porous Materials. *Chem. Soc. Rev.* **2012,** *41* (23), 7761-79.

9 Li, J.-R.; Kuppler, R. J.; Zhou, H.-C., Selective Gas Adsorption and Separation in Metal-Organic Frameworks. *Chem. Soc. Rev.* **2009,** *38* (5), 1477-1504.

10 Ma, L.; Abney, C.; Lin, W., Enantioselective Catalysis with Homochiral Metal-Organic Frameworks. *Chem. Soc. Rev.* **2009,** *38* (5), 1248-1256.

11 Hoskins, B. F.; Robson, R., Infinite Polymeric Frameworks Consisting of Three Dimensionally Linked Rod-Like Segments. *J. Am. Chem. Soc.* **1989,** *111* (15), 5962-5964.

12 Li, H.; Eddaoudi, M.; O'Keeffe, M.; Yaghi, O. M., Design and Synthesis of an Exceptionally Stable and Highly Porous Metal-Organic Framework. *Nature* **1999,** *402*, 276.

13 Serre, C.; Millange, F.; Thouvenot, C.; Noguès, M.; Marsolier, G.; Louër, D.; Férey, G., Very Large Breathing Effect in the First Nanoporous Chromium(III)-Based Solids: MIL-53. *J. Am. Chem. Soc.* **2002,** *124* (45), 13519-13526.

14 Schneemann, A.; Bon, V.; Schwedler, I.; Senkovska, I.; Kaskel, S.; Fischer, R. A., Flexible Metal-Organic Frameworks. *Chem. Soc. Rev.* **2014,** *43* (16), 6062-6096.

15 Férey, G.; Mellot-Draznieks, C.; Serre, C.; Millange, F.; Dutour, J.; Surblé, S.; Margiolaki, I., A Chromium Terephthalate-Based Solid with Unusually Large Pore Volumes and Surface Area. *Science* **2005,** *309* (5743), 2040-2042.

16 Cavka, J. H.; Jakobsen, S.; Olsbye, U.; Guillou, N.; Lamberti, C.; Bordiga, S.; Lillerud, K. P., A New Zirconium Inorganic Building Brick Forming Metal Organic Frameworks with Exceptional Stability. *J. Am. Chem. Soc.* **2008,** *130* (42), 13850-13851.

17 Yuan, S.; Zou, L.; Qin, J.-S.; Li, J.; Huang, L.; Feng, L.; Wang, X.; Bosch, M.; Alsalme, A.; Cagin, T.; Zhou, H.-C., Construction of Hierarchically Porous Metal–Organic Frameworks through Linker Labilization. *Nat. Commun.* **2017,** *8*, 15356.

18 Pang, J.; Yuan, S.; Qin, J.; Liu, C.; Lollar, C.; Wu, M.; Yuan, D.; Zhou, H.-C.; Hong, M., Control the Structure of Zr-Tetracarboxylate Frameworks through Steric Tuning. *J. Am. Chem. Soc.* **2017,** *139* (46), 16939-16945.

19 Shuai, Y.; Ying‐Pin, C.; Junsheng, Q.; Weigang, L.; Xuan, W.; Qiang, Z.; Mathieu, B.; Tian‐Fu, L.; Xizhen, L.; Hong‐Cai, Z., Cooperative Cluster Metalation and Ligand Migration in Zirconium Metal‐Organic Frameworks. *Angew. Chem. Int. Ed.* **2015,** *54* (49), 14696-14700.

20 Feng, L.; Yuan, S.; Zhang, L.-L.; Tan, K.; Li, J.-L.; Kirchon, A.; Liu, L.-M.; Zhang, P.; Han, Y.; Chabal, Y. J.; Zhou, H.-C., Creating Hierarchical Pores by Controlled Linker Thermolysis in Multivariate Metal–Organic Frameworks. *J. Am. Chem. Soc.* **2018,** *140* (6), 2363-2372.

21 Shuai, Y.; Lanfang, Z.; Haixia, L.; Ying‐Pin, C.; Junsheng, Q.; Qiang, Z.; Weigang, L.; B., H. M.; Hong‐Cai, Z., Flexible Zirconium Metal‐Organic Frameworks as Bioinspired Switchable Catalysts. *Angew. Chem. Int. Ed.* **2016,** *55* (36), 10776-10780.

22 Qin, J.-S.; Yuan, S.; Alsalme, A.; Zhou, H.-C., Flexible Zirconium MOF as the Crystalline Sponge for Coordinative Alignment of Dicarboxylates. *ACS Appl. Mater. Interfaces* **2017,** *9* (39), 33408-33412.

23 Pang, J.; Yuan, S.; Du, D.; Lollar, C.; Zhang, L.; Wu, M.; Yuan, D.; Zhou, H. C.; Hong, M., Flexible Zirconium MOFs as Bromine‐Nanocontainers for Bromination Reactions under Ambient Conditions. *Angew. Chem.* **2017,** *129* (46), 14814-14818.

24 Yuan, S.; Chen, Y.-P.; Qin, J.-S.; Lu, W.; Zou, L.; Zhang, Q.; Wang, X.; Sun, X.; Zhou, H.-C., Linker Installation: Engineering Pore Environment with Precisely Placed Functionalities in Zirconium MOFs. *J. Am. Chem. Soc.* **2016,** *138* (28), 8912-8919.

25 Qin, J.-S.; Yuan, S.; Wang, Q.; Alsalme, A.; Zhou, H.-C., Mixed-Linker Strategy for the Construction of Multifunctional Metal-Organic Frameworks. *J. Mater. Chem. A* **2017,** *5* (9), 4280-4291.

26 Yuan, S.; Sun, X.; Pang, J.; Lollar, C.; Qin, J.-S.; Perry, Z.; Joseph, E.; Wang, X.; Fang, Y.; Bosch, M.; Sun, D.; Liu, D.; Zhou, H.-C., PCN-250 under Pressure: Sequential Phase Transformation and the Implications for MOF Densification. *Joule* **2017,** *1* (4), 806-815.

27 Su, J.; Yuan, S.; Wang, H.-Y.; Huang, L.; Ge, J.-Y.; Joseph, E.; Qin, J.; Cagin, T.; Zuo, J.-L.; Zhou, H.-C., Redox-Switchable Breathing Behavior in Tetrathiafulvalene-Based Metal–Organic Frameworks. *Nat. Commun.* **2017,** *8* (1), 2008.

28 Yuan, S.; Qin, J.-S.; Li, J.; Huang, L.; Feng, L.; Fang, Y.; Lollar, C.; Pang, J.; Zhang, L.; Sun, D.; Alsalme, A.; Cagin, T.; Zhou, H.-C., Retrosynthesis of Multi-Component Metal−Organic Frameworks. *Nat. Commun.* **2018,** *9* (1), 808.

29 Yuan, S.; Lu, W.; Chen, Y.-P.; Zhang, Q.; Liu, T.-F.; Feng, D.; Wang, X.; Qin, J.; Zhou, H.-C., Sequential Linker Installation: Precise Placement of Functional Groups in Multivariate Metal–Organic Frameworks. *J. Am. Chem. Soc.* **2015,** *137* (9), 3177-3180.

30 Yuan, S.; Liu, T.-F.; Feng, D.; Tian, J.; Wang, K.; Qin, J.; Zhang, Q.; Chen, Y.-P.; Bosch, M.; Zou, L.; Teat, S. J.; Dalgarno, S. J.; Zhou, H.-C., A Single Crystalline Porphyrinic Titanium Metal-Organic Framework. *Chem. Sci.* **2015,** *6* (7), 3926-3930.

31 Yuan, S.; Qin, J.-S.; Lollar, C. T.; Zhou, H.-C., Stable Metal–Organic Frameworks with Group 4 Metals: Current Status and Trends. *ACS Cent. Sci.* **2018,** *4* (4), 440-450.

32 Shuai, Y.; Liang, F.; Kecheng, W.; Jiandong, P.; Matheiu, B.; Christina, L.; Yujia, S.; Junsheng, Q.; Xinyu, Y.; Peng, Z.; Qi, W.; Lanfang, Z.; Yingmu, Z.; Liangliang, Z.; Yu, F.; Jialuo, L.; Hong‐Cai, Z., Stable Metal‐Organic Frameworks: Design, Synthesis, and

Applications. *Adv. Mater.*, DOI:10.1002/adma.201704303.

33 Bosch, M.; Yuan, S.; Rutledge, W.; Zhou, H.-C., Stepwise Synthesis of Metal–Organic Frameworks. *Acc. Chem. Res.* **2017,** *50* (4), 857-865.

34 Yuan, S.; Qin, J.-S.; Zou, L.; Chen, Y.-P.; Wang, X.; Zhang, Q.; Zhou, H.-C., Thermodynamically Guided Synthesis of Mixed-Linker Zr-MOFs with Enhanced Tunability. *J. Am. Chem. Soc.* **2016,** *138* (20), 6636-6642.

35 Yuan, S.; Qin, J.-S.; Xu, H.-Q.; Su, J.; Rossi, D.; Chen, Y.; Zhang, L.; Lollar, C.; Wang, Q.; Jiang, H.-L.; Son, D. H.; Xu, H.; Huang, Z.; Zou, X.; Zhou, H.-C., $[Ti_8zr_2o_{12}(Coo)_{16}]$ Cluster: An Ideal Inorganic Building Unit for Photoactive Metal–Organic Frameworks. *ACS Cent. Sci.* **2018,** *4* (1), 105-111.

36 Liu, T.-F.; Feng, D.; Chen, Y.-P.; Zou, L.; Bosch, M.; Yuan, S.; Wei, Z.; Fordham, S.; Wang, K.; Zhou, H.-C., Topology-Guided Design and Syntheses of Highly Stable Mesoporous Porphyrinic Zirconium Metal–Organic Frameworks with High Surface Area. *J. Am. Chem. Soc.* **2015,** *137* (1), 413-419.

37 Xu, M.; Yuan, S.; Chen, X.-Y.; Chang, Y.-J.; Day, G.; Gu, Z.-Y.; Zhou, H.-C., Two-Dimensional Metal–Organic Framework Nanosheets as an Enzyme Inhibitor: Modulation of the A-Chymotrypsin Activity. *J. Am. Chem. Soc.* **2017,** *139* (24), 8312-8319.

38 Xia, Q.; Li, Z.; Tan, C.; Liu, Y.; Gong, W.; Cui, Y., Multivariate Metal–Organic Frameworks as Multifunctional Heterogeneous Asymmetric Catalysts for Sequential Reactions. *J. Am. Chem. Soc.* **2017,** *139* (24), 8259-8266.

39 Howe, J. D.; Morelock, C. R.; Jiao, Y.; Chapman, K. W.; Walton, K. S.; Sholl, D. S., Understanding Structure, Metal Distribution, and Water Adsorption in Mixed-Metal MOF-74. *J. Phys. Chem. C* **2017,** *121* (1), 627-635.

40 Zhai, Q.-G.; Bu, X.; Mao, C.; Zhao, X.; Feng, P., Systematic and Dramatic Tuning on Gas Sorption Performance in Heterometallic Metal–Organic Frameworks. *J. Am. Chem. Soc.* **2016,** *138* (8), 2524-2527.

41 Zhao, X.; Bu, X.; Nguyen, E. T.; Zhai, Q.-G.; Mao, C.; Feng, P., Multivariable Modular Design of Pore Space Partition. *J. Am. Chem. Soc.* **2016,** *138* (46), 15102-15105.

42 Deng, H.; Doonan, C. J.; Furukawa, H.; Ferreira, R. B.; Towne, J.; Knobler, C. B.; Wang, B.; Yaghi, O. M., Multiple Functional Groups of Varying Ratios in Metal-Organic Frameworks. *Science* **2010,** *327* (5967), 846-50.

43 Tu, B.; Pang, Q.; Ning, E.; Yan, W.; Qi, Y.; Wu, D.; Li, Q., Heterogeneity within a Mesoporous Metal–Organic Framework with Three Distinct Metal-Containing Building Units. *J. Am. Chem. Soc.* **2015,** *137* (42), 13456-13459.

44 Furukawa, H.; Cordova, K. E.; O'Keeffe, M.; Yaghi, O. M., The Chemistry and Applications of Metal-Organic Frameworks. *Science* **2013,** *341* (6149).

45 Kong, X.; Deng, H.; Yan, F.; Kim, J.; Swisher, J. A.; Smit, B.; Yaghi, O. M.; Reimer, J. A., Mapping of Functional Groups in Metal-Organic Frameworks. *Science* **2013,** *341* (6148), 882-5.

46 Liu, L.; Konstas, K.; Hill, M. R.; Telfer, S. G., Programmed Pore Architectures in Modular Quaternary Metal–Organic Frameworks. *J. Am. Chem. Soc.* **2013,** *135* (47), 17731-17734.

47 Liu, L.; Telfer, S. G., Systematic Ligand Modulation Enhances the Moisture Stability and Gas Sorption Characteristics of Quaternary Metal–Organic Frameworks. *J. Am. Chem. Soc.* **2015,** *137* (11), 3901-3909.

48 Tan, Y.-X.; Yang, X.; Li, B.-B.; Yuan, D., Rational Design of a Flu-Type Heterometallic Cluster-Based Zr-MOF. *Chem. Commun.* **2016,** *52* (94), 13671-13674.

49 Gang, X.; Li ‐ xin, Y.; Bao ‐ yi, R.; Yong ‐ ke, H.; Shu ‐ ju, W.; Ya ‐ guang, S., Structure and Magnetocaloric Effect of Two Kinds of Ln ‐ Mnii Heterometallic Coordination Polymers Produced by Fractional Crystallization. *Eur. J. Inorg. Chem.* **2016,** *2016* (24), 3969-3977.

50 Tu, B.; Pang, Q.; Xu, H.; Li, X.; Wang, Y.; Ma, Z.; Weng, L.; Li, Q., Reversible Redox Activity in Multicomponent Metal–Organic Frameworks Constructed from Trinuclear Copper Pyrazolate Building Blocks. *J. Am. Chem. Soc.* **2017,** *139* (23), 7998-8007.

51 Zhai, Q.-G.; Bu, X.; Zhao, X.; Li, D.-S.; Feng, P., Pore Space Partition in Metal–Organic Frameworks. *Acc. Chem. Res.* **2017,** *50* (2), 407-417.

52 Rosi, N. L.; Eckert, J.; Eddaoudi, M.; Vodak, D. T.; Kim, J.; O'Keeffe, M.; Yaghi, O. M., Hydrogen Storage in Microporous Metal-Organic Frameworks. *Science* **2003,** *300* (5622), 1127-1129.

53 Elsaidi, S. K.; Mohamed, M. H.; Wojtas, L.; Cairns, A. J.; Eddaoudi, M.; Zaworotko, M. J., Two-Step Crystal Engineering of Porous Nets from $[Cr_3o)(Rco_2)_6]$ and $[Cu_3cl)(Rnh_2)_6cl_6]$ Molecular Building Blocks. *Chem. Commun.* **2013,** *49* (74), 8154-8156.

54 Alexander, S.; J., C. A.; Youssef, B.; Lukasz, W.; Mona, M.; Zhenjie, Z.; M., P. D.; Mohamed,

E.; J., Z. M., The Asc Trinodal Platform: Two ‐ Step Assembly of Triangular, Tetrahedral, and Trigonal ‐ Prismatic Molecular Building Blocks. *Angew. Chem. Int. Ed.* **2013,** *52* (10), 2902-2905.

55 Lalonde, M.; Bury, W.; Karagiaridi, O.; Brown, Z.; Hupp, J. T.; Farha, O. K., Transmetalation: Routes to Metal Exchange within Metal-Organic Frameworks. *J. Mater. Chem. A* **2013,** *1* (18), 5453-5468.

56 Tu, B.; Pang, Q.; Wu, D.; Song, Y.; Weng, L.; Li, Q., Ordered Vacancies and Their Chemistry in Metal–Organic Frameworks. *J. Am. Chem. Soc.* **2014,** *136* (41), 14465-14471.

57 Mondloch, J. E.; Bury, W.; Fairen-Jimenez, D.; Kwon, S.; DeMarco, E. J.; Weston, M. H.; Sarjeant, A. A.; Nguyen, S. T.; Stair, P. C.; Snurr, R. Q.; Farha, O. K.; Hupp, J. T., Vapor-Phase Metalation by Atomic Layer Deposition in a Metal–Organic Framework. *J. Am. Chem. Soc.* **2013,** *135* (28), 10294-10297.

58 Nguyen, H. G. T.; Schweitzer, N. M.; Chang, C.-Y.; Drake, T. L.; So, M. C.; Stair, P. C.; Farha, O. K.; Hupp, J. T.; Nguyen, S. T., Vanadium-Node-Functionalized UiO-66: A Thermally Stable MOF-Supported Catalyst for the Gas-Phase Oxidative Dehydrogenation of Cyclohexene. *ACS Catal.* **2014,** *4* (8), 2496-2500.

59 Yang, D.; Odoh, S. O.; Wang, T. C.; Farha, O. K.; Hupp, J. T.; Cramer, C. J.; Gagliardi, L.; Gates, B. C., Metal–Organic Framework Nodes as Nearly Ideal Supports for Molecular Catalysts: Nu-1000- and UiO-66-Supported Iridium Complexes. *J. Am. Chem. Soc.* **2015,** *137* (23), 7391-7396.

60 Yuan, S.; Chen, Y.-P.; Qin, J.; Lu, W.; Wang, X.; Zhang, Q.; Bosch, M.; Liu, T.-F.; Lian, X.; Zhou, H.-C., Cooperative Cluster Metalation and Ligand Migration in Zirconium Metal–Organic Frameworks. *Angew. Chem. Int. Ed.* **2015,** *54* (49), 14696-14700.

61 Park, T.-H.; Hickman, A. J.; Koh, K.; Martin, S.; Wong-Foy, A. G.; Sanford, M. S.; Matzger, A. J., Highly Dispersed Palladium(Ii) in a Defective Metal–Organic Framework: Application to C–H Activation and Functionalization. *J. Am. Chem. Soc.* **2011,** *133* (50), 20138-20141.

62 Choi, K. M.; Jeon, H. J.; Kang, J. K.; Yaghi, O. M., Heterogeneity within Order in Crystals of a Porous Metal–Organic Framework. *J. Am. Chem. Soc.* **2011,** *133* (31), 11920-11923.

63 Diring, S.; Furukawa, S.; Takashima, Y.; Tsuruoka, T.; Kitagawa, S., Controlled Multiscale Synthesis of Porous Coordination Polymer in Nano/Micro Regimes. *Chem. Mater.* **2010,** *22* (16), 4531-4538.

64 Fang, Z.; Dürholt, J. P.; Kauer, M.; Zhang, W.; Lochenie, C.; Jee, B.; Albada, B.; Metzler-

Nolte, N.; Pöppl, A.; Weber, B.; Muhler, M.; Wang, Y.; Schmid, R.; Fischer, R. A., Structural Complexity in Metal–Organic Frameworks: Simultaneous Modification of Open Metal Sites and Hierarchical Porosity by Systematic Doping with Defective Linkers. *J. Am. Chem. Soc.* **2014,** *136* (27), 9627-9636.

65 Fang, Z.; Bueken, B.; De Vos, D. E.; Fischer, R. A., Defect-Engineered Metal–Organic Frameworks. *Angew. Chem. Int. Ed.* **2015,** *54* (25), 7234-7254.

66 Taddei, M., When Defects Turn into Virtues: The Curious Case of Zirconium-Based Metal-Organic Frameworks. *Coord. Chem. Rev.* **2017,** *343*, 1-24.

67 Valenzano, L.; Civalleri, B.; Chavan, S.; Bordiga, S.; Nilsen, M. H.; Jakobsen, S.; Lillerud, K. P.; Lamberti, C., Disclosing the Complex Structure of UiO-66 Metal Organic Framework: A Synergic Combination of Experiment and Theory. *Chem. Mater.* **2011,** *23* (7), 1700-1718.

68 Vermoortele, F.; Ameloot, R.; Vimont, A.; Serre, C.; De Vos, D., An Amino-Modified Zr-Terephthalate Metal-Organic Framework as an Acid-Base Catalyst for Cross-Aldol Condensation. *Chem. Commun.* **2011,** *47* (5), 1521-1523.

69 Beyzavi, M. H.; Klet, R. C.; Tussupbayev, S.; Borycz, J.; Vermeulen, N. A.; Cramer, C. J.; Stoddart, J. F.; Hupp, J. T.; Farha, O. K., A Hafnium-Based Metal–Organic Framework as an Efficient and Multifunctional Catalyst for Facile CO_2 Fixation and Regioselective and Enantioretentive Epoxide Activation. *J. Am. Chem. Soc.* **2014,** *136* (45), 15861-15864.

70 Sang, X.; Zhang, J.; Xiang, J.; Cui, J.; Zheng, L.; Zhang, J.; Wu, Z.; Li, Z.; Mo, G.; Xu, Y.; Song, J.; Liu, C.; Tan, X.; Luo, T.; Zhang, B.; Han, B., Ionic Liquid Accelerates the Crystallization of Zr-Based Metal–Organic Frameworks. *Nat. Commun.* **2017,** *8* (1), 175.

71 Rasero-Almansa, A. M.; Iglesias, M.; Sanchez, F., Synthesis of Bimetallic Zr(Ti)-Naphthalendicarboxylate MOFs and Their Properties as Lewis Acid Catalysis. *RSC Adv.* **2016,** *6* (108), 106790-106797.

72 Islamoglu, T.; Goswami, S.; Li, Z.; Howarth, A. J.; Farha, O. K.; Hupp, J. T., Postsynthetic Tuning of Metal–Organic Frameworks for Targeted Applications. *Acc. Chem. Res.* **2017,** *50* (4), 805-813.

73 Mason, J. A.; Oktawiec, J.; Taylor, M. K.; Hudson, M. R.; Rodriguez, J.; Bachman, J. E.; Gonzalez, M. I.; Cervellino, A.; Guagliardi, A.; Brown, C. M.; Llewellyn, P. L.; Masciocchi, N.; Long, J. R., Methane Storage in Flexible Metal–Organic Frameworks with Intrinsic Thermal Management. *Nature* **2015,** *527*, 357.

74 McDonald, T. M.; Mason, J. A.; Kong, X.; Bloch, E. D.; Gygi, D.; Dani, A.; Crocellà, V.;

Giordanino, F.; Odoh, S. O.; Drisdell, W. S.; Vlaisavljevich, B.; Dzubak, A. L.; Poloni, R.; Schnell, S. K.; Planas, N.; Lee, K.; Pascal, T.; Wan, L. F.; Prendergast, D.; Neaton, J. B.; Smit, B.; Kortright, J. B.; Gagliardi, L.; Bordiga, S.; Reimer, J. A.; Long, J. R., Cooperative Insertion of CO2 in Diamine-Appended Metal-Organic Frameworks. *Nature* **2015,** *519*, 303.

75 Lee, J.; Farha, O. K.; Roberts, J.; Scheidt, K. A.; Nguyen, S. T.; Hupp, J. T., Metal-Organic Framework Materials as Catalysts. *Chem. Soc. Rev.* **2009,** *38* (5), 1450-1459.

76 Wang, H.; Lustig, W. P.; Li, J., Sensing and Capture of Toxic and Hazardous Gases and Vapors by Metal-Organic Frameworks. *Chem. Soc. Rev.* **2018**, DOI: 10.1039/C7CS00885F.

77 Zhang, T.; Lin, W., Metal-Organic Frameworks for Artificial Photosynthesis and Photocatalysis. *Chem. Soc. Rev.* **2014,** *43* (16), 5982-5993.

78 Wu, M. X.; Yang, Y. W., Metal‐Organic framework (MOF)‐Based Drug/Cargo Delivery and Cancer Therapy. *Adv. Mater.* **2017,** *29* (23), 1606134.

79 Hiroyasu, F.; Ulrich, M.; M., Y. O., "Heterogeneity within Order" in Metal–Organic Frameworks. *Angew. Chem. Int. Ed.* **2015,** *54* (11), 3417-3430.

80 Burrows, A. D., Mixed-Component Metal-Organic Frameworks (Mc-MOFs): Enhancing Functionality through Solid Solution Formation and Surface Modifications. *CrystEngComm* **2011,** *13* (11), 3623-3642.

81 Rozes, L.; Sanchez, C., Titanium Oxo-Clusters: Precursors for a Lego-Like Construction of Nanostructured Hybrid Materials. *Chem. Soc. Rev.* **2011,** *40* (2), 1006-1030.

82 Assi, H.; Mouchaham, G.; Steunou, N.; Devic, T.; Serre, C., Titanium Coordination Compounds: From Discrete Metal Complexes to Metal-Organic Frameworks. *Chem. Soc. Rev.* **2017,** *46* (11), 3431-3452.

83 Nguyen, H. L.; Gandara, F.; Furukawa, H.; Doan, T. L. H.; Cordova, K. E.; Yaghi, O. M., A Titanium-Organic Framework as an Exemplar of Combining the Chemistry of Metal- and Covalent-Organic Frameworks. *J. Am. Chem. Soc.* **2016,** *138* (13), 4330-4333.

84 Cavka, J. H.; Jakobsen, S.; Olsbye, U.; Guillou, N.; Lamberti, C.; Bordiga, S.; Lillerud, K. P., A New Zirconium Inorganic Building Brick Forming Metal Organic Frameworks with Exceptional Stability. *J. Am. Chem. Soc.* **2008,** *130* (42), 13850-13851.

85 Mondloch, J. E.; Bury, W.; Fairen-Jimenez, D.; Kwon, S.; DeMarco, E. J.; Weston, M. H.; Sarjeant, A. A.; Nguyen, S. T.; Stair, P. C.; Snurr, R. Q.; Farha, O. K.; Hupp, J. T., Vapor-Phase Metalation by Atomic Layer Deposition in a Metal-Organic Framework. *J. Am. Chem.*

Soc. **2013,** *135* (28), 10294-10297.

86 Furukawa, H.; Gandara, F.; Zhang, Y. B.; Jiang, J.; Queen, W. L.; Hudson, M. R.; Yaghi, O. M., Water Adsorption in Porous Metal-Organic Frameworks and Related Materials. *J. Am. Chem. Soc.* **2014,** *136* (11), 4369-4381.

87 Qin, J. S.; Yuan, S.; Alsalme, A.; Zhou, H. C., Flexible Zirconium MOF as the Crystalline Sponge for Coordinative Alignment of Dicarboxylates. *ACS Appl. Mater. Interfaces* **2017,** *9* (39), 33408-33412.

88 Bai, Y.; Dou, Y. B.; Xie, L. H.; Rutledge, W.; Li, J. R.; Zhou, H. C., Zr-Based Metal-Organic Frameworks: Design, Synthesis, Structure, and Applications. *Chem. Soc. Rev.* **2016,** *45* (8), 2327-2367.

89 Schaate, A.; Roy, P.; Godt, A.; Lippke, J.; Waltz, F.; Wiebcke, M.; Behrens, P., Modulated Synthesis of Zr-Based Metal–Organic Frameworks: From Nano to Single Crystals. *Chem. Eur. J.* **2011,** *17* (24), 6643-6651.

90 Yuan, S.; Liu, T. F.; Feng, D. W.; Tian, J.; Wang, K. C.; Qin, J. S.; Zhang, Q.; Chen, Y. P.; Bosch, M.; Zou, L. F.; Teat, S. J.; Dalgarno, S. J.; Zhou, H. C., A Single Crystalline Porphyrinic Titanium Metal-Organic Framework. *Chem. Sci.* **2015,** *6* (7), 3926-3930.

91 Meng, L.; Cheng, Q.; Kim, C.; Gao, W. Y.; Wojtas, L.; Chen, Y. S.; Zaworotko, M. J.; Zhang, X. P.; Ma, S., Crystal Engineering of a Microporous, Catalytically Active Fcu Topology MOF Using a Custom-Designed Metalloporphyrin Linker. *Angew. Chem. Int. Ed.* **2012,** *51* (40), 10082-10085.

92 Stoeck, U.; Krause, S.; Bon, V.; Senkovska, I.; Kaskel, S., A Highly Porous Metal-Organic Framework, Constructed from a Cuboctahedral Super-Molecular Building Block, with Exceptionally High Methane Uptake. *Chem. Commun.* **2012,** *48* (88), 10841-10843.

93 Xue, D. X.; Cairns, A. J.; Belmabkhout, Y.; Wojtas, L.; Liu, Y.; Alkordi, M. H.; Eddaoudi, M., Tunable Rare-Earth Fcu-MOFs: A Platform for Systematic Enhancement of CO_2 Adsorption Energetics and Uptake. *J. Am. Chem. Soc.* **2013,** *135* (20), 7660-7667.

94 Li, M.; Li, D.; O'Keeffe, M.; Yaghi, O. M., Topological Analysis of Metal-Organic Frameworks with Polytopic Linkers and/or Multiple Building Units and the Minimal Transitivity Principle. *Chem. Rev.* **2014,** *114* (2), 1343-1370.

95 Gomes Silva, C.; Luz, I.; Llabres i Xamena, F. X.; Corma, A.; Garcia, H., Water Stable Zr-Benzenedicarboxylate Metal-Organic Frameworks as Photocatalysts for Hydrogen Generation. *Chem. -Eur. J.* **2010,** *16* (36), 11133-11138.

96 Sun, D.; Fu, Y.; Liu, W.; Ye, L.; Wang, D.; Yang, L.; Fu, X.; Li, Z., Studies on Photocatalytic CO_2 Reduction over NH_2-UiO-66(Zr) and Its Derivatives: Towards a Better Understanding of Photocatalysis on Metal-Organic Frameworks. *Chem. -Eur. J.* **2013,** *19* (42), 14279-14285.

97 Fu, Y.; Sun, D.; Chen, Y.; Huang, R.; Ding, Z.; Fu, X.; Li, Z., An Amine-Functionalized Titanium Metal-Organic Framework Photocatalyst with Visible-Light-Induced Activity for CO_2 Reduction. *Angew. Chem. Int. Ed.* **2012,** *51* (14), 3364-3367.

98 Hendon, C. H.; Tiana, D.; Fontecave, M.; Sanchez, C.; D'Arras, L.; Sassoye, C.; Rozes, L.; Mellot-Draznieks, C.; Walsh, A., Engineering the Optical Response of the Titanium-MIL-125 Metal-Organic Framework through Ligand Functionalization. *J. Am. Chem. Soc.* **2013,** *135* (30), 10942-10945.

99 Cliffe, M. J.; Wan, W.; Zou, X.; Chater, P. A.; Kleppe, A. K.; Tucker, M. G.; Wilhelm, H.; Funnell, N. P.; Coudert, F.-X.; Goodwin, A. L., Correlated Defect Nanoregions in a Metal–Organic Framework. *Nat. Commun.* **2014,** *5*, 4176.

100 Wu, H.; Chua, Y. S.; Krungleviciute, V.; Tyagi, M.; Chen, P.; Yildirim, T.; Zhou, W., Unusual and Highly Tunable Missing-Linker Defects in Zirconium Metal–Organic Framework UiO-66 and Their Important Effects on Gas Adsorption. *J. Am. Chem. Soc.* **2013,** *135* (28), 10525-10532.

101 Shearer, G. C.; Chavan, S.; Ethiraj, J.; Vitillo, J. G.; Svelle, S.; Olsbye, U.; Lamberti, C.; Bordiga, S.; Lillerud, K. P., Tuned to Perfection: Ironing out the Defects in Metal–Organic Framework UiO-66. *Chem. Mater.* **2014,** *26* (14), 4068-4071.

102 Shearer, G. C.; Chavan, S.; Bordiga, S.; Svelle, S.; Olsbye, U.; Lillerud, K. P., Defect Engineering: Tuning the Porosity and Composition of the Metal–Organic Framework UiO-66 Via Modulated Synthesis. *Chem. Mater.* **2016,** *28* (11), 3749-3761.

103 Gutov, O. V.; Hevia, M. G.; Escudero-Adán, E. C.; Shafir, A., Metal–Organic Framework (MOF) Defects under Control: Insights into the Missing Linker Sites and Their Implication in the Reactivity of Zirconium-Based Frameworks. *Inorg. Chem.* **2015,** *54* (17), 8396-8400.

104 Marshall, R. J.; Hobday, C. L.; Murphie, C. F.; Griffin, S. L.; Morrison, C. A.; Moggach, S. A.; Forgan, R. S., Amino Acids as Highly Efficient Modulators for Single Crystals of Zirconium and Hafnium Metal-Organic Frameworks. *J. Mater. Chem. A* **2016,** *4* (18), 6955-6963.

105 Hoang, L. T. M.; Ngo, L. H.; Nguyen, H. L.; Nguyen, H. T. H.; Nguyen, C. K.; Nguyen, B. T.; Ton, Q. T.; Nguyen, H. K. D.; Cordova, K. E.; Truong, T., An Azobenzene-Containing Metal-Organic Framework as an Efficient Heterogeneous Catalyst for Direct Amidation of

Benzoic Acids: Synthesis of Bioactive Compounds. *Chem. Commun.* **2015,** *51* (96), 17132-17135.

106 Yang, Q.; Guillerm, V.; Ragon, F.; Wiersum, A. D.; Llewellyn, P. L.; Zhong, C.; Devic, T.; Serre, C.; Maurin, G., Ch4 Storage and CO2 Capture in Highly Porous Zirconium Oxide Based Metal-Organic Frameworks. *Chem. Commun.* **2012,** *48* (79), 9831-9833.

107 Gao, W.-Y.; Thiounn, T.; Wojtas, L.; Chen, Y.-S.; Ma, S., Two Highly Porous Single-Crystalline Zirconium-Based Metal-Organic Frameworks. *Sci. China Chem.* **2016,** *59* (8), 980-983.

108 Karagiaridi, O.; Bury, W.; Mondloch, J. E.; Hupp, J. T.; Farha, O. K., Solvent-Assisted Linker Exchange: An Alternative to the De Novo Synthesis of Unattainable Metal–Organic Frameworks. *Angew. Chem. Int. Ed.* **2014,** *53* (18), 4530-4540.

109 Kim, M.; Cahill, J. F.; Fei, H.; Prather, K. A.; Cohen, S. M., Postsynthetic Ligand and Cation Exchange in Robust Metal–Organic Frameworks. *J. Am. Chem. Soc.* **2012,** *134* (43), 18082-18088.

110 Deria, P.; Mondloch, J. E.; Tylianakis, E.; Ghosh, P.; Bury, W.; Snurr, R. Q.; Hupp, J. T.; Farha, O. K., Perfluoroalkane Functionalization of Nu-1000 Via Solvent-Assisted Ligand Incorporation: Synthesis and CO_2 Adsorption Studies. *J. Am. Chem. Soc.* **2013,** *135* (45), 16801-16804.

111 Trickett, C. A.; Gagnon, K. J.; Lee, S.; Gándara, F.; Bürgi, H.-B.; Yaghi, O. M., Definitive Molecular Level Characterization of Defects in UiO-66 Crystals. *Angew. Chem. Int. Ed.* **2015,** *54* (38), 11162-11167.

112 Huang, H.; Li, J.-R.; Wang, K.; Han, T.; Tong, M.; Li, L.; Xie, Y.; Yang, Q.; Liu, D.; Zhong, C., An in Situ Self-Assembly Template Strategy for the Preparation of Hierarchical-Pore Metal-Organic Frameworks. *Nat. Commun.* **2015,** *6*, 8847.

113 Yue, Y.; Qiao, Z.-A.; Fulvio, P. F.; Binder, A. J.; Tian, C.; Chen, J.; Nelson, K. M.; Zhu, X.; Dai, S., Template-Free Synthesis of Hierarchical Porous Metal–Organic Frameworks. *J. Am. Chem. Soc.* **2013,** *135* (26), 9572-9575.

114 Yue, Y.; Fulvio, P. F.; Dai, S., Hierarchical Metal–Organic Framework Hybrids: Perturbation-Assisted Nanofusion Synthesis. *Acc. Chem. Res.* **2015,** *48* (12), 3044-3052.

115 Wang, C.; Liu, X.; Chen, J. P.; Li, K., Superior Removal of Arsenic from Water with Zirconium Metal-Organic Framework UiO-66. *Sci. Rep.* **2015,** *5*, 16613.

116 Howarth, A. J.; Katz, M. J.; Wang, T. C.; Platero-Prats, A. E.; Chapman, K. W.; Hupp, J. T.; Farha, O. K., High Efficiency Adsorption and Removal of Selenate and Selenite from Water Using Metal–Organic Frameworks. *J. Am. Chem. Soc.* **2015,** *137* (23), 7488-7494.

117 Lo, S.-H.; Chien, C.-H.; Lai, Y.-L.; Yang, C.-C.; Lee, J. J.; Raja, D. S.; Lin, C.-H., A Mesoporous Aluminium Metal-Organic Framework with 3 Nm Open Pores. *J. Mater. Chem. A* **2013,** *1* (2), 324-329.

118 Lykourinou, V.; Chen, Y.; Wang, X.-S.; Meng, L.; Hoang, T.; Ming, L.-J.; Musselman, R. L.; Ma, S., Immobilization of Mp-11 into a Mesoporous Metal–Organic Framework, Mp-11@Mesomof: A New Platform for Enzymatic Catalysis. *J. Am. Chem. Soc.* **2011,** *133* (27), 10382-10385.

119 Chen, Y.; Ma, S., Biomimetic Catalysis of Metal-Organic Frameworks. *Dalton Trans.* **2016,** *45* (24), 9744-9753.

120 Gkaniatsou, E.; Sicard, C.; Ricoux, R.; Mahy, J.-P.; Steunou, N.; Serre, C., Metal-Organic Frameworks: A Novel Host Platform for Enzymatic Catalysis and Detection. *Materials Horizons* **2017,** *4* (1), 55-63.

121 Li, P.; Modica, Justin A.; Howarth, Ashlee J.; Vargas L, E.; Moghadam, Peyman Z.; Snurr, Randall Q.; Mrksich, M.; Hupp, Joseph T.; Farha, Omar K., Toward Design Rules for Enzyme Immobilization in Hierarchical Mesoporous Metal-Organic Frameworks. *Chem* **2016,** *1* (1), 154-169.

122 Chen, Y.; Lykourinou, V.; Hoang, T.; Ming, L.-J.; Ma, S., Size-Selective Biocatalysis of Myoglobin Immobilized into a Mesoporous Metal–Organic Framework with Hierarchical Pore Sizes. *Inorg. Chem.* **2012,** *51* (17), 9156-9158.

123 Zhou, H.-C.; Long, J. R.; Yaghi, O. M., Introduction to Metal–Organic Frameworks. *Chem. Rev.* **2012,** *112* (2), 673-674.

124 Cohen, S. M., Postsynthetic Methods for the Functionalization of Metal-Organic Frameworks. *Chem. Rev.* **2012,** *112* (2), 970-1000.

125 Yoon, M.; Srirambalaji, R.; Kim, K., Homochiral Metal-Organic Frameworks for Asymmetric Heterogeneous Catalysis. *Chem. Rev.* **2012,** *112* (2), 1196-231.

126 Chun, H.; Dybtsev, D. N.; Kim, H.; Kim, K., Synthesis, X-Ray Crystal Structures, and Gas Sorption Properties of Pillared Square Grid Nets Based on Paddle-Wheel Motifs: Implications for Hydrogen Storage in Porous Materials. *Chem. Eur. J.* **2005,** *11* (12), 3521-3529.

127 Wang, C.; Xie, Z.; deKrafft, K. E.; Lin, W., Doping Metal–Organic Frameworks for Water Oxidation, Carbon Dioxide Reduction, and Organic Photocatalysis. *J. Am. Chem. Soc.* **2011,** *133* (34), 13445-13454.

128 Furukawa, H.; Ko, N.; Go, Y. B.; Aratani, N.; Choi, S. B.; Choi, E.; Yazaydin, A. O.; Snurr, R. Q.; O'Keeffe, M.; Kim, J.; Yaghi, O. M., Ultrahigh Porosity in Metal-Organic Frameworks. *Science* **2010,** *329* (5990), 424-428.

129 Koh, K.; Wong-Foy, A. G.; Matzger, A. J., A Crystalline Mesoporous Coordination Copolymer with High Microporosity. *Angew. Chem. Int. Ed.* **2008,** *47* (4), 677-680.

130 Doonan, C. J.; Morris, W.; Furukawa, H.; Yaghi, O. M., Isoreticular Metalation of Metal-Organic Frameworks. *J. Am. Chem. Soc.* **2009,** *131* (27), 9492-3.

131 Ma, B.-Q.; Mulfort, K. L.; Hupp, J. T., Microporous Pillared Paddle-Wheel Frameworks Based on Mixed-Ligand Coordination of Zinc Ions. *Inorg. Chem.* **2005,** *44* (14), 4912-4914.

132 Fukushima, T.; Horike, S.; Inubushi, Y.; Nakagawa, K.; Kubota, Y.; Takata, M.; Kitagawa, S., Solid Solutions of Soft Porous Coordination Polymers: Fine-Tuning of Gas Adsorption Properties. *Angew. Chem. Int. Ed.* **2010,** *49* (28), 4820-4824.

133 Deria, P.; Mondloch, J. E.; Karagiaridi, O.; Bury, W.; Hupp, J. T.; Farha, O. K., Beyond Post-Synthesis Modification: Evolution of Metal-Organic Frameworks Via Building Block Replacement. *Chem. Soc. Rev.* **2014,** *43* (16), 5896-912.

134 Yamada, T.; Kitagawa, H., Protection and Deprotection Approach for the Introduction of Functional Groups into Metal−Organic Frameworks. *J. Am. Chem. Soc.* **2009,** *131* (18), 6312-6313.

135 Chevreau, H.; Devic, T.; Salles, F.; Maurin, G.; Stock, N.; Serre, C., Mixed-Linker Hybrid Superpolyhedra for the Production of a Series of Large-Pore Iron(III) Carboxylate Metal-Organic Frameworks. *Angew. Chem. Int. Ed. Engl.* **2013,** *52* (19), 5056-60.

136 Dybtsev, D. N.; Chun, H.; Kim, K., Rigid and Flexible: A Highly Porous Metal–Organic Framework with Unusual Guest-Dependent Dynamic Behavior. *Angew. Chem. Int. Ed.* **2004,** *43* (38), 5033-5036.

137 Rankine, D.; Avellaneda, A.; Hill, M. R.; Doonan, C. J.; Sumby, C. J., Control of Framework Interpenetration for in Situ Modified Hydroxyl Functionalised Irmofs. *Chem. Commun.* **2012,** *48* (83), 10328-10330.

138 Dau, P. V.; Cohen, S. M., A Bifunctional, Site-Isolated Metal–Organic Framework-Based

Tandem Catalyst. *Inorg. Chem.* **2015,** *54* (7), 3134-3138.

139 Furukawa, H.; Kim, J.; Ockwig, N. W.; O'Keeffe, M.; Yaghi, O. M., Control of Vertex Geometry, Structure Dimensionality, Functionality, and Pore Metrics in the Reticular Synthesis of Crystalline Metal−Organic Frameworks and Polyhedra. *J. Am. Chem. Soc.* **2008,** *130* (35), 11650-11661.

140 Dau, P. V.; Cohen, S. M., The Influence of Nitro Groups on the Topology and Gas Sorption Property of Extended Zn(Ii)-Paddlewheel MOFs. *CrystEngComm* **2013,** *15* (45), 9304-9307.

141 Chen, J.-C.; Chiang, C.-J.; Liu, Y.-C., Synthesis, Optical and Electrochemical Properties of Novel Hole-Blocking Poly(Biphenylene-1,3,4-Oxadiazole) Containing Electron-Withdrawing Trifluoromethyl Groups. *Synth. Met.* **2010,** *160* (17–18), 1953-1961.

142 Nielsen, A. T.; Norris, W. P.; Atkins, R. L.; Vuono, W. R., Nitrocarbons. 3. Synthesis of Decanitrobiphenyl. *J. Org. Chem.* **1983,** *48* (7), 1056-1059.

143 Hu, X.; Kumar, S.; Polk, M. B.; Gelbaum, L., Synthesis of 2,2',6,6'-Tetramethylbiphenyl-4,4'-Dibenzthiazole. *Synth. Commun.* **1998,** *28* (11), 2049-2055.

144 Hisaki, I.; Shigemitsu, H.; Sakamoto, Y.; Hasegawa, Y.; Okajima, Y.; Nakano, K.; Tohnai, N.; Miyata, M., Octadehydrodibenzo[12]Annulene-Based Organogels: Two Methyl Ester Groups Prevent Crystallization and Promote Gelation. *Angew. Chem.* **2009,** *121* (30), 5573-5577.

145 Burrows, A. D.; Frost, C. G.; Mahon, M. F.; Richardson, C., Sulfur-Tagged Metal-Organic Frameworks and Their Post-Synthetic Oxidation. *Chem. Commun.* **2009,** (28), 4218-4220.

146 Sheldrick, G. M., *SHELXTL*, Version 6.14, Structure Determination Software Suite, Bruker AXS, Madison, WI, 2003.

147 Delgado-Friedrichs, O.; O'Keeffe, M.; Yaghi, O. M., Three-Periodic Nets and Tilings: Edge-Transitive Binodal Structures. *Acta Crystallographica Section A* **2006,** *62* (5), 350-355.

148 Furukawa, H.; Gandara, F.; Zhang, Y. B.; Jiang, J.; Queen, W. L.; Hudson, M. R.; Yaghi, O. M., Water Adsorption in Porous Metal-Organic Frameworks and Related Materials. *J. Am. Chem. Soc.* **2014,** *136* (11), 4369-81.

149 Bon, V.; Senkovska, I.; Weiss, M. S.; Kaskel, S., Tailoring of Network Dimensionality and Porosity Adjustment in Zr- and Hf-Based MOFs. *CrystEngComm* **2013,** *15* (45), 9572-9577.

150 Eddaoudi, M.; Kim, J.; O'Keeffe, M.; Yaghi, O. M., Cu2[O-Br-C6h3(CO2)2]2(H2O)2·(Dmf)8(H2O)2: A Framework Deliberately Designed to Have the Nbo Structure Type. *J. Am. Chem. Soc.* **2001,** *124* (3), 376-377.

151 Mondloch, J. E.; Katz, M. J.; Planas, N.; Semrouni, D.; Gagliardi, L.; Hupp, J. T.; Farha, O. K., Are Zr6-Based MOFs Water Stable? Linker Hydrolysis Vs. Capillary-Force-Driven Channel Collapse. *Chem. Commun.* **2014,** *50* (64), 8944-8946.

152 Simmons, G., *Single-Crystal Elastic Constants and Calculated Aggregate Properties*. 1965.

153 Horcajada, P.; Salles, F.; Wuttke, S.; Devic, T.; Heurtaux, D.; Maurin, G.; Vimont, A.; Daturi, M.; David, O.; Magnier, E.; Stock, N.; Filinchuk, Y.; Popov, D.; Riekel, C.; Ferey, G.; Serre, C., How Linker's Modification Controls Swelling Properties of Highly Flexible Iron(III) Dicarboxylates MIL-88. *J. Am. Chem. Soc.* **2011,** *133* (44), 17839-47.

154 Lescouet, T.; Kockrick, E.; Bergeret, G.; Pera-Titus, M.; Aguado, S.; Farrusseng, D., Homogeneity of Flexible Metal-Organic Frameworks Containing Mixed Linkers. *J. Mater. Chem.* **2012,** *22* (20), 10287-10293.

155 Blatov, V. A. T. P., Commission on Crystallographic Computing, IUCr, 2006. .

156 Corey, E. J.; Suggs, J. W., Pyridinium Chlorochromate. An Efficient Reagent for Oxidation of Primary and Secondary Alcohols to Carbonyl Compounds. *Tetrahedron Lett.* **1975,** *16* (31), 2647-2650.

157 Ladbury, J. W.; Cullis, C. F., Kinetics and Mechanism of Oxidation by Permanganate. *Chem. Rev.* **1958,** *58* (2), 403-438.

158 Dhakshinamoorthy, A.; Alvaro, M.; Garcia, H., Metal-Organic Frameworks as Heterogeneous Catalysts for Oxidation Reactions. *Catalysis Science & Technology* **2011,** *1* (6), 856-867.

159 Hoover, J. M.; Ryland, B. L.; Stahl, S. S., Mechanism of Copper(I)/Tempo-Catalyzed Aerobic Alcohol Oxidation. *J. Am. Chem. Soc.* **2013,** *135* (6), 2357-2367.

160 Hoover, J. M.; Stahl, S. S., Highly Practical Copper(I)/Tempo Catalyst System for Chemoselective Aerobic Oxidation of Primary Alcohols. *J. Am. Chem. Soc.* **2011,** *133* (42), 16901-16910.

161 Cotton, F. A., Transition-Metal Compounds Containing Clusters of Metal Atoms. *Quarterly Reviews, Chemical Society* **1966,** *20* (3), 389-401.

162 Cotton, F. A.; Curtis, N. F.; Harris, C. B.; Johnson, B. F. G.; Lippard, S. J.; Mague, J. T.; Robinson, W. R.; Wood, J. S., Mononuclear and Polynuclear Chemistry of Rhenium (III): Its Pronounced Homophilicity. *Science* **1964,** *145* (3638), 1305-1307.

163 Buchwalter, P.; Rosé, J.; Braunstein, P., Multimetallic Catalysis Based on Heterometallic Complexes and Clusters. *Chem. Rev.* **2015,** *115* (1), 28-126.

164 Adams, R. D.; Rassolov, V.; Wong, Y. O., Facile C H Bond Formation by Reductive Elimination at a Dinuclear Metal Site. *Angew. Chem.* **2014,** *126* (41), 11186-11189.

165 Adams, R. D.; Captain, B., Hydrogen Activation by Unsaturated Mixed-Metal Cluster Complexes: New Directions. *Angew. Chem. Int. Ed.* **2008,** *47* (2), 252-257.

166 Alexeev, O. S.; Gates, B. C., Supported Bimetallic Cluster Catalysts. *Industrial & Engineering Chemistry Research* **2003,** *42* (8), 1571-1587.

167 Liu, J.; Chen, L.; Cui, H.; Zhang, J.; Zhang, L.; Su, C. Y., Applications of Metal-Organic Frameworks in Heterogeneous Supramolecular Catalysis. *Chem. Soc. Rev.* **2014,** *43* (16), 6011-61.

168 Furukawa, H.; Ko, N.; Go, Y. B.; Aratani, N.; Choi, S. B.; Choi, E.; Yazaydin, A. Ö.; Snurr, R. Q.; O'Keeffe, M.; Kim, J.; Yaghi, O. M., Ultrahigh Porosity in Metal-Organic Frameworks. *Science* **2010,** *329* (5990), 424-428.

169 Kurmoo, M., Magnetic Metal-Organic Frameworks. *Chem. Soc. Rev.* **2009,** *38* (5), 1353-79.

170 Greathouse, J. A.; Allendorf, M. D., The Interaction of Water with MOF-5 Simulated by Molecular Dynamics. *J. Am. Chem. Soc.* **2006,** *128* (33), 10678-10679.

171 Guillerm, V.; Ragon, F.; Dan-Hardi, M.; Devic, T.; Vishnuvarthan, M.; Campo, B.; Vimont, A.; Clet, G.; Yang, Q.; Maurin, G.; Férey, G.; Vittadini, A.; Gross, S.; Serre, C., A Series of Isoreticular, Highly Stable, Porous Zirconium Oxide Based Metal–Organic Frameworks. *Angew. Chem. Int. Ed.* **2012,** *51* (37), 9267-9271.

172 Furukawa, H.; Gándara, F.; Zhang, Y.-B.; Jiang, J.; Queen, W. L.; Hudson, M. R.; Yaghi, O. M., Water Adsorption in Porous Metal–Organic Frameworks and Related Materials. *J. Am. Chem. Soc.* **2014,** *136* (11), 4369-4381.

173 Feng, D.; Gu, Z.-Y.; Chen, Y.-P.; Park, J.; Wei, Z.; Sun, Y.; Bosch, M.; Yuan, S.; Zhou, H.-C., A Highly Stable Porphyrinic Zirconium Metal–Organic Framework with Shp-a Topology. *J. Am. Chem. Soc.* **2014,** *136* (51), 17714-17717.

174 Jiang, J.; Gándara, F.; Zhang, Y.-B.; Na, K.; Yaghi, O. M.; Klemperer, W. G., Superacidity in Sulfated Metal–Organic Framework-808. *J. Am. Chem. Soc.* **2014,** *136* (37), 12844-12847.

175 Zhang, Z.-M.; Zhang, T.; Wang, C.; Lin, Z.; Long, L.-S.; Lin, W., Photosensitizing Metal–Organic Framework Enabling Visible-Light-Driven Proton Reduction by a Wells–Dawson-Type Polyoxometalate. *J. Am. Chem. Soc.* **2015,** *137* (9), 3197-3200.

176 Wu, H.; Chua, Y. S.; Krungleviciute, V.; Tyagi, M.; Chen, P.; Yildirim, T.; Zhou, W., Unusual and Highly Tunable Missing-Linker Defects in Zirconium Metal-Organic Framework UiO-66 and Their Important Effects on Gas Adsorption. *J. Am. Chem. Soc.* **2013,** *135* (28), 10525-32.

177 Vermoortele, F.; Bueken, B.; Le Bars, G.; Van de Voorde, B.; Vandichel, M.; Houthoofd, K.; Vimont, A.; Daturi, M.; Waroquier, M.; Van Speybroeck, V.; Kirschhock, C.; De Vos, D. E., Synthesis Modulation as a Tool to Increase the Catalytic Activity of Metal–Organic Frameworks: The Unique Case of UiO-66(Zr). *J. Am. Chem. Soc.* **2013,** *135* (31), 11465-11468.

178 Smith, S. J. D.; Ladewig, B. P.; Hill, A. J.; Lau, C. H.; Hill, M. R., Post-Synthetic Ti Exchanged UiO-66 Metal-Organic Frameworks That Deliver Exceptional Gas Permeability in Mixed Matrix Membranes. *Sci. Rep.* **2015,** *5*.

179 Hon Lau, C.; Babarao, R.; Hill, M. R., A Route to Drastic Increase of CO2 Uptake in Zr Metal Organic Framework UiO-66. *Chem. Commun.* **2013,** *49* (35), 3634-3636.

180 Lee, Y.; Kim, S.; Kang, J. K.; Cohen, S. M., Photocatalytic CO2 Reduction by a Mixed Metal (Zr/Ti), Mixed Ligand Metal-Organic Framework under Visible Light Irradiation. *Chem. Commun.* **2015,** *51* (26), 5735-5738.

181 Ooi, L.-l., *Principles of X-Ray Crystallography*. Oxford University Press: 2010.

182 Sheldrick, G., A Short History of Shelx. *Acta Crystallographica Section A* **2008,** *64* (1), 112-122.

183 Bloch, W. M.; Burgun, A.; Coghlan, C. J.; Lee, R.; Coote, M. L.; Doonan, C. J.; Sumby, C. J., Capturing Snapshots of Post-Synthetic Metallation Chemistry in Metal-Organic Frameworks. *Nature chemistry* **2014,** *6* (10), 906-12.

184 Malaestean, I. L.; Speldrich, M.; Ellern, A.; Baca, S. G.; Kogerler, P., Heterometal Expansion of Oxozirconium Carboxylate Clusters. *Dalton Trans* **2011,** *40* (2), 331-3.

185 Planas, N.; Mondloch, J. E.; Tussupbayev, S.; Borycz, J.; Gagliardi, L.; Hupp, J. T.; Farha, O.

K.; Cramer, C. J., Defining the Proton Topology of the Zr6-Based Metal–Organic Framework Nu-1000. *J. Phys. Chem. Lett.* **2014,** *5* (21), 3716-3723.

186 Tian, J.; Saraf, L. V.; Schwenzer, B.; Taylor, S. M.; Brechin, E. K.; Liu, J.; Dalgarno, S. J.; Thallapally, P. K., Selective Metal Cation Capture by Soft Anionic Metal-Organic Frameworks Via Drastic Single-Crystal-to-Single-Crystal Transformations. *J. Am. Chem. Soc.* **2012,** *134* (23), 9581-4.

187 Elamparuthi, E.; Ramesh, E.; Raghunathan, R., Incl3 as an Efficient Catalyst for Cyclotrimerization of Aldehydes: Synthesis of 1,3,5 - Trioxane under Solvent - Free Conditions. *Synth. Commun.* **2005,** *35* (21), 2801-2804.

188 Nicolaou, K. C.; Vourloumis, D.; Winssinger, N.; Baran, P. S., The Art and Science of Total Synthesis at the Dawn of the Twenty-First Century. *Angew. Chem. Int. Ed.* **2000,** *39* (1), 44-122.

189 Corey, E. J.; Cheng, X.-M., *The Logic of Chemical Synthesis*. Wiley: 1995.

190 Feng, D.; Chung, W.-C.; Wei, Z.; Gu, Z.-Y.; Jiang, H.-L.; Chen, Y.-P.; Darensbourg, D. J.; Zhou, H.-C., Construction of Ultrastable Porphyrin Zr Metal–Organic Frameworks through Linker Elimination. *J. Am. Chem. Soc.* **2013,** *135* (45), 17105-17110.

191 O'Keeffe, M.; Peskov, M. A.; Ramsden, S. J.; Yaghi, O. M., The Reticular Chemistry Structure Resource (Rcsr) Database of, and Symbols for, Crystal Nets. *Acc. Chem. Res.* **2008,** *41* (12), 1782-1789.

192 Shen, J.-Q.; Liao, P.-Q.; Zhou, D.-D.; He, C.-T.; Wu, J.-X.; Zhang, W.-X.; Zhang, J.-P.; Chen, X.-M., Modular and Stepwise Synthesis of a Hybrid Metal–Organic Framework for Efficient Electrocatalytic Oxygen Evolution. *J. Am. Chem. Soc.* **2017,** *139* (5), 1778-1781.

193 Steinhagen, H.; Helmchen, G., Asymmetric Two-Center Catalysis—Learning from Nature. *Angew. Chem. Int. Ed.* **1996,** *35* (20), 2339-2342.

194 Ma, J.-A.; Cahard, D., Towards Perfect Catalytic Asymmetric Synthesis: Dual Activation of the Electrophile and the Nucleophile. *Angew. Chem. Int. Ed.* **2004,** *43* (35), 4566-4583.

195 Haak, R. M.; Wezenberg, S. J.; Kleij, A. W., Cooperative Multimetallic Catalysis Using Metallosalens. *Chem. Commun.* **2010,** *46* (16), 2713-2723.

196 Shibasaki, M.; Kanai, M.; Matsunaga, S.; Kumagai, N., Recent Progress in Asymmetric Bifunctional Catalysis Using Multimetallic Systems. *Acc. Chem. Res.* **2009,** *42* (8), 1117-1127.

197 Strecker, A., Ueber Die Künstliche Bildung Der Milchsäure Und Einen Neuen, Dem Glycocoll Homologen Körper. *Eur. J. Org. Chem.* **1850,** *75* (1), 27-45.

198 Enders, D.; Shilvock, J. P., Some Recent Applications of α-Amino Nitrile Chemistry. *Chem. Soc. Rev.* **2000,** *29* (5), 359-373.

199 Gröger, H., Catalytic Enantioselective Strecker Reactions and Analogous Syntheses. *Chem. Rev.* **2003,** *103* (8), 2795-2828.

200 Wang, J.; Liu, X.; Feng, X., Asymmetric Strecker Reactions. *Chem. Rev.* **2011,** *111* (11), 6947-6983.

201 Jacobsen, E. N., Asymmetric Catalysis of Epoxide Ring-Opening Reactions. *Acc. Chem. Res.* **2000,** *33* (6), 421-431.

202 Aguirre-Díaz, L. M.; Gándara, F.; Iglesias, M.; Snejko, N.; Gutiérrez-Puebla, E.; Monge, M. Á., Tunable Catalytic Activity of Solid Solution Metal–Organic Frameworks in One-Pot Multicomponent Reactions. *J. Am. Chem. Soc.* **2015,** *137* (19), 6132-6135.

203 Hou, Y.-L.; Sun, R. W.-Y.; Zhou, X.-P.; Wang, J.-H.; Li, D., A Copper(I)/Copper(Ii)-Salen Coordination Polymer as a Bimetallic Catalyst for Three-Component Strecker Reactions and Degradation of Organic Dyes. *Chem. Commun.* **2014,** *50* (18), 2295-2297.

204 Tanabe, K. K.; Cohen, S. M., Postsynthetic Modification of Metal-Organic Frameworks-a Progress Report. *Chem. Soc. Rev.* **2011,** *40* (2), 498-519.

205 Hwang, J.; Rao, R. R.; Giordano, L.; Katayama, Y.; Yu, Y.; Shao-Horn, Y., Perovskites in Catalysis and Electrocatalysis. *Science* **2017,** *358* (6364), 751-756.

206 Hunter, B. M.; Gray, H. B.; Müller, A. M., Earth-Abundant Heterogeneous Water Oxidation Catalysts. *Chem. Rev.* **2016,** *116* (22), 14120-14136.

207 Nouar, F.; Breeze, M. I.; Campo, B. C.; Vimont, A.; Clet, G.; Daturi, M.; Devic, T.; Walton, R. I.; Serre, C., Tuning the Properties of the UiO-66 Metal Organic Framework by Ce Substitution. *Chem. Commun.* **2015,** *51* (77), 14458-14461.

208 Elias, J. S.; Risch, M.; Giordano, L.; Mansour, A. N.; Shao-Horn, Y., Structure, Bonding, and Catalytic Activity of Monodisperse, Transition-Metal-Substituted Ceo2 Nanoparticles. *J. Am. Chem. Soc.* **2014,** *136* (49), 17193-17200.

209 Elias, J. S.; Stoerzinger, K. A.; Hong, W. T.; Risch, M.; Giordano, L.; Mansour, A. N.; Shao-

Horn, Y., In Situ Spectroscopy and Mechanistic Insights into Co Oxidation on Transition-Metal-Substituted Ceria Nanoparticles. *ACS Catal.* **2017,** *7* (10), 6843-6857.

210 Montini, T.; Melchionna, M.; Monai, M.; Fornasiero, P., Fundamentals and Catalytic Applications of Ceo2-Based Materials. *Chem. Rev.* **2016,** *116* (10), 5987-6041.

211 Lee, S., Methanol Synthesis from Syngas. In *Handbook of Alternative Fuel Technologies*, CRC Press: 2007; 297-321.